Memristive Dynamics of Ag-based Nanostructures for Neuromorphic Systems

Dissertation

zur Erlangung des akademischen Grades
Doktor der Ingenieurswissenschaften (Dr.-Ing.)
eingereicht an der
Technischen Fakultät
der Christian-Albrechts-Universität zu Kiel

Niko Carstens
Kiel, 2022

Erster Gutachter:	Prof. Dr. Franz Faupel
Zweiter Gutachter:	Prof. Dr. Hermann Kohlstedt
Datum der mündlichen Prüfung:	22. August 2022

Eidesstattliche Erklärung

Hiermit erkläre ich, dass Inhalt und Form dieser Arbeit, abgesehen von Beratung durch meine Betreuer, eigenständig von mir und nur mit den angegebenen Hilfsmitteln angefertigt wurde. Externe Quellen und Zusammenarbeit habe ich in dieser Thesis vermerkt. Ich bestätige, dass diese Arbeit an keiner anderen Stelle im Rahmen eines Prüfungsverfahrens vorgelegen hat. Teile dieser Arbeit sind in wissenschaftlichen Jounals publiziert oder zur Publikation eingereicht. Dies habe ich in der Arbeit entsprechend vermerkt. Diese Arbeit ist unter Einhaltung der Regeln guter wissenschaftlicher Praxis gemäß DFG entstanden. Zudem bestätige ich, dass mir bisher noch kein akademischer Grad entzogen wurde.

Ort, Datum Unterschrift

Im Folgenden sollen die Eigenanteile jener Publikationen angegeben werden, die Bestandteil dieser kumulativen Dissertation sind. Der Eigenanteil wird anhand folgender Faktoren bestimmt: Konzeptualisierung der Untersuchung (**K**), Probenherstellung (**P**), Datensammlung (**D**), Interpretation der Daten (**I**) und Erstellung des Manuskipts (**M**).

Publikation/Manuskript	**K**	**P**	**D**	**I**	**M**
Chapter 4: N. Carstens, A. Vahl, O. Gronenberg, T. Strunskus, L. Kienle, F. Faupel and A. Hassanien, *Nanomaterials*, 2021, 11, 265	hoch	hoch	gering	hoch	hoch
Chapter 5: N. Carstens, T. Strunskus, F. Faupel, A. Hassanien and A. Vahl, *Submitted*, 2022	hoch	hoch	gering	hoch	hoch
Chapter 6: A. Vahl, **N. Carstens**, T. Strunskus, F. Faupel and A. Hassanien, *Scientific Reports*, 2019, 9, 17367	gering	gering	mittel	mittel	gering
Chapter 8: M.-I. Terasa, P. Holtz, **N. Carstens**, S. Kaps, F. Faupel, A. Vahl and R. Adelung, *PLOS One*, 2022, 17(3):e0264846	gering	mittel	kein	mittel	gering
Chapter 9: N. Carstens, B. Adejube, T. Strunskus, F. Faupel, S. Brown and A. Vahl, *Nanoscale Advances*, *Accepted*, 2022	hoch	hoch	hoch	hoch	hoch

Danksagungen

An dieser Stelle möchte ich mich bei allen bedanken, die durch ihr Wirken und ihre Unterstützung einen Teil zu dieser Arbeit beigetragen haben.

Allen voran gilt mein Dank meinem Doktorvater Franz Faupel, der es mir ermöglicht hat diese Arbeit in einem spannenden Projektrahmen und einem tollen Forschungsumfeld anzufertigen. Für sein Vertrauen, Möglichkeiten der eigenen Entfaltung und alle Dinge, die ich von ihm lernen durfte, bin ich zutiefst dankbar.

Besonderer Dank gilt Alexander Vahl. Von der Anfangsphase meiner Arbeit, in der er mich in das Projekt eingearbeitet hat, bis hin zur Abschlussphase, in der er ein prüfendes Auge auf diese Dissertation geworfen hat, stand er mir jederzeit mit Rat und Tat zur Seite. Für allen wissenschaftlichen und freundschaftlichen Austausch mit ihm bin ich sehr dankbar.

Zudem möchte ich mich bei Abdou Hassanien vom Jozef Stefan Institut in Ljubljana und Simon Brown von der Universität Canterbury in Christchurch für die erfolgreichen Kooperationen bedanken. Der enge Austausch mit beiden hat maßgeblich zum Horizont dieser Arbeit beigetragen.

Außerdem bedanke ich mich bei meinen Kollegen aus dem Umfeld der Forschergruppe und des SFBs, insbesondere bei meinen Mit-Doktoranden Ole Gronenberg, Maik-Ivo Terasa, Tom Birkoben, Blessing Adejube und Rohit Gupta. Durch zahlreiche Diskussionen und die daraus entstandenen Ideen haben sie maßgeblich zum tollen Arbeitsumfeld beigetragen.

Ganz herzlich möchte ich mich beim gesamten Lehrstuhl für Materialverbunde für die wunderbare Atmosphäre der letzten Jahre bedanken. Besonderer Dank gilt hierbei meinen Bürokollegen Alex, Jonas, Stefan und Thomas dafür, dass der Arbeitsalltag stets durch tollen Humor aufgelockert wurde und dafür, dass für Fragen und Probleme immer ein offenes Ohr zu finden war. Bei Stefan Rehders bedanke ich mich für die jederzeit kompetente und wertvolle Hilfe bei technischen Problemen.

Zu guter Letzt möchte ich mich bei meiner Familie und meiner Freundin Hanna für sämtliche Unterstützung und guten Zuspruch der vergangenen Jahre bedanken.

Kurzfassung

Aufgrund der zugrundeliegenden transistorbasierten Systemarchitektur sind derzeitige Bestrebungen die Leistungsfähigkeit heutiger Computerhardware zu verbessern stark eingeschränkt. Besonders deutlich wird dies durch den wahrscheinlichen Ablauf des Mooreschen Gesetzes, was impliziert, dass eine weitere Miniaturisierung des Transistors als Strategie zur Entwicklung zukünftiger Hardware nicht mehr umsetzbar sein wird. Zudem sind heutige Computersysteme durch die von-Neumann-Architektur eingeschränkt, welche eine Trennung von Einheiten zur Datenspeicherung und –verarbeitung vorgibt. Die Anwendung einer solchen Architektur impliziert einen enormen Zeit- und Energieaufwand für den permanenten Datentransfer zwischen beiden Einheiten, was besonders problematisch bei der Verarbeitung großer Datenmengen ist. Das Forschungsfeld Neuromorphic Computing hat sich als Ziel gesetzt, neuartige Computersysteme zu entwickeln, die der effizienten Lösung von Problemen im Zusammenhang mit der Verarbeitung riesiger Datenmengen dienen. Als typisches Beispiel hierfür seien Mustererkennungsprobleme genannt. Zur Verwirklichung dienen die außergewöhnlichen Rechenfähigkeiten biologischer neuronaler Systeme als Vorbild für das Design von neuromorphen Systemen. Für die Herstellung neuromorpher Systeme spielen memristive Bauteile eine Schlüsselrolle. Die grundlegende Eigenschaft eines memristiven Bauteils ist die Abhängigkeit seines elektrischen Widerstands von vorausgegangenen elektrischen Inputs. Daraus lassen sich Möglichkeiten erschließen, Funktionen ähnlich denen einer Synapse für den Entwurf von elektrischen Schaltungen zu nutzen. Obwohl ein prinzipieller Anspruch des Neuromorphic Computing darin liegt, Designparadigmen aus der Biologie zu erschließen, fokussierten sich frühe Entwicklungen neuromorpher Systeme auf die Hardwareumsetzung von künstlichen neuronalen Netzen, was eher (menschengemachte) mathematische Konzepte sind. In diesem Zusammenhang wurden neuromorphe Architekturen entwickelt, die durch eine reguläre Anordnung und starre Beschaltung von memristive Bauteilen geprägt ist. Für das Lösen von Rechenproblemen mit solchen Systemen ist es zudem gefordert, dass die Zustände aller Elemente exakt kontrollierbar sind. Im Widerspruch dazu erlangen biologische neuronale Systeme ihre Rechenfähigkeiten durch (evolutionsgemachte) Architekturen, welche durch ein hohes Maß an Konnektivität, Selbstorganisation durch ständige Neuvernetzung und Ausnutzung von emergentem Netzwerkverhalten geprägt sind. Folglich gibt es noch viel Potenzial um Paradigmen für das Design von neuromorphen Systemen näher an das Verhalten von realen biologischen neuronalen Systemen heranzuführen. Diese Thesis untersucht Ag-basierte memristive Systeme hinsichtlich ihrer Anwendbarkeit in neuromorphen Systemen. Ein Hauptaugenmerk liegt darauf, Möglichkeiten zu entwickeln um realitätsgetreue dynamische Merkmale biologischer neuronaler Systeme in Ag-basierten memristiven Systemen nachzubilden. Diesbezüglich orientierte sich die Entwicklung der memristiven Systeme eng an Erkenntnissen aus den Neurowissenschaften. Ein weiterer Aspekt dieser Arbeit war es, Ag-basierte memristive Systeme über verschiedene Systemgrößen zu charakterisieren; von der Dynamik eines einzelnen Ag-Filaments hin zum kollektiven Verhalten in Ag-Nanopartikel(NP)-basierten memristiven Netzwerken. Diese Untersuchungen liefern Erkenntnisse über die

Grenzen zwischen individuellem und kollektivem memristiven Verhalten. Dies ist ebenso durch den biologischen Hintergrund motiviert, wo höherentwickelte Rechenfähigkeiten in neuronalen Systemen durch kollektives Verhalten der zugrundeliegenden einzelnen neuronalen Einheiten entstehen.

In dieser Thesis wurde ein unkonventioneller cAFM Ansatz für die Grundlagenforschung an memristiven Systemen auf der Nanoskala entwickelt. Dieser Ansatz sieht vor, dass das memristive System direkt in der Spitzenregion eines Cantilevers integriert wird, um den Ablauf memristiver Phänomene effizient auf der Nanoskala zu lokalisieren. Dadurch haben sich Möglichkeiten eröffnet die Dynamik von memristiven Strukturen auf der Nanoskala zu charakterisieren, ohne dass experimentelle Unsicherheiten bedingt durch thermische Driftbewegung eine Rolle spielen. Dieser Ansatz wurde genutzt um zwei memristive Systeme zu untersuchen: Ein einzelnes Ag-Filament welches sich aus einer kontinuierlichen Elektrode heraus entwickelt hat und ein in SiO_xN_y eingekapseltes AgPt-NP System. Das einzelne Ag-Filament wurde in einem Bereich stabilen diffusen Schaltens untersucht. Grundsätzlich bietet diffuses Schalten Möglichkeiten synaptische Kurzzeitplastizität in neuromorphen Systemen nachzubilden. Es hat sich gezeigt, dass die diffuse Schaltdynamik eines einzelnen Ag-Filaments keinen komplett zufälligen Charakter aufweist, sondern von zeitlichen Korrelationen geprägt ist. Die Untersuchung des in SiO_xN_y eingekapselten AgPt-NP Systems wurde gezielt in einem hochflüchtigen Bereich durchgeführt. In so einem Bereich wirken die physikalischen Triebkräfte für die Bildung und den spontanen Zerfall von filamentären Strukturen annähernd gleich stark. Dies führt zu einer memristiven Systemantwort die durch eine nicht-reguläre Spikingaktivität geprägt ist und Mustern der neuronalen Informationscodierung ähnelt.

Des Weiteren wurden in SiO_2 eingekapselte AgPt und AgAu Legierungs-NP hinsichtlich ihrer Anwendbarkeit als grundlegende Einheiten zur Implementierung von diffusem Schalten untersucht. Die Dynamik wurde auf dem Level eines individuellen NP (mithilfe von konventionellem cAFM) sowie auf makroskopischem Level von größeren Kompositsystemen charakterisiert. Es hat sich gezeigt, dass memristive Systeme aus AgPt und AgAu Legierungs-NP dahingehend angepasst werden können, dass die diffuse Schaltcharakteristik über mehrere Systemgrößen erhalten werden kann. Außerdem werden Konzepte diskutiert, um die Funktionalität der Legierungs-NP-basierten memristiven Systeme hinsichtlich Memsensoreigenschaften zu erweitern. Memsensoreigenschaften implizieren, dass die memristive Schaltdynamik über externe Stimuli moduliert werden kann. Dies wurde durch serielle Verknüpfungen aus Legierungs-NP-basierten memristiven Systemen und breitbandigen Halbleitern (TiO_2 und ZnO), welche eine Sensitivität des Schaltkreises gegenüber UV-Licht ermöglichen, erprobt. Es hat sich gezeigt, dass in solchen Anordnungen die memristive Dynamik über einen externen UV-Input moduliert werden kann. In Anbetracht dessen, dass sich Lebewesen ständig an ihre Umwelt anpassen müssen, sind memsensitive Systeme ebenso für neuromorphe Anwendungen interessant.

Im Hinblick auf größere Systeme wurden zwei Ansätze für NP-basierte memristive Netzwerke untersucht. Es wurde gezeigt, dass sich AgAu-NP dazu eignen, memristiven Schalten auf lokaler Ebene in einem übergeordneten Netzwerk aus zufällig verteil-

ten Kohlenstoffnanoröhrchen zu vermitteln. Im letzten Teil der Arbeit wurden Ag-NP Netzwerke an der Perkolationsschwelle hinsichtlich ihrer emergenten kollektiven Eigenschaften untersucht. Solche Netzwerke zeigen Kritikalität und zeitliche Korrelationen über große Reichweiten. Diese beiden Merkmale werden mit den Rechenfähigkeiten biologischer neuronaler Systeme in Verbindung gebracht. Um der Frage auf den Grund zu gehen, wie memristive Ag-NP Netzwerke in einen Bereich der Kritikalität gebracht werden können, wurden freiliegende Netzwerke, sowie in einer nicht-leitfähigen Matrix eingebettete Netzwerke untersucht. Die Idee dahinter war, dass das Vorhandensein oder die Abwesenheit einer Matrix die memristiven Eigenschaften auf fundamentaler Ebene beeinflusst. Eine wichtige Erkenntnis daraus ist, dass Kritikalität und zeitliche Korrelationen über große Reichweiten nicht durch das Vorhandensein oder die Abwesenheit einer nicht-leitfähigen Matrix abhängen. Zusammenfassend wurden in dieser Thesis umfassende Einblicke in die Dynamik von Ag-basierten memristiven Systemen gewonnen, welche sich über individuelles und kollektives dynamisches Verhalten hinweg erstrecken. Daraus können Paradigmen für das Design von neuromorphen Systemen vorangebracht werden, die sich eng an das Verhalten realer biologischer neuronaler Systeme anlehnen.

Abstract

Current efforts to improve the performance of contemporary computational hardware are impeded by fundamental limitations of the underlying transistor-based system architectures. This becomes particularly apparent by the envisioned end of Moore's law, saying that further miniaturization of transistors will terminate as a feasible strategy for future hardware engineering. Additional limitations arise from the von-Neumann architecture of contemporary computational systems, that predefines a strict separation between data storage and processing units. Application of such an architecture implies excessive time and energy costs for permanent data transfer, which is especially problematic for dealing with massive data amounts. The field of neuromorphic computing aims to develop computational systems, that are more efficient in solving specific computational problems requiring the analysis of high amount of data, like e.g. pattern recognition. To realize this, design principles are mainly inspired by the remarkably efficient computational capabilities of biological neuronal systems. Key elements to build neuromorphic systems are memristive devices. The fundamental property of a memristive device, a resistance that depends on previous electrical inputs, provides pathways to implement synaptic-like functionalities in electrical circuits. Although neuromorphic computing generally claims to follow design paradigms inspired by biology, the development of neuromorphic systems was mainly oriented towards the hardware implementation of artificial neural network algorithms, which are rather man-made mathematical concepts. In this context, highly regular and hardwired architectures were built by memristive devices where computation requires a precise control of each individual element of the system. In contrast to that, biological neuronal systems gain their computational capabilities by evolution-made architectures, shaped by a high connectivity, self-organization through continuous rewiring and exploitation of emergent network behavior. Hence, there is still much room for shifting the design paradigms of neuromorphic systems closer towards features of real biological neuronal systems. This thesis is dedicated to the investigation of Ag-based memristive systems regarding to their applicability in neuromorphic systems. One main aspect of this thesis is to explore the capabilities of Ag-based memristive systems to emulate realistic dynamical features of biological neuronal systems. In this regard, the development of memristive systems was closely oriented towards findings from neuroscience. Another main aspect is to characterize Ag-based memristive systems over different system scales, ranging from the dynamics of an individual Ag-filament to the collective behavior in Ag-nanoparticle (NP) based memristive networks. By this, the border between individual and collective memristive behavior shall be explored. This also motivated from biology, where advanced computational capabilities of neuronal systems emerge through collective dynamics resulting from the interplay of the underlying individual neuronal units.

In this thesis, an unconventional cAFM approach was developed to enhance basic research on nanoscale memristive systems. This approach intends to integrate the memristive system at the apex region of a cantilever, to achieve an efficient nanoscale localization of the memristive action. It proved beneficial to characterize the dynamics

of nanoscale memristive features under mitigation of experimental uncertainties related to thermal drift. Two memristive systems were investigated via this approach: An individual Ag-filament evolved from a continuous active electrode and a AgPt-NP system embedded in SiO_xN_y. The individual Ag-filament was studied in a stable diffusive switching regime. Generally, diffusive switching is relevant to emulate biological short-term synaptic plasticity in neuromorphic systems. It was found, that the diffusive switching dynamics of an individual Ag-filament is not completely random, but governed by temporal correlations. The investigation of the memristive AgPt-NP system focused on the operation within a highly volatile switching regime. In this regime, physical forces promoting the formation and spontaneous disintegration of filamentary structures appear to be balanced. This leads to irregular spiking responses of the memristive system, showing similarities to neuronal information encoding schemes.

Moreover, AgPt and AgAu alloy-NPs embedded in SiO_2 are investigated regarding their applicability as fundamental building units for diffusive memristive switching. The dynamics were studied on the level of an individual NPs (via conventional cAFM) and on macroscopic scales of larger composites systems. It is demonstrated, that memristive systems consisting of AgPt and AgAu alloy-NPs can be tailored accordingly, that diffusive switching characteristics are preserved across multiple system scales. Furthermore, concepts are discussed to expand the functionalities of alloy-NP based memristive devices towards memsensing, meaning that the diffusive switching dynamics can be modulated by external stimuli. This is done by serial connection of alloy-NP based diffusive memristive systems and wide-bandgap semiconductors (TiO_2 and ZnO) that incorporate UV-sensitivity to the circuit. Such a configuration proves well to implement memristive responses that are modulated by external UV stimulation. Reasoning from the fact that living beings permanently adapt to their environment, memsensor functionalities are likewise relevant for neuromorphic systems.

Regarding to larger-scale systems, two approaches for NP-based memristive networks were investigated. It is shown, that AgAu-NPs are able to implement memristive switching locally in a higher level network created by random assembly of carbon nanotubes. Finally, networks of Ag-NPs poised at the percolation threshold were investigated with respect to their emergent collective behavior. Such networks exhibit critical dynamics and long-range temporal correlations, both features that are associated with the computational capabilities of biological systems. To elaborate on the question how memristive Ag-NP networks are tuned to criticality, networks were investigated at exposed conditions and embedded in an insulating matrix, with the intention that memristive dynamics are fundamentally altered upon presence or absence of a matrix material. An important finding of this thesis is, that critical dynamics and long-range temporal correlations in Ag-NP networks are not disturbed upon presence or absence of a matrix.

All in all, this thesis develops comprehensive insights into Ag-based memristive systems from individual to collective dynamical behavior and promotes design paradigms for neuromorphic systems that are closely inspired the realistic behavior of biological neuronal systems.

Contents

List of Abbreviations

ANN	artificial neural network
NP	nanoparticle
EEG	electroencephalography
LRTC	long-range temporal correlations
ECM	electrochemical metallization
MIM	metal-insulator-metal
HRS	high-resistive state
LRS	low-resistive state
IV	current-voltage
RC	reservoir computing
cAFM	conductive atomic force microscopy
PVD	physical vapor deposition
DC	direct current
GAS	gas aggregation source
ITO	indium tin oxide
CNT	carbon nanotube

1. Introduction

It is unambiguous that innovations related to computational systems had substantial impacts on our everyday life and that upcoming innovations in this field will influence our future society. Starting from the advent of integrated circuits, significant improvements of current hardware were achieved by following mainly one design principle: To increase the complexity of silicon-based integrated circuits through extreme miniaturization of the underlying individual transistor units. This strategy expresses itself in Moore's law, which describes the observation that the number of transistors integrated on a chip is doubled after periods of roughly two years [1]. However, this trend which was kept alive by the joint effort from parties all across the chip-making industry experienced a slowdown since the 2010s years, as the decrease of feature size unveiled physical limits of downscaling [2]. These limits are defined, for instance, by unavoidable thermal noise or by quantum effects like tunneling that makes the control of electron flow within nanoscales on a chip highly uncertain [3, 4]. Additional concerns of current hardware are related to the fundamental design principle how computer systems are constructed, known as the von-Neumann architecture [5]. This architecture predefines a strict separation between information processing and storage units within a computer system, which implies a continuous necessity for (i.e. energy and time consuming) data transfer between both units and hampering of parallel computation approaches. These drawbacks of current computer architecture is commonly referred to as the von-Neumann bottleneck. Contradictory to the narrowed perspectives in the development of current hardware systems, there will be a continuously increasing demand for computational power in the future. This demand will be accompanied by the emergence of applications where the handling of massive amount of data is required, such as Internet of Things or autonomous driving. In particular, computational tasks are focused more and more on finding of patterns and data categorization, which are nowadays successfully solved via artificial neural network (ANN) algorithms [6–8]. Regarding to the future demand on computational systems, it is estimated that the total number of binary operations in the year 2040 will sum up to approximately 10^{40} [9]. Under the assumption that the energy consumption per binary operation will stay at the current value of around 0.1 pJ, the computational needs cannot be satisfied in the future with current technologies, since the amount of energy which can be produced will be barely sufficient [9]. As a consequence, there is a need for novel hardware concepts which excel at solving specific problems (such as pattern recognition) at high energy efficiency, in order to meet our demands on computational power in the future.

An alternative direction for future computational hardware is given by the field of neuromorphic computing, that aims to build systems inspired by information storage and processing principles of biological neuronal systems [10–14]. The ambition of this field is not to achieve a complete replacement of contemporary transistor-based hardware, but rather to develop alternative architectures that can be used complementary to current hardware systems for specific tasks, like e.g. pattern recognition. Memristive devices play a key role for the creation of neuromorphic systems [9, 15–17]. The fundamental property of a memristive device is a resistive state that depends on the history of electrical stimuli applied to it. In other words, applying a voltage or current input to a memristive device may cause a modification of its resistivity and in consequence, its efficiency to transmit electrical signals. This property is typically reflected in current-voltage characteristics having the form of a pinched hysteresis loop [18]. In addition, such a property resembles the behavior of biological synapses, which makes memristive devices highly relevant to imitate learning capabilities of neuromorphic systems [17, 19]. A broad variety of different memristive systems has been reported so far [20–23], that allows for the emulation of various types of synaptic dynamics in electrical circuits. Examples for this are long-term potentiation [24] or short-term plasticity [25]. Moreover, memristive devices were applied in electrical circuits attempting to emulate specific neuron models, like the leaky integrate-and-fire or Hudgkin-Huxley model [26, 27]. In addition, memristive devices are also suitable circuit elements for the physical implementation of artificial neurons, which are originally mathematical models forming the fundamental units of ANN algorithms [3]. In fact, many matured memristive devices are applied as fundamental units in neuromorphic systems, that are specifically tailored for solving ANN algorithms [28–32].

The working principle of many memristive devices, among other mechanisms, relies on the formation and disintegration of conductive filaments within an insulating matrix between two electrodes [33–35]. The resistivity of such a system depends on the morphology of the conductive filament, i.e. the resistivity may be higher or lower, when the conductive filament forms a strong or weak connection between both electrodes, respectively. Memristive devices based on the electrochemical metallization (ECM) mechanism are of particular interest. In ECM systems, conductive filaments consisting of an electrochemically active metal are manipulated within an insulating matrix. Many ECM-based devices are built with Ag as active metallic species. According to the ECM mechanism, redistribution of Ag in the insulating matrix of the memristive system (and consequently formation and disintegration of filaments) takes places via electrical-field driven oxidation of Ag, subsequent migration of Ag^+-species, and redeposition via reduction of Ag^+-species [36–38].

Despite great advances in the design of neuromorphic systems via memristive devices, there is still much room for emulating additional aspects of biological neuronal systems. This can be argued from the fact, that many design paradigms for neuromorphic systems were inspired from artificial neurons (and according ANNs), which are rather rigid mathematical constructs and not capable of projecting the full dynamical complexity of real biological neurons (and accordingly whole neuronal systems). In fact,

neuroscience developed many insights into the dynamical features of biological neuronal system that provide indications on the origin of computational capabilities of biological systems. These insights could guide the elaboration of alternative design paradigms for neuromorphic systems. Among others, some dynamical features that shape the computational capabilities of biological neuronal systems (and which are moreover relevant in the framework of this thesis) are short-term synaptic plasticity [39, 40], excitatory and inhibitory synaptic contributions [41, 42], critical dynamics [43] and long-range temporal correlations (LRTC) [44]. Several approaches have been reported, that aim for emulating these biologically-plausible dynamical features in neuromorphic systems. For instance, diffusive memristive switching has been introduced as a promising candidate for the emulation of biological short-term synaptic plasticity [25, 45, 46]. Diffusive memristive systems are characterized by threshold dynamics and volatile conductive states, which commonly originates from filamentary structures that are prone to spontaneous disintegration. Moreover, approaches to build more biologically-plausible neuromorphic architectures oriented towards the highly complex connectivity of biological neuronal systems have been reported, that rely on the creation of self-organized networks of memristive switches [47–49]. So far, Ag-nanowires [50, 51], Au-nanoparticles (NPs) [52–55] and Sn-NPs [56–58] have been commonly used as fundamental building units for self-organized memristive networks. Besides similarities in the underlying architecture, it was also shown that self-organized memristive networks exhibit complex dynamical features, which are similar to those in biological neuronal systems, including critical dynamics and long-range temporal correlations [57, 59–61].

The development of bio-realistic design paradigms for neuromorphic systems requires comprehensive understanding of memristive phenomena alongside with involvement of progresses from neuroscience. Central research questions of this thesis revolve around pathways to emulate dynamical features of biological neuronal system via Ag-based memristive systems closely oriented towards findings from neuroscience. Consequently, this work differs from a large part of established memristor technology, which focuses on the engineering of memristive devices on following more strict definitions of artificial neurons and are oriented towards (rather mathematical) ANNs. Understanding the emergence of computational capabilities in biological neuronal systems requires on the one hand side studying the small-scale behavior on the level of individual synapses and neurons and, on the other hand side, studies on large-scale network behavior resulting from large populations of neurons [62–64]. In the course of this thesis, Ag-based memristive systems are likewise studied across different system scales, ranging from the dynamics of individual Ag-filaments to the behavior of self-organized memristive networks formed by Ag-NPs. In this connection, another central research aim of this thesis is contributing to the long-term goal of understanding the limit between memristive phenomena having an individual character (single filaments) to collective phenomena (in memristive networks), which is relevant to understand neuromorphic systems based on self-organized architectures.

A brief outline of this thesis is given in the following. Central research questions are:

- What dynamical similarities exist between biological neuronal systems and Ag-based memristive systems?
- What are the properties of individual and collective memristive phenomena caused by single and multiple Ag-filaments, respectively?

As memristive phenomena related to metallic filaments occur on nanoscale dimensions, access to them via analytical methods in many cases challenging. In **Chapter 4**, an unconventional conductive atomic force microscopy (cAFM) method is developed, that serves as a novel strategy to investigate dynamics of filamentary memristive systems. The idea of this method is to integrate the memristive system directly on a conductive cantilever, to ensure stable localization of memristive phenomena at the apex region of the cantilever during cAFM studies. This method was introduced by investigating the diffusive switching dynamics of an individual Ag-filament within a Si_3N_4 matrix, that evolved from a thin film active electrode. This study focused on unveiling temporal correlations in the characteristic threshold switching features of diffusive memristive systems. The same unconventional cAFM method was applied in **Chapter 5** to investigate the memristive dynamics of an intermediate-scale AgPt-NP assembly embedded in SiO_xN_y. Here, the focus was put on memristive phenomena that arise during operation in a highly volatile switching regime. In this operation regime, the memristive system responds via irregular spiking patterns to a regular voltage stimulation, which is discussed in the context of inhibitory and excitatory contributions of biological neuronal systems.

Moreover, the applicability of AgAu and AgPt-alloy NPs encapsulated in SiO_2 as fundamental building units for stable diffusive memristive systems is investigated in **Chapter 6**. Building memristive devices via Ag-alloy based NPs would provide several enhanced design strategies related to inherent field-enhancement at the NP surface, anchoring of filamentary channels at the NP location or tailoring the reservoir of active species via the NP composition. In this context, the memristive dynamics of Ag-alloy NPs were investigated on the level of an individual NP via conventional cAFM, as well as on larger-scale composite systems via a macroscopic electrical probing. From the complementary insights on the dynamics on nano and macroscale, consequences upon scaling of memristive systems composed by Ag-alloy NPs are deduced. Furthermore, concepts to expand the functionalities of Ag-alloy NP based memristive systems towards memsensing are discussed in **Chapter 7**. For biological systems, it is important to adapt to environmental stimuli (e.g. light), meaning that the plasticity of synapses is also influenced by sensory inputs. Memsensor circuits aim to imitate such a behavior by combining memristive and sensor functionalities. Approaches to achieve memsensor functionalities are discussed by the combination of NP-based diffusive memristive devices and wide-bandgap semiconductors (such as TiO_2 or ZnO), that are sensitive towards UV-light.

In the further course of this thesis, self-organized memristive networks that incorporate Ag-based NPs are treated. In **Chapter 8**, memristive networks built by random

assembly of carbon nanotubes and subsequent decoration with AgAu-NPs are introduced. In this context, the question will be addressed, whether non-embedded Ag-alloy NPs are feasible building units (also in comparison to the embedded NP of Chapter 6), to mediate memristive switching in the lateral network across gaps between two carbon nanotubes. Finally, in **Chapter 9** self-organized networks of Ag-NPs poised at the percolation threshold are investigated. The Ag-NP networks are characterized regarding their emergent behavior, such as critical dynamics and LRTC, similarly to the collective behavior in biological neuronal networks. An important question in this context (likewise in neuronal and physical systems) is to understand which system parameters tune the dynamics into a critical regime. To approach this question Ag-NP networks at exposed conditions and capped by an insulating SiO_xN_y matrix were fabricated and compared. It is investigated whether the presence of an insulating matrix, which should fundamentally affect the memristive properties of the underlying gaps, disturbs the emergence of critical dynamics or not.

2. Theoretical Background

This chapter treats the theoretical background for this thesis. Firstly, the reader is guided through fundamental principles of neuromorphic computing. After that, since concepts for the design of neuromorphic systems are majorly inspired by biological neuronal systems, several important findings from the neuroscience literature are briefly illustrated. These findings shall clarify dynamical features of biological neuronal systems, that are seen as essential for the endowment of computational capabilities. Moreover, the reader will be provided with a comprehensive insight into memristive phenomena based on electrochemical metallization (ECM). All Ag-based memristive systems designed in this thesis will be governed by ECM-based switching dynamics. The last part of this chapter illustrates self-organized networks of memristive switches, which embody distinct architectures for the design of neuromorphic systems. In this context, a brief overview on percolation theory is given, which provides a helpful context to understand the dynamics of NP-based memristive networks.

2.1 Introduction to Neuromorphic Computing

A large branch of future computation concepts, which forms the framework of this thesis, is the field of neuromorphic computing. Motivated by the remarkable energy efficiency of the human brain (it operates at ≈20 Watts), neuromorphic computing aims to create hardware for emulating computational approaches inspired from biology [9, 65, 66]. In the decade of the 2010s, the engineering of neuromorphic hardware was strongly influenced by ANN algorithms, which are computation schemes loosely inspired by biological neuronal systems. The basis of ANNs is the emulation of neuron-like behavior on the software level via so-called artificial neurons as fundamental computation units. In the following lines, as well as in Figures 2.1a and b, the functional parts of biological and artificial neurons are described. Biological neurons can be represented by three major components: Dendrites, the soma and axons including the terminating synapses that realize information transmission to dendrites of adjacent neurons[67]. Neurons are receiving their information input from other cells via the dendrites. Computational capabilities of biological neurons are embedded in the soma. In a very simplified picture, all inputs received via the dendrites are collected upon temporal integration, followed by a decision, whether the information is further processed and transported (via electrical voltage fluctuations called action potentials) through the axon. When an action

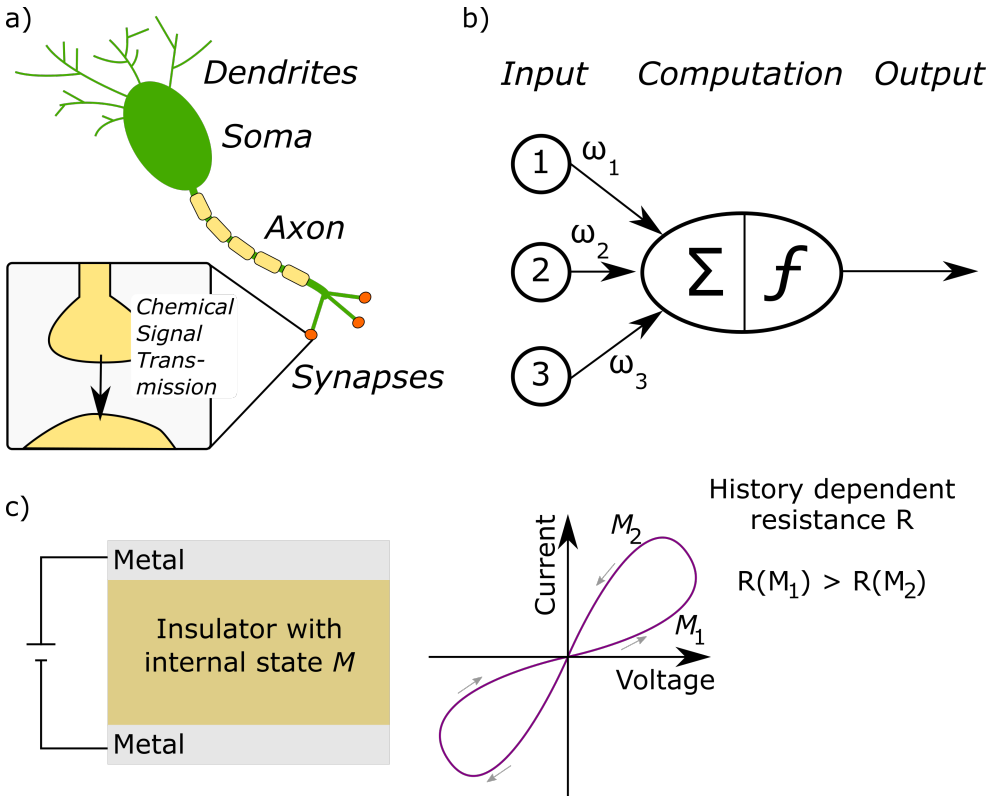

Figure 2.1: Fundamental building units of information processing in different systems. a) A biological neuron b) An artificial neuron, which is the key element of many ANN algorithms. c) A memristive device showing its fundamental property: A resistivity that is dependent on the previous electrical input.

potential reaches the axon terminal, an input may be transmitted to the dendrites of adjacent cells. The connectivity between axon terminals and dendrites of adjacent neurons is modulated by synapses. Through mechanisms which are generally referred to as synaptic plasticity, the efficiency of information transmission between two neuronal cells can be adapted in dependence on how the synapse was excited in the past [68]. The ability of synapses to adapt to excitation patterns is known to play the key role for learning and memory capabilities. In contrast to their biological counterparts, artificial neurons are basically mathematical functions which are loosely inspired by the behavior of biological neurons [69]. Generally, computation via artificial neurons involves the following steps: Firstly, the inputs to the artificial neuron are weighted by multiplication with an adjustable factor. Then, the sum of all weighted inputs is calculated and given into a transfer function. The result of the transfer function is the output, which will be transmitted in the ANN. In the model of artificial neurons, the step of input weighting can be seen as an analogy to the behavior of biological synapses. From this, the great strength arise that ANNs can be trained to solve specific problems, through careful adjustment of the weights. This resembles learning in biological neuronal sys-

tems. However, running ANN algorithms on contemporary transistor-based hardware is done at the expense of low energy efficiency, due to the fact that an enormous amount of computation steps must be solved sequentially. Therefore, great effort has been spent to engineer novel types of hardware specifically optimized for the execution of ANNs. One strategy to tackle this is to rely on transistor-based computation and already established fabrication processes of chip-making industry, but to build hardware highly specialized for solving solely ANN algorithms [70]. Such kind of alternative hardware is commonly referred to as AI accelerators. One principle to design AI accelerators is, for instance, the creation of multi-core structures, to enhance the parallel execution of commands to improve the expenditure of energy. Another strategy for the physical implementation of ANNs opens up by introducing a new type of electrical circuit element - the memristor.

Leon Chua originally defined the memristor in 1971 as a two-terminal circuit element with a characteristic functional relationship between magnetic flux linkage and electric charge. Further, he stated that the memristor plays the role as a fourth fundamental circuit element, besides the resistor, capacitor and inductor [15]. Two decades after its postulation, the concept of a memristor was rather subject to theoretical considerations until an impactful work from researchers around R. Stanley Williams in 2008 claimed, that memristors can be physically realized by the resistive switching properties of nanoscopic thin film systems [17]. From this point on, the practical importance of memristors became widely accepted, as a technology which allows to implement elements in electrical circuits which can modulate the information transmission efficiency [12, 71]. In other words, memristors open up the physical implementation of synaptic functionalities in electrical circuits. Nowadays, the term memristive device is commonly used as a differentiation from the memristor as a theoretical concept. Memristive devices are more practically seen as two-terminal devices, whose resistance depends on the history of the applied voltage or current stimulus, leading to a voltage-current characteristic having the form of a pinched hysteresis loop. Figure 2.1c illustrates the principal characteristics of an ideal memristor. However, the dynamical behavior among different types of memristive devices is highly diverse. Technologically matured neuromorphic hardware using memristive devices is commonly built in crossbar array architectures, which can be understood as a physical implementation of ANN algorithms. Thus, such a crossbar array architecture drastically facilitates in-memory computing, meaning that information processing and storage is combined on the level of a single device. This enhances the capabilities for parallel computing. For a comprehensive review of memristive crossbar arrays see [31]. Figure 2.2 illustrates an example of a very basic crossbar array. There are a number of input and output lines, where a memristive device is integrated at each cross-point. Here, the advantage of the two-terminal character of a memristive devices becomes apparent, meaning that integration of crossbar arrays is more straightforward than with three-terminal transistors. The memristive devices at each cross-point allow to tailor the conductance, which corresponds to adjusting a synaptic weight. Following Ohm's law, the current flowing through each cross-point results from multiplication of the input voltage and the memristor conductance (i.e. the input is weighted like in a synapse). Further, according to Kirchhoff's law, the current flowing through each output

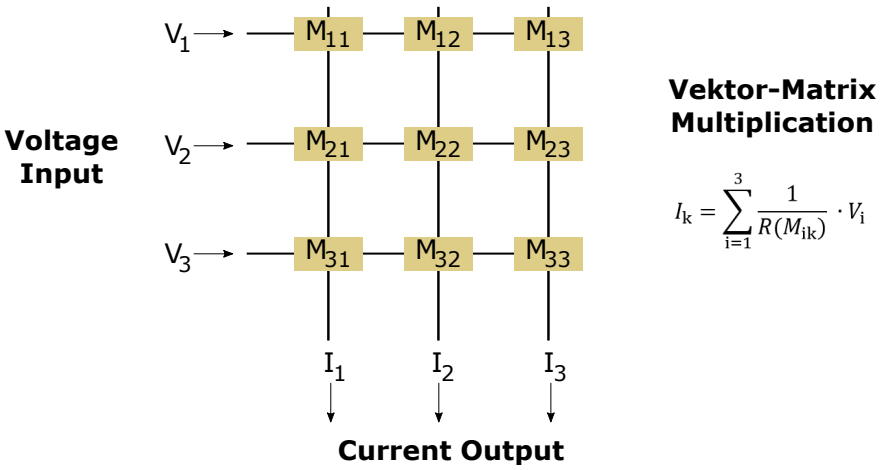

Figure 2.2: Illustration of the basic principle of a crossbar array. Highly matured hardware realized by memristive devices is built as crossbar arrays, that allow for a highly efficient way of computing vector-matrix multiplications.

line is the sum of all currents fed through the cross-points, which is similar to the integration of inputs at dendrites. Effectively, this reflects the functionalities of an artificial neuron (see Figure 2.1b), namely modulating inputs by synaptic weights and integration of those inputs for further processing. By the design of larger crossbar arrays, vector-matrix multiplications on a physical level are allowed, which are fundamental computation steps in ANN algorithms [3], and can be performed in a highly parallel and energy-efficient manner.

The reader shall now be faced with the question: How bio-inspired are the highly matured neuromorphic hardware architectures like crossbar arrays of memristive devices? Actually, engineering of neuromorphic hardware was to a great extent inspired by (man-made) ANNs, which are rather rigid mathematical constructs, instead of attempts to mimic the real complex dynamical behavior (made by evolution) of biological neuronal systems. Thus, there is still much room for incorporating bio-inspired dynamics in memristive systems to pave the way for more unconventional computational approaches. To reach this, findings from neuroscience must be consulted, that give insights into the dynamics governing biological neuronal systems. Some of the dynamical features of biological neuronal systems giving insights into brain-like computational principles are discussed in the next section.

2.2 Dynamical Features of Biological Neuronal Systems

Although the question, how biological neuronal systems achieve their remarkable computational performance is not clarified to its full extent, progresses in neuroscience already revealed a variety of different mechanisms that contribute to the endowment of com-

putational capabilities. In this section, some dynamical features are described which are seen as essential for the functional behavior of biological neuronal systems, namely excitatory and inhibitory synaptic contributions, short-term plasticity, critical dynamics and long-range temporal correlations. Excitatory and inhibitory synaptic contributions

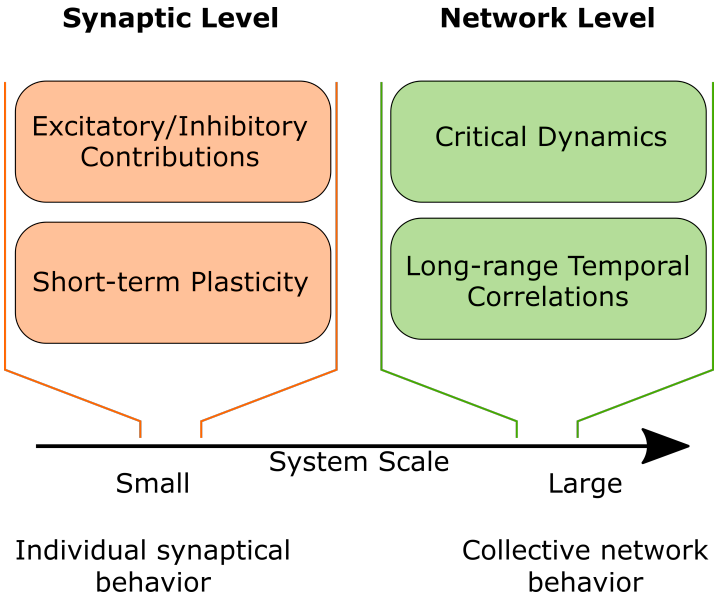

Figure 2.3: Dynamical features of biological neuronal systems that are relevant in the context of in this thesis. The features are categorized according to the scale they are acting, ranging from individual synapses to the collective dynamical behavior of a large population of neurons.

refers to the ability of synapses, to either increase or decrease the probability for neuronal firing of an action potential, respectively. They are of fundamental importance to encode information and to regulate neuronal activity. Short-term plasticity is a temporal increase of information transmission efficiency of synapses. This is important for neuronal systems to adapt to new situations over short time scales, as long as required to solve computational tasks in the moment of the new situation. Generally, critical dynamics are of broader significance across various physical systems consisting of many interacting dynamical units, which are poised at the border between two phases. Systems at criticality exhibit universal characteristics, such as scale-invariance and divergent correlation functions. With regard to neuronal systems, findings from neuroscience indicate that larger populations of neurons also operate in a critical state. This is reasoned by the fact, that spontaneous activity in neuronal tissue is organized via firing pattern, having the form of scale-invariant avalanches. Long-range temporal correlations can be found in the spontaneous oscillations of neuronal systems. Generally, it implies that any neuronal activity in the past has an impact on the current activity, and can be therefore interpreted as a dynamical memory. These dynamical features mentioned here, and especially their capabilities of promoting computation within a system, gave major inspiration for

their emulation by Ag-based memristive systems in this work. These features act on different scales within a biological neuronal system. Excitatory and inhibitory synaptic contributions and short-term plasticity are acting individually on the synaptic and neuronal level. In contrast to that, critical dynamics and long-range temporal correlations are observations of a collective network behavior, that emerge from complex interplay of the underlying dynamical units (i.e. synapses and neurons). This categorization is emphasized in Figure 2.3. The following subsections describe these dynamical features in more detail.

2.2.1 Excitatory and Inhibitory Synaptic Contributions

Synapses are at the heart of information transmission in biological neuronal systems. They implement the coupling between different neurons and their dynamics incorporate important principles on how information (having the form of voltage fluctuations) is encoded and processed. Information can be transmitted over longer distances by neurons that successively excite each other, resulting in the propagation of action potentials from neuron to neuron. More precisely, this procedure of information transmission is enabled by *excitatory synapses*. The role of excitatory synapses is, that they increase the probability for post-neuron firing, when they get an action potential from the pre-neuron [72]. In other words, excitatory synapses promote the transmission of information through biological neuronal systems. However, not all synapses are acting excitatory-like. A considerable fraction of all synapses in the brain (estimated as 20-30 % in mammalians [73]) are acting in an inhibitory manner. *Inhibitory synapses* decrease the probability that an action potential is transferred from one neuron to another. The interplay between excitatory and inhibitory synaptic contributions plays a key role for information encoding and processing in biological neuronal systems. Generally, synaptic inhibition is an important function to regulate the overall activity. In particular, it is frequently reported that neuronal systems tune itself into a regime that is most favorable for computation by balancing excitatory and inhibitory contributions [74]. Deviations from this balance are associated to a disturbed brain activity, like it is the case in epilepsy [75]. For a more comprehensive insight on the relevance of inhibition, the reader is referred to elaborated reviews [41, 42]. Some fundamental considerations on how excitatory and inhibitory contributions regulate neuronal activity are illustrated in Figure 2.4. It can be modeled, that neurons respond via highly regular firing pattern, when excitatory contributions are permanently dominating [76]. However, the presence of spiking patterns with high regularity does not match with many *in-vivo* studies on biological neuronal systems. Instead, evoked neuronal activity as measured *in-vivo* appears to be more complex, showing a more irregular spiking pattern [77]. This activity can be achieved, when excitatory and inhibitory contributions to the signal transmission are balanced (see 2.4b). Based on this, it is assumed that the close interplay between excitatory and inhibitory contributions regulates the neuronal activity and shapes efficient information encoding and processing schemes [78–80]. In fact, neuronal activity is commonly regulated by certain circuits schemes [41]. One distinct examples is shown in Figure 2.4c, a feedback inhibition loop, that is commonly found to organize the interplay between

excitatory and inhibitory contributions, for the information encoding and processing in evoked neuronal activity.

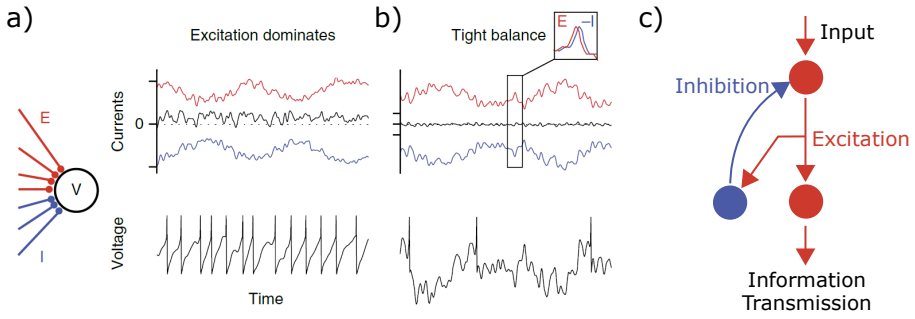

Figure 2.4: Excitatory and inhibitory synaptic contributions regulate neuronal activity. When solely excitation (red) dominates, highly regular spiking patterns are produced (a). Instead, the state of a neuron is regulated by inhibition (blue), causing a more irregular neuronal output (b). Reprinted from [76]. Excitatory and inhibitory contributions are frequently organized by feedback inhibition loops (c).

2.2.2 Short-term Synaptic Plasticity

Synaptic plasticity is of fundamental importance for biological neuronal systems to adapt to environmental influences and to realize learning capabilities [39, 40]. It refers to various phenomena, where the signal transmission efficiency of synapses is improved or suppressed, in response to electrical signals that arrived earlier at the synapse. Consequently, it can be said that synaptic plasticity shapes the future neuronal activity (and therefore provides a proper response) based on previous inputs (that could be referred to as experience). Generally, one can categorize synaptic plasticity into long-term and short-term, depending on the time scales on how long the modulation of signal transmission efficiency of a synapse is retained. Long-term synaptic plasticity implements enduring memory in biological neuronal systems, which lasts longer than several minutes. In case of short-term plasticity, the transmission efficiency will return to a base level within milliseconds to minutes, when activity incoming to the synapse is terminated. This allows biological neuronal systems to adapt temporarily to new situations, where problem solving is required on short time scales and a long-lasting memory is not necessary. Short-term plasticity modifications of synapses could be described as a working memory of biological neuronal systems [40]. For example, when a problem related to an external stimulus must be solved (like e.g. voice recognition), the biological neuronal network adapts to the situation in such a way, that it is able to solve the problem. In this case, the short-term plasticity modifications of synapses may be a reflection of the external stimulation, which is temporarily retained only for the period of solving this task.

2.2.3 Critical Dynamics

In the two preceding sections, dynamical features of biological neuronal systems were discussed that occur on the lower-scale level of synapses and neurons. In the following, dynamics are described that can be found on network scales, i.e. on the level of a large population of interconnected neurons, where collective neuronal activity emerges from interactions between the underlying neurons and synapses. One distinct mode of collective behavior that can be found in the spontaneous activity of larger biological neuronal networks is the so-called "*neuronal avalanches*". A definition of a neuronal avalanche and early evidence on their presence in biological neuronal systems can be found in the work from Beggs and Plenz from 2003 [43]. In this work, they characterized the spontaneous activity of neuronal tissues on multiple-electrode grids, that allowed to acquire the spatio-temporal structures present in the tissue activity. It was found that the spontaneous activity was not uniform in time, but organized in burst-like signals, with alternating periods of pronounced activity separated by periods of quiescence. Furthermore, they claimed that local activity within the neuronal tissue was not independent, but is spread through the whole tissue in a correlated manner. They called the observed sequences of burst-like correlated activity *neuronal avalanches*. Experimental results which lead to the definition of a neuronal avalanche are shown in Figure 2.5a. There, the activity was measured on an evenly arranged grid of 60 electrodes (see panel b for schematic depiction of electrode grids). The activity level of all 60 electrodes are plotted for a time window of one minute. There it can be recognized, that local activity across all electrodes occur in narrow periods separated by periods of quiescence. It was claimed, that such burst-like activity emerges from the interconnectivity between neurons in the network, where a local event may trigger a cascade of subsequent local activities, that ultimately may spread across the whole system. In their experiment, a neuronal avalanche that spreads through the whole system would cause measured activity over all 60 electrodes within a narrow time interval. More importantly, the distribution of avalanche sizes (defined as number of electrodes where activity was measured during an avalanche) were found to be scale-invariant. This is expressed by the fact, that the probability distribution of measured avalanche sizes S follows a power law with $P(S) \propto S^{\alpha}$, where the characteristic power law exponent α was invariant towards external modifications of the system. This is supported in Figure 2.5b, where the power law scaling is not disturbed upon changing the system size (in terms of number of electrodes for measuring the neuronal tissue activity). Furthermore, the characteristic power law exponent for avalanche sizes turned out to be invariant towards the distance between electrodes in the grid, as shown in 2.5c. Because similar dynamics (i.e. scale-invariant avalanches) can be found universally in a broad range of physical systems, that are poised at the border of a second-order phase transitions [81], the findings from Beggs and Plenz were followed by assumptions, that biological neuronal systems also operate at such a critical point, between phases of complete order and disorder [82]. This is further reasoned by several computational benefits that are implied by critical state [83, 84]. As an example, a critical state maximizes the information capacity of dynamical systems, a property that is inevitable for computational tasks [79]. Information capacity quantifies the amount

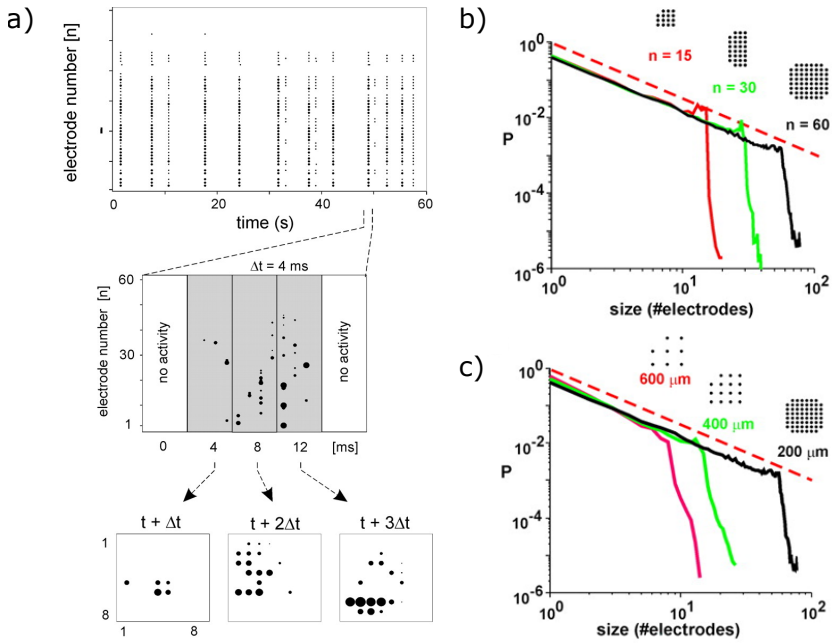

Figure 2.5: Definition of neuronal avalanches and power law distributions. A neuronal avalanche is defined by a sequence of time frame where spontaneous network activity was detected, separated by periods of quiescence (a). Power law distribution of avalanche sizes indicating scale-invariant and critical dynamics as point of operation of biological neuronal systems. Occurence of power law distributions measured on an electrode grid is irrespective of system size (b) or distance between electrode (c). Reprinted from [43]. Copyright 2003 Society for Neuroscience.

of different (distinguishable) activity patterns a system can exhibit. It represents a bottleneck for computation, because it determines how informative the dynamics of a system can be. Imagine a system that can only occupy two different states. No matter how much information is carried by the input to the system, all information must be projected into one of either states. This reduction of information apparently impedes computation. Considering the question, how systems can be tuned into a critical regime without external tuning, the concept of self-organized criticality became a popular explanatory approach [85]. Self-organized criticality describes the property of dynamical systems, which have the critical point between two states as an attractor. This means, when a system that is governed by self-organized criticality gets excited, it is always driven towards the critical point by itself.

2.2.4 Long-range Temporal Correlations

Another dynamical feature that can be found on the network level of biological neuronal systems is the presence of long-range temporal correlations (LRTC). In more detail, LRTC can be detected in the amplitude fluctuations of spontaneous neuronal oscillations.

Generally, LRTC are defined as correlations in the time domain, which can be described by a slow decay of autocorrelation function in the form of a power law [61]. Figure 2.6 depicts a phenomenological description of LRTC in neuronal oscillations and key results from Linkenkaer-Hansen *et al.*, who developed early empirical evidence on the presence of LRTC in 2001 [44]. A method to acquire signals resulting from the spontaneous neuronal oscillations is, for instance, electroencephalography (EEG) [86], which detects voltage fluctuations at the scalp resulting from ionic currents in neurons. Examples of neuronal oscillations as detected by EEG for three different strengths of LRTC is depicted in Figure 2.6a. The presence of temporal correlations can be recognized in the signal

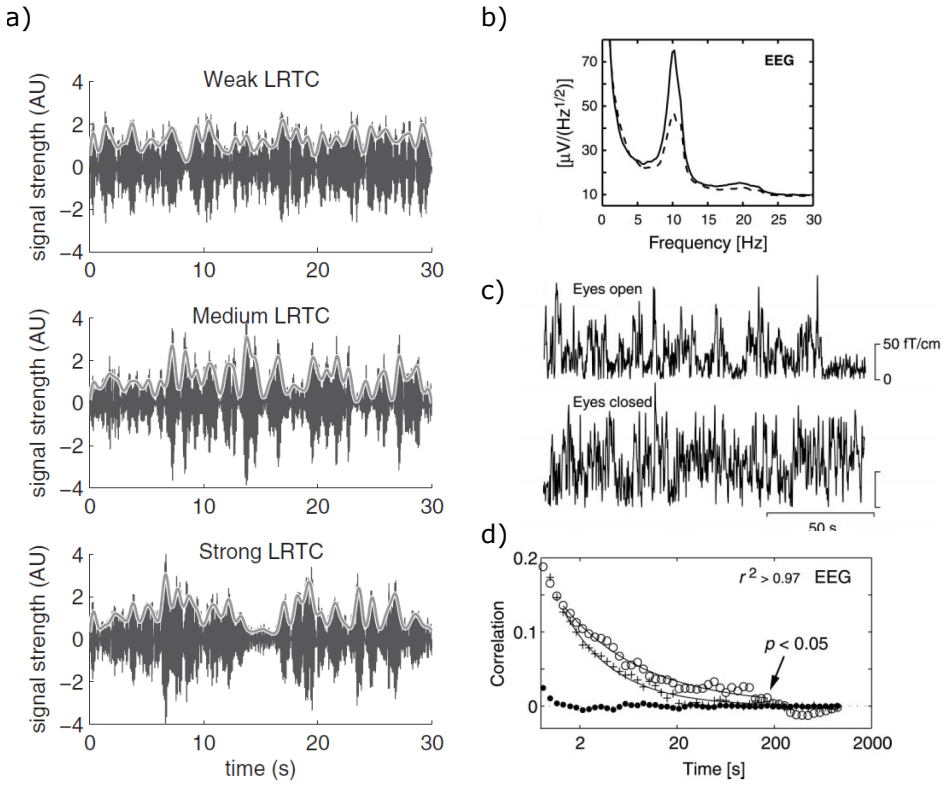

Figure 2.6: Illustration of long-range temporal correlations in neuronal oscillations and empirical evidence. Different strengths of LRTC in the amplitude modulation of neuronal oscillations (a). Reprinted from [87]. Early empirical evidence for LRTC by Linkenkaer-Hansen *et al.* is summarized in (b)-(d). The alpha frequency band (8-13 Hz) in an EEG signal (b) was investigated in eyes open and closed conditions (c). A power law decay of the autocorrelation function indicates LRTC (d). Reprinted from [44]. Copyright 2001 Society for Neuroscience.

envelope, which represents the modulation of the oscillation amplitude. In case of weak LRTC, the fluctuation of oscillation amplitude appears to be rather uniform. However, in case of strong LRTC, the neuronal oscillation amplitudes seems to be highly variant, with alternating periods of higher and lower oscillation amplitudes. Essential results

developed from Linkenkaer-Hansen *et al.* in 2001 are shown in Figures 2.6b-d, where they described the presence of LRTC in such neuronal oscillations by autocorrelation functions [44]. In this work, they focused on oscillations within the alpha frequency band measured by EEG. Figure 2.6b shows a typical amplitude spectrum of an EEG signal with strong prominence of the alpha frequency band between 8 and 13 Hz. Figure 2.6c illustrates the signal filtered to the alpha frequency band. Similar to how it is illustrated in Figure 2.6a, the fluctuation of the neuronal oscillation amplitude was tested towards temporal correlations by means of autocorrelation functions. It was found, that the autocorrelation function exhibits a slow power-law decay, as shown in Figure 2.6d. Principally, the presence of LRTC implies, that the past activity has an impact on the current activity of a system. Based on this, it can be argued, that LRTC plays the role of a dynamical memory for computational tasks in biological neuronal systems [88].

2.3 Electrochemical Metallization Devices

After shortly introducing basic concepts to build neuromorphic hardware via memristive devices and important findings from neuroscience that indicate on the strategies for computation in biological systems, this section describes the origin of memristive phenomena in Ag-based systems. More generally, there is a broad variety of different memristive material systems that have been reported so far. Widely spread are systems, that form conductive filaments based on the reconfiguration of metal cations (*electrochemical metallization*) or oxygen vacancies (*valence change mechanism*). Besides filamentary memristive devices, there are also interface-type devices, where the modulation of device conductance relies on manipulations of electrode-interface properties. Another well-reported type of memristive devices is based on the *phase change mechanisms*, where the conductance can be switched by inducing an either crystalline or amorphous phase. For comprehensive reviews on the broad range of memristive systems, the reader is referred to the works of [20–23]. Memristive phenomena of Ag-based systems that are investigated in this work arise from the electrochemical metallization (ECM) mechanism. This section covers fundamental insights on the physical origins of this particular switching mechanism and discusses how variable memristive dynamics can be engineered using this mechanism.

2.3.1 Mechanism

Most generally, the ECM mechanism explains the reconfiguration of metallic filaments in a metal-insulator-metal (MIM) structure, driven by externally applied electrical fields, where the state of the structure can switch between a high-resistive state (HRS) and a low-resistive state (LRS). When a continuous filament created from an active metallic species exists in contact to both metal electrodes, electron transport across the insulator is enabled, meaning that the structure is in a LRS. However, when the filament is not continuous, the whole structure has an insulating character, i.e. it is in a HRS. This very basic working principle of such kind of structure, often called ECM device, is

illustrated in Figure 2.7. The reconfiguration of metallic filaments is realized by electrochemical redox reactions. When an ECM device is designed, one metal electrode is usually electrochemically more active than the other electrode. The active electrode (Ag

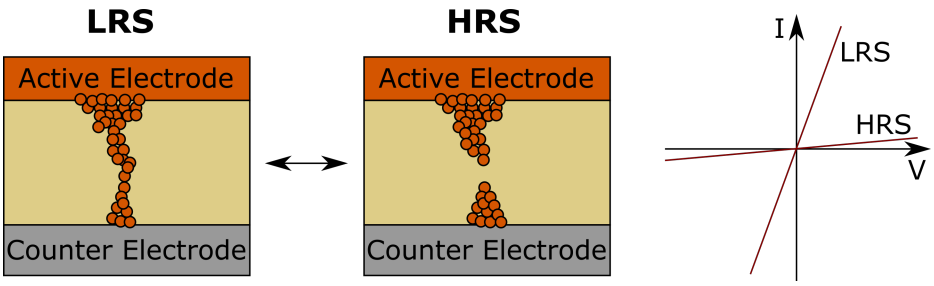

Figure 2.7: Basic working principle of an ECM device. Upon reconfiguration of a metallic filament consisting of an electrochemically active metal, the device can be switched between a high and low-resistive state.

or Cu are frequently used) provides material from which the filament is formed, whereas the counter electrode (e.g. Pt, W or Au) remains passive. A huge diversity of different materials has been reported as insulating mediums between both electrodes. Examples range from typical insulators like SiO_2 [89] or ZrO_2 [90] to solid ion electrolytes like AgI [91]. Application of an electrical field across the ECM device induces oxidation of the active electrode, causing the release of metal cations that can subsequently migrate towards the inert electrode, where they deposit as metallic species upon electrochemical reduction. The reactions occurring at both electrode-insulator interfaces can be summarized as follows, where Z and e denote the charge number involved in the redox reactions and elementary charge, respectively:

$$\text{Active Electrode: } \mathrm{Me} \longrightarrow \mathrm{Me}^{Z+} + \mathrm{Ze}^{-}$$
$$\text{Counter Electrode: } \mathrm{Me}^{Z+} + \mathrm{Ze}^{-} \longrightarrow \mathrm{Me}$$

In the following paragraph, physical mechanisms are discussed that contribute to the electrochemical growth and disintegration of metallic filaments. Comprehensive insights on modeling the kinetics of filament formation in Ag-based ECM devices can be found, for instance, in the works of [36–38, 92]. It can be assumed, that three different kinetic contributions govern the formation of Ag-filaments: Nucleation of Ag-deposits that are building up the filament, field-driven and thermally activated hopping of Ag^+-species and electron transfer at the interface between active electrode and insulator. These three contributions are schematically depicted in Figure 2.8. The kinetics of filament formation, and connected to this dynamical features such as the switching speed, can be limited by one of these kinetic contributions [36, 37]. When a Ag-filament is formed in an ECM device, energetic barriers related to nucleation may determine the kinetics. In this connection, two scenarios must be considered which both can occur prior to the formation of a continuous filament: A stable Ag-nucleus may form directly at the interface on the counter electrode (heterogeneous nucleation) or somewhere within the insulating layer (homogeneous nucleation). Generally speaking, an energetic barrier

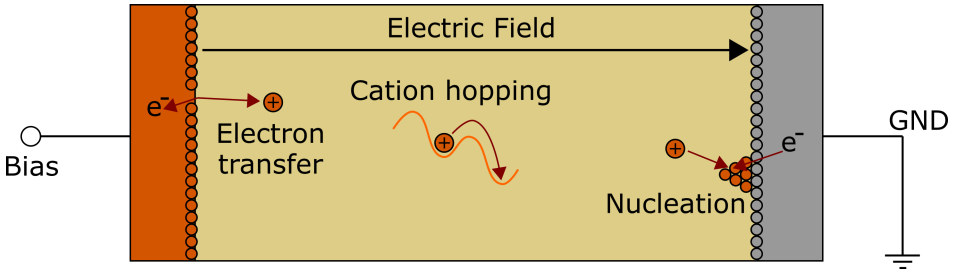

Figure 2.8: Kinetic contributions that govern the filament formation in ECM devices. Electron transfer at interfaces, cation hopping across the insulator or nucleation of Ag-deposits can be considered as rate determining step during the formation of Ag-filaments.

ΔG_{crit} must be overcome to create a stable nucleus and the corresponding kinetics in terms of a nucleation rate j_{nuc} has an exponential form [93], where k_{B} and T are the Boltzmann constant and temperature, respectively:

$$j_{\mathrm{nuc}} \propto \exp(-\frac{\Delta G_{\mathrm{crit}}}{k_{\mathrm{B}}T}) \tag{2.1}$$

The migration of Ag^+-species across the insulating layer is driven by the external electrical field, as well as by thermal activation. This kinetic contribution can be described by the Mott-Gurney law [37], which calculates the current density resulting from ion hopping j_{ion} as:

$$j_{\mathrm{ion}} = 2Zeca\nu \exp(-\frac{\Delta G_{\mathrm{hop}}}{k_{\mathrm{B}}T}) \sinh(\frac{aZe}{2k_{\mathrm{B}}T}E) \tag{2.2}$$

In this formula, c denotes the ion concentration in the insulating layer, a the hopping distance, ν the attempt frequency, ΔG_{hop} the energetic barrier for ion hopping and E the applied electrical field. Regarding to the third kinetic contribution, the electron transfer during oxidation at the interface between active electrode and insulating layer can be described by the Butler-Volmer equation [37]. It calculates the current density $j_{\mathrm{etransfer}}$, that originates from redox reactions at an electrode (and therefore corresponds to the reaction rate), depending on the potential ϕ, that is applied to the electrode. It can be calculated as follows, where ϕ_{eq} is the equilibrium potential at the electrode-insulator interface and α the charge transfer coefficient:

$$j_{\mathrm{etransfer}} = j_{0,\mathrm{etransfer}}[\exp(\frac{(1-\alpha)Ze}{k_{\mathrm{B}}T}(\phi - \phi_{\mathrm{eq}})) - \exp(\frac{\alpha Ze}{k_{\mathrm{B}}T}(\phi - \phi_{\mathrm{eq}}))] \tag{2.3}$$

The prefactor $j_{0,\mathrm{etransfer}}$ denotes the exchange current density. This is a material dependent parameter and describes the intrinsic tendency of the active species for electron transfer. Each of the above mentioned mechanisms involved in the formation of filaments, namely nucleation of Ag-deposits, Ag^+-hopping and electron transfer, contribute with a distinct rate equation. Principally, each of the presented mechanisms could be a rate determining step, which mainly defines the behavior of an ECM device. Consid-

ering the range of material parameters included in these equations (like ΔG_{crit}, ΔG_{hop} or $j_{0,\mathrm{etransfer}}$), the choice of the material system (consisting of active electrode, insulating layer and inert electrode) could induce different dynamical properties between ECM devices.

Now, physical origins that lead to the disintegration of metallic filaments are discussed, i.e. mechanisms that switch an ECM device from the LRS back to the HRS. Generally, one can distinguish between mechanisms, causing the disintegration of filaments under application of a bias or under zero-bias conditions. In other words, transitions to the HRS can be induced or spontaneous, respectively. An induced filament disintegration can be achieved under application of a reversed bias voltage to the ECM device. In such a case, the filament gets destroyed by electrochemical reactions assisted by Joule heating effects [94]. Considering that typical dimensions of a filament are in the 10 nm-range [95], high current densities evolve that could cause a thermally induced rupture(most likely at the thinnest part). As a consequence, the electrical field across the insulating layer increases and the residual filament gets electrochemically dissolved (similar to the processes occurring during filament formation, but at different polarity, see Figure 2.9). Furthermore, electromigration can also be considered as a mechanism, that contributes to filament rupture at thin parts, induced by high current densities [96]. The driving force for the spontaneous disintegration can be mainly ascribed to the minimization of interfacial energies [25, 97]. Filamentary structures in an ECM device bring due to their high surface-to-volume ratio larger interfacial energy to the system, that could be reduced by the formation of more spherical structures, as shown in Figure 2.9. A possible mechanism to reach the disintegration into spherical cluster is connected to surface diffusion [98], which describes that filament rupture can occur especially at parts with a high curvature.

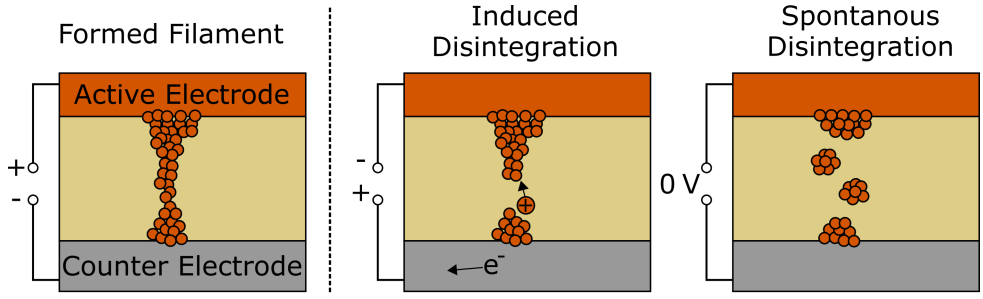

Figure 2.9: Schematics of filament disintegration. It can be distinguished between an induced and spontaneous disintegration, that occurs under application of a (reversed) bias or at zero-bias conditions, respectively.

2.3.2 Design of ECM Devices and Switching Dynamics

After reviewing the physical mechanisms that realize memristive switching in ECM devices, design principles are now discussed that allows for tailoring their switching dynamics. Figure 2.10 illustrates two distinct dynamics that can be commonly observed in

ECM devices: Bipolar [20] and diffusive memristive switching [46, 99–101]. Their main difference is the volatility of the LRS. In case of bipolar switching, the LRS is retained at zero-bias conditions (note the origin-crossing in the current-voltage(IV) characteristic) and transition back to the HRS is induced at reversed polarity. On the other side, a diffusive switching device is always in the HRS at zero-bias conditions and shows a spontaneous decay of the LRS before reaching the origin in the IV characteristic. Both types

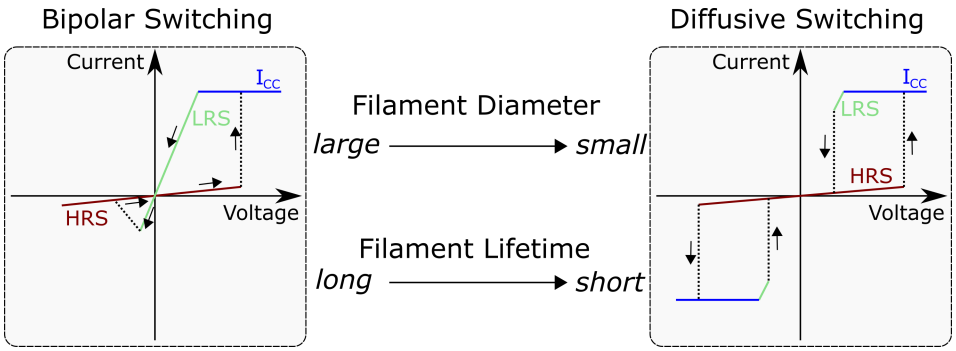

Figure 2.10: Bipolar versus diffusive memristive switching. ECM devices can show different dynamical behavior such as non-volatile bipolar switching or volatile diffusive switching. The emerging dynamics mainly depends on the filament diameter.

of switching dynamics provide valuable functionalities for the design of neuromorphic systems. Due to its non-volatility, bipolar switching allows to store information in neuromorphic systems on longer time scales. The volatile behavior of diffusive memristive devices facilitates the emulation of short-term synaptic plasticity (see Section 2.2.2) in neuromorphic systems [19, 24, 25]. Moreover, another important application of diffusive memristive devices is as selectors in crossbar array architectures. The purpose of selector devices is to suppress so-called sneak-path currents through unaddressed crosspoints in the arrays, which is reliably realized by the threshold character of diffusive memristors [102]. Whether a device exhibits volatile or non-volatile dynamics depends on the lifetime of the metallic filament at zero-bias conditions. Filamentary structures on the nanoscale are principally unstable because of the high surface-to-volume ratio, but their relaxation can be kinetically limited. The filament lifetime, is determined by the time scales that spontaneous disintegration mechanisms need, to create rupture of one part in the filament, which is mainly determined by the diameter of the filament [98]. All in all, the filament diameter is of major importance to tailor the switching dynamics of ECM devices in terms of volatility. An effective way to influence the filament diameter during operation is to limit the current flowing through the device, for example by adding a resistor in series or by adjusting a compliance current I_{CC} [98]. An explanation for this is, that the extend of Ag-mass transport depends on the electrical current flowing through the system [103]. Less Ag-mass transport leads to formation of thinner filaments. Furthermore, application of a serial resistor or compliance current implies, that the electrical field across a memristive devices is strongly reduced in the LRS, meaning that the driving force for filament formation drops. Overall, adjusting the

operation conditions of an ECM device in terms of current limitation must be carefully considered, as it influences the diameter of filaments and therefore pathways to constrain the dynamics into a volatile or non-volatile regime. Additionally, when it comes to the emulation of short-term plasticity, the engineering of filament lifetimes become especially relevant, because design of this dynamical parameter allows to tailor the temporal scales, on which information is stored.

Another type of ECM-devices that exhibit a rather special switching behavior are atomic contact memristors, that allow to adjust discrete conductance values in units of the quantum conductance $G_0 = 2e^2/h = 7.748 \cdot 10^{-5}$S [104, 105]. For instance, quantized conductance levels have been observed Ag/Ta_2O_5/Pt-systems, that can be adjusted to integer multiples of G_0 [106]. Also, the formation of Ag-filament based atomic contacts in 1 nm wide air-gaps has been demonstrated [107].

Aside from device structures (having a MIM sequence) taken into account so far, another principle for the design of ECM devices opens up through integration of the active species directly into the insulating layer [108]. Figure 2.11 presents an approach from Jo *et al.*, where the active medium was a co-sputtered layer consisting of Ag and silicon, that was integrated between two inert electrodes [109]. Such an approach provides en-

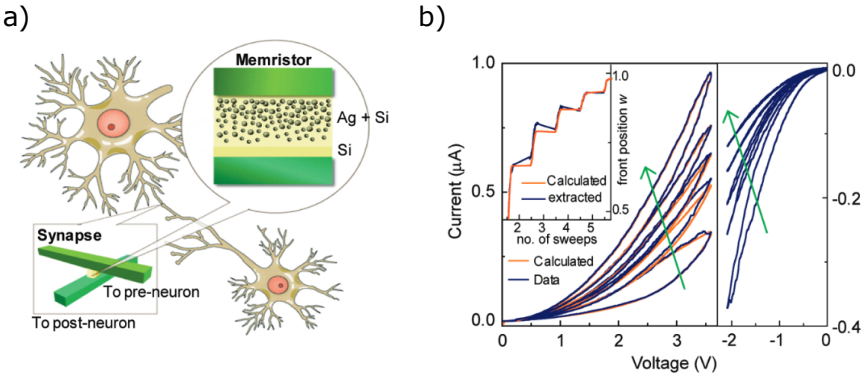

Figure 2.11: ECM based approach with Ag embedded in the insulating layer. This constitutes an alternative approach that is feasible to implement memristive switching without a continuous active electrode as in MIM structures. Reprinted from [109]. Copyright 2010 American Chemical Society.

hanced strategies for the design of ECM devices. Firstly, the availability of active species can be carefully restricted (by tailoring the filling factor of the active species inside the insulating layer) compared to MIM structures, where the continuous electrode provides a rather large reservoir of active species. Secondly, field-enhancement effects can be exploited, that may promote the reliability of filamentary devices and lower the operation voltages [110]. Thirdly, the requirement for an electroforming step [111, 112] can be eliminated. Many ECM devices having a MIM structure need an increased power input, to form the initial filament starting from the virgin state, compared to the required power for switching into the LRS during regular operation. This is because a residual filamentary structure provides an inherent field-enhancement that facilitates switching,

which is missing when the operation starts from the virgin state. When the reservoir of active species is already implemented in the insulating layer, the need for an increased power input to form the first filament can be significantly reduced.

2.3.3 Probing of Memristive Switching on the Nanoscale

Progresses in the design of memristive devices go hand in hand with methods that are able to characterize memristive switching, which is witnessed by many papers dealing solely with the question, how to probe memristive switching in the most convenient way [95, 113, 114]. Due to the fact, that the phenomena behind memristive switching proceeds at the nanoscale, probing of such phenomena can be challenging. A method that is able to probe memristive switching down to the nanoscale is conductive atomic force microscopy (cAFM). A schematic illustration of a cAFM measurement scenario is given in Figure 2.12. There, a conductive probe, called cantilever, is brought into contact with the filamentary feature that is responsible for memristive switching. Instead of having an electrode integrated on top of the insulating layer, the cantilever acts as inert electrode and therefore effectively completes the MIM structure. A typical dimen-

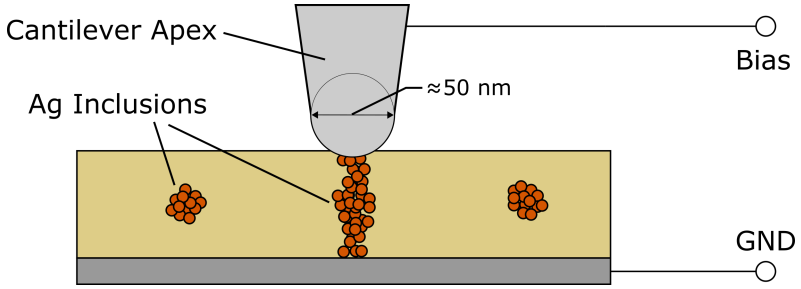

Figure 2.12: Illustration of a cAFM probing scenario. Filamentary structures are brought into contact with a cantilever.

sion of the apex region is a curvature radius of 25 nm (however, this value is different between cantilever models). The memristive switching of the filamentary feature can be probed upon biasing the cantilever while measuring the current response. As the position of the cantilever is not fixed, but can be scanned over the surface, cAFM is an excellent method to characterize the feature size [115] of the filament. This makes cAFM highly relevant to determine the ultimate scalability limit of a memristive device (because the dimensions of a memristive device cannot be below the feature size of the filament). However, long-term measurements by cAFM, that are relevant to test the endurance of a device, are unsuitable. This is because the cantilever is subjected to thermal drift, having a typical order of approximately 10 nm h^{-1}[113], which is in the range of typical filament sizes. Consequently, reliable cAFM probing, without uncertainties regarding the position of the cantilever, can only be done over a short time. One part of this thesis (presented in Chapter 4) deals with the development of an unconventional cAFM approach for the probing of filamentary switching dynamics under mitigation of experimental uncertainties related to thermal drift.

2.4 Self-organized Networks of Memristive Switches

As discussed in the previous section, (ECM-type) memristive devices constitute a group of two-terminal electrical devices, that can implement synaptic-like functionalities with a scalability down to the nanoscale. To create functional neuromorphic systems in the end, a large quantity of memristive device has to be integrated in complex networks [116, 117]. This can be achieved by following two distinctly different strategies. Firstly, individual memristive devices can be integrated in highly ordered systems via sophisticated top-down methods [28–32]. In this case, a precise control of the behavior of each individual device is aimed and the complex wiring in the system has to be engineered in detail. Crossbar arrays are typical examples (see Figure 2.2) for neuromorphic systems of such kind. A fundamental characteristic of such architectures is that each memristive device can be individually addressed. A second approach, which involves a fundamentally different architecture for neuromorphic systems, is to create networks by (bottom-up) random dispersion and interconnection of memristive switches [47–49]. In such networks, the arrangement of memristive switches and response to external stimulation is said to be *self-organized*. In other words, it is not aimed to address single memristive units individually, but to consider their emergent dynamics (emergent may be understood as "more than the sum of its parts"[82]), which arise from the collective interplay of the underlying individual memristive switches. One potential application of self-organized networks of memristive switches for the design of neuromorphic systems is reservoir computing (RC), which is briefly described here. A schematic depiction of RC is shown in Figure 2.13. The central element of RC is a fixed network structure

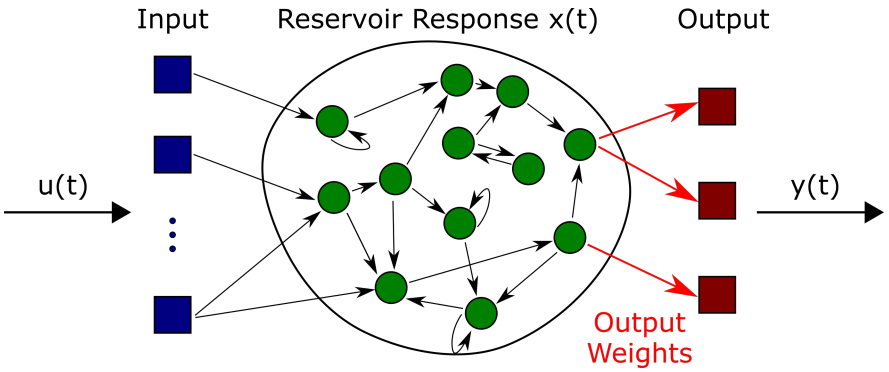

Figure 2.13: Basic scheme of reservoir computing. An input signal u(t) is fed via an input layer over fixed connections into a "reservoir". The reservoir embodies a fixed recurrent network with non-linearly interacting units. The input signal is mapped into the reservoir evoking a response x(t). Learning is realized by adjusting the output weights, so that the output y(t) recognizes the input fed into the reservoir.

(called a "reservoir") that consists of many (non-linearly) interacting units, that are linked by recurrent and feedforward connections. Further, when the reservoir gets an input, it must be able to store information in the evoked response. When an input signal is given into the reservoir, it is mapped into the (high-order) response. The reser-

voir response in turn is recorded at a read-out stage. Computational capabilities are realized by learning at the readout state, i.e. through adjusting the weights in such a way, that the reservoir response allows to recognize the mapped input. The read-out stage is created by a simple one-layer network, which is an important advantage of RC. Comprehensive insights into the concept of RC can be found in the works of [118, 119]. Self-organized networks of memristive switches and their emergent dynamics turned out to be promising candidates for the physical implementation of RC. Significant work in this direction was done on the investigation of networks of memristive Ag-nanowires [50, 51, 59, 120–122]. Recently, metallic NPs gained interest as fundamental building units for the creation of self-organized networks of memristive switches [53, 58]. The next sections cover theoretical considerations, that are fundamentally relevant for the design of memristive networks based on NPs.

2.4.1 Percolation Transition

One major design principle for self-organized networks of memristive switches, that must be considered to establish a dynamical regime that is meaningful for neuromorphic tasks, is the tailoring of network connectivity. Roughly speaking, here the connectivity can be understood as density of all (nanoscopic) memristive junctions between individual network units (such as electrically connected nanowires or NPs), that determines the macroscopic network dynamics. Closely related to this problem is the theoretical concept of percolation, which is briefly introduced in this section. Generally, percolation theory plays an important role in a broad variety of network systems (like epidemics or forest fires for example) and to explain scale-invariant structures in physical systems [123–125]. A typical percolation problem can be defined as follows: A network with fixed sites is given. These sites are randomly occupied by individual network units, where p and $1-p$ describes the probability, whether a site is occupied or not, respectively. This scenario is referred to as *site percolation*. As p increases, more sites become occupied in the network and clusters are forming. A cluster within a network denotes larger structures of interconnected occupied sites. The percolation transition is quantified by a probability for site occupation p_c, where one cluster exists that spans over the dimensions of the whole network. Considering the theoretical scenario of an infinite network, this means that at $p < p_c$ all clusters in the network have a finite size, whereas at $p > p_c$ there is one dominating cluster having an infinite size. A slightly different view on percolation problems is provided by *bond percolation*, where p describes the probability that an edge, connecting two adjacent sites, exists.

The percolation transition can be treated as a phase transition, where the site occupation probability p acts as a control parameter. The probability that a site belongs to the infinite cluster P_{inf} can be regarded as the corresponding order parameter. Generally, the order parameter describes the macroscopic appearance of a system. In real physical systems, the magnetization or conductance of a network can be seen as order parameters. Typical characteristics of a percolation transition are shown in Figure 2.14. These illustrated characteristics can be universally recognized in many percolation problems of physical systems.

During a percolation transition, the order parameter P_{inf} is governed by the following relationship, whose main characteristic is a critical exponent β:

$$P_{\text{inf}} \propto \begin{cases} 0 & \text{for} \quad p < p_c \\ (p - p_c)^{\beta} & \text{for} \quad p > p_c \end{cases} \tag{2.4}$$

Another characteristic quantity at the percolation transition is the mean count of sites that belong to a finite cluster S, that diverges at p_c. For this quantity, it holds with an exponent γ:

$$S \propto |p - p_c|^{-\gamma} \tag{2.5}$$

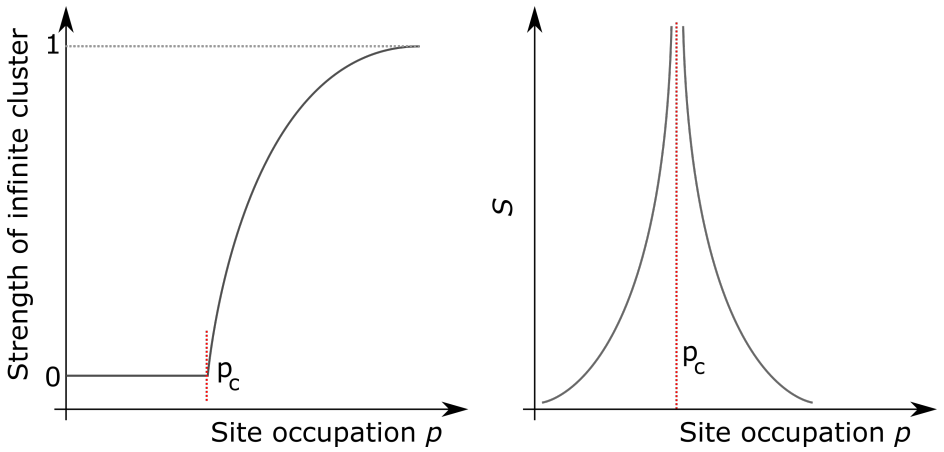

Figure 2.14: Characteristics of a percolation transition. In an infinite network, an infinite cluster appears at a particular probability for site occupation p_c. This infinite cluster growths until a site occupation probability of one (left). The mean count of sites that form a cluster S diverge at p_c (right).

2.4.2 Nanoparticle Networks

The percolation theory is a helpful background to understand the correlation between morphological properties and the macroscopic electrical behavior of a NP-based network of memristive switches. Considering a network, that is statistically filled with NPs over time, the network experiences a transition from a globally insulating to a conducting regime. This transition can be understood as an electrical percolation transition, that occurs when a conduction path is formed that spans over the whole network [54, 126]. Three distinct regimes, that mark different network states, are depicted in Figure 2.15. For each regime, a different dynamical behavior can be expected. In the range below the percolation transition, the average gaps between NPs are too large in order to enable any (tunneling) conduction mechanism, meaning that a network just behaves insulating without any dynamical behavior. This state is frequently referred to as *subcritical*. With

increasing amount of NPs, the gaps in the network become closer and closer. At the onset of percolation, non-linear conduction properties can be observed [127]. This comes from the emergence of conduction mechanisms like direct tunneling. The tunneling current

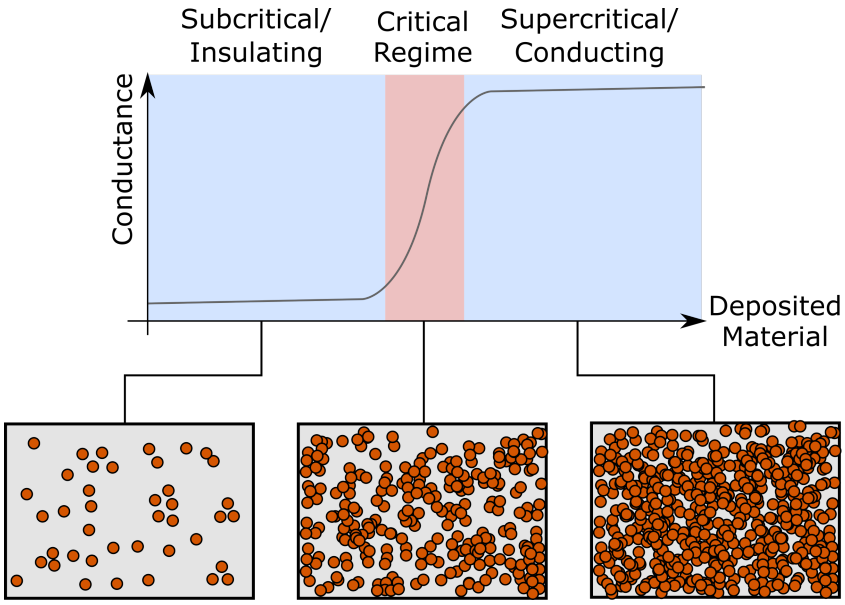

Figure 2.15: Schematic illustration of an electrical percolation transition in NP networks. Depending on the amount of deposited NPs during deposition, the network experiences a transition from an insulating to a conducting state. In the critical regime around the percolation transition, the network conductance varies over orders of magnitude.

that is enabled in a sufficiently small gap between NPs can be described by the Simmons' formula[128, 129]

$$\begin{aligned} I \propto (\Phi_B - \frac{eV}{2}) \exp(-\frac{2(2m)^{1/2}}{\hbar}\alpha(\Phi_B - \frac{eV}{2})^{1/2}d) \\ -(\Phi_B + \frac{eV}{2}) \exp(-\frac{2(2m)^{1/2}}{\hbar}\alpha(\Phi_B + \frac{eV}{2})^{1/2}d) \end{aligned} \tag{2.6}$$

where Φ_B is the height of a non-ideal potential barrier, α a parameter describing the non-ideal character of the tunneling barrier, d the gap width, V the field across the gap, m the free electron mass and $\hbar$ the reduced Planck constant. Another effect of approaching the percolation transition is, that the gaps between NPs become sufficiently small, so that electrical fields across the gaps are strong enough to induce memristive action. In Ag-based networks of memristive switches, ECM can be considered as dominant mechanism that causes memristive action in the gaps within the network [121]. However, there are also different mechanism reported, besides ECM, that could be relevant for the memristive action in NP networks, especially when the gap width approaches atomic dimensions. Alternative memristive mechanisms include atomic modifications induced by field-enhanced surface diffusion [58, 130] or gap modifications by electromigration [96,

131]. Furthermore, rearrangements at grain boundaries between interconnected NPs were also considered as a memristive mechanism [53]. The range around the percolation transition is referred to as *critical* regime. The group around Simon Brown recognized, that the implementation of NP networks in the critical regime (through careful poising at the electrical percolation threshold) is a feasible strategy to emulate highly complex neuronal connectivity together with emergent functional behavior, useful for neuromorphic applications [56, 128]. It was found that NP networks poised at the percolation threshold exhibit brain-like behavior, such as scale-invariant avalanches [57] and LRTC [61], both features that are related to the critical regime. It was further shown, that the emergent behavior in the critical regime can be described when a deterministic leaky integrate-and-fire model is assumed for the memristive switching in individual gaps [60]. It should be noted, that fingerprints on critical dynamics were also found in systems build of Ag-nanowires [59]. The *supercritical* regime of a NP network is reached, when a dense nanogranular film exists, that allows for conduction at low resistivity. Many systems that have surpassed the electrical percolation threshold can be treated as a stable Ohmic-type conductor, however, this belief is not necessarily true for NP-assembled systems. It was demonstrated that Au-NP films well above the percolation threshold can exhibit memristive switching phenomena and non-linear conduction characteristics [55]. The origin of memristive switching in these systems was traced back to atomic rearrangements occuring at grain boundaries [53]. Furthermore, it is assumed that memristive switching events in supercritical Au-NP network also have a correlated nature [53]. A short notice should be put on the fact, that self-organized networks for neuromorphic systems not necessarily require preformed nanowires or NP as building units. Instead, it was shown that correlated memristive behavior can be also obtained in evaporated (i.e. atomically assembled) discontinuous Au thin films [133].

3. Fabricational Methods

Different physical vapor deposition (PVD) methods were applied in this thesis for the fabrication of memristive systems based on Ag-nanostructures. Direct current (DC) magnetron sputtering was applied for deposition of metallic thin films (relevant for Chapter 4). The integration of insulating layers into the memristive systems was realized by reactive DC magnetron sputtering. Insulating layer materials that were applied in this thesis are SiO_xN_y (Chapters 4, 5, 7 and 9) as well as SiO_2 (Chapter 6). Designing memristive nanostructures via metallic NPs is of fundamental interest in this thesis. A Haberland-type gas aggregation source (GAS) was used for the gas phase synthesis of Ag-NPs (Chapter 9) or AgPt and AgAu alloy-NPs (Chapters 5, 6, 7, 8). Some memristive systems in this work are integrated on structured back electrodes (Chapters 7, 9), that were fabricated by a UV lithography process. The following sections provide details of these aforementioned methods.

3.1 Magnetron Sputter Deposition

Magnetron sputtering is a routinely applied method for the growth of thin films, including a broad range of metals and insulators, on various substrate materials [134]. The fundamental principle relies on the erosion of target material by energetic ion impact under vacuum conditions. Figure 3.1 illustrates the basic setup of a magnetron sputter head. Main components are a target (which is set to negative potential during sputtering), a grounded cap acting as counter electrode, inlets for gas supply as well as water cooling and permanent magnets at the target backside. Operation of the process under vacuum conditions is crucial to achieve a mean free path of sputtered target atoms, that establishes a permanent flux of target material towards the substrate. The ion bombardment on the target is realized by a stable glow discharge of an inert gas (Ar is typically used). The target is put at negative potentials in the order of a few 100 volts and Ar^+-species from the plasma are therefore accelerated towards the target. Upon acceleration, the Ar^+-species gain energy which is transferred during impact on the target surface. This triggers a collision cascade on the target surface, causing the release of target atoms and secondary electrons into the gas phase. A portion of sputtered target atoms then reaches the substrate where it contributes to the growing thin film. Noble metals grow on non-metallic substrates commonly in an island-like fashion [135, 136]. The release of secondary electrons is important to retain the glow discharge.

They collide in the gas phase with neutral Ar-atoms causing impact ionization, which leads to the ongoing production of Ar^+-species and free electrons in the plasma. Among other influences, the efficiency (i.e. deposition rate) of the sputter process depends on the amount of ionized gas in the plasma. For this purpose, magnetron sputter heads are supplied with permanent magnets that are located at the target backside. Due to the permanent magnetic fields, free electrons in the plasma experience a Lorentz force, which confines their motion above the target surface. By this, the collision rate per electron is increased, which leads to a higher ionization rate of inert gas atoms. Another effect of the permanent magnetic field is an inhomogeneous electron density in the plasma region above the target, that causes characteristic sputter trenches during prolonged usage of a target. The procedure as described above is more precisely referred to as DC magnetron

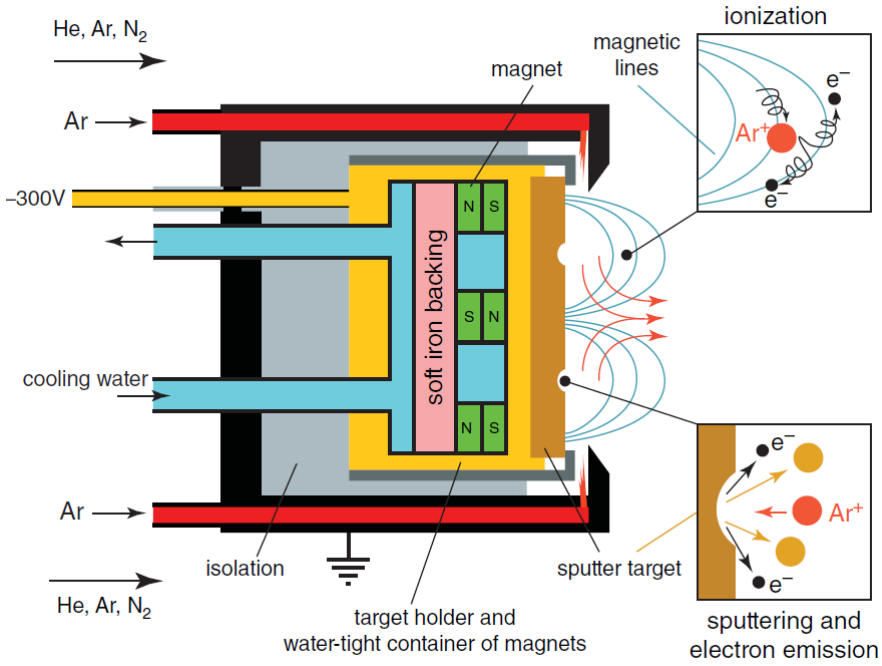

Figure 3.1: Illustration of a magnetron sputter head. The basic sputter process involves bombardment of the target surface by high energetic Ar^+-species causing release of target atoms into the gas phase and their transport towards a substrate material. Reprinted from [137].

sputtering, which is suitable for metallic target materials. However, this process can be modified to enable the growth of insulating thin films by additionally introducing a reactive gas, besides the inert gas [138, 139]. Such a process is called reactive sputtering. The reactive gas (such as oxygen or nitrogen) dissociates in the plasma and reacts with target atoms either at the target surface, in the gas phase or on the substrate (leading to the formation of oxides or nitrites). Due to the danger, that the target surface can heavily react and therefore become insulating (called "target poisoning"), reactive sput-

tering processes typically requires a more careful control than sputtering of metals. This is because target poisoning hinders the charge balancing at the target surface, which is usually accompanied by a drastic decrease of sputter rate. To circumvent this issue, reactive sputtering processes are commonly driven by a pulsed power supply, instead of DC conditions [140]. During pulsed reactive sputtering, the process is divided in periods (alternating at a frequency of typically some 10 kHz) where the target is set to a negative potential (periods where target is sputtered) and where the target is set to a zero-bias or even positive potential (periods where charge balancing is realized at target surface by mobile electrons from the plasma).

3.2 Gas Aggregation Sources

The concept of a GAS allows for the gas phase synthesis of NPs via a slight modification of the magnetron sputtering method presented in the previous section. It was originally described by Haberland *et al.* in 1992 [141]. The idea is to create a sub-chamber, that is separated by a small orifice from the main deposition chamber. A general illustration of such a setup and fundamental processes occurring during NP aggregation are given in Figure 3.2. The magnetron head together with the according gas inlet is mounted

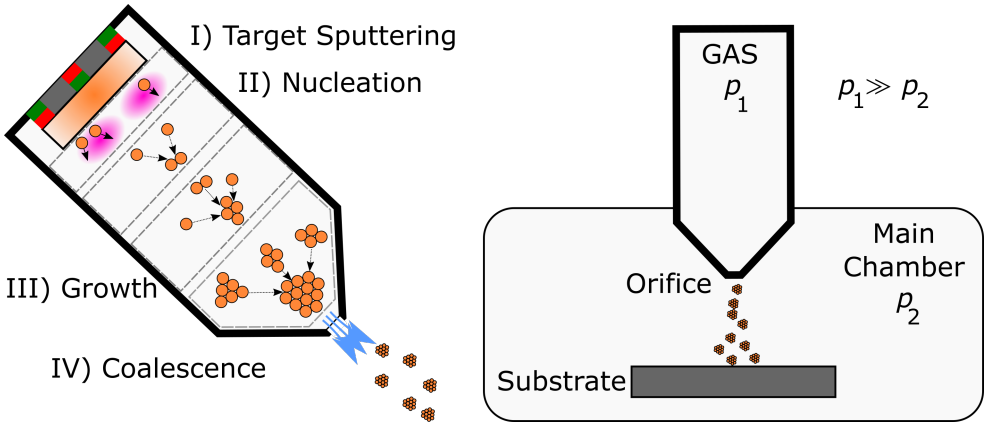

Figure 3.2: Illustration of a gas aggregation source. A higher-pressure sub-chamber is mounted to the deposition chamber. Conditions in the sub-chamber enables gas phase aggregation of NPs that are transported along the pressure gradient towards the substrate in the deposition chamber.

to the sub-chamber. As a consequence, the target atoms are sputtered into a higher pressure (in the order of 10 to 100 Pa) gaseous environment with an increased density of sputtered atoms. Under such conditions, a supersaturated vapor of target atoms is created, that allows for the aggregation of sputtered atoms into larger clusters. Typically, aggregation of metallic clusters involves the following steps: Firstly, a process to create stable nuclei could be the formation of metal dimers by a three body collision [142]. This involves two sputtered metal atoms and an inert gas atom. Upon collision of those three species, excess energy is transferred to the gas atom which allows the two metal atoms

to form a stable dimer. Further growth of metallic clusters takes place through the attachment of single atoms to existing stable clusters. Moreover, different clusters can merge together by coalescence processes. All of these processes occur in the gas phase and aggregated NPs are transported along the pressure gradient through the orifice into the main chamber.

The physical processes taking place inside a GAS during NP formation is still an active research field [143–145]. For instance, it has been found that the operational pressure inside the GAS determines the target surface area where materials becomes sputtered, which can be exploited for the *in-operando* control of alloy-NP composition [146]. The foundation for this is a special multicomponent-target design, where one component is embedded via concentric rings within a target consisting of the second component, directly in the area where the sputter trench evolves. Hence, manipulating the area of erosion changes the sputtered fraction between the first (embedded rings) and second component (bulk target) [146]. Moreover, it was identified that the complex trajectories of NPs inside the GAS are important to understand the growth of NPs [147]. Consequently, the engineering of GAS with respect to gas flow pattern is an important aspect to control the synthesis of NPs.

3.3 Photolithography

Photolithography refers to a broad range of different manufacturing techniques that allow for the patterning of thin film systems on a substrate. For a more comprehensive overview, the reader is referred to textbooks such as [148]. Here, the basic steps involved in photolithography that are relevant for this thesis are briefly outlined. Those steps are illustrated in Figure 3.3 on the basis of an exemplary metal line patterning. Firstly,

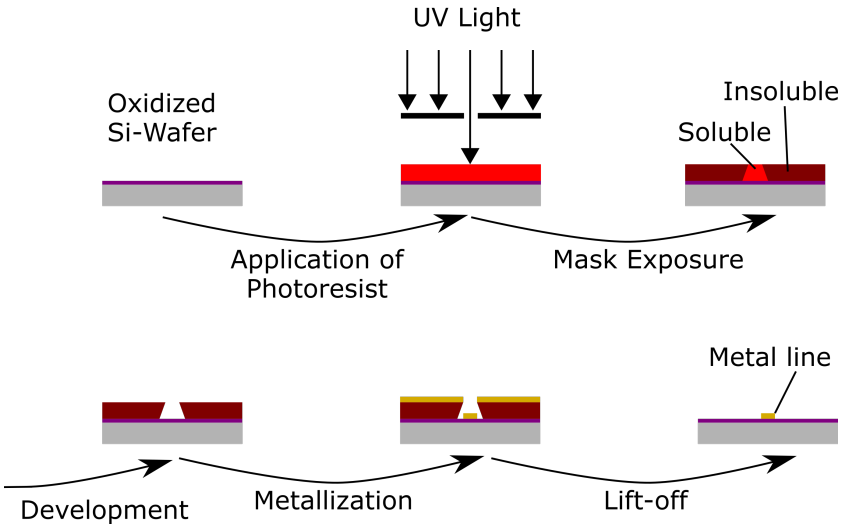

Figure 3.3: Basic steps involved in photolithography. As an example, manufacturing of a metal line following a lift-off process is shown.

an oxidized wafer is coated with a photoresist via spin coating. The photoresist is responsible for the pattern transfer from a purpose-built photomask to the substrate. An image of the photomask is then transferred on the photoresist by UV exposure in a mask alignment system. After UV exposure, the pattern is represented via soluble and insoluble areas of the photoresist. During a development step, soluble areas of the photoresist can be washed away. This paves the way for substrate patterning via either subtractive (e.g. etching) or additive processing steps. In the example of Figure 3.3, a typical lift-off process is shown. There, a metallization layer is added over the whole substrate. During lift-off, the photoresist acts as a sacrificial layer that can be dissolved, meaning that only metal structures that were deposited directly on the substrate remain.

4. Diffusive Memristive Dynamics of an Individual Ag-filament Investigated by an Unconventional cAFM Approach

An unconventional cAFM approach was developed, that offers enhanced possibilities to study the memristive dynamics of individual nanoscale Ag-filaments. The main idea is, to integrate the memristive system directly at the cantilever, to constrain the memristive action at the apex region during electrical characterization. This is showcased here via a cantilever functionalized by a Ag/Si_3N_4 thin film system. The data acquisition from the functionalized cantilevers was conducted by Abdou Hassanien at the Jozef Stefan Institute in Ljubljana. It is demonstrated, that this approach combines usual benefits of cAFM (e.g. access to nanoscale electrical characterization) with mitigation of undesired thermal drift effects. Furthermore, this approach allows to acquire the characteristics of the very same Ag-filament under various contact scenarios. This opens up considerably enhanced characterization strategies and was demonstrated by a cantilever with an integrated Ag/Si_3N_4 memristive system, that was contacted to a Au and indium tin oxide (ITO) surface in consecutive measurements. This experiment revealed an energy barrier (i.e. non-linear characteristics) during operation of the very same filament on ITO, which was absent in the case of Au. Using this approach, the diffusive switching dynamics of a Ag-filament was characterized over longer times scales ($\approx$ 18 h of continuous operation), which revealed temporal correlation effects governing the switching dynamics. Regarding to the context of this thesis, an individual filament can be seen as an elemental unit for the design of Ag-based neuromorphic systems. Consequently, the development of more sophisticated neuromorphic systems composed of many filamentary units directly relies on the understanding of individual filaments. The cAFM approach presented here proved well to gain deep insights into dynamical features of an individual Ag-filament and may be suitable for basic studies on other memristive systems.

This chapter is a reprint from the following publication:

N. Carstens, A. Vahl, O. Gronenberg, T. Strunskus, L. Kienle, F. Faupel and A. Hassanien, *Nanomaterials*, 2021, 11, 265

nanomaterials

MDPI

Article

Enhancing Reliability of Studies on Single Filament Memristive Switching via an Unconventional cAFM Approach

Niko Carstens [1], Alexander Vahl [1], Ole Gronenberg [2], Thomas Strunskus [1], Lorenz Kienle [2], Franz Faupel [1,*] and Abdou Hassanien [3,*]

[1] Chair for Multicomponent Materials, Institute for Materials Science, Faculty of Engineering, Christian-Albrechts-University of Kiel, Kaiserstraße 2, D-24143 Kiel, Germany; nic@tf.uni-kiel.de (N.C.); alva@tf.uni-kiel.de (A.V.); ts@tf.uni-kiel.de (T.S.)

[2] Chair for Synthesis and Real Structure, Institute for Materials Science, Faculty of Engineering, Christian-Albrechts-University of Kiel, Kaiserstraße 2, D-24143 Kiel, Germany; og@tf.uni-kiel.de (O.G.); lk@tf.uni-kiel.de (L.K.)

[3] Department of Condensed Matter Physics, J. Stefan Institute, Jamova 39, 1000 Ljubljana, Slovenia

* Correspondence: ff@tf.uni-kiel.de (F.F.); Abdou.Hassanien@ijs.si (A.H.)

Abstract: Memristive devices are highly promising for implementing neuromorphic functionalities in future electronic hardware, and direct insights into memristive phenomena on the nanoscale are of fundamental importance to reaching this. Conductive atomic force microscopy (cAFM) has proven to be an essential tool for probing memristive action locally on the nanoscale, but the significance of the acquired data frequently suffers from the nonlocality associated with the thermal drift of the tip in ambient conditions. Furthermore, comparative studies of different configurations of filamentary devices have proven to be difficult, because of an immanent variability of the filament properties between different devices. Herein, these problems are addressed by constraining the memristive action directly at the apex of the probe through functionalization of a cAFM tip with an archetypical memristive stack, which is comprised of Ag/Si_3N_4. The design of such functionalized cantilevers (entitled here as "memtips") allowed the capture of the long-term intrinsic current response, identifying temporal correlations between switching events, and observing emerging spiking dynamics directly at the nanoscale. Utilization of an identical memtip for measurements on different counter electrodes made it possible to directly compare the impact of different device configurations on the switching behavior of the same filament. Such an analytical approach in ambient conditions will pave the way towards a deeper understanding of filamentary switching phenomena on the nanoscale.

Keywords: neuromorphic engineering; cAFM; diffusive memristive switching; resistive switching; memristors; spiking dynamics

Citation: Carstens, N.; Vahl, A.; Gronenberg, O.; Strunskus, T.; Kienle, L.; Faupel, F.; Hassanien, A. Enhancing Reliability of Studies on Single Filament Memristive Switching via an Unconventional cAFM Approach. *Nanomaterials* **2021**, *11*, 265. https://doi.org/10.3390/nano11020265

Received: 16 December 2020
Accepted: 15 January 2021
Published: 20 January 2021

1. Introduction

The research field of memristive switching phenomena has already experienced huge interest for more than a decade. An important stimulus to this field came in 2008 [1], where for the first time a physically implemented resistive switching device was related to the originally proposed theory postulated in 1971, in which the memristor was described as the missing, fourth fundamental circuit element [2]. Despite the arising controversy following this claim [3], the application potential of memristive devices in technologies like in neuromorphic computation architectures [4–6], novel data storage [7], and memsensing [8,9] is unambiguous. Typically, memristors are two-terminal devices, which are capable of occupying different distinct resistive states, resulting from stimulation by an external electrical field. This functionality emulates certain aspects of the behavior of biological synapses, and makes memristors promising candidates for fundamental building units in brain-inspired hardware design [10]. Up to now a broad variety of physical mechanisms

have been explored, which allow for the realization of memristive switching functionality, of which the electro-chemical metallization (ECM), the valence change mechanism (VCM), and the phase change mechanism (PCM) are the most prominent [11,12]. Among these different mechanisms, special attention has been paid to the ECM concept, which relies on an electrochemical redox reaction and migration of active metallic species, like Ag or Cu, between two electrodes. The application of controlled voltage stimuli on an ECM device allows the modification of the atomic configuration of the active species between the electrodes, and therefore influencing the resistive state, depending on whether or not both electrodes are electrically connected via a metallic path [13]. Taking the ECM mechanism as a fundamental working principle, memristive devices with a broad range of characteristics and different operation regimes have been created, like bipolar switching, complementary switching, or multilevel switching [14]. Special interest has been paid to memristive devices showing a diffusive switching characteristic, i.e., devices with very short filament lifetimes leading to volatility of the conductive state at low voltages. Diffusive memristive switching has been adapted to emulate short-term plasticity in neural systems [15], for the implementation of random number generators [16], or for selector devices [17]. The principal approaches for achieving diffusive switching are effectively limiting the amount of active species, e.g., by using nanoparticles as a reservoir for active species [18], or through severe current limitation during the filament formation process, e.g., by applying a current compliance, or by inclusion of a serial resistance [19].

A deep understanding of memristive switching phenomena is essential to reach the next levels in device maturity. Since investigating memristive features down to the nanoscale is inevitable, the exploitation of reliable and non-invasive analytical methods is challenging. In this regard, conductive atomic force microscopy (cAFM) is an established analytical tool, because it enables monitoring the electrical properties by a nano-sized probe at the required scale [20,21], and allows drawing conclusions between the measured electrical data and the morphology of the conducting filament [18,22,23]. Nevertheless, several prospects for cAFM, like studying the possible failure mechanism from endurance tests, are restricted by thermal drift effects, such as a spatial drift between the conducting filament and probe, leading to a considerable loss in data significance. Another challenge arises from the fact that measurements on different samples, representing the same filamentary device, might not be comparable to each other, because the switching performance of an individual filament considerably depends on the initial forming conditions and the matrix defect structure surrounding the filament [24]. Hence, complications exist when the influence of a parameter, like various counter electrode materials, must be studied over a sample series consisting of different devices, due to the inherent randomness of the filament switching performance. This problem has been encountered in many studies on memristive devices, and is commonly referred to as device-to-device variability [25,26]. Consequently, unconventional cAFM approaches are required to cope with the aforementioned problems. A promising strategy is to use cantilevers, which are functionalized with the memristive materials of interest. Instead of contacting the sample with a regular conducting cantilever, like in conventional cAFM, direct integration of the memristive thin film stack of interest on the apex of the cantilever is a versatile and unelaborate strategy to circumvent challenges like thermal drift, and to enable studies of different device configurations with the same active filament. Such an unconventional cAFM approach has been successfully used for a detailed characterization of memristive TiO_2-based systems, with a focus on the chemical bonding status at interfaces in the device [27].

This work adapts this analytical approach towards ECM systems, which substantially extend the capabilities of cAFM for the investigation of memristive switching phenomena on the nanoscale. To demonstrate this, commercially available cantilevers were functionalized with a representative memristive device consisting of a stack of an active Ag layer and a Si_3N_4 dielectric layer. We note that there are other memristive systems which are also promising for future large scale device integration. The focus of our work, however, is to demonstrate pathways for reliable studies of single filament switching, for basic

research purposes. Electrical characterization was done by contacting the functionalized cantilevers to planar counter electrodes, and measuring the IV-curve via a conventional cAFM instrument. In the following, the functionalized cantilever samples are referred to concisely as "memtips". Figure 1 illustrates the approach of using memtips for enhanced cAFM studies. It should be noted, that the memtips could be applied principally to any conducting surface, and therefore testing of a variety of application scenarios is possible. The results presented in this work give fundamental insights into the diffusive switching of ECM devices, and are discussed in the individual sections under elucidation of the decisive advantages of the memtip approach. First, observations from a long-term measurement of a memtip are discussed, with a focus on temporal correlations between subsequent switching events. The focus on temporal correlations is motivated by the fact that encoding information in temporal patterns of memristor activity is seen as the next step in the development of artificial neural network hardware. Utilization of a memtip for the long-term observation turned out to be highly beneficial, because the filament formation was constrained to the vicinity of the apex and, accordingly, no drift between filament and apex was possible. This work further demonstrates a study on the influence of two different counter electrodes, namely Au and indium tin oxide (ITO), on the switching performance of the same active filament. This was enabled by the memtip approach, because here an identical memtip can be contacted to different counter electrodes. The last part of this work is dedicated to the occurrence of highly dynamic transitions between different resistive states, leading to distinct spiking patterns, which inherently arise when ECM devices are operated at the border of filament stability. Fundamentally, the characterizations done by the memtip approach resemble those of conventional cAFM on similar memristive devices. Principally, every conventional cAFM study on any memristive device could be converted to the memtip approach. The chosen approach of integrating the memristive stack directly on the cAFM tip mitigates thermal drift effects, and allows the study of the same active filament in different device configurations, ultimately leading towards an enhanced level of reliability and significance.

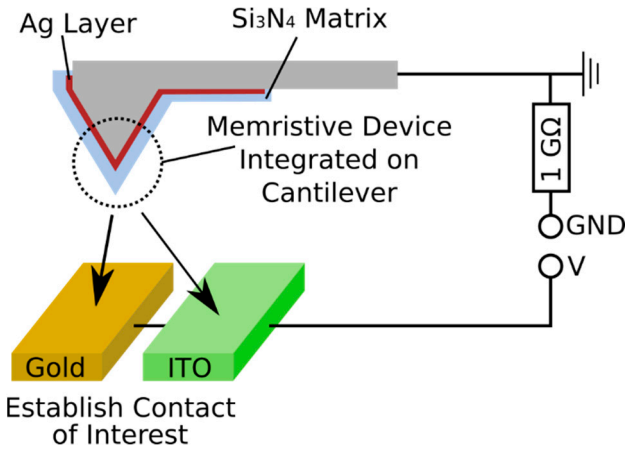

Figure 1. Schematic of the memtip approach. The memristive device, consisting of an Ag layer and an overlaying Si_3N_4 layer is integrated directly on the tip of the cantilever. By using conductive atomic force microscopy (cAFM) instrumentation, a reliable contact between the memtip and counter electrode of interest (which are Au and ITO in this work) is established and characterized by electrical measurements. A serial resistance of 1 GΩ was added in each measurement to limit the current through the memtip.

2. Materials and Methods

2.1. Preparation of Memtips

The fabrication of memtips was realized by covering commercially available cantilevers (Bruker OTESPA-R3, Camarillo, CA, USA) with an inert conducting layer over the entire surface, followed by integration of a memristive device directly on the apex on

the cantilever by different physical vapor deposition methods in a self-built high vacuum deposition system. In the first vacuum deposition step, each cantilever was covered with a Ti layer acting as an adhesion promoter, followed by covering with an Au layer acting as a chemically inert electrode to make the memtip applicable for cAFM. In the second vacuum deposition step, a Ag layer and Si_3N_4 layer on top were deposited onto the apex of the cantilever under shadowing of the cantilever body, to integrate the memristor functionality.

The deposition system consisted of a turbo molecular pump (Pfeiffer Vacuum, TMU 262, Asslar, Germany) combined with a dry scroll pump (Agilent Technologies, SH-110, Santa Clara, CA, USA), to realize high vacuum conditions. Two independent DC magnetron sources (Thin Film Consulting, ION'X-2UHV, Grafenberg, Germany) connected to a high voltage power supply (Advanced Energy, MDX 500, Frankfurt, Germany) and mounted to the system were used for deposition of the corresponding layers in each step. The angle of incidence of each magnetron source with respect to the sample holder was 55°. Two flow controllers (Pfeiffer, EVR116 with attached hot ion cathode IMR 285, Asslar, Germany) regulated the inlet of inert Ar gas and reactive N_2 gas for the according depositions. The sample holder in the deposition chamber was enabled for 360° rotations, which allowed uniform coating of the memtip from all sides, where it was needed.

Deposition of the Ti adhesion promoter was done by DC magnetron sputtering at 30 W and an Ar flow of 50 sccm from a Ti target. The subsequent Au deposition was done by DC magnetron sputtering at 30 W and an Ar flow of 50 sccm from an Au target. During both Ti and Au deposition steps, the cantilever was mounted vertically on the sample holder, and performed a complete 360° rotation over the deposition time, to ensure coverage of the entire surface. Deposition of the Ag layer was done by DC magnetron sputtering at 30 W and an Ar flow of 50 sccm from an Ag target. The final Si_3N_4 deposition was done by DC reactive sputtering from a Si target, at a power of 20 W and under a gas mixture of 50 sccm Ar and 0.44 sccm N_2. The memtip was positioned in front of the magnetron source during Ag and Si_3N_4 deposition, to ensure vertical incidence of sputtered material to achieve homogeneous deposition in the apex region.

The memtips discussed in Sections 3.1 and 3.2 were prepared with effective thicknesses of 3.5 nm for Ag and 4 nm for Si_3N_4. To realize the investigations on filament instability related to a limitation of active Ag species, the memtips discussed in Section 3.3 were prepared with effective thicknesses of 2 nm for Ag, and 6 nm for Si_3N_4.

2.2. Conductive AFM Instrumentation

The electrical measurement was carried out at room temperature using a commercial AFM microscope (Dimension 3000, Bruker, Camarillo, CA, USA). The electrical signals to the AFM were customized, using a break box, for device initialization and subsequent data acquisition. Non-invasive measurements were achieved with a contact force of 1.2 nN. The tip quality was also checked before and after measurements, to ensure that the tip apex suffered no degradation during prolonged measurements. The details of the measurements are described elsewhere [18].

2.3. TEM Investigation

TEM measurements were performed using a JEOL-2100 (Tokyo, Japan) with acceleration voltage of 200 kV and a LaB6 cathode. The memtip was mounted on a high-tilting holder, and tilted to 60° to almost obtain a sideview of the tip.

3. Results and Discussion

3.1. Long-Term Observation of Nanoscale Filamentary Switching

Results from long-term studies acquired by AFM methods frequently suffer from thermal drift effects, since they cause uncertainties with regard to the cantilever position relative to the feature under investigation. The lateral motion of the cantilever due to thermal drift is more than 10 nm h^{-1} making reliable long-term observation of nanoscalar features on the same order challenging [28]. As many memristive phenomena, especially

those where filament formation is involved, take place in a region of several nm, conventional cAFM is not a reliable tool for long-term observation. This drawback of cAFM motivates the application of memtips for the study of filamentary-based memristive devices. Integrating the memristive device on the cantilever constrains the filament formation to occurring directly at the apex, and consequently prevents that filament and cantilever drifting apart from each other.

In this section, the capabilities of memtips for the long-term observation of nanoscale memristive phenomena under the significant mitigation of thermal drift effects are demonstrated. Figure 2a depicts the apex of a memtip investigated by transmission electron microscopy (TEM). For this purpose, the entire cantilever was examined in the TEM in projection onto the side view. It can be seen, that the active area of the cantilever is uniformly covered with the Si_3N_4 layer. The dielectric layer has a thickness in the range of 4 nm $\pm$1 nm (cf. Supporting Information Figure S1). We noted that the thickness variation of Si_3N_4 and the non-flat contour of the tip would be exclusion criteria for their applicability as electronic devices. However, for basic research into the switching activity of a single filament, these influences are secondary. From the TEM image the radius of the curvature can be estimated as 46.5 nm. The effective radius of curvature at the apex exceeds the specifications of the manufacturer due to the fabrication procedure of the memtip with additional Au, Ag, and Si_3N_4 layers. However, the thin coating ensures that the apex is still sharp enough to image features of less than 3 nm (cf. Supporting Information Figure S2). Due to beam damage, the cantilever examined in the TEM did not show diffusive switching, which was most likely based on a depletion of Ag atoms at the apex location. Those morphological changes also makes TEM studies on operated memtips critical. Further details can be found in the Supporting Information Figure S3, where morphological changes are illustrated. Electrical studies of the memtips were conducted by mounting the memtip into a conventional cAFM instrument, and adjusting the contact to an Au counter electrode. For the long-term study the memtip was operated continuously for roughly 18 h. The resulting electrical characteristics showed reliable diffusive memristive switching for over 12,000 cycles, with about 95% of all cycles showing a clear diffusive switching fingerprint. In the residual 5% that were characterized as no clear diffusive switching, no switching events, a nearly ohmic behavior, or a negligible switching window below 0.2 V were observed. The underlying physical mechanisms, together with a representative cycle, are depicted in Figure 2b,c, respectively. Under initial conditions, with no external field applied, the memtip is in a high resistance state (HRS) with a current level of 1 pA corresponding only to noise. Upon the application of an external electrical field, i.e., by ramping up the voltage towards either polarity, electrochemical oxidation of Ag takes place at anodic sites in the memtip, leading to the release of Ag+-cations into the dielectric layer. The Ag+-cations migrate along the field gradient until they become reduced at cathodic sites. By this mechanism Ag is removed from anodic sites, and accumulated at cathodic sites until a continuous filament has grown up and connects the cantilever apex with the counter electrode. The moment of completed filament formation is denoted as a SET event, and causes the transition to a low resistive state (LRS). In the LRS a current in the order of 1 nA flows through the memtip. Here, the resistance is not dominated by the memtip anymore, but by the 1 GΩ serial resistance, which is incorporated in the experimental setup. Subsequent reduction of the external field causes a spontaneous disintegration of the filament before reaching the zero-crossing, and accordingly results in a transition back into the HRS. This moment is denoted as a RESET event. As this mechanism takes place equally at both polarities, a full cycle is governed by four threshold switching events, namely one SET and one RESET event for each, positive or negative, bias voltage polarity. The fact that the LRS is not maintained at zero volt conditions is the most prominent feature of diffusive switching devices, and discriminates them from bipolar or unipolar memristive devices. A possible origin of this diffusive switching behavior are the short filament lifetimes, arising from the small filament diameters. If the formed filament is not thick enough, the overall energy of the system can be minimized by disintegration

of the filament into individual clusters because of the high surface-to-volume ratio and the resulting interface energy minimization [19]. In the measurement presented here, the current limitation from the serial resistance of 1 GΩ restricts the Ag mass transport, and consequently effectively narrows the filament growth. Thus, the experimental conditions under incorporation of the 1 GΩ serial resistance constrained the operation of the memtip in the diffusive switching regime. Generally, for a SET event, driving forces leading to interface energy minimization must be outweighed by the driving forces promoting filament formation, which originates from the external voltage. Accordingly, the RESET voltage indicates the operation regime where the driving forces for energy minimization cannot be compensated anymore. Both SET and RESET switching show a certain degree of randomness, and the respective threshold voltages underlay a statistical distribution. This is shown in Figure 2d, where 100 sequential cycles are depicted, showing that SET and RESET voltages span up a voltage interval.

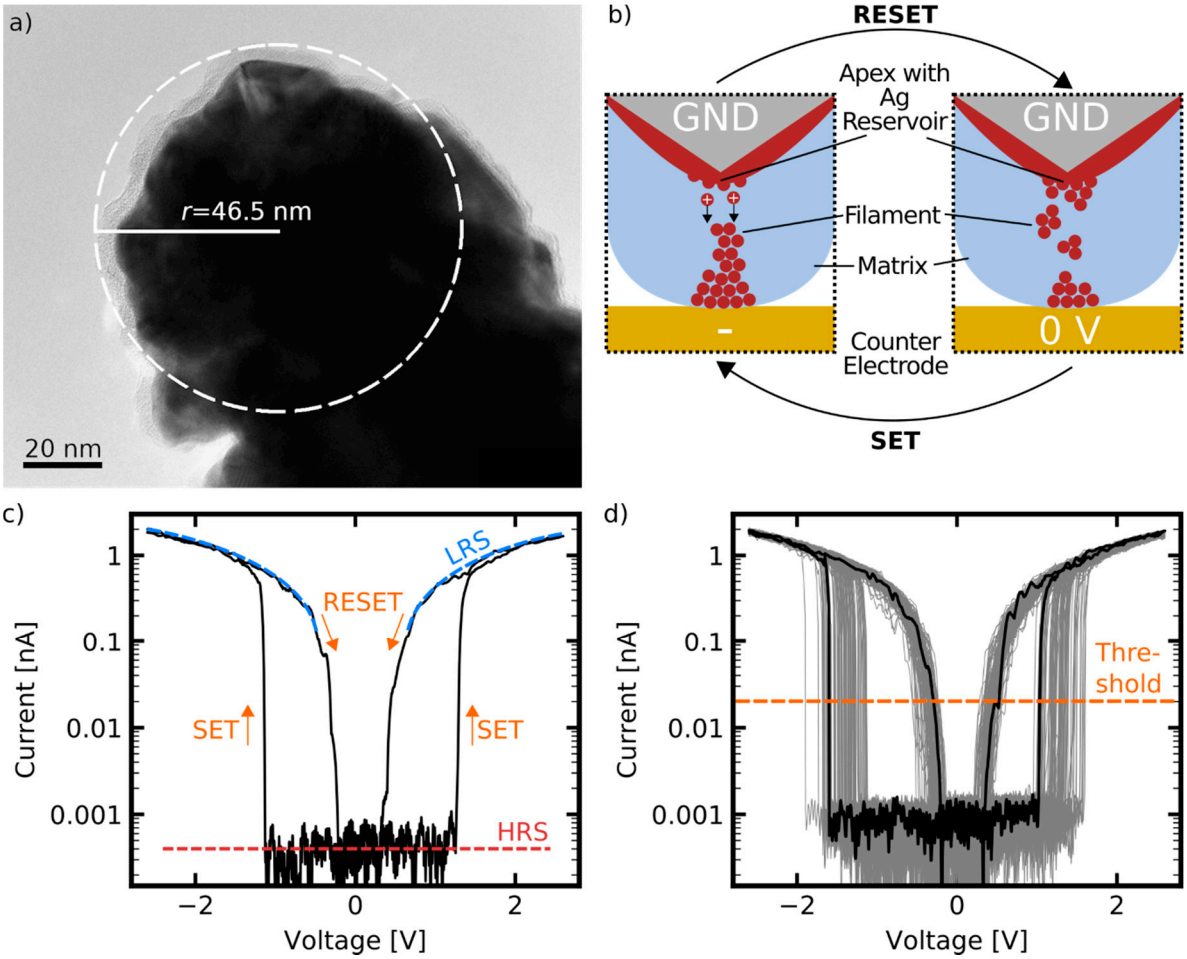

Figure 2. (**a**) TEM image of a memtip indicating a radius of curvature of 46.5 nm. (**b**) Schematic representation of the switching mechanism from electro-chemical metallization (ECM) principles. Upon application of an electrical field between the memtip and counter electrode, electrochemical oxidation of Ag is induced at positive polarity, leading to release and migration of Ag+-cations through the dielectric layer towards the negative polarity. Reduction of Ag+-cations occurs at negative polarity, causing the buildup of a conducting Ag filament, and leading to a SET switching event. Reduction of the electrical field causes a spontaneous disintegration of the filament because of interface energy minimization, resulting in a RESET switching event. (**c**) Representation of a single cycle from cAFM operation depicts the diffusive memristive switching characteristic of the memtip. The current in the low resistive state (LRS) is limited by the 1 GΩ serial resistor incorporated in the experimental setup. The high resistance state (HRS) is given by the detection limit of the setup. (**d**) Representation of 100 sequential cycles showing a consistent switching window. A threshold level of 20 pA, as indicated, is chosen for a reliable detection of SET and RESET.

Knowledge about the variability of switching parameters from cycle to cycle is of crucial importance for the application of memristive devices. Switching variability is an unwanted feature for certain applications like selector devices, because the state of each individual device has to be under precise control. However, the intrinsic randomness also offers promising approaches like probabilistic computing, or for hardware security applications, like true random number generators, where diffusive memristors are used as a source of uncertainty to create bit streams, which could be used as cryptographic keys [16]. Thus, basic research on the inherent variability of fundamental switching entities (like one single filament) is required to understand the implications on the device performance. However, the acquisition of reliable cycle-to-cycle variability data from switching phenomena on the nanoscale by conventional cAFM investigation is challenging because a large amount of sequential cycles must be measured to make meaningful statements, which is made impossible by thermal drift. Here, the long-term measurement of a memtip was used to gain deeper insights into the inherent variability of diffusive switching of one single filament. In Figure 3a, all threshold voltages are extracted and plotted against cycle number. A corresponding histogram plot and cumulative distribution function can be found in the Supporting Information Figures S4 and S5, respectively. Only cycles showing a clear diffusive switching characteristic, with a minimum switching window of 0.2 V were taken into account for this evaluation. A current level of 20 pA was consulted as criterion for threshold voltage detection, i.e., exceeding this level marks a SET event, and falling below this level marks a RESET event. Calculation of the variances (cf. Supporting Information Figure S4) for each threshold switching event indicated that the SET voltages (at both polarities) possess a more pronounced stochasticity than the RESET events. A notable observation is that the positions of threshold voltages are not stochastically independently distributed over the whole measurement, but the evolution of threshold voltages follows a common tendency over narrow intervals. This indicates a dependence on the history of device operation, and could be used to encode information in temporal correlations. To elucidate this, two regimes were highlighted. Systematic drifts of SET and RESET voltages at positive polarity governed the regime going from cycle 4000 to 7000. Separate drifts ranged over periods in the order of 100 cycles. In contrast to this, the threshold voltages in the regime from cycle 9000 to 11,000 occurred at a more constant level on average, and less occasional drifts were apparent. This suggests that individual SET and RESET voltages are not statistically independent from each other on compulsion, but correlated to the switching parameters from the previous cycles, and that the strength of correlation is an altering variable. Figure 3b,c plot the individual SET voltages at positive polarity against the respective values from the previous cycle for the first (cycles 4000 to 7000), and the second regime (cycles 9000 to 11,000), respectively, to illustrate the correlation strength. The same is shown for RESET voltages in Figure 3d,e. The Pearson coefficient was consulted as a measure to quantify the linear correlation between the pairs of values (i.e., the threshold voltage and the corresponding threshold voltage from the previous cycle) and given in the respective graphs. Regarding the first regime (cycle 4000 to 7000) the Pearson coefficient quantifying the correlation between SET events amounted to 0.879, and to 0.889 for RESET events. In the second regime (cycles 9000 to 11,000), the Pearson coefficient was calculated as 0.435 for SET events, and 0.581 for RESET events. Based on the quantification by the Pearson coefficient, the correlation between the individual threshold voltages and the respective former values from the previous cycle was stronger than in the first regime from cycle 4000 to 7000. A comparison of SET and RESET events within one cycle also reflects the higher degree of correlation in the regime from cycle 4000 to 7000 (cf. Supporting Information Figure S6). The appearance of correlation suggests the introduction of a type of autocorrelation function over the amount of cycles passed between the correlated cycles (cf. Supporting Information Figure S7). The fact that the degree of correlation reduces with a higher separation of the correlated cycles (in terms of number of cycles, which have been conducted in the interim period) is an important consideration for the design of filamentary diffusive switching devices, and could be used for bio-inspired

information processing. The dependence of threshold voltages on the values from previous cycles becomes evident under consideration of the morphological configuration of the disintegrated filament after a RESET event. This is because the reconfiguration after the filament disintegration determines the preconditions for the subsequent SET switching, in terms of number of gaps between individual clusters and the corresponding separation lengths. As the electrical field is the decisive driving force for SET switching, any variation in the morphology of the disintegrated filament and its characteristic separation lengths affects the electrical field, and consequently the SET voltage for the following SET event. In the case that the disintegrated filament already shapes a pronounced preformed filament, SET switching is eased, and lower SET voltages are necessary. The subsequent RESET event will leave behind a disintegrated filament with similar morphological configuration. On the contrary, when the morphological configuration of the disintegrated filament exhibits poor filament preforming, SET switching is impeded, and higher SET voltages are required. The fact that the morphological configuration of the filament does not change drastically from cycle to cycle, but only over larger time scales, interprets the observed correlation between individual threshold voltages and the respective former value from the previous cycle. The observed alteration of the degree of correlation underlines the assumption that some morphological configurations of the filament bear more inherent randomness of the switching voltage than other configurations, and that the degree of correlation evolves in correspondence with the long-term change of the morphological configuration. Furthermore, it can be observed that the degree of correlation may also depend on the polarity of the external field. This is most prominent in the high correlation regime for SET and RESET at positive polarity (cycles 4000 to 7000). In this regime, the correlation coefficients for SET (0.574) and RESET (0.652) at negative polarity are significantly lower. This can be attributed to the geometrical asymmetry of the electrodes leading to different field distributions across the filament. The asymmetric field can cause polarity dependent switching kinetics with different degrees of correlation, because the number and morphology of anodic and catholic sites in the system can differ. These findings, facilitated by the memtip approach, indicate that correlations between sequential switching events are an essential feature of diffusive switching. Since the degree of correlation defines fundamental constraints on the applicability of diffusive switching devices, deeper understanding of this behavior is highly important.

3.2. Study of Switching Properties of an Identical Filament on a Gold and ITO Counter Electrode

One major issue for progressing with the reliable design of neuromorphic hardware is coping with different filament properties between different devices, that arise even though identical forming conditions were applied. Despite of great effort for achieving highly reproducible manufacturing of memristive devices, for example in a crossbar array architecture, there can be critical differences in the performance between individual devices within the hardware [25,26]. Critical differences affect fundamental parameters of the memristive device, like the SET and RESET voltages, or the forming and retention time of the state. A major source for such device-to-device variability is the necessity of an electroforming step in many memristive devices to initiate the first filament formation from the virgin state. Since precise control of the electroforming step is very challenging, and the morphology of the first evolved filament impacts on the device performance for all subsequent cycles, it is a major origin of the stochasticity between individual devices. Recent studies have shown that the defect state in the dielectric layer plays a crucial role in the switching kinetics [24]. Grain boundaries, for example, act as efficient conduction channels for Ag+-ions, and therefore assist the formation of a metallic filament in the dielectric layer. Differences in the defect state between individual memristive devices lead to different given conditions for the filament formation, and therefore to a different device performance. The variable filament properties in different devices not only complicate reaching the next level of hardware maturity, but also the search for the right analytical method, because it is always an unknown influence when the performance of different

devices is compared. These difficulties have been encountered in several previous studies dedicated to the influence of the counter electrode in memristive devices [29–31].

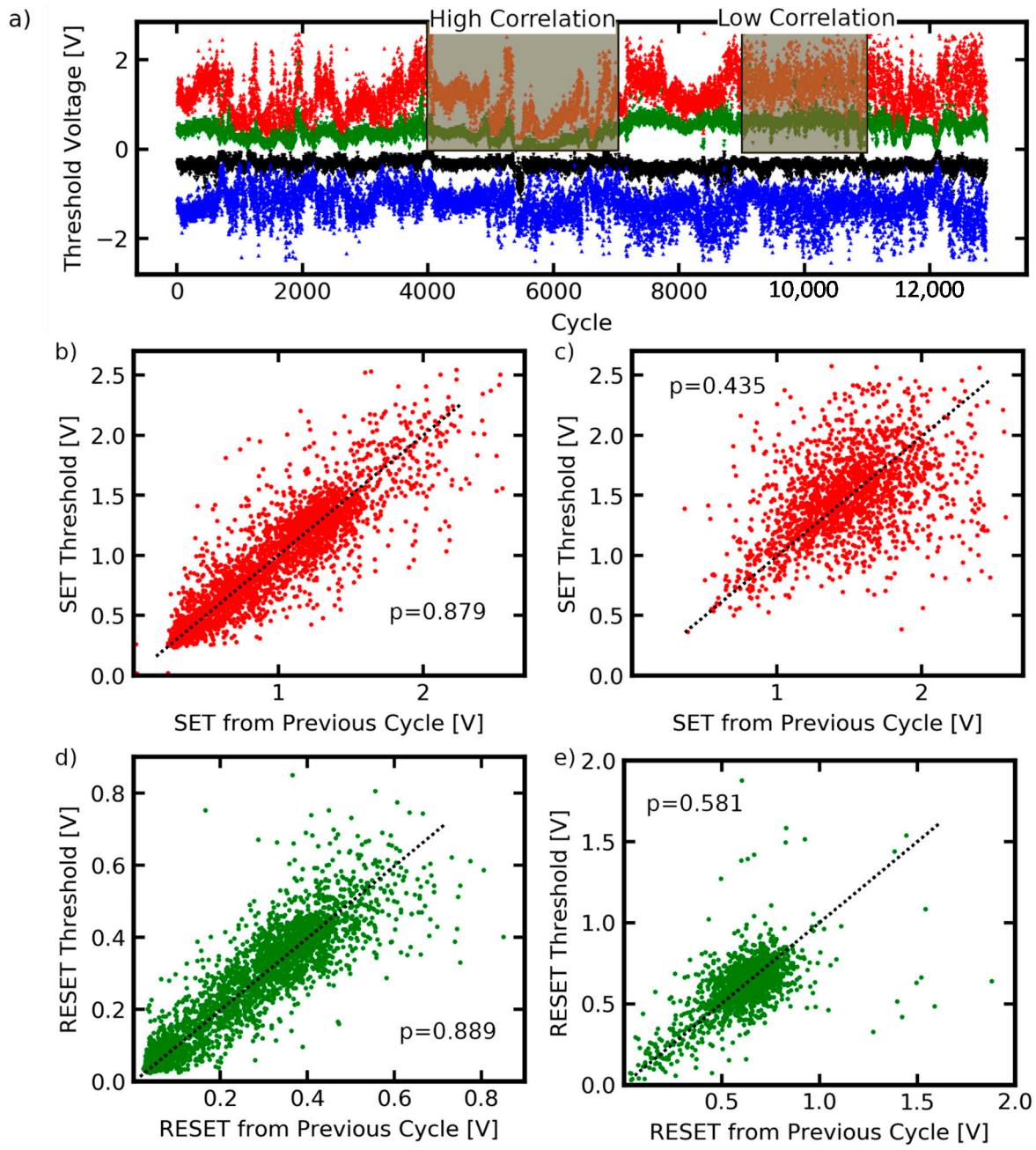

Figure 3. (**a**) All threshold voltages extracted from the long-term measurement ranging over 12,000 cycles of one memtip sample and plotted against the cycle number. In the indicated high correlation regime (cycles 4000 to 7000) the threshold voltages show a significant dependence on the former values from the previous cycles, resulting in pronounced trends in threshold voltage evolution over several cycles. In a later regime (cycles 9000 to 11,000), which suggests a low correlation, the individual threshold voltages are more independent from each other, and no pronounced trends are observable. The Pearson coefficient quantifies the linear correlation between the individual threshold voltages and the respective former value from the cycle before, for the SET and RESET events in the high correlation regime, (**b**,**d**), respectively, and the low correlation regime, (**c**,**e**), respectively.

Using the concept of memtips, IV hysteresis data on the impact of different counter electrodes can be obtained using the identical memtip, bringing it into reproducible electrical contact with different counter electrode materials in consecutive measurements. As an

identical memtip is used, all conditions coming from the active electrode and dielectric layer, like defect structure or electroformed filament, are kept constant. The only varying parameter in this approach is the electrical contact between the memtip and counter electrode, which allows investigating the influence of this parameter with the same active filament. This approach is demonstrated in this section by the operation of an identical memtip on two different technologically relevant counter electrode materials, namely Au and ITO. We note, that such an approach is only meaningful for the purpose of basic research, and will not address the problem of filament variability with respect to practical applications. Furthermore, the application of memtips is only meaningful when data from an identical memtip is considered, as the variability between different memtips is expected to be high.

Figure 4 compares the switching characteristics of an identical memtip under operation on an Au, and an ITO, counter electrode. From this it becomes apparent that the switching characteristics of an identical memtip can be modified through variation of the memtip-to-counter-electrode contact. This can be most prominently described by a variation of the operation window, which is defined by the bias regime, where both HRS and LRS can be occupied. Regarding the highlighted representative cycle for Au in Figure 4, one can see that upon operation of the memtip on an Au counter electrode, the operation window in reference to the positive regime ranges from +0.3 V and +1.9 V. In comparison to this, the operation window on ITO, also in reference to the positive regime, is shifted to higher bias voltages above +2.5 V. A further important point is that the memtip can go into the LRS reliably when operated on Au for voltages between 0 V and +2.5 V, while on ITO only a HRS is observed in the same voltage range.

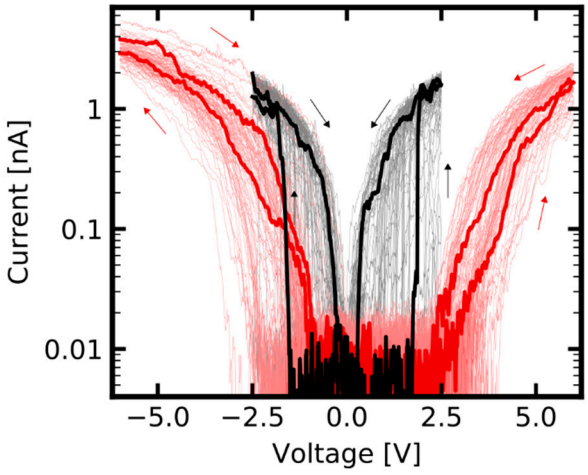

Figure 4. Electrical characteristic of an identical memtip operated over 50 cycles between −2.5 V and +2.5 V on an Au counter electrode (black cycles), and over 50 cycles between −6 V and +6 V on an ITO counter electrode (red cycles). Investigating an identical memtip allows the operation of the very same active filament on different counter electrode materials. For operation on ITO the switching window lies at higher voltages compared to operation on Au.

The good stability of the memtip approach enabled us to record a high number of cycles, with some cycles purely showing a LRS, i.e., no filament disintegration at low voltages. The sequences of such cycles, which purely show a LRS behavior, were evaluated in more detail to gain a deeper insight into the influence of different counter electrodes, and their consequences on device design, because those states reflect the most extensive filament formation and consequently the best contact between filament and counter electrode. The electrical characteristics during the LRS of the memtip on each of the two electrodes are shown in Figure 5. In the case of Au as the counter electrode, a clearly ohmic characteristic evolved when the memtip is in its conducting state, as is expected for memristive samples having an inert metal–dielectric medium–active metal structure. In the ohmic state, the

overall resistance corresponds to the serial resistance in the cAFM instrumentation. Therefore, a deficient filament formation, or energetic barriers with corresponding rectifying properties of the contact between memtip and Au counter electrode, can be excluded as limiting mechanisms. However, upon operation of the identical memtip on an ITO counter electrode the conducting state became substantially different, since the electrical characteristics exhibited rectifying and asymmetric properties. Hence, the current was not limited solely by the 1 GΩ serial resistance anymore, but from an additional barrier arising from a Schottky contact between the memtip and the n-type ITO (cf. Supporting Information Figure S8).

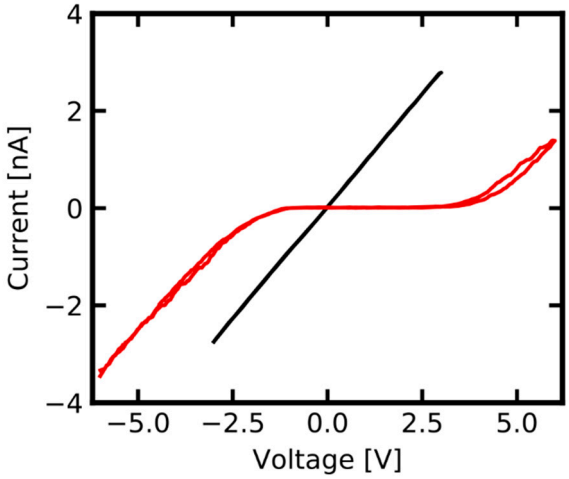

Figure 5. Comparison of the LRS of an identical memtip on an Au (black) and an ITO (red) counter electrode. For this representation, the medians of 10 sequential cycles on each electrode were taken which were consistently in LRS. The LRS on Au is clearly ohmic, and reflects the 1 GΩ serial resistance in the experimental setup. The LRS of the identical memtip on ITO is fundamentally different, and shows a non-linear behavior.

3.3. Highly Dynamic HRS-LRS Transitions at the Border of Filament Stability

This section focusses on features of diffusive memristive switching that emerge when a filamentary device is operated under conditions where persistent transitions between HRS and LRS are impeded. The operation under such conditions is characterized by multiple back and forth switching between HRS and LRS, leading to highly dynamic switching patterns, as shown in Figure 6.

The memtips which were discussed in Sections 2.1 and 2.2 were fabricated with effective thicknesses of 3.5 nm for Ag, and 4 nm for Si_3N_4 and exhibited stable diffusive switching in roughly 95% of the cycles. In particular, it was seen that the SET switching events were persistent, meaning that a following RESET event must be triggered by decreasing the voltage close to zero volts. In contrast, the memtip discussed in this section had an effective thicknesses of 2 nm for Ag, and 6 nm for Si_3N_4, i.e., the reservoir for mobile Ag+-cations is more limited, and the minimum filament length in order to bridge the dielectric layer is enlarged. From the electrical characterization of the memtip with 2 nm Ag and 6 nm Si_3N_4 on an Au counter electrode by IV-sweeps from −2 V to +2 V, we found a drastically lower yield of cycles exhibiting clear diffusive switching, of about 22%. The residual 78% of all cycles showed persistent occupation of the HRS, or only occasional switching events. This indicates that stable filament formation was impeded in this memtip under the given experimental conditions. Among all cycles, a considerable amount of switching events exhibited pronounced highly dynamic HRS–LRS transitions prior to occupation of the LRS. The presented highly dynamic HRS–LRS transitions in Figure 6 were extracted from the SET switching events at negative polarity (i.e., in these extracts the voltage is ramped from zero to −2 V) of four subsequent cycles. One can see that there are various attempts at SET switching, which are, however, directly abandoned.

Furthermore, it can be seen that the frequency of the incomplete SET switching attempts gets higher with increasing absolute voltage. This can be clearly seen, for instance in the first cycle of the sequence, where the first and second switching attempts that occur are more isolated, followed by a burst-like sequence of six switching attempts, before the memtip finally switched into the LRS. To confirm that the observed behavior arises from the Ag filament dynamics, we performed a reference measurement with a memtip prepared without Ag layer, showing no indication of memristive switching (cf. Supporting Information Figure S9). Such a behavior closely resembles the spiking patterns in neural coding schemes [32]. A view of interspike intervals, which is an essential characteristic in neural coding, for the observed dynamic patterns can be found in Figure 7. The evaluation of interspike intervals underlines the observation that the frequency of switching attempts increases with increasing absolute voltage.

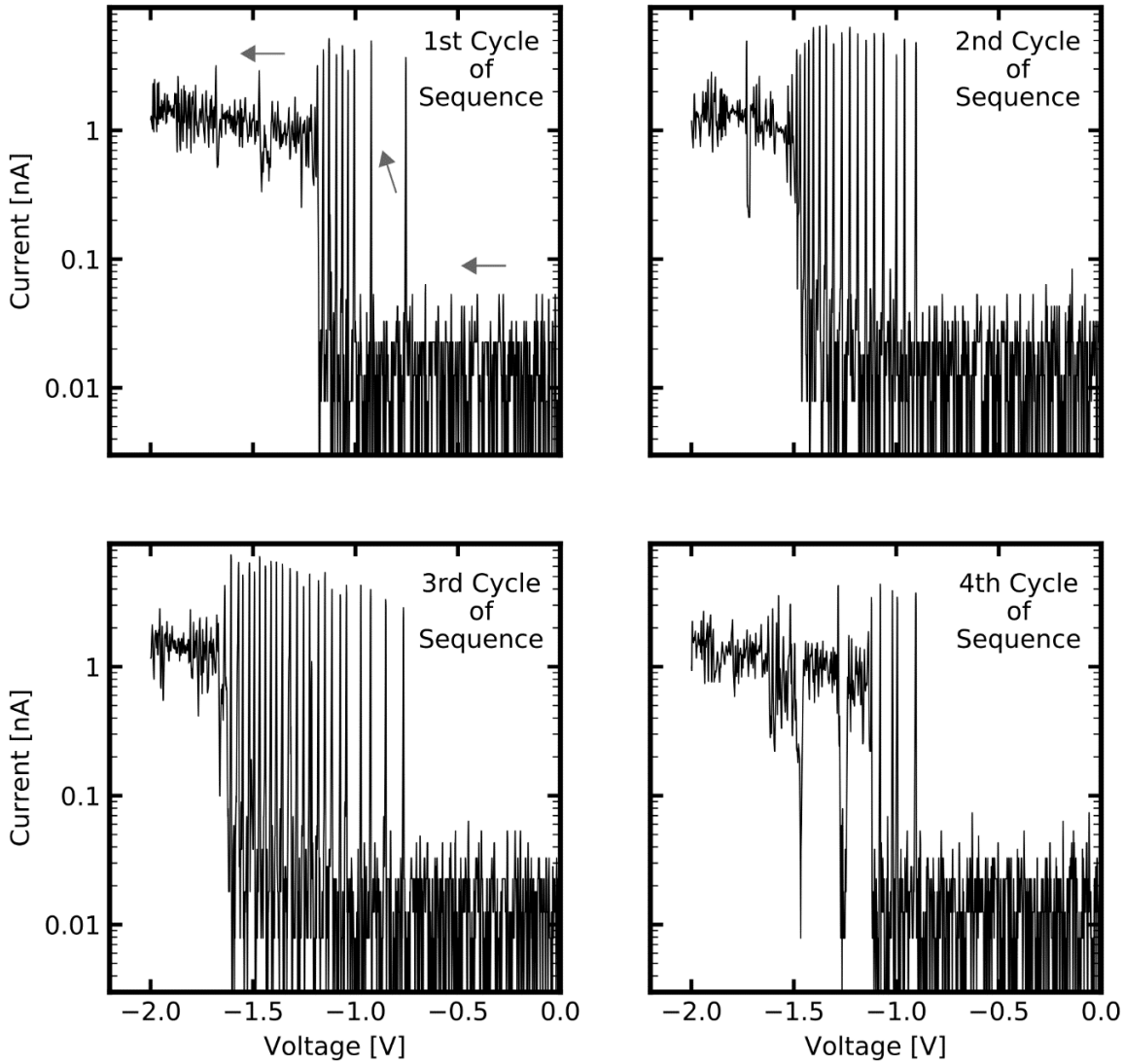

Figure 6. Highly dynamic HRS-LRS transitions, as observed when a memtip is operated at the border of filament stability. Shown are SET events at negative polarity extracted from four subsequent cycles. The arrows in the first panel indicate the direction of voltage sweep in these extracts (i.e., from zero towards 2 V). There is no persistent threshold switching but a dynamic behavior, arising from multiple attempts at filament formation followed by immediate disintegration.

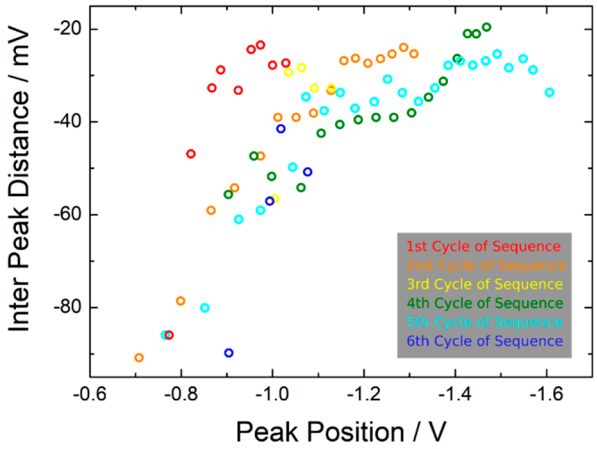

Figure 7. Data of highly dynamic SET switching patterns at negative polarity from six consecutive cycles evaluated with a view on interspike intervals (ISIs). The ISIs from the 3rd to 6th cycle of the given sequence correspond to the highly dynamic SET switching patterns presented in Figure 6. One can see that the ISIs decrease (i.e., the number of switching attempts increases) with increasing stimulation from the external voltage ramp (i.e., peak position).

It can be supposed, that such dynamic patterns occur at the border of filament stability because a distinct occupation of either HRS or LRS is impeded in a narrow voltage interval, as observed. One can argue that filament instability is induced in this memtip by increasing the thickness of Si_3N_4 and more limiting the Ag reservoir (in comparison to the memtips in Sections 2.1 and 2.2), while keeping the magnitude of current flowing through the device during operation constant. This can be understood from the Rayleigh instability, which is widely claimed to be responsible for spontaneous filament disintegration [19,33,34]. Accordingly, spontaneous disintegration is energetically favored in case of a thinner filament diameter, and kinetically accelerated by the number of perturbations at the filament. The main influence on the filament diameter, which is the current limitation, was kept constant throughout this whole work. However, the probability for perturbations, which scale with the length of the filament, leading to acceleration of filament disintegration, is increased because of the longer filament which is required to override a thicker dielectric layer.

In combination with the induced filament instability, the occurrence of highly dynamic HRS–LRS transitions can be understood from the fact that the driving force promoting the filament formation is given by the external potential and immediately drops at the moment of SET switching, because of the formed conductive path connecting both electrodes. Here, the serial resistor implemented in the experimental setup plays a crucial role: As long as the memtip is in its LRS, the majority of external potential drops over the serial resistance. If a critical diameter for filament stability is not reached at that point, the filament immediately disintegrates due to interface energy minimization, and the LRS will not be maintained. This, in turn, is accompanied by an increase of the external potential which triggers the next switching attempt, until a persistent filament has been formed. Those described counteracting driving forces play a fundamental role in many filamentary diffusive memristive switching devices. Based on the assumption that the interplay of those counteracting driving forces is essentially responsible for the observed spiking behavior, one can argue that such spiking dynamics can be expected in most filamentary diffusive switching devices.

Regarding applications, the design and investigation of devices which are able to transfer electrical signal inputs into a spiking pattern is of great interest in the field of neuromorphic engineering. From this, memristive systems with short-term memory behavior can be derived, which could play an important role in the hardware-based processing of sensory data [35–37]. The utilization of memtips turned out to be advantageous for observations at the border of filament stability and related spiking behavior, because con-

straining the action of the filament to the apex through direct integration of the memristive device provides the most reliable contact between probe and filament.

4. Conclusions and Outlook

In this work, an unconventional cAFM approach [27] was adapted, which provided us enhanced capabilities for the electrical characterization of ECM memristive devices on the nanoscale. This approach intended to integrate the memristive device of interest directly on the apex of a conductive cantilever instead of conventional probing. By contact establishment between the functionalized cantilever to any kind of counter electrode material, electrical characterization is done via regular cAFM instrumentation. Considerable advantages emerge from such an approach, such as mitigation of thermal drift effects during long-term measurements, because the active area for switching is constrained to the apex of the cantilever. Furthermore, it enables measurement strategies for testing the same active filament on different counter electrodes. Along with the demonstration of this approach for ECM devices, fundamental insights into the diffusive switching performance of an Ag/Si_3N_4 stack, which is an archetypical filamentary memristive device, were gained. The stability of the memtip approach facilitated a long-term measurement over 12,000 consecutive cycles. From this, regimes with different degrees of temporal correlation between subsequent switching events were identified during the long-term operation. Moreover, an energetic barrier between the Ag filament and an ITO counter electrode was identified, by comparing the IV characteristics of an identical memtip in electrical contact to an Au and an ITO counter electrode, respectively. Finally, highly dynamic HRS–LRS transitions were observed, which presumably occur at the border of filament stability. This work shows, that investigations on ECM devices using memtips are a reliable and powerful tool for gaining insights into the performance of memristive devices, and provide experimental possibilities that go beyond conventional cAFM. This approach can be easily extended towards various materials systems and contact scenarios, and offers the potential to gain a deeper understanding of memristive switching on the nanoscale.

Supplementary Materials: The following are available online at https://www.mdpi.com/2079-4991/11/2/265/s1, Figure S1: Thickness estimation of the Si_3N_4 matrix from the TEM micrograph. Figure S2: Topographic AFM images acquired with a memtip. Figure S3: TEM micrographs before and after prolonged TEM investigation on memtips. Figure S4: Histogram plot representation of threshold voltages extracted from the long-term measurement. Figure S5: Cumulative distribution function of threshold voltages extracted from the long-term measurement. Figure S6: Correlation between SET and RESET events. Figure S7: Pearson coefficient versus separation of the correlated cycles. Figure S8: Band diagram discussing the energetic barrier between Ag and ITO. Figure S9: Reference measurement from a memristive cantilever sample reproduced without active Ag layer.

Author Contributions: Conceptualization, A.H., F.F., T.S., A.V. and N.C.; validation, A.H., F.F., T.S., A.V. and N.C.; formal analysis, N.C. and A.V.; investigation, A.H., O.G. and N.C.; data curation, A.H. and N.C.; writing—original draft preparation, N.C. and A.V.; writing—review and editing, O.G., A.H., T.S., L.K. and F.F.; visualization, N.C.; supervision, L.K., T.S. and F.F.; project administration, A.H., L.K. and F.F.; funding acquisition, A.H., L.K. and F.F.; All authors have read and agreed to the published version of the manuscript.

Funding: This work was financially supported by the German Research Foundation (DFG) via the coordinated effort FOR2093 "Memristive Components for Neuromorphic Circuits" through project A2 and B2. A.H would like to acknowledge the financial support by the Slovenian Research Agency (ARRS) under Program No. P1-0099 and support for his research stays in Kiel by FOR2093.

Data Availability Statement: The data presented in this study are available on request from the corresponding author.

Acknowledgments: We acknowledge the CENN Nanocenter for the use of AFM. The authors would like to thank Stefan Rehders for assistance in designing and operating the PVD setup.

Conflicts of Interest: The authors declare no conflict of interest.

References

1. Strukov, D.B.; Snider, G.S.; Stewart, D.R.; Williams, R.S. The missing memristor found. *Nature* **2008**, *453*, 80–83. [CrossRef] [PubMed]
2. Chua, L. Memristor-The missing circuit element. *IEEE Trans. Circuit Theory* **1971**, *18*, 507–519. [CrossRef]
3. Vongehr, S.; Meng, X. The missing memristor has not been found. *Sci. Rep.* **2015**, *5*, 11657. [CrossRef] [PubMed]
4. Zhu, X.; Lee, S.H.; Lu, W.D. Nanoionic Resistive-Switching Devices. *Adv. Electron. Mater.* **2019**, *5*, 1900184. [CrossRef]
5. Zhang, Y.; Wang, Z.; Zhu, J.; Yang, Y.; Rao, M.; Song, W.; Zhuo, Y.; Zhang, X.; Cui, M.; Shen, L.; et al. Brain-inspired computing with memristors: Challenges in devices, circuits, and systems. *Appl. Phys. Rev.* **2020**, *7*. [CrossRef]
6. Li, Y.; Wang, Z.; Midya, R.; Xia, Q.; Joshua Yang, J. Review of memristor devices in neuromorphic computing: Materials sciences and device challenges. *J. Phys. D Appl. Phys.* **2018**, *51*. [CrossRef]
7. Ielmini, D. Resistive switching memories based on metal oxides: Mechanisms, reliability and scaling. *Semicond. Sci. Technol.* **2016**, *31*. [CrossRef]
8. Vahl, A.; Carstensen, J.; Kaps, S.; Lupan, O.; Strunskus, T.; Adelung, R.; Faupel, F. Concept and modelling of memsensors as two terminal devices with enhanced capabilities in neuromorphic engineering. *Sci. Rep.* **2019**, *9*, 4361. [CrossRef]
9. Zhou, L.; Zhang, S.R.; Yang, J.Q.; Mao, J.Y.; Ren, Y.; Shan, H.; Xu, Z.; Zhou, Y.; Han, S.T. A UV damage-sensing nociceptive device for bionic applications. *Nanoscale* **2020**, *12*, 1484–1494. [CrossRef]
10. Kendall, J.D.; Kumar, S. The building blocks of a brain-inspired computer. *Appl. Phys. Rev.* **2020**, *7*. [CrossRef]
11. Wang, H.; Yan, X. Overview of Resistive Random Access Memory (RRAM): Materials, Filament Mechanisms, Performance Optimization, and Prospects. *Phys. Status Solidi Rapid Res. Lett.* **2019**, *13*, 1900073. [CrossRef]
12. Edwards, A.H.; Barnaby, H.J.; Campbell, K.A.; Kozicki, M.N.; Liu, W.; Marinella, M.J. Reconfigurable memristive device technologies. *Proc. IEEE* **2015**, *103*, 1004–1033. [CrossRef]
13. Waser, R.; Dittmann, R.; Staikov, C.; Szot, K. Redox-based resistive switching memories nanoionic mechanisms, prospects, and challenges. *Adv. Mater.* **2009**, *21*, 2632–2663. [CrossRef]
14. Linn, E.; Rosezin, R.; Kügeler, C.; Waser, R. Complementary resistive switches for passive nanocrossbar memories. *Nat. Mater.* **2010**, *9*, 403–406. [CrossRef] [PubMed]
15. Wang, Z.; Joshi, S.; Savel'ev, S.E.; Jiang, H.; Midya, R.; Lin, P.; Hu, M.; Ge, N.; Strachan, J.P.; Li, Z.; et al. Memristors with diffusive dynamics as synaptic emulators for neuromorphic computing. *Nat. Mater.* **2017**, *16*, 101–108. [CrossRef] [PubMed]
16. Jiang, H.; Belkin, D.; Savel'Ev, S.E.; Lin, S.; Wang, Z.; Li, Y.; Joshi, S.; Midya, R.; Li, C.; Rao, M.; et al. A novel true random number generator based on a stochastic diffusive memristor. *Nat. Commun.* **2017**, *8*. [CrossRef] [PubMed]
17. Midya, R.; Wang, Z.; Zhang, J.; Savel'ev, S.E.; Li, C.; Rao, M.; Jang, M.H.; Joshi, S.; Jiang, H.; Lin, P.; et al. Anatomy of Ag/Hafnia-Based Selectors with 1010 Nonlinearity. *Adv. Mater.* **2017**, *29*, 1660457. [CrossRef]
18. Vahl, A.; Carstens, N.; Strunskus, T.; Faupel, F.; Hassanien, A. Diffusive Memristive Switching on the Nanoscale, from Individual Nanoparticles towards Scalable Nanocomposite Devices. *Sci. Rep.* **2019**, *9*, 17367. [CrossRef]
19. Wang, W.; Wang, M.; Ambrosi, E.; Bricalli, A.; Laudato, M.; Sun, Z.; Chen, X.; Ielmini, D. Surface diffusion-limited lifetime of silver and copper nanofilaments in resistive switching devices. *Nat. Commun.* **2019**, *10*, 81. [CrossRef]
20. Znidarsic, A.; Kaskela, A.; Laiho, P.; Gaberscek, M.; Ohno, Y.; Nasibulin, A.G.; Kauppinen, E.I.; Hassanien, A. Spatially resolved transport properties of pristine and doped single-walled carbon nanotube networks. *J. Phys. Chem. C* **2013**, *117*, 13324–13330. [CrossRef]
21. Hassan, M.H.; Alkordi, M.H.; Hassanien, A. Probing the conductivity of metal-organic framework-graphene nanocomposite. *Mater. Lett.* **2019**, *246*, 13–16. [CrossRef]
22. Sun, W.; Gao, B.; Chi, M.; Xia, Q.; Yang, J.J.; Qian, H.; Wu, H. Understanding memristive switching via in situ characterization and device modeling. *Nat. Commun.* **2019**, *10*, 3453. [CrossRef] [PubMed]
23. Yang, Y.; Huang, R. Probing memristive switching in nanoionic devices. *Nat. Electron.* **2018**, *1*, 274–287. [CrossRef]
24. Lübben, M.; Cüppers, F.; Mohr, J.; von Witzleben, M.; Breuer, U.; Waser, R.; Neumann, C.; Valov, I. Design of materials properties and device performance in memristive systems. *Sci. Adv.* **2020**, *6*. [CrossRef] [PubMed]
25. Grossi, A.; Walczyk, D.; Zambelli, C.; Miranda, E.; Olivo, P.; Stikanov, V.; Feriani, A.; Sune, J.; Schoof, G.; Kraemer, R.; et al. Impact of Intercell and Intracell Variability on Forming and Switching Parameters in RRAM Arrays. *IEEE Trans. Electron Devices* **2015**, *62*, 2502–2509. [CrossRef]
26. Grossi, A.; Perez, E.; Zambelli, C.; Olivo, P.; Miranda, E.; Roelofs, R.; Woodruff, J.; Raisanen, P.; Li, W.; Givens, M.; et al. Impact of the precursor chemistry and process conditions on the cell-to-cell variability in 1T-1R based HfO2 RRAM devices. *Sci. Rep.* **2018**, *8*, 11160. [CrossRef]
27. Moon, H.; Zade, V.; Kang, H.S.; Han, J.W.; Lee, E.; Hwang, C.S.; Lee, M.H. Interfacial chemical bonding-mediated ionic resistive switching. *Sci. Rep.* **2017**, *7*, 1264. [CrossRef] [PubMed]
28. Lanza, M.; Wong, H.S.P.; Pop, E.; Ielmini, D.; Strukov, D.; Regan, B.C.; Larcher, L.; Villena, M.A.; Yang, J.J.; Goux, L.; et al. Recommended Methods to Study Resistive Switching Devices. *Adv. Electron. Mater.* **2019**, *5*, 1800143. [CrossRef]
29. Lübben, M.; Menzel, S.; Park, S.G.; Waser, R.; Valov, I. SET kinetics of electrochemical metallization cells: Influence of counter-electrodes in SiO2/Ag based systems. *Nanotechnology* **2017**, *28*, 135205. [CrossRef]
30. Ke, J.J.; Wei, T.C.; Tsai, D.S.; Lin, C.H.; He, J.H. Surface effects of electrode-dependent switching behavior of resistive random-access memory. *Appl. Phys. Lett.* **2016**, *109*. [CrossRef]

31. Kim, W.; Menzel, S.; Wouters, D.J.; Guo, Y.; Robertson, J.; Roesgen, B.; Waser, R.; Rana, V. Impact of oxygen exchange reaction at the ohmic interface in Ta2O5-based ReRAM devices. *Nanoscale* **2016**, *8*, 17774–17781. [CrossRef] [PubMed]
32. Suh, D.I.; Bae, G.Y.; Oh, H.S.; Park, W. Neural coding using telegraphic switching of magnetic tunnel junction. *J. Appl. Phys.* **2015**, *117*, 17D714. [CrossRef]
33. Dananjaya, P.A.; Loy, D.J.J.; Chow, S.C.W.; Lew, W.S. Unidirectional Threshold Switching Induced by Cu Migration with High Selectivity and Ultralow OFF Current under Gradual Electroforming Treatment. *ACS Appl. Electron. Mater.* **2019**, *1*, 2076–2085. [CrossRef]
34. Hsiung, C.P.; Liao, H.W.; Gan, J.Y.; Wu, T.B.; Hwang, J.C.; Chen, F.; Tsai, M.J. Formation and instability of silver nanofilament in Ag-based programmable metallization cells. *ACS Nano* **2010**, *4*, 5414–5420. [CrossRef]
35. Stieg, A.Z.; Avizienis, A.V.; Sillin, H.O.; Martin-Olmos, C.; Aono, M.; Gimzewski, J.K. Emergent criticality in complex turing B-type atomic switch networks. *Adv. Mater.* **2012**, *24*, 286–293. [CrossRef]
36. Ohno, T.; Hasegawa, T.; Tsuruoka, T.; Terabe, K.; Gimzewski, J.K.; Aono, M. Short-term plasticity and long-term potentiation mimicked in single inorganic synapses. *Nat. Mater.* **2011**, *10*, 591–595. [CrossRef]
37. Ohno, T.; Hasegawa, T.; Nayak, A.; Tsuruoka, T.; Gimzewski, J.K.; Aono, M. Sensory and short-term memory formations observed in a Ag2S gap-type atomic switch. *Appl. Phys. Lett.* **2011**, *99*. [CrossRef]

Supporting Information

Enhancing Reliability of Studies on Single Filament Memristive Switching via an Unconventional cAFM Approach

Niko Carstens, Alexander Vahl, Ole Gronenberg, Thomas Strunskus, Lorenz Kienle, Franz Faupel *, and Abdou Hassanien *

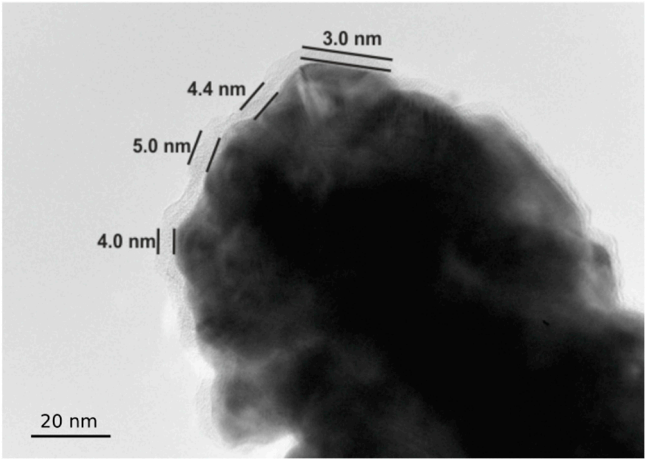

Figure S1. Thickness estimation of the Si_3N_4 matrix from the TEM micrograph.

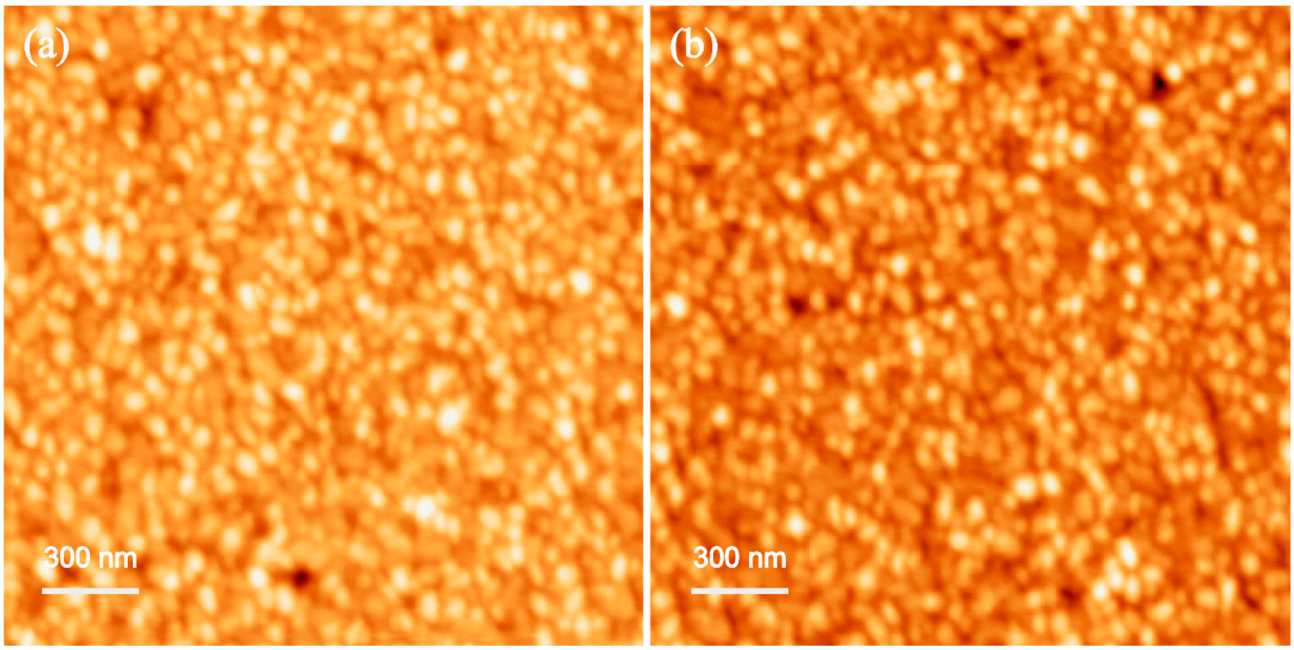

Figure S2. Topographic AFM images in tapping mode showing the structure of Au electrode imaged by memristive cantilever sample before (a) and after (b) prolonged IV measurements with a maximum current set to a few nA. Small

features of less than 20 nm can be easily identified in both images which indicate that the tip apex remained intact during measurements.

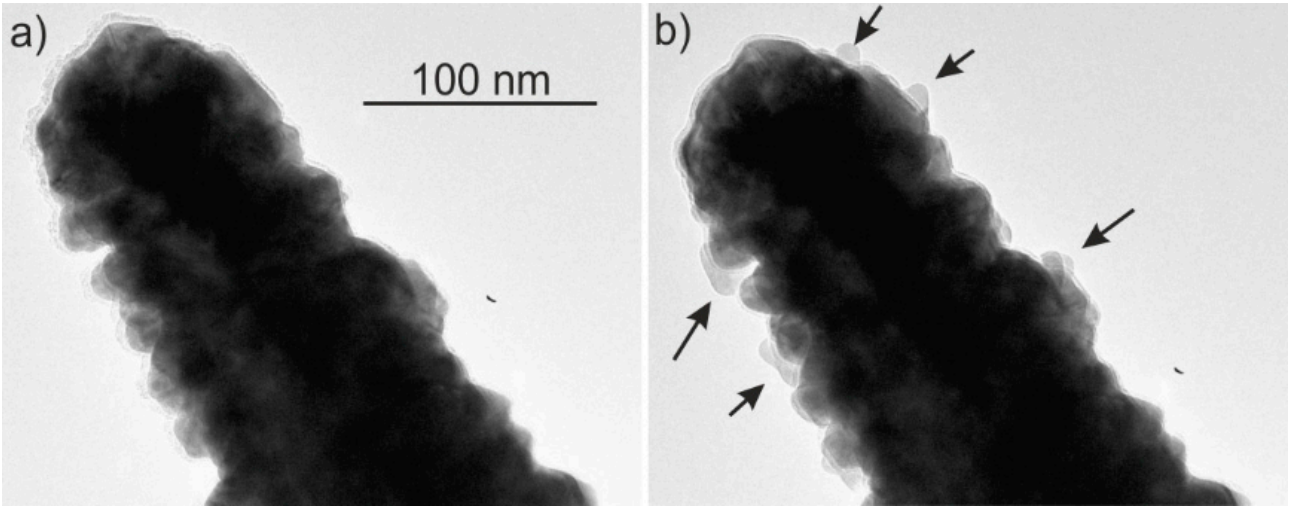

Figure S3. TEM micrographs before (a) and after (b) prolonged TEM investigation. Electron beam irradiation during TEM investigation of memristive cantilever samples causing morphological changes. After prolonged investigation Ag protrusions (marked by the arrows) are forming. Further, the dielectric matrix changes its morphology from rough to thinner and smooth. The insulating behavior is most likely due to the migration of the Ag from the apex to the protrusions so that not sufficient active Ag remains at the apex.

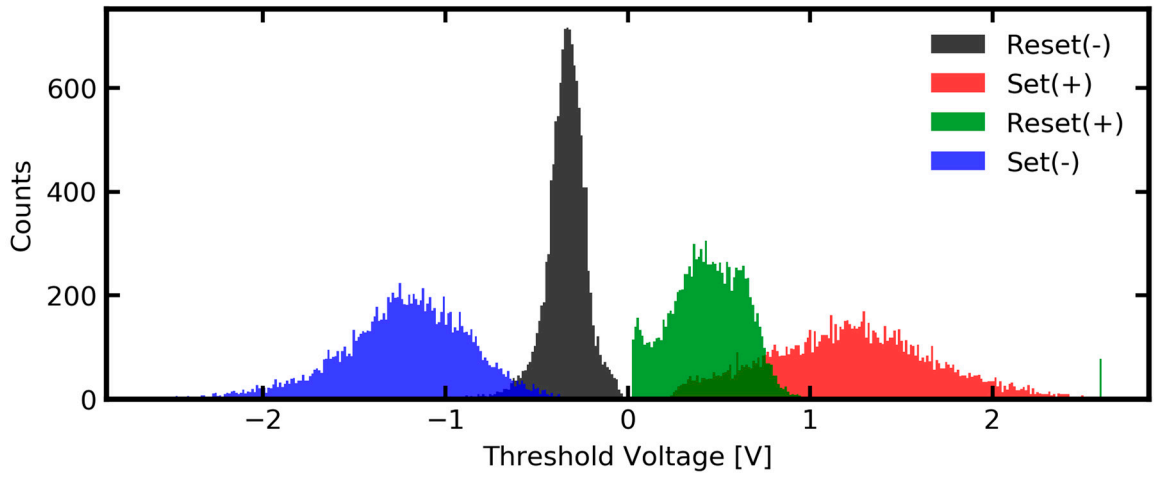

Figure S4. Histogram plot representation of threshold voltages extracted from the long-term measurement (cf. figure 3a in main text). The variances of the distributions can be calculated as 0.0132 for Reset(-), 0.2072 for SET(+), 0.0435 for RESET(+) and 0.1245 for SET(-).

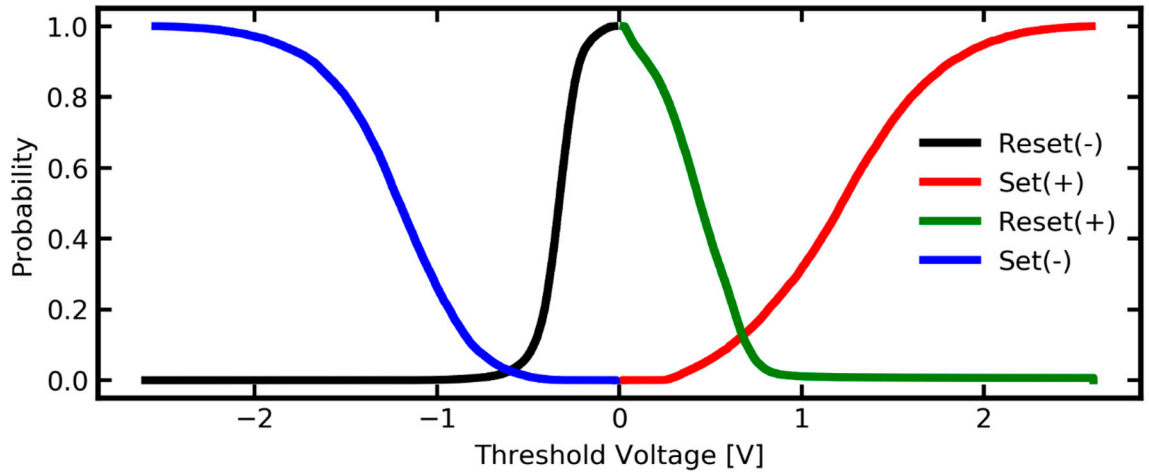

Figure S5. Cumulative distribution function of threshold voltages extracted from the long-term measurement (cf. figure 3a in main text).

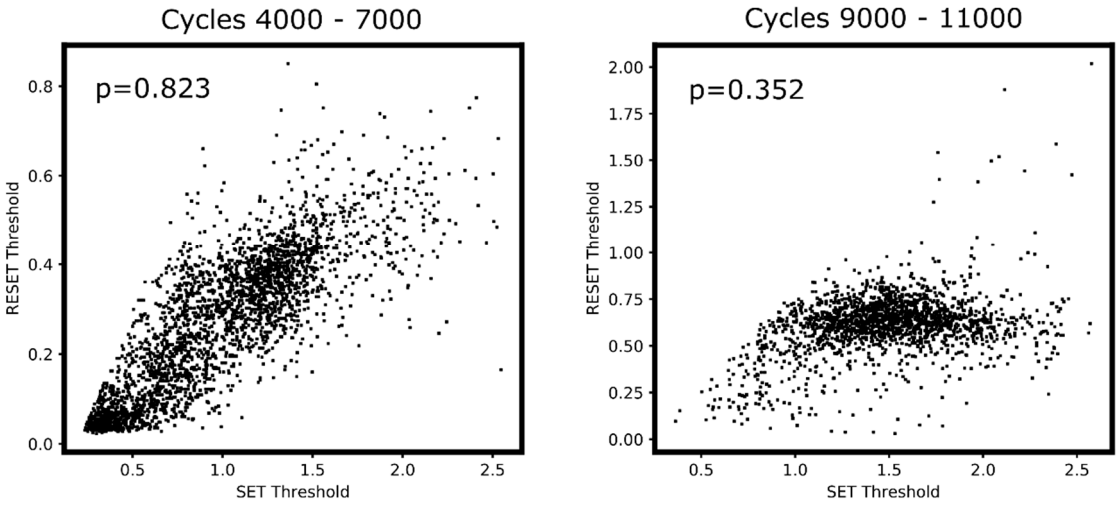

Figure S6. Correlation of SET and following RESET voltages for the period between cycles 4000 to 7000 and 9000 to 11000. It can be seen that the switching in the first period is clearly correlated, whereas it is more random in the second period.

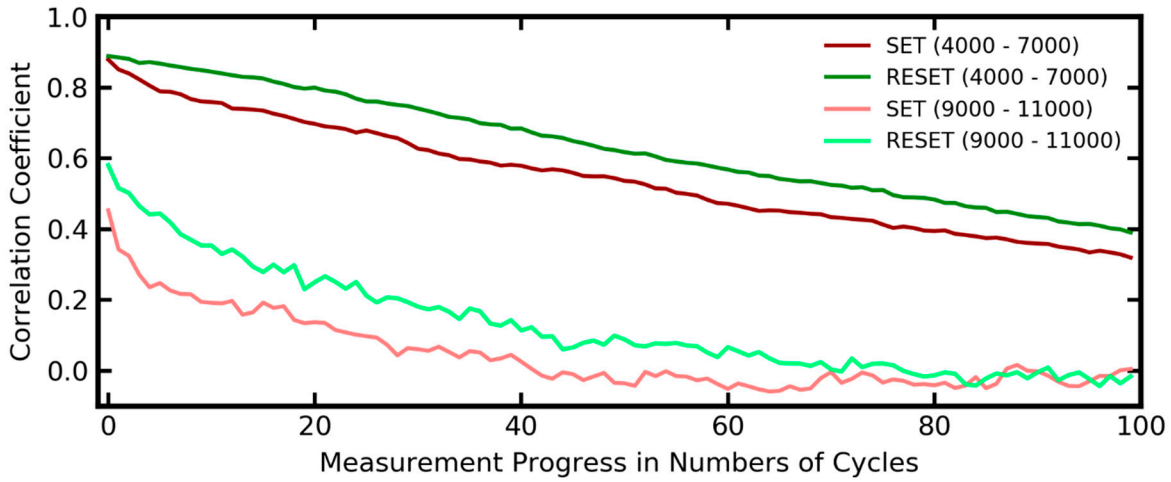

Figure S7. Pearson coefficient versus separation of the correlated cycles (separation is given in number of cycles which are conducted between the cycles). The more cycles were conducted in between the lower the correlation becomes. SET and RESET events in the region from cycle 4000 to 7000 show also consistently a stronger a correlation than in the region from cycle 9000 to 11000 when the correlated cycles are zero to 100 conducted cycles apart from each other.

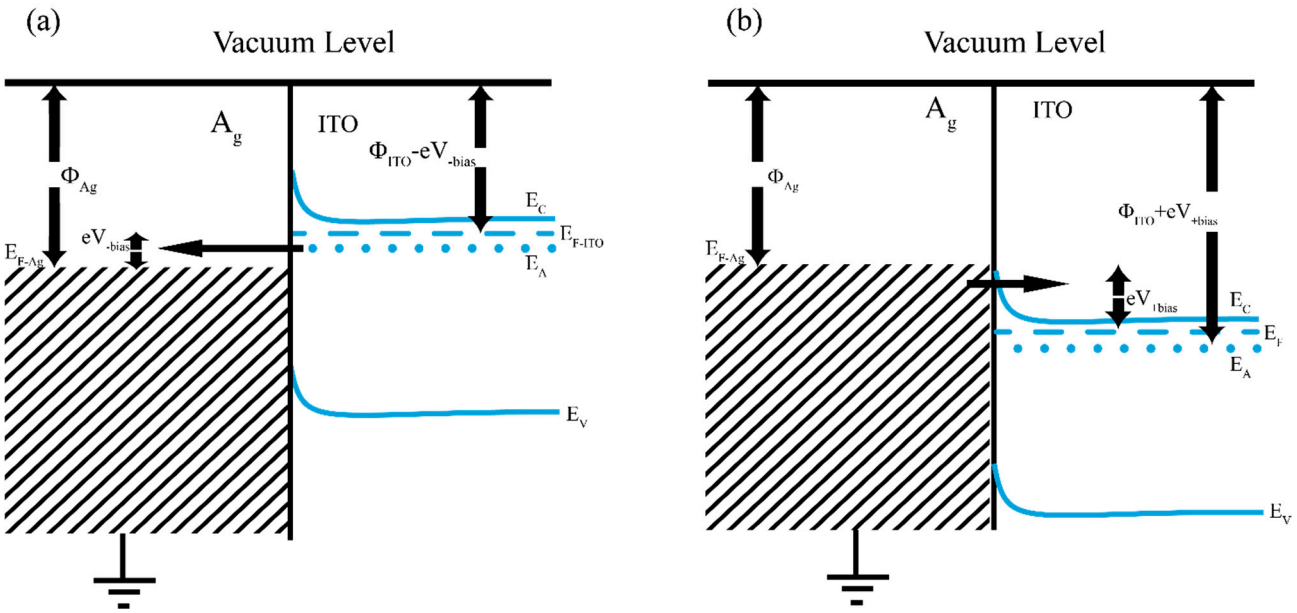

Figure S8. Schematic illustration of energy band diagram of Ag filament and ITO substrate. The rectifying behavior arises from Schottky contact where electrons flow easier when ITO is negatively biased as in (a) than positively biased as in (b).

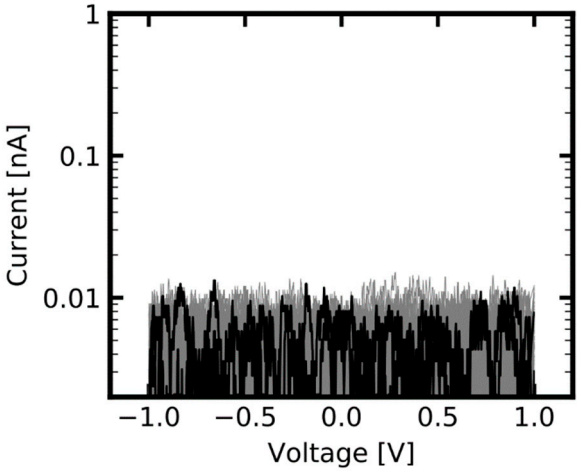

Figure S9. Reference measurement (40 cycles) from a memristive cantilever sample reproduced without active Ag layer. There are no indications on switching events, which approves that the memristive action originates from the Ag layer.

5. Imitation of Neuronal-like Irregular Spiking Dynamics in Intermediate-scale Assemblies of Memristive Nanoparticles

The unconventional cAFM approach as developed in Chapter 4 was applied to investigate the memristive switching dynamics of AgPt-NPs encapsulated in SiO_xN_y. The data acquisition from the functionalized cantilevers was conducted by Abdou Hassanien at the Jozef Stefan Institute in Ljubljana. Here, the operation of the memristive system through voltage sweeps was driven into a highly volatile switching regime. In this operational regime, physical forces acting on the memristive system that promote the formation (i.e. ECM) and causing the spontaneous decay of filamentary structures (i.e. minimization of system energy) are assumed to be approximately balanced. In this case, the memristive system responds via an irregular spiking pattern to the stimulation by a more regular input. Similarities of this memristive switching regime with biological information encoding schemes on the neuronal level are discussed in the context of inhibitory and excitatory synaptic contributions.

This chapter is a reprint of a manuscript submitted for publication:

N. Carstens, T. Strunskus, F. Faupel, A. Hassanien and A. Vahl, *Submitted*, 2022

Neuronal-like Irregular Spiking Dynamics in Highly Volatile Memristive Intermediate-scale AgPt-Nanoparticle Assemblies

*Niko Carstens[1], Thomas Strunskus[1], Franz Faupel[1], Abdou Hassanien[2] and Alexander Vahl[1]**

[1]Institute for Materials Science, Chair for Multicomponent Materials, Faculty of Engineering, Christian-Albrechts-University of Kiel, Kaiserstraße 2, D-24143 Kiel, Germany

[2]Department of Condensed Matter Physics, J. Stefan Institute, Jamova 39, 1000 Ljubljana, Slovenia

Keywords: neuromorphic computing, spiking memristor, diffusive memristor, cafm, nanoparticle

Abstract:

The field of neuromorphic computing seeks for functional materials and electronic systems, that are capable of emulating brain-like dynamics to solve computational problems with time and energy efficiency outclassing current transistor-based hardware architectures. Major efforts are focused on the integration of memristive devices into highly regular circuits (i.e. crossbar arrays), to build physical implementations of artificial neural networks, where the information representation in individual memristive devices is closely oriented towards the behavior of artificial neurons. However, artificial neurons are rather rigid mathematical concepts than realistic projections of complex neuronal dynamics. Experiments from neuroscience suggest that highly efficient information representation on the level of individual neurons relies on dynamical features such as excitatory and inhibitory contributions, irregularity of firing patterns or correlations in the time domain. In this work, we apply a cAFM approach to probe the memristive dynamics of nanoscale assemblies of AgPt-nanoparticles at the stability border of the conducting state, where physical forces causing the formation and decay of filamentary structures appear to be balanced. This unveils a dynamical regime, where the memristive response upon a regular voltage input is governed by irregular firing patterns. We motivate the significance of such a dynamical regime by close similarities to excitation and inhibition governed behavior in biological neuronal systems, which is crucial to tune biological neuronal systems into a state most suitable for information representation and computation.

1. Introduction

Technical implementation of computational principles from complex neuronal assemblies such as mammalian brains is currently in the focus of the search for unconventional hardware approaches, which aims to overcome fundamental limitations set by modern transistor-based hardware technology, such as limited miniaturization capabilities or the *von-Neumann bottleneck* [1]. Closely connected to this is the development of memristive devices, which embodies two-terminal resistive switching elements with non-linear

dynamical behavior [2]. The major significance of memristive devices is their ability to implement synaptic-like functionalities in technical circuits through their reconfigurable conductance [3–6]. Current approaches for the implementation of brain-inspired computation paradigms are mostly focused on highly regular crossbar arrays of memristive devices [7,8]. Despite of substantial advances in this technology, which was mainly driven by opportunities to perform artificial neural network algorithms directly from the underlying physics of memristor crossbar arrays[9–11], it is still away from reaching a level of brain-like complexity with emergent dynamical features as found in biological neuronal systems [12]. One reason for this is that design principles for memristive devices are commonly oriented towards rather rigid mathematical constructs, effectively modelling isolated aspects of synaptic or neuronal behavior omitting the full complexity of a realistic biological neuron. In contrast to that, computational capabilities of biological neuronal systems arise from complex networks incorporating rich adaptability mechanisms on the local level (i.e. on the level of individual synapses and neurons), which allows the whole network to self-organize into a regime which is functional for information representation and processing [13]. Some functional principles found on the local level of biological neuronal systems are, among others, balancing of excitatory and inhibitory synaptic contributions to signal processing [14–16] or modulation of synaptic signal transmission efficiency [17] on short- and long-term scales. In particular, for an efficient representation of information, which is present in biological systems in the form of irregular spike trains, the interplay between excitatory and inhibitory contributions has major importance [18,19]. The combination of local neuronal and synaptic behavior along with the complex network connectivity are leading to emergent dynamics, which are considered as crucial for the computational capabilities of the brain [12,13]. Taking these aspects as an inspiration, there are recent approaches to build neuromorphic systems which focus more on experimental findings from neuroscience and less on artificial neural network algorithms. For example, long-range temporal correlations and scale-free avalanches (both are well-described dynamics governing the spontaneous activity of biological neuronal systems [12,20,21]) were implemented in randomly assembled networks of metallic nanowires [22] or nanoparticles [23–25]. This allows for the creation of neuromorphic systems approaching brain-like complexity in the dynamics, which are beneficial for the mapping of spatio-temporal information and therefore believed to be suitable for computational schemes like reservoir computing [26,27]. Furthermore, diffusive memristive switching attracted interest for the implementation of enhanced synaptic functionalities in neuromorphic systems [28–30]. The characteristic feature of a diffusive memristor is the volatility of the conducting state, which originates from permanently acting relaxation forces driven by interfacial energy minimization, causing spontaneous decay of conductive filaments [31]. Diffusive memristors in a conventional sense implement a highly non-linear threshold behavior, characterized by a certain threshold voltage V_T. When a voltage $V > V_T$ is applied, a diffusive memristor occupies its conducting state, otherwise it relaxes back to its insulating state [32]. Based on the inherent volatility, functionalities like short-term plasticity [30]

and regular spike-pattern generators [33] can be deduced, which are both important contributions to create neuromorphic system inspired by the real behavior of biological neuronal systems.

Pathways for the imitation of the realistic complex behavior of individual biological neurons towards emulation of excitatory and inhibitory contributions were not pursued so far. However, this would open up new approaches for the design of neuromorphic systems with close orientation towards biological neuronal systems. One major reason why biological neuronal systems adapts excitatory and inhibitory contributions is to maximize the dynamical range [18,34,35], a parameter which is crucial for computational capabilities [13,36]. To explore pathways, that allow to emulate principles of biological excitatory and inhibitory contributions, we investigated the dynamics of a memristive system built by an intermediate-scale AgPt-nanoparticles (NPs) assembly. Moreover, the memristive dynamics of the intermediate-scale AgPt-NPs assembly was studied, when the system was constrained to a highly volatile switching regime. We expected that in highly volatile switching regimes (i.e. during operation at the border of filament stability), physical forces causing the formation and spontaneous decay of filamentary structures become equally dominant, and can be treated as excitatory or inhibitory-like, respectively, to the memristive system. The studies in this work were realized by an unconventional cAFM approach, where a test system was created by integration of the intermediate-scale AgPt-NP assembly directly at the apex region of a conductive cantilever. This functionalized cantilever was used to probe the current response upon application of a voltage stimulus over prolonged times via a common cAFM setup. The main advantage of using this unconventional cAFM approach is an efficient localization of the memristive action of the intermediate-scale AgPt-NPs assembly to the cantilever apex, even over longer measurement durations. This approach already proved well for probing the dynamics on longer time scales of an individual Ag-filament evolved from a thin film electrode (full details of this previous study can be found elsewhere [37]). In this work, a highly dynamical switching regime (in the nA-range) for the intermediate-scale AgPt-NPs assembly was characterized, which is strongly governed by repeated decays of the conducting state, leading to the emergence of irregular spiking patterns, resembling the firing activity of neurons in biological systems. We believe that the findings in this study unveil novel perspectives for the design of neuromorphic systems.

2. Design of Memristive Test System and Operation Conditions

AgPt-NPs were chosen in this work for the formation of the memristive system. Such bimetallic NPs were already reported to be feasible for the stable implementation of diffusive memristive switching on the nanoscale [32]. For the studies in this work, we made use of an unconventional cAFM approach, which already proved beneficial for the investigation of diffusive memristive dynamics of nanoscale Ag-filaments [37]. This approach implies a persistent integration of the memristive system directly at the cantilever apex, instead of conventional cAFM probing. Following this approach, the test system for this work is a cantilever

functionalized with a memristive system of AgPt-NPs encapsulated in an insulating matrix consisting of SiO_xN_y. This test system was fabricated by taking a commercially available Pt-covered cantilever (Bruker CONTV-PT) and successive coating starting with 5 nm SiOxNy, followed by AgPt-NPs and finally a 5 nm SiOxNy covering. A schematic depiction of the test system, as well as a SEM image, are given in Figures 1a and b, respectively.

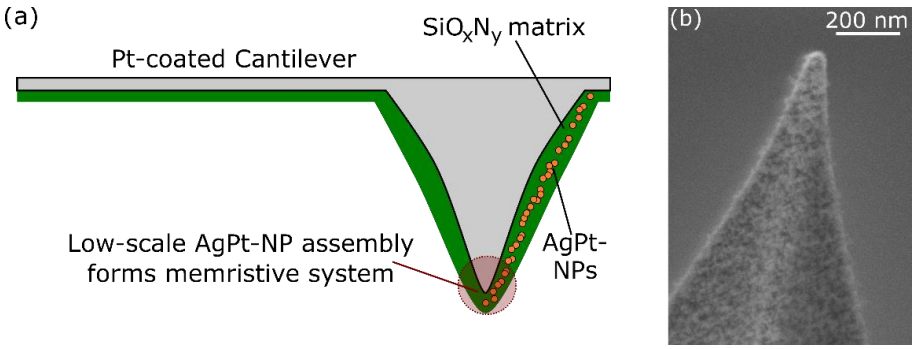

Figure 1. Illustration of the test system. The memristive dynamics of a nanoscale assembly of AgPt-NPs are probed via an unconventional cAFM approach, as given in (a), where the memristive system consisting of AgPt-NPs encapsulated in an insulating SiOxNy matrix is persistently integrated at the cantilever tip. By this, the memristive action of AgPt-NPs is efficiently constrained to the electrical field enhanced apex area with the intention to avoid experimental uncertainties induced by thermal drift and lacking localizability of memristive action. A SEM micrograph of the cantilever decorated with AgPt-NPs is shown in (b).

Resulting from the cantilever functionalization, the studied memristive system can be understood as an intermediate-scale assembly of AgPt-NPs. Reservoirs of mobile species from which filamentary structures are formed (i.e. Ag) are distributed over the location of NPs. Furthermore, each gap between adjacent NPs could contribute to the memristive response of the system. The according scale of the memristive system is defined by the geometry of the apex region, i.e. it is determined by the active area during cAFM measurements. The scale of the memristive system can be estimated from the order of the apex curvature radius, that is 25 nm according to the specifications of the used cantilever model. From this it can expected that the memristive systems extends over multiple AgPt-NPs and that the response of the system includes the memristive activity of several nanogaps across the system. Characterizations were done via establishing a contact between the cantilever with integrated memristive system and a Au surface (as a typical representative for an inert counter electrode) and conduction of voltage sweep experiments. Figure 2 illustrates the experimental scenario designed in this work. The advantage of using a functionalized cantilever as

memristive test system is, that it creates stable conditions regarding to the nanoscale positioning of probe and sample. Therefore, any stochastic drift (e.g. induced by thermal motion) between cantilever and memristive system consisting of AgPt-NPs, which would impose considerable experimental uncertainties during longer measurements [38,39], are mitigated. Due to the inherent electrical field enhancement, the memristive action is efficiently constrained to the cantilever apex, which reduces uncertainties with respect to spatial localization of memristive action. Consequently, this ensures that the observed memristive action originates consistently from the same intermediate-scale AgPt-NP assembly. We took three different measures to establish operation conditions, which drives the AgPt-NP system into a highly volatile switching regime. Firstly, AgPt-alloy NPs were deliberately chosen to achieve a strict limitation of active species. Pt as a noble metal remains electrochemically inert and resides as immobile anchor points in the system, whereas only the Ag-fraction contributes to the formation of filamentary structures. Secondly, a serial 1 GΩ resistor was integrated in the measurement circuit. This strongly restricts the (Ag^+-ion based) material transport and avoids the formation of persistent conducting paths, which arise when the diameter of filamentary structures approaches the regime of long-term stable filaments [31]. Lastly, we stimulated the system with a regular triangular voltage signal with amplitudes of 1 V and -2.5 V to include lower-bias periods, allowing the system to relax repeatedly, which turned out to be non-destructive for longer measurements.

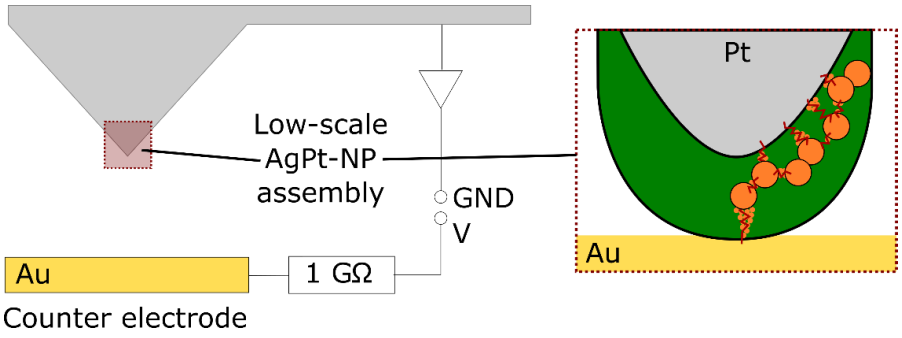

Figure 2. Experimental Design. The cantilever with integrated memristive system is brought into contact to a Au counter electrode and probed via voltage ramps. Memristive action is triggered in the apex area causing field-induced rearrangements of Ag atoms within the SiOxNy matrix and measured conductance depends on the configuration of potential switching gaps. Potential filamentary-type switching gaps are indicated by red zigzag lines.

3. Results

The utilization of a cantilever with integrated memristive system consisting of AgPt-NPs encapsulated in SiOxNy, together with the operation conditions as described above, proved to be suitable to investigate the dynamics in a highly volatile regime. We operated the intermediate-scale AgPt-NP assembly over 8000 repeating voltage cycles, where a considerable fraction of cycles exhibited switching patterns, as represented in Figure 2a. Regarding to the positive polarity, we entirely observed an insulating state and absence of any switching activity. Hence, periods with positive polarity had a sub-threshold character, where forces leading to decay of conducting states are prominently acting on the AgPt-NP system. At periods with negative polarity, sufficient driving forces exists to form filamentary structures and to trigger transitions into conducting states. It can be seen, that the AgPt-NP system responded via complex switching patterns, governed by several switching events accompanied by repetitive decay of conducting states. This is indicative for the high volatility of the conducting states established by this operation regime. Details on the physical mechanisms which are manipulating the states of the AgPt-NP system and its conductivity are treated in the discussion part. We note, that not the entire amount of measured cycles exhibited such a complex switching pattern. Among the entire measurement, there are also many cycles included that show the dynamics of a conventional diffusive memristor, as shown in the supplementary information S1. Additionally, many measurement cycles suggest, that the intermediate-scale AgPt-NP assembly can occupy multiple conductive states. A typical example for this is shown in the supplementary information S2. An alternative illustration of the highly volatile memristive dynamics is given in Figure 2b, showing the memristive response from sequential cycles in terms of conductance of the AgPt-NP system in series with the $1\mathrm{G}\Omega$ resistor versus time. From this, it can be seen that the memristive response partially resembles that of a diffusive memristor, i.e. there are clear threshold switching events between the insulating and conducting states and at zero-bias conditions there is only an insulating state present. However, the complexity of memristive dynamics described here goes beyond to that of a conventional diffusive memristor. That is, because at voltages which are higher than the threshold for the transition into conducting states, there is a certain probability for a spontaneous decay of the conducting state, whereas for a conventional diffusive memristor a permanent occupation of the conducting state is assumed. A magnified view in Figure 2c shows a more clear illustration. Despite of an increasing voltage stimulation, switching into the conducting state is not permanent above the threshold voltage, but superimposed by repetitive spontaneous decays, as indicated by the vertical red lines in the figure. These dynamical features, evoked by highly volatile operation conditions, goes beyond the dynamics of conventional diffusive memristors [30,32].

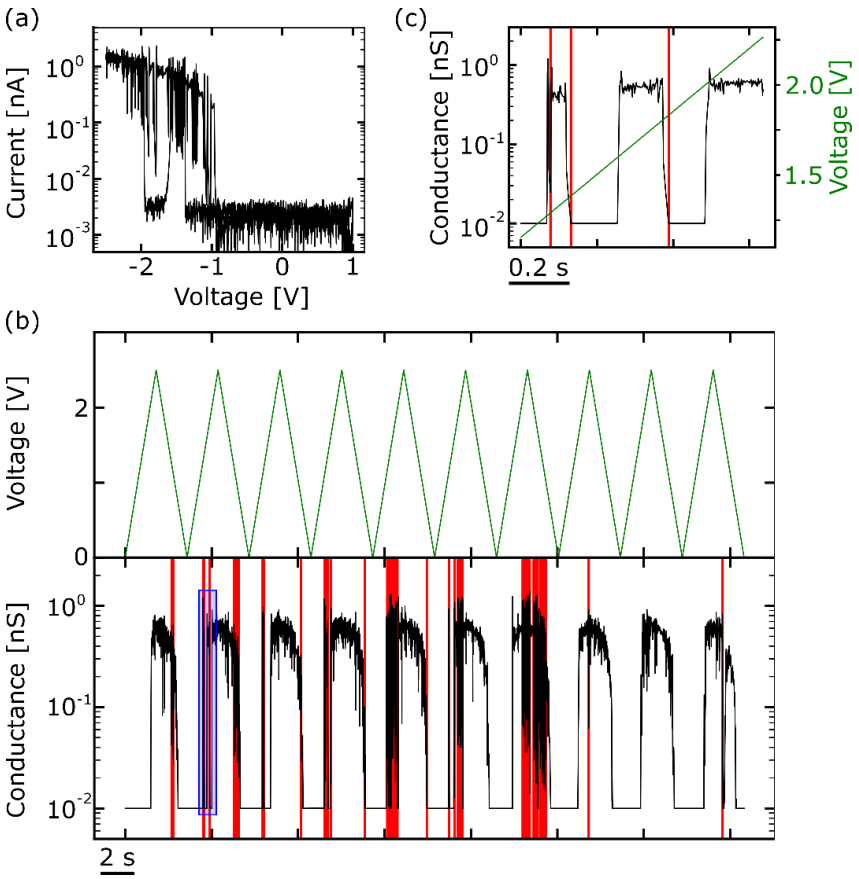

Figure 3. Representation of highly volatile memristive switching dynamics of the intermediate-scale AgPt-NP assembly. (a) A representative IV-diagram showing the current response upon triangular voltage stimulation. At negative polarity, the threshold region for transitions into conducting states is reached, where the memristive dynamics is governed by irregular fluctuations between insulating and conducting states. The observed repeating decays of the conducting state are denoted in the frame of this work as "inhibitory-like" spiking events (ISEs). (b) Alternative illustration of ISEs via plotting conductance versus time for 10 consecutive cycles. For a convenient representation, data points belonging to positive polarity are discarded and all conductance values lower than 0.01 nS are set to an equal level of 0.01 nS (corresponding to insulating state). Detected (see methods) ISEs are indicated by red vertical lines. (c) shows a magnified view of the purple box in (b).

Overall, the dynamics exhibited by the AgPt-NP system are expressed by irregular fluctuations between insulating and conducting states. In this regard, there is a close resemblance to neuronal spiking patterns in biological systems [40–42]. We note, that our system is not equivalent to spike pattern generation via a relaxation oscillator circuit realized with a diffusive memristor, like in [33]. Relaxation oscillator circuits

implement regular spiking patterns with the aid of an external capacitance (which allows to regulate spiking frequencies), whereas the spiking in our system has a more probabilistic nature. In biological neuronal systems, information is encoded on the level of individual neurons by irregular trains of voltage spikes, emerging from excitatory and inhibitory signal inputs coming from adjacent neurons [41]. For biological neuronal systems, it is important to maintain balanced contributions of excitatory and inhibitory inputs, to achieve optimum capabilities to represent and process information [13]. We propose that the highly volatile switching regime of the intermediate-scale AgPt-NP assembly is able to emulate the balanced state of excitatory and inhibitory contributions known from individual neurons and therefore offers similarities to the information encoding scheme as known from biological neuronal systems. This will be argued more deeply in the discussion part. In order to characterize the irregular conductance fluctuations in the highly volatile operation regime more deeply, we introduce an "inhibitory-like" spiking event (ISE) as an edge, where a conducting state of the AgPt-NP system spontaneously decays (see red vertical lines in Figures 2b and 2c). A function in Python was written to detect ISEs in the whole measurement, where an ISE was detected as a monotonic decrease of conductivity by at least one order of magnitude. Following this definition, approximately 20.5 % of all measurement cycles had at least 2 detected ISEs, i.e. they had an increased dynamical complexity compared to conventional diffusive switching. The count statistics of ISEs for the whole measurement over 8000 cycles can be found in greater detail in Figure 3a. The temporal sequence of number of ISEs in an individual measurement cycle is shown as a plot against cycle number in Figure 3b. Here, it is observed that the number of ISEs per cycle varies between cycles with only one ISE and cycles with up to 104 ISEs. The distribution of the variation in the ISE occurrence implies that the degree of activity (in terms of number of ISEs) has a temporally correlated nature. This follows from the observation, that cycles with a high number of ISEs appear to occur accumulated and not evenly distributed over the whole measurement. The autocorrelation function (ACF) [43] calculated from the sequence of number of ISEs per cycle reveals the presence of temporal correlations, as shown in Figure 3c. This means, that cycles with a high/low number ISEs are likely to be followed by cycles with again a high/low number of ISEs. The fact that dynamical features of the volatile switching regime show autocorrelation behavior fits with earlier studies on Ag-based memristive nanostructures [37]. Under the assumption, that the spike count within a cycle is substantially determined by the momentary morphology of the intermediate-scale AgPt-NP assembly (i.e. momentary Ag-mass distribution in the system), the occurrence of autocorrelation behavior can be explained from timescales that govern significant morphological changes. Autocorrelations in the switching dynamics occur, when the timescales for significant morphological changes (which have a major influence for the ISE count) is larger than the time for one measurement cycle. Based on this, the dynamics of consecutive cycles is similar and considerably different spike counts mainly arise, when the measurement has proceed over a larger amount of cycles.

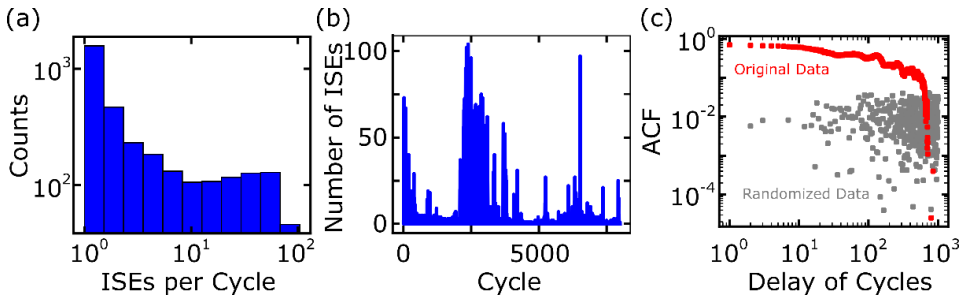

Figure 4. Count statistics of ISEs detected in individual measurement cycles and autocorrelation behavior. (a) histogram plot (logarithmic bin widths) exhibiting the count of measurement cycles in dependence on the number of ISEs detected within an individual cycle. (b) temporal evolution of ISE activity as a bar plot of number of ISEs detected in an individual cycle versus cycle number. (c) autocorrelation function (ACF) calculated for the sequence of spike counts in (b), shown in red, indicates temporal correlations, meaning that cycles with high/low number of ISEs are followed by cycles with again high/low number of ISEs. The grey data points plot the ACF when the sequence of spike counts is shuffled, indicating the destruction of temporal correlations.

Furthermore, we characterized the temporal structure of ISEs within individual cycles by means of the probability distribution of inter-event intervals (IEIs). One IEI was defined as time between subsequent ISEs occurring within one measurement cycle. Therefore, only measurement cycles showing at least 2 ISEs contributed to the IEI evaluation. The probability density function (PDF) represented on a log-log scale of all detected IEIs is shown in Figure 4. It can be seen that the PDF has a skewed shape. Skewed shapes commonly originate from underlying lognormal statistics, which generally arise when the random variable (IEI in this case) is a consequence from multiplication of a multitude of other independent random variables [44]. The occurrence of a skewed IEI distribution additionally supports dynamical similarities between spiking of biological neurons and the memristive AgPt-NP system, because neuronal firing rates result from various interacting processes and therefore frequently follow skewed distributions [44]. For similar reasons, skewed distributions can be found in the dynamical features of filamentary switching systems [45,46]. Here, we speculate that the skewed distribution of IEIs is a reflection of the multiple gap character on the intermediate-scale AgPt-NP assembly, meaning that transitions between insulating and conducting state (and connected to this the detection of ISEs) requires a multiplicative interplay[44] of multiple gaps in the system.

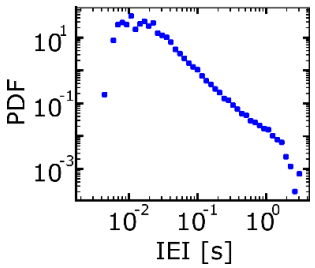

Figure 5. Temporal structure of ISEs within individual measurement cycles. Shown in the probability density function (PDF) of all time intervals between sequential ISEs (inter-event interval IEI) extracted from individual cycles. The PDF suggests a skewed shape.

4. Discussion

In the following discussion, we argue that the physical forces, which are acting on the intermediate-scale AgPt-NP assembly and driving the highly volatile operation regime, can be categorized into excitatory-like and inhibitory-like contributions for meaningful reasons. Excitatory-like contributions include all physical forces that promote the formation of filamentary structures within the memristive system, whereas inhibitory-like contributions include all physical forces that cause the decay of filaments. We further argue that this closely resembles the interplay of exhibitory and inhibitory synaptic inputs, which determines the dynamics on a local level in biological neuronal systems [14–16,35].

4.1 Origin of Highly Volatile Switching Regime

Firstly, physical mechanisms that govern the observed irregular spiking behavior are discussed. Most fundamentally, the measured conductance reflects the internal distribution of Ag within the system [47]. If there is a continuous metallic filament from cantilever apex to the Au counter electrode a conducting state is measured and, vice versa, the sample is in an insulating state when a continuous filament is missing. In analogy to the behavior of biological synapses [5,30], a conducting state of the memristive system corresponds to high information transmission, whereas there is no information transmission in an insulating state. For Ag-based memristive systems, electrochemical metallization (ECM) is the dominating mechanism leading to the formation of filamentary structures [48,49]. Triggered by the external electrical field across the memristive system, electrochemical oxidation of Ag occurs at anodic sites in the system and Ag^{+}-ions are released into the matrix. The Ag^{+}-ions are able to migrate in the dielectric matrix (which is partially directed due to the external field) until they become reduced at cathodic sites in the system. Following these processes, a continuous metallic filament may be formed causing a transition into a conducting state. Hence, the external electrical potential constitutes a force driving the system into a conducting state, and therefore

it can be seen to act excitatory-like on the memristive system. Filamentary structures in the memristive systems are destabilized by an increased amount of interfacial energy, causing spontaneous decay of filamentary structures [30,31]. This is because filamentary structures possess a larger surface-to-volume ratio with high interfacial energy and the overall energy of the system can be minimized through decay of filaments into spherical clusters. In particular, according to this mechanism the volatile dynamics of a diffusive memristor, i.e. the presence of an insulating state at low bias conditions, can be explained by shorter retention times of thinner filaments. Generally, this driving force persistently acts against the formation of filamentary structures. Therefore, it can be considered to give inhibitory-like contributions to the AgPt-NP system, i.e. it drives the system towards the insulating state. Furthermore, the incorporation of the 1GΩ serial resistor to the circuit evokes additional filament instabilities when the system is in a conducting state due to a voltage divider arrangement. After switching into a conducting state, the electrical field across the memristive system becomes strongly reduced (nearly the entire field now drops across the 1GΩ $\mathrm{resistor}$), meaning that the excitatory-like driving force (i.e. the electrical field across the memristive system) is inherently removed, as soon as the memristive system reaches a conducting state. At this point, the main difference to conventional metal cation-based filamentary memristors has to be pointed out: While the fundamental mechanisms of filament formation and disintegration are valid throughout different device classes, the balance between excitatory and inhibitory forces changes from stable bipolar devices over conventional diffusive devices towards the highly volatile switching, which is described in this work. The filament lifetimes (i.e. retention time of conducting state) is consequently either much larger than the IV loop recording time (for bipolar memristive switching), similar (for conventional diffusive switching) or lower (for highly volatile switching), respectively. Similar to the memristive system in this work, Ag-based nanostructures have been previously reported in the context of diffusive memristive devices [28,30,32]. In such conventional diffusive memristors, the operational regime has characteristic threshold voltages V_{SET} and V_{RESET}. These threshold voltages define a stable conducting regime (when voltages $V > V_{SET}$ are applied) and insulating regime (at voltages $V < V_{RESET}$). A distinct threshold voltage for the transition into a conducting state as in conventional diffusive memristors is observed, when at voltages $V > V_{SET}$ the forces causing filament decay are compensated. Filaments are more resilient towards a spontaneous decay when they have a larger diameter [31]. In a previous work, this conventional diffusive memristive switching behavior could also be observed at the level of a single Ag-based alloy nanoparticle, which was probed by cAFM [32]. In contrast, the intermediate-scale AgPt-NP system, which was investigated in this work, do not exhibit distinct threshold voltages Instead, after the first switching event to a conducting state (i.e. notably at voltages $V > V_{SET}$) within one measurement cycle, repetitive decays and reformations of the conducting state are observed, leading to the irregular spiking pattern. These features, which are introduced here as ISEs, constitute an extension of conventional diffusive switching towards a highly volatile regime.

We hypothesize, that such dynamics can be observed, when neither the excitatory-like nor inhibitory-like mechanism acting on the filamentary structures is dominant, but rather balanced, causing morphological fluctuations of the filament, which repetitively opens and closes a conducting path. To support this hypothesis, the transition from conventional diffusive memristive behavior towards highly volatile switching (see supporting information S3) was reproduced in a lookup-table model based on experimental data from a single SiO_2/AgPt-NP/SiO_2 junction [32]. As the applied serial resistance effectively limits excitatory contributions when the device is in a conducting state, the transition towards a highly volatile regime is observed when the serial resistance was increased. This corroborates that via precise tailoring of the balance between excitatory and inhibitory contributions different operational regimes of diffusive memristive systems can be obtained.

4.2 Similarities to Neuronal Behavior

Interestingly, the highly volatile memristive regime observed in this work resembles operational principles on the level of few neurons in biological neuronal systems, which is discussed in the following. In certain neuronal configurations, excitatory and inhibitory synaptic inputs play a crucial role for the activity of an individual neuron. This is emphasized in Figure 5 (left) by a typical feedback inhibition configuration [35,50]. A neuron (E1) receives an input, causing it to excite an adjacent neuron (E2), which denotes regular information transmission in biological neuronal system. Besides excitation of E2, a recurrent connection (I1) gets also excited, which again inhibits the excitability of neuron E1. All in all, the fact, that neuron E1 transmits information within a neuronal network, inherently triggers its own inhibition. We argue that such kind of behavior can be imitated by the physical mechanisms acting during the highly volatile operation regime of a filamentary memristive system. Figure 5 (right) depicts the scenario for a memristive system in analogy to the neuronal configuration. When an input (e.g. voltage signal) is received by the memristive system, transmission of information may be triggered (i.e. switching to a conducting state). As a consequence, this shifts the electrical field across the serial resistor and the inhibitory-like mechanisms now significantly contributes to the state of the memristive system.

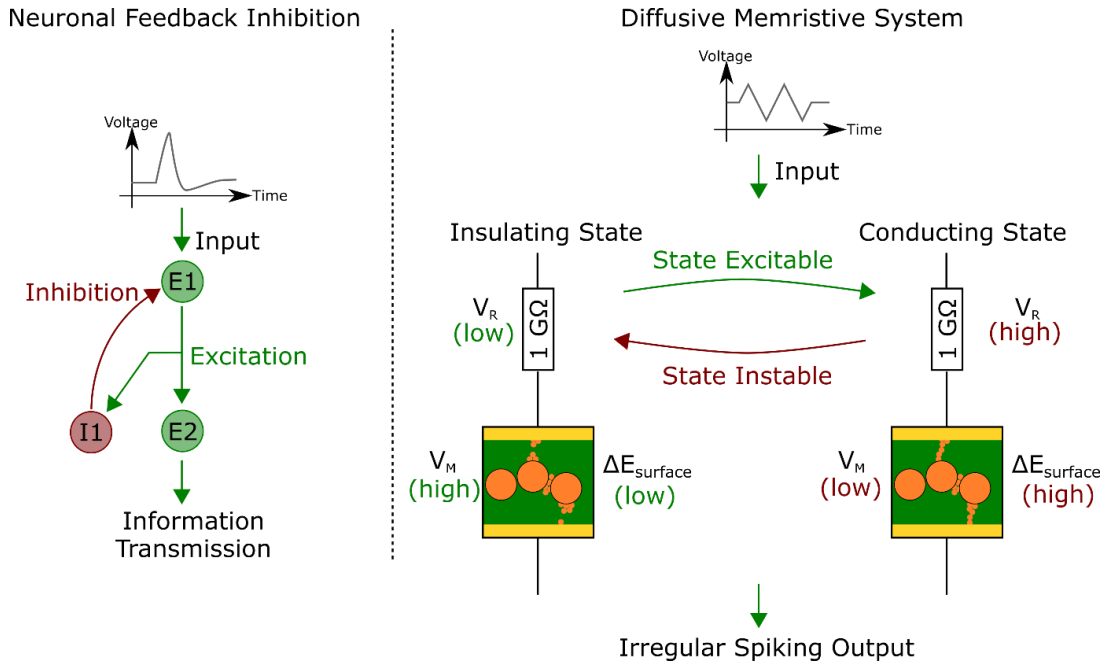

Figure 6. Analogy between neuronal feedback inhibition circuit and diffusive memristive systems in a highly volatile regime. Left: Illustration of feedback inhibition, which substantially contributes to information representation and processing in biological neuronal systems [35,50]. An Input (sketched as an action potential) arrives at neuron E1, which in turn excites neurons E2 and I1. E2 is responsible for a feedforward flow of information, whereas I2 incorporates a feedback loop which inhibits the activity of E1 (meaning that activity of E1 causes its own inhibition). Right: Representation of driving forces acting on the memristive system. Starting with the insulating state (i.e. no continuous filament exists), when an external voltage is applied, the majority of the electrical field drops across the memristive system (V_R/V_M denotes the field across the serial resistor/ memristive system), which excites the formation of a filament. In the conducting state, V_M is low and interfacial energy in the system $\Delta E_{surface}$ gets increased due to filamentary structures, both promoting the instability of the conducting state. Hence, when the memristive system switching into the conducting state, the filamentary structures are inherently destabilized.

In biological neuronal systems, the excitatory and inhibitory contributions are inseparable, and especially to have a balance between both, has major importance for the computational capabilities [35,41]. Biological neuronal systems optimize the ratio of excitatory and inhibitory contributions, to reach an activity level of neurons with a maximized dynamical range [18,34]. The dynamical range can be understood as the number of different spiking patterns a population of neurons can show evoked by stimulation [13]. If a neuronal population could only occupy few different activity patterns (i.e. dynamical range is low), this population

would have no chance to represent a broad range of information, which is strongly obstructive for computation. When excitation within the biological neuronal system would be highly dominating, any evoked activity would trigger highly correlated and exploding activity between neurons, which makes separation of the evoking stimulus difficult (on the other extreme, a too high degree of inhibition would suppress any information transmission). For this reason, in biological neuronal systems, the activity is regulated by inhibitory contributions, to increase the dynamical regime of neurons to bring the whole network into a state which is most efficient for information representation and transmission.

In a similar way, as inhibition increases the dynamical range in biological neuronal systems, the pronounced impact of physical forces causing repetitive decay of conducting states also strongly increases the dynamical range of the memristive system. By this, a broad range of spiking patterns can be realized with a nanoscale memristive system, in close resemblance the behavior of neurons. This enhances the role of diffusive memristive systems for the design of neuromorphic systems by the strategy, to increase the dynamical range through confinement in a highly volatile switching regime. It could be interesting, to explore this strategy for applications in reservoir computing, which requires that information input (having a spatio-temporal nature) is mapped into a higher-order complex space, called a reservoir [26,51]. Recently, it was demonstrated that diffusive memristive systems are suitable as network elements to create a reservoir [52]. Overall, considering that the dynamic range of diffusive switching can be increased when the memristive system is operated in a highly volatile regime, similarly as it is done in biology through balancing excitatory and inhibitory contributions, enhanced strategies for engineering reservoirs with improved computational capabilities could be realized.

5. Conclusion and Outlook

In summary, the memristive switching dynamics of an intermediate-scale AgPt-NP assembly were investigated via cAFM under constraint operation in a highly volatile regime. Establishment of the high volatility was reached through measures (incorporation of 1GΩ serial resistor, limited reservoir of Ag, operation under a triangular voltage signal) which strongly limits the Ag-mass transport. The memristive switching was governed by repetitive formation and decay of conducting states, resulting in a highly dynamical regime resembling the irregular spiking patterns of neurons in biological neuronal systems. To describe this regime, we introduced "inhibitory-like" spiking events as probabilistic decays of conducting states at voltages above the threshold voltage for diffusive switching. By this, the investigated dynamics can be understood as an extension of conventional diffusive switching towards an increased dynamical range, which could provide computational benefits for the design of neuromorphic systems. This was argued by the close resemblance to the behavior of individual neurons in biological neuronal systems, where the dynamics

are shaped through a balance of excitatory and inhibitory contributions in order to tune the system into a dynamical regime which has a high potential for bio-inspired computation.

This study demonstrates on a fundamental level that intermediate-scale filamentary memristive systems can be constrained into a highly diffusive regime, which may prove interesting for a later transfer to real device implementation. Engineering of devices which implement the highly volatile operation regime could be useful for the physical implementation of reservoir computing substrates [26]. To pave the way for this, more detailed studies on the kinetics acting on the volatile filament (and especially the interplay between different physical forces) is required, such as presented here [49]. All in all, due to the apparent dynamical similarities to excitatory and inhibitory synaptic contributions (that are increasing and decreasing neuronal firing, respectively), this work provides novel perspectives for the design of neuromorphic systems.

6. Materials and Methods

Sample Fabrication

A commercially available Pt-coated cantilever (Bruker CONTV-PT) was loaded to a high-vacuum physical vapor deposition system, that is equipped with two independent sources for SiO_xN_y and AgPt-NP deposition. The orientation of the cantilever inside the deposition chamber was adjusted in such a way, that the cantilever apex was oriented toward the SiO_xN_y source and one edge of the pyramid geometry oriented towards the AgPt-NP source. This orientation lead to a sample structure as shown in Figure 1. The SiO_xN_y layers were fabricated by DC reactive sputtering under a gas mixture of 50 sccm Ar and 0.44 sccm N_2. Slight oxidation of the as-deposited SiN_x upon exposure to ambient atmosphere is expected, which consequently leads to the formation of SiO_xN_y. AgPt-NPs were deposited by a Haberland-type gas aggregation source (GAS) (details of NP deposition are reported in earlier studies [53]). The fabrication of the sample was separated in two vacuum steps. During the first step, a 5 nm SiO_xN_y layer and the AgPt-NPs were deposited. After confirming the applicability of the sample via SEM (it has to be ensured, that the active region around the apex has proper amount of NPs forming the memristive system), a 5 nm SiO_xN_y layer covering the AgPt-NPs was deposited in a second vacuum step.

Data Acquisition

The IV characteristics were acquired by a conventional cAFM electrical setup with the exception of adding a serial resistor of 1 GΩ to limit the current within sub-nanoamp range. To minimize the pickup and other unwanted electrical noise the preamplifier was placed close to the sample (~1cm away) and in addition all cables and sample area were shielded to the circuit ground. The preamplifier has a gain of 10^9 and capable of measuring currents from 2pA up to 1μA at a minimum acquisition time of 20 μs per data point. A typical IV cycle was acquired at a rate of 0.3 Hz. We have used commercially available Au(111) on mica as a counter

electrode which was purchased from Phasis Sàrl, Switzerland. The sample cleanliness was verified by cAFM prior to measurements to ensure its suitability for the long-term data acquisition. In case of any visualized defects, the sample was cleaned by two sputtering and annealing cycles. However, all fresh substrates did not require such an extra step.

Data Evaluation

A Python script was applied to extract the "inhibitory-like" spiking events (ISEs) from the raw data. Firstly, the raw data was converted to a conductance versus time representation, as shown in Figure 3b and c. For a more convenient presentation of data, datapoints belonging to sequences where positive voltages were applied a discarded, because they do not exhibit any memristive activity. Nevertheless, it must be considered that these periods have a meaning for the physical behavior of the system, because these are periods where the intermediate-scale AgPt-NP system is allowed to relax. Moreover, during the conversion to the conductance versus time representation, all conductance values below 0.01 nS were set to an equal level of 0.01 nS and slight smoothing via a Savitzky-Golay filter with lowest possible window length of 3 was performed. An ISE was detected in the conductance versus time representation, whenever the conductance (starting from a conductive state) exhibited a monotonic decrease over at least one order of magnitude. We estimate that this definition of an ISE is rather conservative and it can be assumed, that more ISE causing conductance drops below one order of magnitude are present in the data. For the ISE count statistics in Figure 4a, a histogram with logarithmic bin widths was calculated. The autocorrelation function $\boldsymbol{\rho_k}$ in Figure 4c was calculated according to[43]

$$\boldsymbol{\rho_k} = \frac{\frac{\mathbf{1}}{\boldsymbol{N-k-1}}\sum_{i=k+1}^{N}(\boldsymbol{x_i}-\boldsymbol{\mu})(\boldsymbol{x_{i-k}}-\boldsymbol{\mu})}{\frac{\mathbf{1}}{\boldsymbol{N-1}}\sum_{i=1}^{N}(\boldsymbol{x_i}-\boldsymbol{\mu})^2}$$

where $\boldsymbol{k}$ is the lag of measurement cycles, $\boldsymbol{N}$ = 8000 is the total number of measurement cycles, $\boldsymbol{x_i}$ is the number of ISEs in cycle $\boldsymbol{i}$ and μ is the total mean of all ISEs. An interevent-interval (IEI) was defined as time between two consecutive ISEs. IEIs were only calculated within one measurement cycles, i.e. there are no IEIs between more than one measurement cycles possible. The PDF of IEIs in Figure 5 was estimated by logarithmic binning.

Acknowledgements

Funded by the Deutsche Forschungsgemeinschaft (DFG, German Research Foundation) – Project-ID 434434223 – SFB 1461.

Conflict of Interest

The authors declare no conflict of interest.

Author Contributions

N.C., T.S., F.F., A.H. and A.V. conceived the studies on cantilevers decorated with intermediate-scale AgPt-NP based memristive systems. N.C. and A.V. fabricated the functionalized cantilevers in this work. N.C. and A.V. performed the SEM measurements A.H. performed the cAFM measurements of the functionalized cantilevers. N.C., A.H. and A.V. evaluated the highly volatile switching dynamics and elaborated on the statistical description. A.V. conceived the lookup-table model based of diffusive switching in supplementary information S3. N.C. wrote the original draft of the manuscript. T.S., F.F., A.H. and A.V. reviewed and edited the manuscript. A.V. supervised the work of N.C. F.F. and A.V. acquired funding of the project.

Data Availability

The data generated and analyzed in this study is available from the corresponding author upon reasonable request.

References

1. Zidan, M.A.; Strachan, J.P.; Lu, W.D. The future of electronics based on memristive systems. *Nat. Electron.* **2018**, *1*, 22–29, doi:10.1038/s41928-017-0006-8.

2. Yang, J.J.; Strukov, D.B.; Stewart, D.R. Memristive devices for computing. *Nat. Nanotechnol.* **2013**, *8*, 13–24, doi:10.1038/nnano.2012.240.

3. Edwards, A.H.; Barnaby, H.J.; Campbell, K.A.; Kozicki, M.N.; Liu, W.; Marinella, M.J. Reconfigurable memristive device technologies. *Proc. IEEE* **2015**, *103*, 1004–1033, doi:10.1109/JPROC.2015.2441752.

4. Zhu, J.; Zhang, T.; Yang, Y.; Huang, R. A comprehensive review on emerging artificial neuromorphic devices. *Appl. Phys. Rev.* **2020**, *7*, doi:10.1063/1.5118217.

5. Wang, Z.; Wang, L.; Nagai, M.; Xie, L.; Yi, M.; Huang, W. Nanoionics-Enabled Memristive Devices: Strategies and Materials for Neuromorphic Applications. *Adv. Electron. Mater.* **2017**, *3*, doi:10.1002/aelm.201600510.

6. Sangwan, V.K.; Hersam, M.C. Neuromorphic nanoelectronic materials. *Nat. Nanotechnol.* **2020**, *15*, 517–528, doi:10.1038/s41565-020-0647-z.

7. Xia, Q.; Yang, J.J. Memristive crossbar arrays for brain-inspired computing. *Nat. Mater.* **2019**, *18*, 309–323, doi:10.1038/s41563-019-0291-x.

8. Ielmini, D.; Wong, H.S.P. In-memory computing with resistive switching devices. *Nat. Electron.* **2018**,

1, 333–343, doi:10.1038/s41928-018-0092-2.

9. Yao, P.; Wu, H.; Gao, B.; Eryilmaz, S.B.; Huang, X.; Zhang, W.; Zhang, Q.; Deng, N.; Shi, L.; Wong, H.S.P.; et al. Face classification using electronic synapses. *Nat. Commun.* **2017**, *8*, 1–8, doi:10.1038/ncomms15199.

10. Serb, A.; Bill, J.; Khiat, A.; Berdan, R.; Legenstein, R.; Prodromakis, T. Unsupervised learning in probabilistic neural networks with multi-state metal-oxide memristive synapses. *Nat. Commun.* **2016**, *7*, doi:10.1038/ncomms12611.

11. Prezioso, M.; Merrikh-Bayat, F.; Hoskins, B.D.; Adam, G.C.; Likharev, K.K.; Strukov, D.B. Training and operation of an integrated neuromorphic network based on metal-oxide memristors. *Nature* **2015**, *521*, 61–64, doi:10.1038/nature14441.

12. Chialvo, D.R. Emergent complex neural dynamics. *Nat. Phys.* **2010**, *6*, 744–750, doi:10.1038/nphys1803.

13. Shew, W.L.; Plenz, D. The functional benefits of criticality in the cortex. *Neuroscientist* **2013**, *19*, 88–100, doi:10.1177/1073858412445487.

14. Froemke, R.C. Plasticity of Cortical Excitatory-Inhibitory Balance. *Annu. Rev. Neurosci.* **2015**, *38*, 195–219, doi:10.1146/annurev-neuro-071714-034002.

15. Zhou, S.; Yu, Y. Synaptic E-I balance underlies efficient neural coding. *Front. Neurosci.* **2018**, *12*, 1–11, doi:10.3389/fnins.2018.00046.

16. Denève, S.; Machens, C.K. Efficient codes and balanced networks. *Nat. Neurosci.* **2016**, *19*, 375–382, doi:10.1038/nn.4243.

17. Dan, Y.; Poo, M.M. Spike timing-dependent plasticity of neural circuits. *Neuron* **2004**, *44*, 23–30, doi:10.1016/j.neuron.2004.09.007.

18. Shew, W.L.; Yang, H.; Yu, S.; Roy, R.; Plenz, D. Information capacity and transmission are maximized in balanced cortical networks with neuronal avalanches. *J. Neurosci.* **2011**, *31*, 55–63, doi:10.1523/JNEUROSCI.4637-10.2011.

19. Yu, L.; Shen, Z.; Wang, C.; Yu, Y. Efficient coding and energy efficiency are promoted by balanced excitatory and inhibitory synaptic currents in neuronal network. *Front. Cell. Neurosci.* **2018**, *12*, 1–13, doi:10.3389/fncel.2018.00123.

20. Linkenkaer-Hansen, K.; Nikouline, V. V.; Palva, J.M.; Ilmoniemi, R.J. Long-range temporal

correlations and scaling behavior in human brain oscillations. *J. Neurosci.* **2001**, *21*, 1370–1377, doi:10.1523/jneurosci.21-04-01370.2001.

21. Beggs, J.M.; Plenz, D. Neuronal Avalanches in Neocortical Circuits. *J. Neurosci.* **2003**, *23*, 11167–11177, doi:10.1523/jneurosci.23-35-11167.2003.

22. Hochstetter, J.; Zhu, R.; Loeffler, A.; Diaz-Alvarez, A.; Nakayama, T.; Kuncic, Z. Avalanches and edge-of-chaos learning in neuromorphic nanowire networks. *Nat. Commun.* **2021**, *12*, doi:10.1038/s41467-021-24260-z.

23. Pike, M.D.; Bose, S.K.; Mallinson, J.B.; Acharya, S.K.; Shirai, S.; Galli, E.; Weddell, S.J.; Bones, P.J.; Arnold, M.D.; Brown, S.A. Atomic scale dynamics drive brain-like avalanches in percolating nanostructured networks. *Nano Lett.* **2020**, *20*, 3935–3942, doi:10.1021/acs.nanolett.0c01096.

24. Mallinson, J.B.; Shirai, S.; Acharya, S.K.; Bose, S.K.; Galli, E.; Brown, S.A. Avalanches and criticality in self-organized nanoscale networks. *Sci. Adv.* **2019**, *5*, 1–8, doi:10.1126/sciadv.aaw8438.

25. Shirai, S.; Acharya, S.K.; Bose, S.K.; Mallinson, J.B.; Galli, E.; Pike, M.D.; Arnold, M.D.; Brown, S.A. Long-range temporal correlations in scale-free neuromorphic networks. *Netw. Neurosci.* **2019**, *4*, 432–447, doi:10.1162/netn_a_00128.

26. Tanaka, G.; Yamane, T.; Héroux, J.B.; Nakane, R.; Kanazawa, N.; Takeda, S.; Numata, H.; Nakano, D.; Hirose, A. Recent advances in physical reservoir computing: A review. *Neural Networks* **2019**, *115*, 100–123, doi:10.1016/j.neunet.2019.03.005.

27. Milano, G.; Pedretti, G.; Montano, K.; Ricci, S.; Hashemkhani, S.; Boarino, L.; Ielmini, D.; Ricciardi, C. In materia reservoir computing with a fully memristive architecture based on self-organizing nanowire networks. *Nat. Mater.* **2021**, doi:10.1038/s41563-021-01099-9.

28. Wang, Z.; Rao, M.; Midya, R.; Joshi, S.; Jiang, H.; Lin, P.; Song, W.; Asapu, S.; Zhuo, Y.; Li, C.; et al. Threshold Switching of Ag or Cu in Dielectrics: Materials, Mechanism, and Applications. *Adv. Funct. Mater.* **2018**, *28*, doi:10.1002/adfm.201704862.

29. Wang, R.; Yang, J.-Q.; Mao, J.-Y.; Wang, Z.-P.; Wu, S.; Zhou, M.; Chen, T.; Zhou, Y.; Han, S.-T. Recent Advances of Volatile Memristors: Devices, Mechanisms, and Applications. *Adv. Intell. Syst.* **2020**, *2*, 2000055, doi:10.1002/aisy.202000055.

30. Wang, Z.; Joshi, S.; Savel'ev, S.E.; Jiang, H.; Midya, R.; Lin, P.; Hu, M.; Ge, N.; Strachan, J.P.; Li, Z.; et al. Memristors with diffusive dynamics as synaptic emulators for neuromorphic computing. *Nat. Mater.* **2017**, *16*, 101–108, doi:10.1038/nmat4756.

31. Wang, W.; Wang, M.; Ambrosi, E.; Bricalli, A.; Laudato, M.; Sun, Z.; Chen, X.; Ielmini, D. Surface diffusion-limited lifetime of silver and copper nanofilaments in resistive switching devices. *Nat. Commun.* **2019**, *10*, 1–9, doi:10.1038/s41467-018-07979-0.

32. Vahl, A.; Carstens, N.; Strunskus, T.; Faupel, F.; Hassanien, A. Diffusive Memristive Switching on the Nanoscale, from Individual Nanoparticles towards Scalable Nanocomposite Devices. *Sci. Rep.* **2019**, *9*, 1–10, doi:10.1038/s41598-019-53720-2.

33. Midya, R.; Wang, Z.; Asapu, S.; Joshi, S.; Li, Y.; Zhuo, Y.; Song, W.; Jiang, H.; Upadhay, N.; Rao, M.; et al. Artificial Neural Network (ANN) to Spiking Neural Network (SNN) Converters Based on Diffusive Memristors. *Adv. Electron. Mater.* **2019**, *5*, doi:10.1002/aelm.201900060.

34. Deco, G.; Ponce-Alvarez, A.; Hagmann, P.; Romani, G.L.; Mantini, D.; Corbetta, M. How local excitation-inhibition ratio impacts the whole brain dynamics. *J. Neurosci.* **2014**, *34*, 7886–7898, doi:10.1523/JNEUROSCI.5068-13.2014.

35. Isaacson, J.S.; Scanziani, M. How inhibition shapes cortical activity. *Neuron* **2011**, *72*, 231–243, doi:10.1016/j.neuron.2011.09.027.

36. Shew, W.L.; Yang, H.; Petermann, T.; Roy, R.; Plenz, D. Neuronal avalanches imply maximum dynamic range in cortical networks at criticality. *J. Neurosci.* **2009**, *29*, 15595–15600, doi:10.1523/JNEUROSCI.3864-09.2009.

37. Carstens, N.; Vahl, A.; Gronenberg, O.; Strunskus, T.; Kienle, L.; Faupel, F.; Hassanien, A. Enhancing reliability of studies on single filament memristive switching via an unconventional cafm approach. *Nanomaterials* **2021**, *11*, 1–16, doi:10.3390/nano11020265.

38. Lanza, M.; Wong, H.S.P.; Pop, E.; Ielmini, D.; Strukov, D.; Regan, B.C.; Larcher, L.; Villena, M.A.; Yang, J.J.; Goux, L.; et al. Recommended Methods to Study Resistive Switching Devices. *Adv. Electron. Mater.* **2019**, *5*, 1–28, doi:10.1002/aelm.201800143.

39. Yang, Y.; Huang, R. Probing memristive switching in nanoionic devices. *Nat. Electron.* **2018**, *1*, 274–287, doi:10.1038/s41928-018-0069-1.

40. Shadlen, M.N.; Newsome, W.T. Noise, neural codes and cortical organization. *Curr. Opin. Neurobiol.* **1994**, *4*, 569–579, doi:10.1016/0959-4388(94)90059-0.

41. Shadlen, M.N.; Newsome, W.T. The Variable Discharge of Cortical Neurons: Implications for Connectivity, Computation, and Information Coding. *J. Neurosci.* **1998**, *18*, 3870–3896, doi:10.1523/JNEUROSCI.18-10-03870.1998.

42. Stevens, C.F.; Zador, A.M. Input synchrony and the irregular firing of cortical neurons. *Nat. Neurosci.* **1998**, *1*, 210–217, doi:10.1038/659.

43. Eke, A.; Herman, P.; Kocsis, L.; Kozak, L.R. Fractal characterization of complexity in temporal physiological signals. *Physiol. Meas.* **2002**, *23*, doi:10.1088/0967-3334/23/1/201.

44. Buzsáki, G.; Mizuseki, K. The log-dynamic brain: How skewed distributions affect network operations. *Nat. Rev. Neurosci.* **2014**, *15*, 264–278, doi:10.1038/nrn3687.

45. Karpov, V.G.; Niraula, D. Log-Normal Statistics in Filamentary RRAM Devices and Related Systems. *IEEE Electron Device Lett.* **2017**, *38*, 1240–1243, doi:10.1109/LED.2017.2734961.

46. Acharya, S.K.; Galli, E.; Mallinson, J.B.; Bose, S.K.; Wagner, F.; Heywood, Z.E.; Bones, P.J.; Arnold, M.D.; Brown, S.A. Stochastic Spiking Behavior in Neuromorphic Networks Enables True Random Number Generation. *ACS Appl. Mater. Interfaces* **2021**, *13*, 52861–52870, doi:10.1021/acsami.1c13668.

47. Cho, B.; Yun, J.M.; Song, S.; Ji, Y.; Kim, D.Y.; Lee, T. Direct observation of Ag filamentary paths in organic resistive memory devices. *Adv. Funct. Mater.* **2011**, *21*, 3976–3981, doi:10.1002/adfm.201101210.

48. Waser, R.; Dittmann, R.; Staikov, C.; Szot, K. Redox-based resistive switching memories nanoionic mechanisms, prospects, and challenges. *Adv. Mater.* **2009**, *21*, 2632–2663, doi:10.1002/adma.200900375.

49. Chekol, S.A.; Menzel, S.; Ahmad, R.W.; Waser, R.; Hoffmann-Eifert, S. Effect of the Threshold Kinetics on the Filament Relaxation Behavior of Ag-Based Diffusive Memristors. *Adv. Funct. Mater.* **2021**, 2111242, doi:10.1002/adfm.202111242.

50. Kullmann, D.M. Interneuron networks in the hippocampus. *Curr. Opin. Neurobiol.* **2011**, *21*, 709–716, doi:10.1016/j.conb.2011.05.006.

51. Lukoševičius, M.; Jaeger, H. Reservoir computing approaches to recurrent neural network training. *Comput. Sci. Rev.* **2009**, *3*, 127–149, doi:10.1016/j.cosrev.2009.03.005.

52. Midya, R.; Wang, Z.; Asapu, S.; Zhang, X.; Rao, M.; Song, W.; Zhuo, Y.; Upadhyay, N.; Xia, Q.; Yang, J.J. Reservoir Computing Using Diffusive Memristors. *Adv. Intell. Syst.* **2019**, *1*, 1900084, doi:10.1002/aisy.201900084.

53. Vahl, A.; Strobel, J.; Reichstein, W.; Polonskyi, O.; Strunskus, T.; Kienle, L.; Faupel, F. Single target sputter deposition of alloy nanoparticles with adjustable composition via a gas aggregation cluster

source. *Nanotechnology* **2017**, *28*, doi:10.1088/1361-6528/aa66ef.

Supplementary Information

Neuronal-like Irregular Spiking Dynamics in Highly Volatile Memristive Intermediate-scale AgPt-Nanoparticle Assemblies

*Niko Carstens[1], Thomas Strunskus[1], Franz Faupel[1], Abdou Hassanien[2] and Alexander Vahl[1]**

[1]Institute for Materials Science, Chair for Multicomponent Materials, Faculty of Engineering, Christian-Albrechts-University of Kiel, Kaiserstraße 2, D-24143 Kiel, Germany

[2]Department of Condensed Matter Physics, J. Stefan Institute, Jamova 39, 1000 Ljubljana, Slovenia

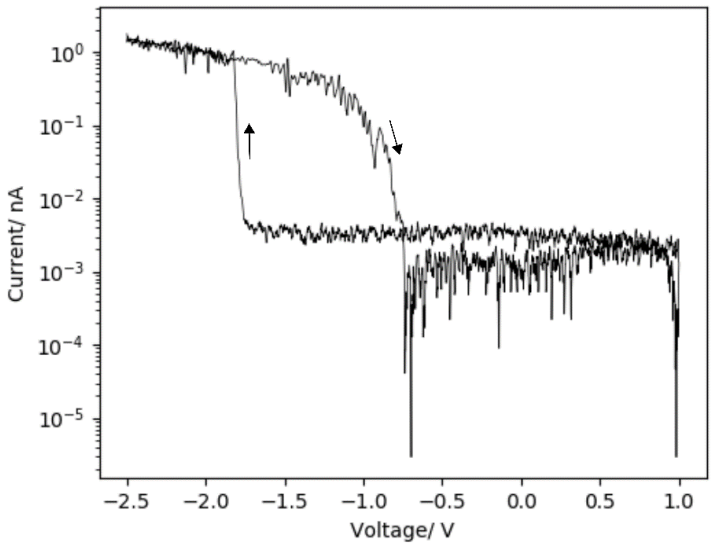

Figure S1. Typical measurement cycle exhibiting a conventional diffusive switching character.

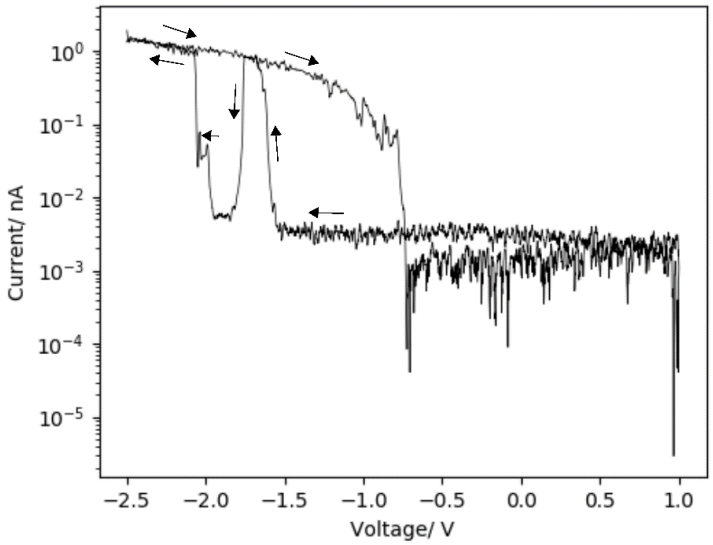

Figure S2. Typical measurement cycle exhibiting the presence of multiple conductive states.

Supporting Note S3

To explore on possible origins of a highly volatile switching behavior, a simple model is presented that could explain the transition from conventional diffusive switching towards a highly volatile regime by the magnitude of the applied serial resistance. As a basis for the probabilistic model of diffusive memristive switching, experimental data of a single SiO_2/AgPt-NP/SiO_2 junction, as probed by conventional cAFM, were used. A full description of this dataset can be found in [1]. From 70 consecutive IV hysteresis cycles the distribution of V_{SET} and V_{RESET} voltages (the according switching events are denoted as SET and RESET in the following) was obtained and a cumulative probability distribution was calculated. It is important to mention, that in this earlier study a serial resistor of only 101 MΩ was used and the memristive system was not directly incorporated to the cantilever, which limited the possibilities to perform long-term measurements at the location of an identical SiO_2/AgPt-NP/SiO_2 junction and motivates the selection of only a subset of the recorded cycles (i.e. in this case 70 consecutive cycles) for the determination of SET and RESET probabilities. In contrast, in this study a 1 GΩ serial resistor was used and the SiO_xN_y/AgPt-NP/SiO_xN_y nanocomposite was directly integrated to the region around the apex of the cantilever. Despite the minute differences in the sample arrangement, we are convinced that both systems are similar enough to yield a meaningful comparison.

In order to model the diffusive memristive switching properties, the probabilistic numeric model includes the following assumptions:

- The memristive system exhibits two distinct resistance states, namely a state with high resistance (HRS) $R_{m,HRS}$ and a state with low resistance (LRS) $R_{m,LRS}$. This binary condition is expressed in terms of an internal state variable ω by Eq.S1:

(Eq. S1) $$R_m(\omega) = R_{m,HRS} - \omega(R_{m,HRS} - R_{m,LRS}) \quad \text{with} \quad \omega \in \{0,1\}$$

- The transitions between resistance states follow the switching probabilities that are extracted from the experimentally obtained cumulative probabilities.
- In each simulation step a random number is generated and compared to the respective switching probability at the applied voltage. In case the random number is lower than the cumulative switching probability, the internal state variable is updated (corresponding to a switch from HRS to LRS or vice versa). Accordingly, the switching between HRS and LRS is modelled to occur immediately in a single simulation step. Therefore, this model does not account for potential multilevel switching, which is reasonable because in most instances the experimentally obtained IV hysteresis loops exhibit nearly binary switching.
- A single simulation step corresponds to a single data point in the IV hysteresis. For a common experiment, the IV hysteresis loops were recorded with an acquisition rate in the order of magnitude of 10 Hz.

In order to validate the model, the experimentally obtained (Figure S4) and simulated (Figure 5 top and middle) I vs t plots for multiple and V vs t plots are compared. In general, the probabilistic model is capable to reproduce all qualitative features that are observed in the experimentally obtained data. This includes the diffusive memristive switching characteristics with varying SET and RESET voltages for every cycle and the binary nature of the resistance states. The assumption of a purely ohmic HRS and LRS does not impact the usability of the model for qualitative comparison, but could be refined in the future to yield an even better match of the simulated results. In both cases, every cycle exhibits exactly one SET and RESET event, as expected in conventional diffusive memristive switching. This observation however completely changes, when the resistance of the serial resistor is changed from 101 MΩ to 1 GΩ. In the simulation, this change in serial resistance was accomplished by adding an additional serial resistor of 899 MΩ, which effectively reduces the potential drop over the memristive devices. Interestingly, the simulation for 1 GΩ (Figure S5 bottom) shows a highly volatile switching regime, which exhibits features that are very similar to the features observed in Figure 3b. Instead of a single SET and RESET event in each part of the hysteresis loop, a multitude of transition events is observed. Here it is worth noting that the simulation uses the same lookup table for the switching probabilities as in Figure S5 middle and the only difference is the transition from a 101 MOhm to 1 GOhm serial resistance. In the picture of excitatory and inhibitory contributions, the increase in the serial resistance is expected to shift the balance by reducing the excitatory contribution while the filament bridges the dielectric. As a result, the retention time of the formed filament is apparently reduced, leading to multiple SET and RESET processes within one hysteresis loop.

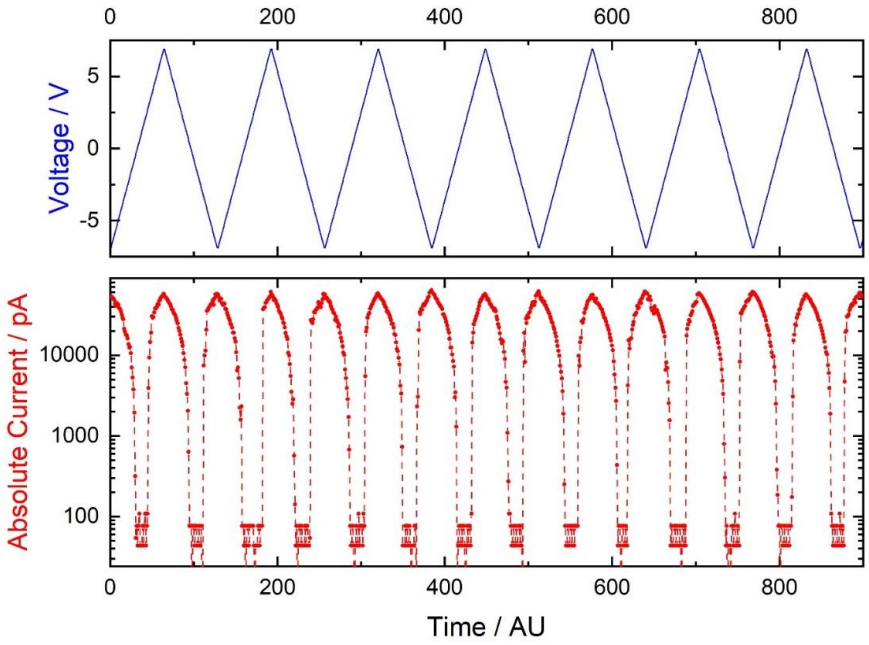

Figure S4. Experimental data of a single SiO_2/AgPt-NP/SiO_2 junction from [1].

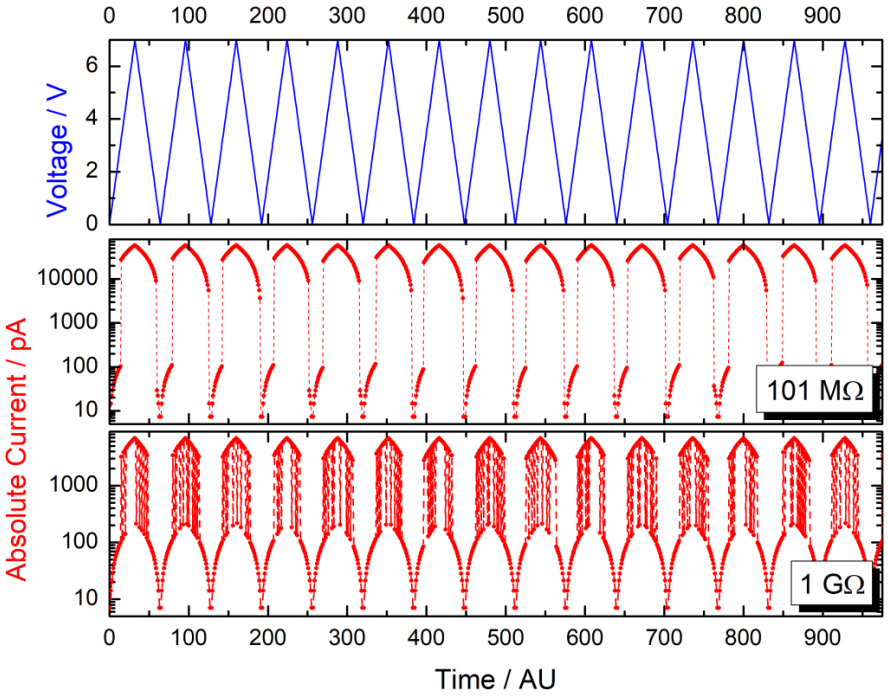

Figure S5. Simulated behavior of a single SiO_2/AgPt-NP/SiO_2 junction exhibiting conventional diffusive switching under application of a 101 MΩ resistor and highly volatile switching under application of a 1 GΩ resistor.

References in Supplementary Information

1. Vahl, A.; Carstens, N.; Strunskus, T.; Faupel, F.; Hassanien, A. Diffusive Memristive Switching on the Nanoscale, from Individual Nanoparticles towards Scalable Nanocomposite Devices. *Sci. Rep.* **2019**, *9*, 1–10, doi:10.1038/s41598-019-53720-2.

6. Diffusive Memristive Devices based on AgPt and AgAu Alloy-NPs

This chapter deals with the implementation of diffusive switching devices using AgPt and AgAu alloy-NPs. The design of this study was conceived by Alexander Vahl in the framework of his PhD thesis [149]. All measurements related to cAFM were conducted by Abdou Hassanien at the Jozef Stefan Institute in Ljubljana. Own contributions to this work partially include the fabrication and measurement of multistack devices, statistical evaluation of the diffusive switching dynamics, interpretation of data and manuscript writing. In the context of the present thesis, it is shown that diffusive switching dynamics (as already demonstrated for individual nanoscale Ag-filaments evolved from a continuous electrode, Chapter 4) are maintained even in larger scale systems, built by multiple stacking of NP and SiO_2 layers. These findings reveal important implications for the scalability of diffusive switching systems from the nanoscale towards a more macroscopic scale. Regarding to applications in neuromorphic systems, diffusive switching dynamics are promising to emulate biological short-term synaptic plasticity. Moreover, the use of Ag-based NPs is reasoned by enhanced design principles, which are only hardly viable in case of a thin film active electrode. Firstly, due to the inherent field enhancement, memristive switching can be facilitated at NP-interfaces. Secondly, taking AgPt or AgAu-alloy NPs, the more noble component acts as a stable inclusion within the insulating layer, which could be exploited to predefine switching channels. Thirdly, adjusting the alloy-NP composition allows for a careful tailoring of the mobile species availability, which could be interesting to influence filament diameters.

This chapter is a reprint from the following publication:

A. Vahl, **N. Carstens**, T. Strunskus, F. Faupel and A. Hassanien, *Scientific Reports*, 2019, 9, 17367

SCIENTIFIC REPORTS
nature research

OPEN

Diffusive Memristive Switching on the Nanoscale, from Individual Nanoparticles towards Scalable Nanocomposite Devices

Alexander Vahl[1], Niko Carstens[1], Thomas Strunskus[1], Franz Faupel[1*] & Abdou Hassanien[2*]

Nanoscale memristive phenomena are of great interest not only to miniaturize devices and improve their performance but also to understand the details of the underlying mechanism. Herein, we utilize conductive atomic force microscopy (C-AFM) as a non-invasive method to examine the nanoscale memristive properties of individual noble metal alloy nanoparticles that are sparsely encapsulated in a thin SiO_2 dielectric matrix. The measurement of current-voltage hysteresis loops at the level of individual nanoparticles, enabled by the nanoscopic contact area of the C-AFM tip, indicates reliable memristive switching for several hours of continuous operations. Alongside the electrical characterization on the nanoscale, the method of C-AFM offers the potential for *in situ* monitoring of long term operation induced morphological alterations and device failure, which is demonstrated at the example of nanoparticle-based devices with additional Cr wetting layer. The application of alloy nanoparticles as reservoir for mobile silver species effectively limits the formation of stable metallic filaments and results in reproducible diffusive switching characteristics. Notably, similar behaviour is encountered on macroscopic nanocomposite devices, which incorporate multiple stacks of nanoparticles and offer a high design versatility to tune switching properties and engineer scalable memristive devices with diffusive switching characteristics. No additional forming step is required for the operation of the presented alloy nanoparticle based memristive devices, which renders them very attractive for applications.

With the postulation of the experimental realization of a memristor in 2008[1], Strukov *et al.* related resistive switching phenomena in sub-stoichiometric oxide thin films to the theoretical model of a memristor as initially proposed by L. Chua in 1971[2], and initiated a huge increase in research interest in this field. While the memristor as a fundamental element has been under severe debate recently[3], the innovative power of the use of memristive switching phenomena remains unquestioned. Within the past decade, a broad variety of device concepts was reported in the context of memristive switching, which range from electro-chemical metallization (ECM) over valance change mechanism (VCM) and phase change materials (PCM) and beyond[4–7]. Memristive devices are commonly discussed as promising devices for an application as novel memory[8], for beyond-von-Neumann logics[9] and in the context of neuromorphic engineering[10–14]. Among the various reported devices, different switching characteristics are commonly observed, including bipolar, unipolar and diffusive memristive switching[4,15,16]. While in the context of the application as memory device typically bipolar and unipolar switching characteristics are preferred, diffusive memristive devices offer the potential of being used as selector devices or as true random number generators[17,18].

Amongst the various device classes, special interest is paid to memristive devices relying on ECM, i.e. the reversible formation of a conductive path upon field-driven motion of mobile metal cations (e.g. silver cations) between two electrodes. Typical setup of such devices consists of a dielectric layer, which is sandwiched between two planar electrodes of which one serves as a reservoir for mobile metallic cations (e.g. Cu or Ag). The underlying mechanisms that lead to the reversible changes in resistivity trace back to local rearrangement of atoms and

[1]Institute for Materials Science – Chair for Multicomponent Materials, Faculty of Engineering, Christian-Albrechts-University of Kiel, Kaiserstraße 2, D-24143, Kiel, Germany. [2]Department of Condensed Matter Physics, J. Stefan Institute, Jamova 39, 1000, Ljubljana, Slovenia. *email: ff@tf.uni-kiel.de; Abdou.Hassanien@ijs.si

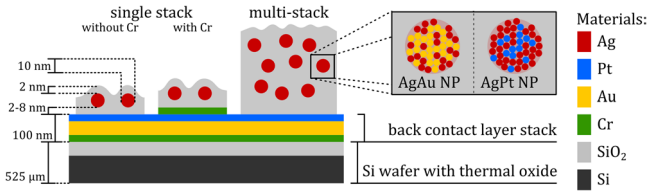

Figure 1. Schematic depiction of the typical setup of nanoparticle-based memristive devices in cross-sectional view, including approximate dimensions of the characteristic features. For a detailed assessment of memristive action of single nanoparticles, single stack SiO_2/NP/SiO_2 devices (with and without an additional Cr wetting layer) are characterized by C-AFM. The transition towards multi-stack arrangements allowed for reliable contacting of nanoparticle-based memristive devices with macroscopic electrodes.

ions on the nanoscale, even in macroscopic memristive devices[19]. As such, recently there is a high interest to progress from planar electrodes towards nanoscale or nanostructured electrodes. In this context, inert Pt nanoparticles dispersed in SiO_2 matrix are discussed as efficient means to predefine switching channels and locally increase electrical fields and resistive switching is reported in networks of Au nanoparticles[20,21]. For an optimization of switching uniformity in ECM memristive devices, nanostructured electrodes (e.g. nanocones) have been successfully prepared and quantum-dot electrodes have been applied for well-defined local field enhancement at the nanoscale[22–25]. Instead of nanostructured bulk electrodes, also nanoparticles as reservoirs for the mobile metallic species are under investigation, e.g., Ag nanoparticles embedded in dielectric matrices such as a-Si, SiO_2, TiO_2, HfO_2 or MgO[15,18,26,27]. This transition towards nanoparticles for mediating memristive switching is a consequent step as it combines the advantages of local enhancement of the electrical field by the nanoparticles in the dielectric matrix and the pre-definition of the location of memristive switching.

In this work, we substantially extend the concept of nanoparticle-based memristive switching by using gas phase synthesis of alloy nanoparticles and sequential deposition to prepare nanoparticles with controlled size, composition and coverage and embed them into a SiO_2 matrix in a controlled manner. Compared to earlier studies in this field, in which nanoparticles were mainly formed by self-organization in a co-deposition process, the gas phase synthesis approach offers the capability to independently vary filling factor and size of the nanoparticles. Moreover, the application of alloy nanoparticles instead of pure Ag NPs allows controlling filament formation by limiting the amount of mobile silver species while simultaneously the nobler alloy component may act as a stable anchor in the matrix for enhanced reliability.

This work is devoted to the investigation of memristive switching at the level of individual alloy nanoparticles, which are embedded in a dielectric SiO_2 matrix. In such nanoscale arrangements, the thorough experimental assessment of memristive switching renders rather challenging. Although there are a variety of reports on observations of filament formation by *in situ* TEM[28], the high demands on sample preparation as well as the resulting severe changes in sample surface and the considerable effect of electron beam irradiation on the electrical properties of dielectric matrices impose certain restrictions to such TEM methods in the context of memristive devices[29]. In this work, we apply a facile, non-invasive nanoscale method to study the memristive action at the level of individual nanoparticles and visualize *in situ* any possible structural degradation. In this method we utilize a conducting atomic force microscope (C-AFM) operated in a mixed feedback loop to measure the nanoscale current-voltage (IV) characteristics of nanoparticle-based memristive devices against both structural and geometrical variations. By using a sharp PtIr tip (of radius 2 nm) as scanning electrode, the C-AFM method proved to be advantageous to test the local properties of nanoparticle-based memristive devices as it allows to perform measurements on only one nanoparticle at a time. To ensure this possibility, the contact force between the tip and the sample must be kept below 1.2 nN during electrical measurements to yield contact area of roughly 7 nm^2 [30]. Furthermore we report on the scalability of the nanoparticle-based approach towards multilayer nanocomposites and investigate limiting factors for device stability and reliability, such as the impact of adding an additional Cr contact layer.

In the following sections, we first (section 2.1) discuss nanoscale memristive switching with diffusive switching characteristics as observed utilizing C-AFM method at the level of individual noble metal alloy nanoparticles. Moreover, to achieve robust memristive action, devices must be subjected to a stress test in order to find the conditions under which failure occurs. Interestingly, C-AFM offers the possibility to monitor *in situ* signatures of plastic deformation and the subsequent device failure, which will be studied in terms of device stability and degradation against prolonged operations especially for devices with a Cr wetting layer in section 2.2. Finally, in section 2.3 the feasibility of expanding the concept of nanoparticle-based memristive devices to multi-stack nanocomposites will be covered and we will show that the transition towards multi-stack nanocomposites is a versatile approach to design robust memristive devices while preserving the diffusive switching characteristics of individual nanoparticles.

Results and Discussion

In this work we investigate memristive switching relying on nanoparticle assemblies, which consist of noble metal alloy nanoparticles sandwiched between dielectric layers. The typical setup of individual SiO_2/NP/SiO_2 stacks as well as multi-stack nanoparticle-based devices is depicted schematically in Fig. 1.

As essential components, two types of noble metal alloy nanoparticles were investigated in the context of nanoparticle-based memristive switching, namely AgPt and AgAu nanoparticles. In both cases, the alloy

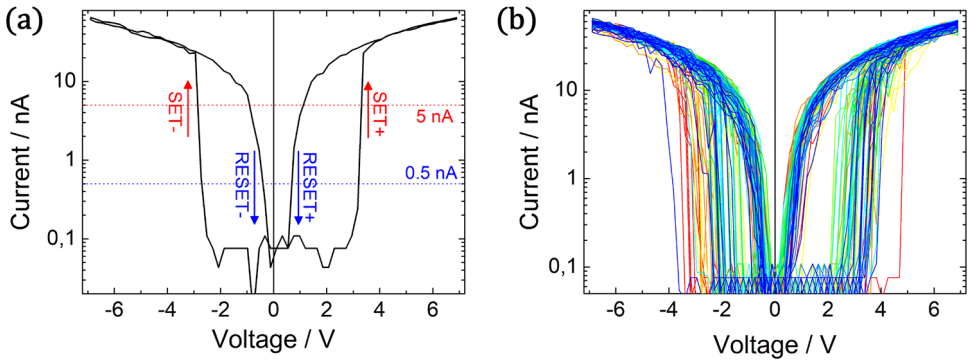

Figure 2. Diffusive memristive switching is observed by AFM measurements on an individual AgPt nanoparticle using a conductive tip. In a single hysteresis loop (**a**) the device shows a SET (switching towards LRS) and RESET (switching towards HRS) event for both, positive and negative polarity. For the reliable determination of the respective switching voltages, the current threshold of 5 nA is selected for a SET and 0.5 nA for a RESET. The comparison of 70 consecutive hysteresis loops (**b**) implies a certain distribution of the respective switching voltages. The individual hysteresis cycles are colour coded (first cycles: red colour, last cycles: blue colour).

nanoparticles exhibit a narrow size distribution with the mean diameter being roughly 11 nm (in case of AgAu) or 9 nm (in case of AgPt). TEM bright field micrographs of the respective AgAu and AgPt NPs are depicted in Fig. S1 in the supplementary data. The composition of the respective nanoparticles was determined by XPS (as depicted in Fig. S2 in the supplementary data) and the quantification yields a mole fraction of Ag of roughly 0.33 in case of AgAu nanoparticles and 0.73 in case of AgPt nanoparticles. More detailed investigations on AgAu nanoparticles deposited by an identical approach are shown in previous work[31].

Single nanoparticles for diffusive memristive switching. Based on the aforementioned alloy nanoparticles, single SiO_2/NP/SiO_2 stacks were prepared and the electrical characteristics were recorded by C-AFM technique at the location of individual nanoparticles. The following discussion is devoted to the memristive switching properties of AgPt NPs in a SiO_2/AgPt NP/SiO_2 stack (nominal thickness of bottom and top oxide layer is 8 nm and 2 nm respectively), which is chosen as an example to illustrate the diffusive memristive switching behaviour observed in alloy NPs. The IV characteristics of this device are depicted in Fig. 2. A representative hysteresis loop of a full switching cycle is depicted in Fig. 2(a). Continuous measurements of 70 consecutive switching cycles are shown in Fig. 2(b).

The IV characteristics as depicted in Fig. 2(a) exhibit diffusive memristive switching (also termed threshold switching), thus for both polarities there is a transition from HRS to LRS (SET) and from LRS to HRS (RESET) and upon zero crossing, the device always is in its HRS. The full hysteresis loop of such nanoparticle-based memristive device can be described as follows:

In the initial state without bias, the nanoparticle device is in its HRS, which results in a current in the order of 100 pA, corresponding to the limit of detection. Upon increasing the voltage to a certain threshold, the device switches to its LRS and the IV curve is mainly dominated by the serial resistance of 101 MΩ (applied in order to limit the current through the C-AFM tip). When the applied voltage is subsequently reduced, the LRS is preserved until reaching a certain threshold voltage at which the device switches back into its HRS. A similar diffusive switching cycle with transitions from HRS to LRS and vice versa is observed at reversed polarity. In the following evaluation of the statistics of multiple cycles of diffusive memristive switching, the corresponding switching voltages are referred to as "SET+" and "RESET+" or "SET−" and "RESET−" for positive and negative polarity respectively.

In contrast to the diffusive memristive switching observed in individual alloy nanoparticles, the IV characteristics recorded on a pure SiO_2 layer exhibits no indication for any switching event (cf. Fig. S6).

The origin of this diffusive memristive switching is expected to be related to the mechanism of electrochemical metallization (ECM)[32]. In the presence of an electrical field silver cations are released from their reservoir (in this case the individual nanoparticle), are transported through the SiO_2 matrix and form a metallic filament upon being reduced. Due to the nanoscopic thickness of dielectric layer, even the limited amount of mobile silver species released from a single nanoparticle allows for the formation of a metallic filament, describing the transition from HRS to LRS above a certain threshold voltage.

For a thorough explanation of the RESET step, two aspects have to be considered. On the one hand, in case the nanoparticle-based device is in its LRS, a conductive filament is formed across the device and the potential drop is mainly over the serial resistor, which is applied to limit the current in the C-AFM measurement (cf. Fig. S9). The current flow through the metallic nanoparticle-based connection results in Joule heating and electromigration, which is typically associated with a RESET due to rupture of the metallic filament. On the other hand, the incorporation of alloy nanoparticles instead of bulk electrodes limits the amount of available silver species. Consequently, in our nanoparticle-based memristive devices the filament cannot grow to the full extent and is inherently unstable, which results in diffusive memristive switching. This is in contrast to conventional ECM

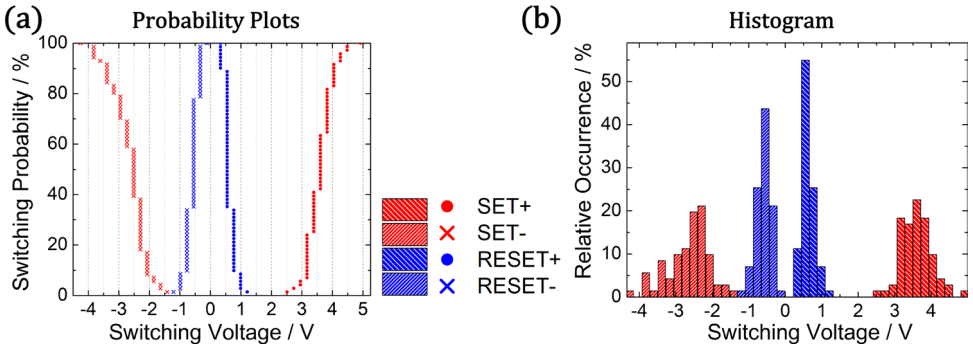

Figure 3. Statistical evaluation of the switching voltages obtained from 70 consecutive hysteresis loops measured for a SiO_2/AgPt NP/SiO_2 stack. The probability plot (**a**) and histogram (**b**) shows a general trend of higher SET voltages for positive polarity.

devices relying on bulk electrodes, which offer an (almost) unlimited reservoir of mobile silver species and typically exhibit stable bipolar memristive switching.

Recently, Wang *et al.* reported a significant dependency of the filament lifetime on the diameter of the metallic filament, which is mainly motivated by the disintegration of a thin filament due to surface diffusion[33]. Similarly, our nanoparticle-based device can be put into the context of these considerations on filament lifetime by using the following assumptions: In case of a AgPt nanoparticle with a mole fraction of silver of roughly 0.73 and a diameter of 9 nm and a dielectric thickness of 8 nm would result in a filament diameter (under the assumption of a cylindrical filament) of less than 2.3 nm, which would result at zero bias, following the argumentation of Wang *et al.*[33], in a filament lifetime of less than some tens of microseconds. Realistically, due to entropic considerations (entropy of mixing) it is unlikely that the whole amount of silver would be released from the respective nanoparticle and it is expected that the filament does not form in a perfectly cylindrical shape with constant diameter. Accordingly, the diameter and consequently the lifetime of the real filament are expected to be even lower, which immediately explains the observed diffusive switching and the instability of the LRS in the low voltage regime.

The IV characteristics were recorded at the location of an individual nanoparticle for 70 consecutive hysteresis cycles and are depicted in Fig. 2(b). In general, diffusive memristive switching is observed for each cycle and the respective switching voltages for the SET and RESET switching are distributed over a certain range. For a proper evaluation of the statistical distribution of switching voltages, the SET and RESET voltages are defined as the voltage at which the current raises above 5 nA or falls below 0.5 nA respectively. Based on these evaluation criteria, the switching voltages are extracted from the 70 hysteresis loops and are depicted by means of a cumulative switching probability plot (a) and a histogram (b) in Fig. 3.

In general, the SET+ voltage (3.60 ± 0.42 V) is shifted to higher voltages and exhibits a narrower distribution compared to the corresponding SET− process at opposite polarity (-2.65 ± 0.57 V). The observation of a higher SET+ voltage is in line with the expectation based on the asymmetry of the SiO_2 separation layers (8 nm and 2 nm as bottom and top layer respectively). The histogram of the distribution of switching voltages implies that there is a clear separation between the SET and RESET voltages, especially at positive polarity. Within this operation window, both resistance states (LRS and HRS) are stable and the presence of a particular state depends on the history of applied voltage. Considering an interval of three standard deviations (1.26 V for SET+ and 0.54 V for RESET+) around the mean values (3.60 V and 0.62 V respectively), the corresponding operation window exhibits a width of 1.18 V with 99.7% confidence (under the assumption of a Gaussian distribution of the respective switching voltages).

Essentially, memristive switching on the basis of individual alloy nanoparticles was observed to be stable and reproducible switching behaviour was detected for many consecutive cycles by C-AFM method. For illustration, the switching voltages (as extracted from the individual hysteresis measurements) corresponding to 2000 consecutive cycles of a representative measurement on the SiO_2/AgPt/SiO_2 stack are depicted in Fig. 4. In general, the switching voltages are found to be statistically distributed as described in detail for 70 cycles in Fig. 3. In addition, for a small number of cycles (e.g. around cycle 1100), no memristive switching was observed and the detected switching voltages consequently turn out to be very low. A representative IV hysteresis loop for a cycle without distinct switching events is shown in Fig. S10. These occasional deviations in memristive behaviour may be attributed to the limitations of the C-AFM measurement, which is operated at ambient atmosphere and temperature. However, more importantly, no time-dependent, systematic drift of the switching voltages is observed, which indicates the high stability of memristive switching based on individual noble metal alloy nanoparticles.

Considering the insights gained by C-AFM measurements, nanoparticle-based memristive switching appears highly promising in the context of designing memristive devices with diffusive switching characteristics. For this purpose, two main design routes will be explored in the next sections, namely (1) the incorporation of a Cr wetting layer for a better conformity of the dielectric layer and (2) the transition towards multiple stacks of nanoparticles allowing for additional degrees of freedom for tailoring the switching parameters.

Long-term stability of nanoparticle-based memristive switching in the presence of a Cr wetting layer. In thin film technology, transition metals such as Cr or Ti are widely applied to enhance the adhesion between different materials like SiO_2 and Pt. In order to investigate the impact of the addition of a Cr layer on

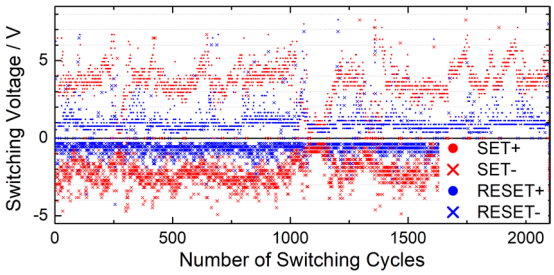

Figure 4. Overview over the switching voltages as extracted from individual hysteresis loops for 2000 switching cycles in a SiO_2/AgPt/SiO_2 stack, measured by C-AFM on an individual AgPt nanoparticle. While occasionally variations in the switching voltages occur due to limitations of the AFM setup (room temperature, ambient air), no systematic drift is observed.

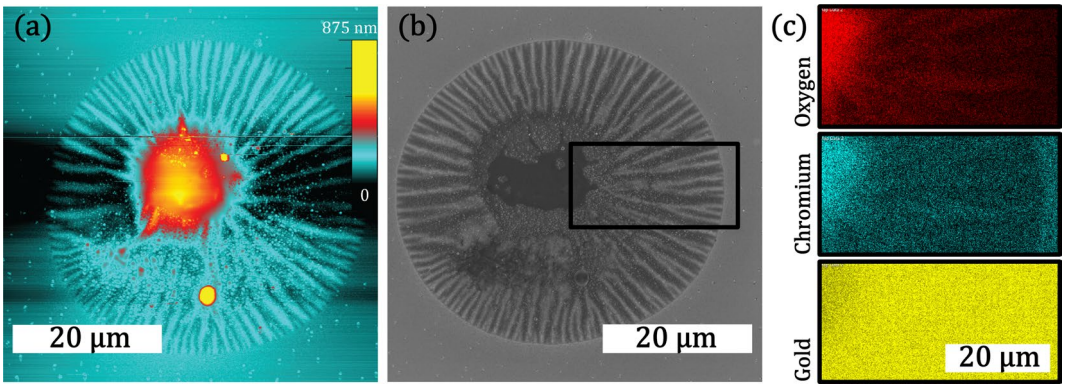

Figure 5. Morphological alterations of the thin film surface on the micrometre scale are induced by the migration of chromium during a two-day continuous IV-hysteresis measurement: The AFM topography map (**a**) as well as the corresponding SEM top view micrograph (**b**) indicate severe changes of the thin film morphology on a circular area with a diameter of roughly 40 µm. The migration and oxidation of Cr is revealed as the origin of these structural changes by SEM EDX spectroscopy maps (**c**) of a selected area (black rectangle).

the electrical properties, a Cr/SiO_2/AgPt/SiO_2 thin film stack with SiO_2 separation layer thickness of 2 nm was characterized by C-AFM. Over the whole measurement period of two days, IV hysteresis loops were recorded continuously and exhibited qualitatively similar behaviour (cf. Fig. S3 in supplementary data for a comparison of hysteresis loops recorded within the first hour and after two days).

While the electrical characteristics are preserved, severe morphological alterations of the nanoparticle thin film are observed. Initially, the surface is smooth and does not exhibit significant irregularities regarding roughness and topography. After the two-day measurement, a severe structural deformation is observed (Fig. 5), ranging with a radius in the order of 20 µm around the location of the tip. Within this area there are two dominating features: A dome-like elevation is located at the centre (red and yellow colour, diameter of roughly 20 µm) and radially surrounded by fluctuating height distributions (diameter of roughly 40 µm). Considering the nanoscopic size of the AFM tip, such morphological modifications on the microscale are particularly surprising.

In order to uncover the origin of these morphological changes, SEM and SEM EDX were applied to image and characterize the respective region. The overall appearance of the structural deformation as observed in AFM topography map is well reproduced in the SEM top view micrograph (Fig. 5(b)). A selected rectangular region, containing the dome-like structure (left) as well as the radial fluctuations (middle) and an undisturbed region (right) was investigated by SEM EDX. The occurrence of the elements oxygen, chromium and gold is depicted in terms of elemental maps in Fig. 5(c) (high colour saturation corresponds to high signal). While the dome-like structure shows strong signal corresponding to Cr and O and considerable signal corresponding to Au, the undisturbed region contains Cr and Au, but considerably less O. The presence of signal corresponding to Au is attributed to the conducting thin film stack on the substrate, which mainly consist of Au. Within the intermediate region, the stripe-like features correlate to a radial depletion of Cr. Within this region, the strong Cr and O signals overlap. Judging from the results of SEM EDX investigations, the morphological changes are attributed to the migration and oxidation of Cr, which is brought to the surface of the Cr/SiO_2/AgPt/SiO_2 thin film stack in the form of chromium oxide and results in the dome-like feature as well as the radial height fluctuations.

Notably, these morphological alterations evolve over time. While in the early stages (e.g. after one hour of continuous IV hysteresis measurement) already first indications of dome-like features are present (see AFM topography map in Fig. S3(a) in supplementary data), the radial features are growing at later stages. Alongside a steady change in the morphology, the electrical characteristics are qualitatively preserved over the whole measurement

period of two days (as shown in Fig. S3(b,c) in Supplementary Data). Representative consecutive hysteresis loops for two thin film stacks with either AgPt or AgAu nanoparticles are depicted in Fig. S4 in the supplementary data. In contrast to similar stacks without Cr wetting layer, in these devices no diffusive memristive switching is observed within the investigated voltage range. The respective hysteresis loops remind of a typical cyclic voltammetry measurement and exhibit a non-zero crossing (no pinched hysteresis) as well as several peaks corresponding to oxidation and reduction processes. Although qualitatively the overall shape of the IV hysteresis loop remains similar for consecutive cycles, changes in peak position and height of the individual peaks are strong indications for instabilities and can be related to a change in active area due to the reported morphological alterations.

In essence, at the example of long-term measurement induced migration of Cr, C-AFM has proven as an efficient method to monitor device stability and degradation during prolonged operations. Due to the detected instability, the wetting layer of Cr is not considered to be feasible for the development of multi-stack memristive devices as described in following section.

Memristive switching in multiple stacks of nanoparticles. The scalability of memristive switching devices is one key aspect concerning hardware implementation. The nanoscopic dimensions of the individual SiO_2/NP/SiO_2 layers (with the dielectric being only a few nanometres thick) make reliable contacting by conventional probes very challenging. Thus, we expand our investigation from single nanoparticles towards multi-stack devices, which consist of multiple stacks of nanoparticles embedded in a dielectric SiO_2 matrix. The transition from individual layers towards multiple stacks results in an increase in overall device layer thickness and consequently reduces the risk of short circuiting by pin holes or due to mechanical failure (pinching). The multi-stack samples discussed in this section comprised of 5 layers of individual AgAu and AgPt nanoparticles separated by thin SiO_2 layers in between. While in case of the AgAu NP multi-stack device the nominal layer thickness of the separating SiO_2 layers was selected to be 2 nm, the AgPt NPs were nominally separated by 4 nm of SiO_2. The different SiO_2 separation layer thickness was chosen due to the difference in the silver concentration in the respective nanoparticles. Accordingly, for the design of a multi-stack device relying on nanoparticles two general degrees of freedom open up: On the one hand the composition of the respective alloy nanoparticles and on the other hand the width of the dielectric separation layer, which is deposited in between the deposition of the individual nanoparticle layers, can be tailored.

For the electrical characterization of the multi-stack devices, the top contact was realized by a soft Pt wire (combined with a serial resistance of 1 MΩ, see method section). As the Pt wire has a diameter of 125 µm, the effective contact is expected to be significantly larger than in case of the C-AFM investigations on single nanoparticles. Thus, the contact area expands from individual nanoparticles (in case of C-AFM measurements) towards a larger nanoparticle assembly. However, as shown in Fig. 6, the corresponding multi-stack devices featuring AgAu **(a)** and AgPt **(b)** nanoparticles show similar diffusive memristive switching, which demonstrates that upon upscaling from single nanoparticles to a multi-stack device the fundamental switching characteristics are preserved. Interestingly, no distinct electroforming step at higher voltages is required to initialize memristive switching in the nanoparticle-based devices, which underlines their application potential. For both, the AgAu and AgPt nanoparticle-based device, the IV hysteresis loops exhibit reproducible diffusive memristive switching over multiple consecutive cycles with a narrow distribution of the SET and RESET voltages, which underlines the fact that macroscopic contact hosts large number of independent nanoscale memristive devices. A closer look at the distribution of the switching voltages (cf. histograms in Fig. 6) indicates for both devices a distinct separation between the SET and RESET, which results in a stable operation window. The main differences between the AgAu and AgPt multi-stack device are found in the HRS resistance and the magnitude of the switching voltages.

While the AgAu device exhibits a HRS resistance in the order of 70 MΩ, a much higher resistance is observed for the AgPt device (current in HRS is below limit of reliable detection). This difference can be attributed to the SiO_2 separation layer thickness, which is 2 nm in case of the AgAu device and 4 nm in case of the AgPt device.

While the switching voltages observed for the AgAu device are around 0.89 ± 0.06 V (SET) and 0.23 ± 0.03 V (RESET), the AgPt device exhibits a lower SET voltage around 0.61 ± 0.03 V and a higher RESET voltage around 0.32 ± 0.03 V. A comprehensive overview over the evaluated switching voltages is given in Table S1 in the supplementary data. Considering the higher SiO_2 separation layer thickness in case of the AgPt device, the observed trend in the SET voltage at first glance seems rather counterintuitive, as the higher separation width is expected to result in a lower electrical field at identical applied voltage. However, the availability of Ag in case of AgPt nanoparticles (with Ag mole fraction of roughly 0.8) is much higher than in the AgAu device (with Ag mole fraction of roughly 0.3). Accordingly, the higher availability of silver species facilitates the filament formation (and as such the SET process).

In a similar approach, Wang *et al*. recently reported diffusive memristive switching in MgO_x:Ag, SiO_xN_y:Ag and HfO_x:Ag thin films, which were fabricated by co-sputtering in reactive atmosphere, and attributed the instability of the LRS to the coalescence of individual nanoparticles due to a minimization in surface energy[15]. The diffusive memristive switching characteristics of the multi-stack devices are very well competitive to these devices, especially with respect to the distribution of switching voltages as well as the operation window and switching stability. Unlike the multi-stack nanoparticle-based memristive devices, diffusive memristive devices prepared by Wang *et al*. incorporate Ag as mobile species in pure Ag nanoparticles, which are most likely formed by self-organization during co-sputtering. Following the concept of multi-stack nanoparticle-based memristive devices as reported in this work, the individual alloy nanoparticles as building blocks are already fully formed in the gas phase with a well-defined composition and size synthesis and are subsequently embedded into the dielectric, which grants multiple degrees of freedom (e.g. tailored filling factor and alloy composition) in the design of memristive devices.

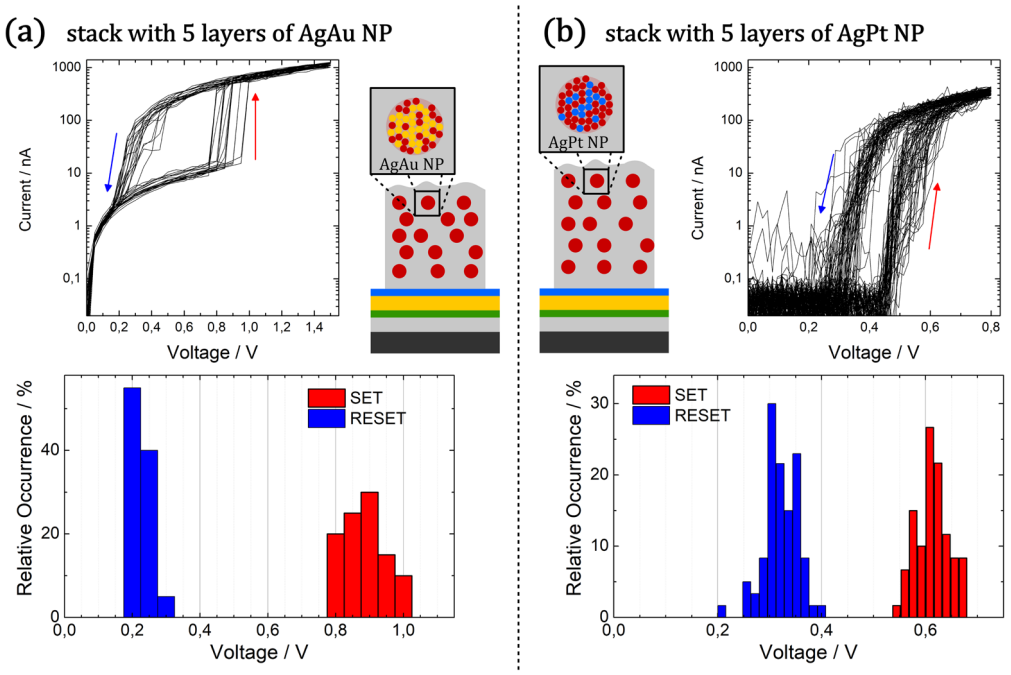

Figure 6. Multi-stack nanoparticle-based memristive devices relying on AgAu (left) and AgPt (right) nanoparticles exhibit diffusive memristive switching characteristics. (**a**) The switching characteristics are depicted for 20 consecutive cycles (top) of an AgAu nanoparticle device with 2 nm SiO_2 separation layers. The corresponding histogram (bottom) shows a narrow distribution of SET (around 0.89 V) and RESET (around 0.23 V) voltages with a clear separation in between. (**b**) For a AgPt nanoparticle-based multi-stack device with SiO_2 separation layers of 4 nm each, the switching characteristics are depicted for 60 consecutive cycles (top) and the corresponding histogram (bottom) shows a narrow distribution of SET (around 0.61 V) and RESET (around 0.32 V) voltages with a clear separation in between.

Conclusion

In this work nanoscale memristive switching is examined in memristive thin film devices, which rely on noble metal alloy nanoparticles of the system AgAu or AgPt that are embedded in a SiO_2 dielectric matrix. Applying C-AFM as a non-invasive method and making use of the nanoscopic contact area of the tip, we studied the electrical characteristics at the level of individual nanoparticles and observed reliable memristive switching for several hours of continuous operations. In these nanoscale junctions, reliable diffusive memristive switching with a reasonably narrow distribution of SET and RESET voltages and clear operation window in between has been found. The observation of diffusive memristive switching implies that the formation of stable filaments and bipolar switching characteristics is efficiently suppressed by limiting the reservoir of potentially mobile silver species to the alloy nanoparticles. Besides the nanoscale electrical characterization, the method of C-AFM allows to monitor long term operation induced morphological alterations and device failure *in situ*, which is demonstrated at the example of nanoparticle-based devices with an additional Cr wetting layer. Herein, during continuous IV hysteresis measurement over a time period of two days, severe morphological alterations on the microscale originating from the migration and oxidation of Cr were detected by the C-AFM method.

In addition to the investigations on memristive action in individual alloy nanoparticles, the concept of nanoparticle-based memristive switching was extended to nanocomposites featuring assemblies of multiple stacks of nanoparticles. Notably, the diffusive memristive properties were found to be preserved in such multi-stack devices and the respective switching voltages exhibit a narrow distribution and a clear operation window. Accordingly, the underlying concept of embedding alloy nanoparticles as reservoirs for mobile metal cations in a dielectric matrix possesses a high versatility, which makes it highly promising for the future design of forming-free memristive switches with tailored diffusive switching properties.

Methods

Deposition of nanoparticle-based memristive devices. The memristive devices consist of noble metal nanoparticles embedded into a dielectric SiO_2 matrix. For the C-AFM investigations, a single layer of nanoparticles was deposited in between SiO_2 layers (as schematically shown in Fig. 7(a)). In addition, stacks consisting of 5 layers of noble metal alloy nanoparticles separated by SiO_2 were fabricated by consecutively depositing every layer (as schematically shown in Fig. 7(b) without breaking the vacuum. As substrates, phosphor doped, (100) oriented Si wafer pieces with native oxide ($1 \times 1\,cm^2$, SiMat) were used. In order to achieve a smooth common back electrode, the substrates were coated with a stack of Cr, Au and Pt by magnetron sputtering (CS730S, Von Ardenne GmbH) from metallic Cr, Au and Pt targets respectively.

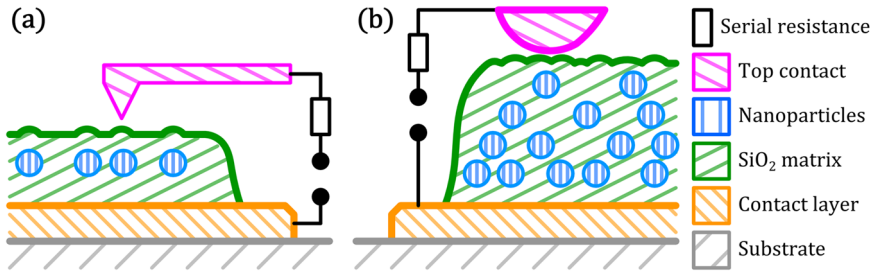

Figure 7. Schematic cross section of nanoparticle-based memristive devices for testing with C-AFM (**a**) or in a conventional two-probe setup (**b**). The nanoparticles (blue) are embedded in a dielectric matrix (SiO_2, green), which is deposited on a metal contact layer (Au or Au/Cr, orange). The AFM tip (magenta) locally contacts individual nanoparticle switches, while macroscopic contacts such as a PtRh wire exhibit a significantly larger contact area.

The fabrication of nanoparticle-based memristive devices was realized by physical vapour deposition (PVD) processes in a custom-build high vacuum (HV) deposition system. HV conditions were accomplished by using a turbo molecular pump (Pfeiffer Vacuum, TMU 262) combined with a dry scroll pump (Agilent Technologies, SH-110).

For the gas phase synthesis of noble metal nanoparticles, unipolar DC magnetron sputtering using an in-house Haberland type gas Aggregation Source (GAS)[34] was applied. The GAS was separated from the main chamber by an orifice of 2 mm diameter at a distance of 90 mm from substrate position. The respective AgAu or AgPt target was attached to a DC planar magnetron source (Thin Film Consulting, ION'X-2UHV) inside the GAS. For the deposition of noble metal alloy AgAu and AgPt nanoparticles, a segmented target approach was employed[31]. The corresponding targets consist of Ag targets (Kurt J. Lesker, 99.99%, 5 cm diameter) with Au (Alfa Aesar, 1.0 mm dia, 99.95%) or Pt (Alfa Aesar, 1.0 mm dia, 99.95%) wires embedded in the racetrack. A flow of Ar (purity 99.999%) as process gas was regulated by gas regulating valve (Pfeiffer, EVR116 with attached hot ion cathode IMR 285) at the gas inlet of the GAS. DC power of 40 W was supplied by power source (Advanced Energy, MDX 500).

The dielectric SiO_2 matrix was deposited by pulsed DC reactive magnetron sputtering either directly on the Pt surface of the substrate or on an intermediate Cr wetting layer. The Cr layer was deposited from a Cr target (Alfa Aesar, 99.95%, 2 inch diameter), attached to a magnetron (Thin Film Consulting, ION'X-2UHV) by DC magnetron sputtering (Advanced Energy, MDX 500) for 120 s at 100 W in a pure Ar plasma, which corresponds to a layer thickness of roughly 20 nm. For the deposition of SiO_2, a Si target (Goodfellow GmbH, 99.999%, 2 inch diameter) was mounted onto a DC planar magnetron source (Thin Film Consulting, ION'X-2UHV) at a distance of 70 mm from substrate position. As a reactive gas, O_2 (purity 99.999%) was introduced into the main chamber through a mass flow controller (Alicat, H-MC-100SCCM-D/5 M). Pulsing of the DC power source (Advanced Energy, MDX 500) was realized by a high power MOSFET (Behlke Power Electronics, HTS 31 CF I), which was triggered by a frequency generator (PeakTech, DDS Function Generator 4025, rectangular 0–5 V signal, 80 kHz, 30% duty cycle).

Prior to every deposition process the chamber was evacuated to 10^{-4} Pa and cleaning of target and conditioning of deposition were performed for sufficient time to reach stable deposition conditions, but at least for 30 s. Subsequently the shutter was opened and deposition performed.

Electrical characterization of nanoparticle-based memristive devices. Electrical characterization of nanoparticle-based memristive switching was performed on the one hand by conductive atomic force microscopy (C-AFM) for the selective contacting of individual nanoparticles and on the other hand by a two-point measurement on a four-point probe station in case of the multi-stack devices.

C-AFM investigation was carried out using an AFM microscope (Dimension 3000, Bruker), which was modified to incorporate mixed feedback control as well as custom-made summing amplifier, resistor box and pulse generator for device initialization. The details of the measurements are described elsewhere[35]. Briefly, a topographic image was obtained using the conventional tapping mode technique, then the conducting AFM tip is positioned at the desired location before being lowered to contact the surface with a force of 1.2 nN. This force was kept constant during all measurements using a feedback system. A representative AFM topography map, clearly showing the sparse lateral distribution of nanoparticles, which is necessary for the contacting of individual nanoparticles, is provided in Fig. S5 in the supplementary data. The tip voltage was then ramped and the resulting current was detected using a fast preamplifier (Bruker C-AFM sensor). The shielded preamplifier's input was closely positioned (about 25 mm away) from the cantilever's contact to minimize noise in the low current measurements. The period of a typical IV cycle was typically 5 seconds with reading averaged 10 times at each point. To protect the thinly coated (20 nm thickness) PtIr AFM tip and the sample, especially during device initialization, the current was limited by a serial resistor (typically 1 GΩ or 101 MΩ). These settings proved to be non-invasive as we didn't detect any changes to the topography or tip after the initialization process. To condition devices a few pulses of duration 30 ms at bias $\leq$5 V were applied to initialize ionic conduction within the memristive matrix. Once the current is detected, the voltage is ramped initially at a reduced range from −2 to 2 V, then increased gradually to higher values to capture the full range of switching onsets. In all cases the sweeping window is kept

within ±7 V range with a maximum current of 70 nA. Most of the investigated devices have survived prolonged IV measurements when current is kept below 2 nA range, except those having Cr as a wetting layer.

The electrical characterization of the multi-stack nanoparticle devices was performed using a source meter (Keithley, 2400 Source Measure Unit) and a four-point probe station (Signatone, H150W). The common contact layer was contacted with a conventional tungsten tip (Signatone, SE-T) as a back electrode. In order to achieve a soft contact to the top of the memristive stack, a flexible PtRh wire (Alfa Aesar, 13 wt% Rh, 127 µm diameter) was used as a top contact. In analogy to the AFM setup, involving a serial resistance for all measurements, the PtRh wire was connected to a serial resistance in order to achieve comparable measurement conditions. The characterization by PtRh wire instead of conducting AFM tip allowed for higher currents, so that the serial resistance was chosen to be 1 MΩ. To measure the switching characteristics, DC voltage sweeps were applied with the top contact biased and the back electrode grounded. No current compliance was set by the source measure unit, as the serial resistance provides current limitation and suppresses overshoot effects. No electroforming steps at higher voltages were performed for measurements; instead memristive switching was initialized within the identical voltage range as applied for subsequently recorded IV hysteresis loops.

Further characterization techniques. For a detailed analysis of the long-term measurement induced morphological changes in nanoparticle based memristive devices with additional Cr wetting layer, scanning electron microscopy (SEM; Zeiss, Supra 55VP) was performed in top view configuration. Chemical information was recorded by energy dispersive X-ray analysis (Oxford Instruments, x-act) in connection with the aforementioned SEM studies. For comparison, topographical information was obtained by AFM. AFM was performed in tapping mode with a rectangular cantilever (spring constant, $k = 2$ N/m) and tetrahedral tip, oscillated at its resonance frequency of 85 kHz. Areas of measurements were 50×50 µm^2 and 3×3 µm^2. Scanning area was divided by 512 lines per image and 512 points per line.

X-ray photoelectron spectroscopy (XPS, Omicron Full lab, Omicron Nano-Technology GmbH, Al-anode, 240 W, EA125 hemispherical analyser with pass energy 100 eV) was applied in order to determine the stoichiometry of the alloy nanoparticles of the system AgAu and AgPt, which were deposited onto a Si wafer piece with native oxide. During XPS analysis, the base pressure in the main chamber was of the order of 10^{-7} Pa. The C-1s line of advantageous carbon at 285.0 eV was used to correct the charging in all recorded spectra respectively by using the software CasaXPS (version 2.3.16).

Transmission electron microscopy (TEM) analysis was conducted using a FEI Tecnai F30 STwin microscope (300 kV, field emission gun (FEG) cathode, spherical aberration coefficient $C_s = 1.2$ mm). Micrographs of AgAu and AgPt nanoparticles on carbon film copper TEM grids (Plano, S160-4) were recorded in bright field mode.

Data availability. The data generated and analysed in this study are shown in the present publication as well as the supplementary information and access to specific datasets is available from the corresponding author on reasonable request. This study was included in parts in the PhD thesis entitled "On the Development of Memsensors"[36].

Received: 21 June 2019; Accepted: 31 October 2019;
Published online: 22 November 2019

References

1. Strukov, D. B., Snider, G. S., Stewart, D. R. & Williams, R. S. The missing memristor found. *Nature* **453**, 80–3 (2008).
2. Chua, L. O. Memristor—The Missing Circuit Element. *IEEE Trans. Circuit Theory* **18**, 507–519 (1971).
3. Vongehr, S. & Meng, X. The Missing Memristor has Not been Found. *Sci. Rep.* **5**, 1–7 (2015).
4. Edwards, A. H. *et al.* Reconfigurable Memristive Device Technologies. *Proc. IEEE* **103**, 1004–1033 (2015).
5. Jeong, D. S. *et al.* Emerging memories: resistive switching mechanisms and current status. *Reports Prog. Phys.* **75**, 076502 (2012).
6. Sun, J., Fu, Y. & Wan, Q. Organic synaptic devices for neuromorphic systems. *J. Phys. D. Appl. Phys.* **51**, 314004 (2018).
7. Wang, Z. *et al.* Nanoionics-Enabled Memristive Devices: Strategies and Materials for Neuromorphic Applications. *Adv. Electron. Mater.* **3** (2017).
8. Zhu, L., Zhou, J., Guo, Z. & Sun, Z. An overview of materials issues in resistive random access memory. *J. Mater.* **1**, 285–295 (2015).
9. Linn, E., Rosezin, R., Tappertzhofen, S., Böttger, U. & Waser, R. Beyond von Neumann—logic operations in passive crossbar arrays alongside memory operations. *Nanotechnology* **23**, 305205 (2012).
10. Ielmini, D. Brain-inspired computing with resistive switching memory (RRAM): Devices, synapses and neural networks. *Microelectron. Eng.* **190**, 44–53 (2018).
11. Hong, X. L. *et al.* Oxide-based RRAM materials for neuromorphic computing. *J. Mater. Sci.* **53**, 8720–8746 (2018).
12. Wang, Z., Xia, Q., Yang, J. J., Midya, R. & Li, Y. Review of memristor devices in neuromorphic computing: materials sciences and device challenges. *J. Phys. D. Appl. Phys.* **51**, 503002 (2018).
13. Zhao, Y. & Jiang, J. Recent Progress on Neuromorphic Synapse Electronics: From Emerging Materials, Devices, to Neural Networks. *J. Nanosci. Nanotechnol.* **18**, 8003–8015 (2018).
14. Kim, S. Y. S. G., Han, J. S., Kim, H., Kim, S. Y. S. G. & Jang, H. W. Recent Advances in Memristive Materials for Artificial Synapses. *Adv. Mater. Technol.* **3**, 1–30 (2018).
15. Wang, Z. *et al.* Memristors with diffusive dynamics as synaptic emulators for neuromorphic computing. *Nat. Mater.* **16**, 101–108 (2017).
16. Valov, I. Electrochemical Metallization Memories. In *Memristive Phenomena - From Fundamental Physics to Neuromorphic Computing* (eds Waser, R. & Wuttig, M.) 677–699 (Forschungszentrum Jülich GmbH, 2016).
17. Yoo, J., Woo, J., Song, J. & Hwang, H. Threshold switching behavior of Ag-Si based selector device and hydrogen doping effect on its characteristics. *AIP Adv.* **5**, 127221 (2015).
18. Jiang, H. *et al.* A novel true random number generator based on a stochastic diffusive memristor. *Nat. Commun.* **8**, 882 (2017).
19. Zhu, X., Lee, S. H. & Lu, W. D. Nanoionic Resistive-Switching Devices. *Adv. Electron. Mater.* **1900184**, 1900184 (2019).
20. Minnai, C., Bellacicca, A., Brown, S. A. & Milani, P. Facile fabrication of complex networks of memristive devices. 1–8, https://doi.org/10.1038/s41598-017-08244-y (2017).
21. Choi, B. J. *et al.* Electrical performance and scalability of Pt dispersed SiO_2 nanometallic resistance switch. *Nano Lett.* **13**, 3213–3217 (2013).

22. Kim, S. G. *et al*. Fabrication of a Cu-Cone-Shaped Cation Source Inserted Conductive Bridge Random Access Memory and Its Improved Switching Reliability. *Adv. Funct. Mater.* **1806278**, 1806278 (2019).
23. You, B. K. *et al*. Reliable Memristive Switching Memory Devices Enabled by Densely Packed Silver Nanocone Arrays as Electric-Field Concentrators. *ACS Nano* **10**, 9478–9488 (2016).
24. Yan, X. *et al*. Graphene Oxide Quantum Dots Based Memristors with Progressive Conduction Tuning for Artificial Synaptic Learning. *Adv. Funct. Mater.* **28**, 1803728 (2018).
25. Yan, X. *et al*. Self-Assembled Networked PbS Distribution Quantum Dots for Resistive Switching and Artificial Synapse Performance Boost of Memristors. *Adv. Mater.* **31**, 1805284 (2019).
26. Jo, S. H. *et al*. Nanoscale memristor device as synapse in neuromorphic systems. *Nano Lett.* **10**, 1297–301 (2010).
27. Yan, X. *et al*. Memristor with Ag-Cluster-Doped TiO2 Films as Artificial Synapse for Neuroinspired Computing. *Adv. Funct. Mater.* **28**, 1705320 (2018).
28. Yang, Y. & Huang, R. Probing memristive switching in nanoionic devices. *Nat. Electron.* **1**, 274–287 (2018).
29. Neelisetty, K. K. *et al*. Electron Beam Effects on Oxide Thin Films—Structure and Electrical Property Correlations. *Microsc. Microanal.*, 1–9, https://doi.org/10.1017/S1431927619000175 (2019).
30. Hassan, M. H., Alkordi, M. H. & Hassanien, A. Probing the conductivity of metal-organic framework-graphene nanocomposite. *Mater. Lett.* **246**, 13–16 (2019).
31. Vahl, A. *et al*. Single target sputter deposition of alloy nanoparticles with adjustable composition via a gas aggregation cluster source. *Nanotechnology* **28**, 175703 (2017).
32. Valov, I., Waser, R., Jameson, J. R. & Kozicki, M. N. Electrochemical metallization memories - Fundamentals, applications, prospects. *Nanotechnology* **22**, 289502 (2011).
33. Wang, W. *et al*. Surface diffusion-limited lifetime of silver and copper nanofilaments in resistive switching devices. *Nat. Commun.* **10**, 81 (2019).
34. Haberland, H., Karrais, M., Mall, M. & Thurner, Y. Thin films from energetic cluster impact: A feasibility study. *J. Vac. Sci. Technol. A Vacuum, Surfaces, Film.* **10**, 3266–3271 (1992).
35. Znidarsic, A. *et al*. Spatially Resolved Transport Properties of Pristine and Doped Single-Walled Carbon Nanotube Networks. *J. Phys. Chem. C* **117**, 13324–13330 (2013).
36. Vahl, A. On the Development of Memsensors, https://macau.uni-kiel.de/receive/dissertation_diss_00025980 (PhD Thesis, CAU Kiel, 2019).

Acknowledgements

This work was financially supported by the German Research Foundation (DFG) via the coordinated effort FOR2093 "Memristive Devices for Neuronal Systems" through project A2. A.H would like to acknowledge the financial support by the Slovenian Research Agency (ARRS) under Program No. P1-0099 and support for his research stays in Kiel by FOR2093. The authors would like to thank Stefan Rehders for technical assistance in the context of designing and operating the PVD setup, Anne Kittmann for the preparation of the conductive Cr-Au-Pt thin film stack on the substrates and Julian Strobel as well as Prof. Dr. Lorenz Kienle for performing all TEM-related studies. We acknowledge the *CENN Nanocenter* for the use of AFM. This study was included in parts in the PhD thesis entitled "On the Development of Memsensors" by A.V.

Author contributions

F.F., A.H., T.S. and A.V. developed the idea and initial design of the study. A.V. and N.C. prepared the nanoparticle-based devices by establishing a suitable PVD setup and performing the respective depositions. The C-AFM method was tailored by A.H. in order to fulfil the special requirements for investigating memristive switching on the level of individual nanoparticles and all AFM-related studies in the context of this work were carried out by A.H. N.C. and A.V. characterized the electrical response of multi-stack memristive devices. A.V. performed the SEM, EDX and XPS measurements. N.C., A.H. and A.V. evaluated the memristive switching behaviour of nanoparticle-based devices and composed the manuscript. F.F. supervised the work of A.V. and N.C. All authors discussed the experimental results and contributed to the manuscript.

Competing interests

The authors declare no competing interests.

Additional information

Supplementary information is available for this paper at https://doi.org/10.1038/s41598-019-53720-2.

Correspondence and requests for materials should be addressed to F.F. or A.H.

Reprints and permissions information is available at www.nature.com/reprints.

Publisher's note Springer Nature remains neutral with regard to jurisdictional claims in published maps and institutional affiliations.

7. Memsensor Concepts based on Diffusive Memristive Devices

This chapter contains unpublished results.

Introduction

Biological neuronal systems permanently adapt to their environment. Consequently, changes in synaptic information transmission efficiency are effectively the result from an always ongoing influx of sensory stimuli (like visible light, acoustic waves, pressure on skin, etc.) [150, 151]. Similarly, the question how to interface data processing and storage units effectively with the acquisition of environmental input is of equal interest for neuromorphic systems. A promising approach is the development of memsensors, which embody two-terminal circuit elements that combine both memristive and sensitive properties, i.e. they are expected to combine capabilities for information acquisition, storage and processing in single devices [152]. In this context, different concepts have been reported, that aim to integrate sensors and memristors [153, 154]. For example, an architecture was proposed based on UV-sensitive In_2O_3-wires combined with bipolar switching in Al_2O_3-films, to realize an artificial visual memory [155]. Another example includes a piezoelectric material, that transduces haptic inputs into electrical signals, which are fed into a memristive system [156]. It this chapter, two approaches for the design of memsensitive systems are discussed. The approaches in this chapter were motivated by a work from Vahl *et al.*, where memsensor concepts based on serial connections of memristive and sensitive elements were described[152]. Here, two device configurations were tested, based on combining NP-based diffusive switching devices (as discussed in Chapter 6) with wide-bandgap semiconductors (TiO_2 and ZnO), that incorporate sensitivity towards UV light into the memsensitive system. In other words, it is aimed that a UV-input modulates the diffusive switching response of the memristive system.

Results

First Memsensor Concept

A schematic depiction of the first tested memsensor concept is shown in Figure 7.1a. A diffusive memristive system consisting of AgPt-NPs embedded in SiO_xN_y was integrated on a TiO_2 surface (meaning that TiO_2 effectively acts as a backelectrode). The substrate material, a TiO_2 film deposited by reactive sputtering on a silicon wafer, was provided by Salih Veziroglu from the Chair for Multicomponent Materials in Kiel. The dynamics of this system was probed (in the same way as described for the multistack memristive devices in Chapter 6) by a soft-contact to the AgPt-NPs:SiO_xN_y composite with a PtRh-wire. The TiO_2 surface was contacted by a tungsten wire. A LED mounted to the electrical measurement setup allowed to measure the memristive dynamics under influence of topside UV illumination (having a peak wavelength of 365 nm, denoted as UV ON) and under dark conditions (UV OFF). Using such a measurement setup, the memsensitive system was probed over 64 voltage sweeps between -3.5 V and 3.5 V, under alternating UV ON and UV OFF conditions. Principal results from the characterization of this memsensitive system are shown in Figures 7.1b and c and described in the following. Generally, at negative voltages, no memristive activity was observed. However, a significant current was measured in the negative voltage regime, especially at UV ON conditions, even though memristive switching was absent. From this, it can be suggested that the negative voltage regime during this characterization was dominated by parasitic currents, which were able to flow through the memristive system, even though a LRS was not present. In contrast to that, the positive voltage regime was dominated by diffusive memristive behavior, however, with a rather low yield in terms of measurement cycles that exhibited a diffusive switching event. Diffusive switching in the AgPt-NP based system integrated on TiO_2 was observed in 34 % of all 64 cycles. A reference measurement of an equally fabricated memristive system, but integrated on a Au backelectrode (see Figure 7.1d) exhibited a higher yield of diffusive switching events of 90 % out of 32 cycles. It can be assumed based on this experiment, that using TiO_2 as a backelectrode decreases the yield of diffusive switching events among all measured cycles. This could be explained by the fact, that TiO_2 significantly restricts the electron transport through the whole circuit (i.e. it acts as a higher serial resistance compared to a metal like Au), which generally impedes the formation of filaments. Despite the observation, that the yield of diffusive switching events is decreased when TiO_2 is used as backelectrode, there are indications that the presence of UV illumination modulates the memristive activity. Firstly, under UV ON conditions, the chance for a diffusive switching event was slightly increased (41%) compared to UV OFF conditions (28 %). Typical cycles showing diffusive switching at UV ON conditions and absence of switching at UV OFF are given in Figure 7.1b. Secondly, the LRS of the memsensitive system was tendentially shifted to lower resistances at UV ON conditions, which can be recognized in the scatter plot of Figure 7.1c. This scatter plot depicts the superposition of all 64 measured cycles (black/purple are 32 cycles with UV OFF/ON). There it can be seen that in the positive voltage regime, a high density of (purple) data points indicating the

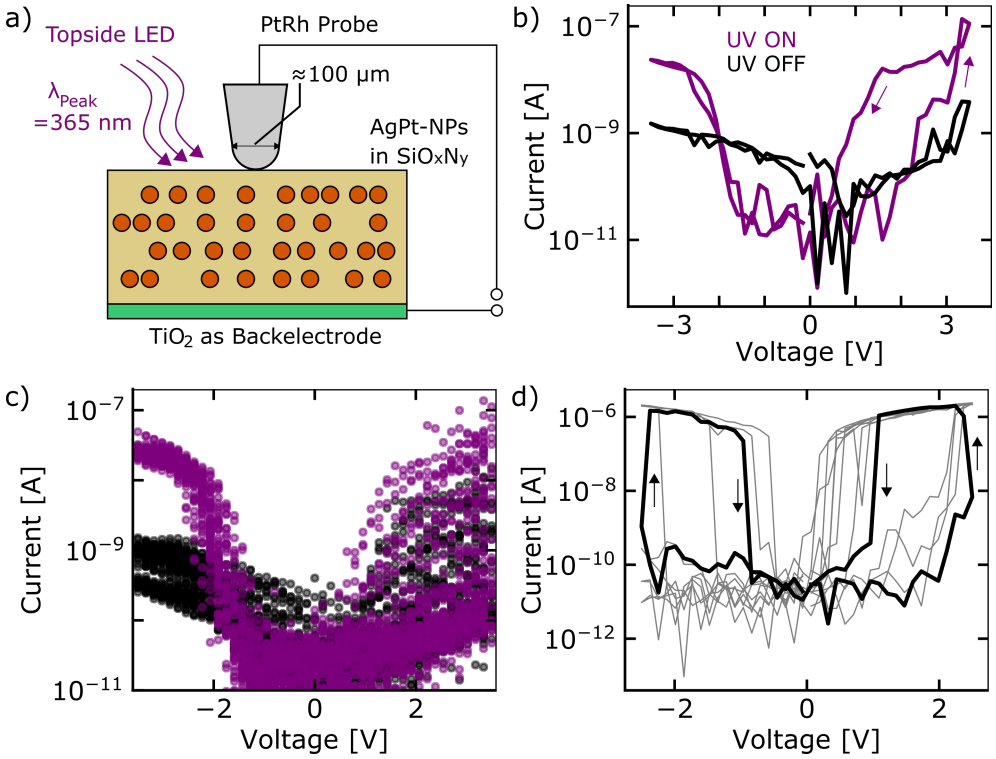

Figure 7.1: Memsensor concept based on integration of AgPt-NPs embedded in SiO_xN_y on a TiO_2 backelectrode. A schematic of this approach is shown in (a). Electrical characteristics were probed during illumination with UV light (colorcode purple) and at dark conditions (black). Examples of IV characteristics under UV ON and OFF conditions are shown in (b). A scatter plot showing the data of 64 consecutive measurement cycles (c) where the half of all cycles were measured at UV ON and OFF conditions, respectively. Reference data from an equally fabricated memristive system, but integrated on a Au backelectrode is shown in (d).

LRS at UV ON conditions are located at higher currents, than all (black) data points indicating the LRS at UV OFF conditions. All in all, these results give first indications, that the diffusive memristive activity of the AgPt-NP based device can be modulated by UV light when it is integrated on a TiO_2 substrate. This is reasoned by a higher chance for diffusive switching and a shift of the LRS towards higher currents, when the system is illuminated by UV light.

Second Memsensor Concept

Now, another memsensor design will be discussed, as shown in Figure 7.2a. Here, a separated sensitive element and memristive system were interconnected. A schematic of the memsensitive system tested in this section is given in Figure 7.2a. The sensitive element was created by drop-coating of a ZnO powder film between two electrodes.

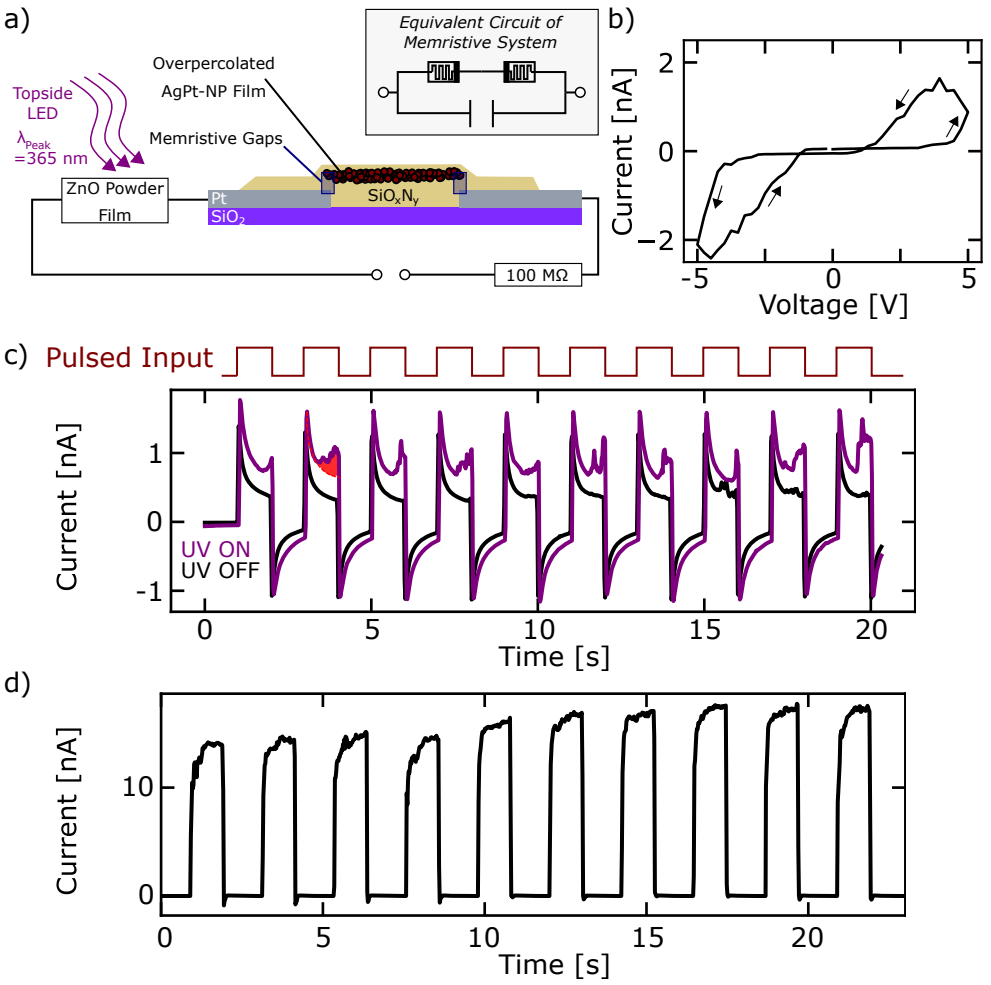

Figure 7.2: Memsensor concept based on a serial interconnection of a ZnO powder film with a memristive system integrated on Pt backelectrodes. The serial ZnO powder film can be stimulated by UV light. The memristive system integrated on Pt backelectrodes can be described as two memristive gaps in series that are parallel to a parasitic capacitance, arising from the backelectrode structure (a). (b) IV characteristic of purely the memristive system and the 100 MΩ resistance. (c) Stimulation of the memsensitive system (including ZnO) via voltage pulses with 0.8 V amplitude under 0.5 Hz. The current responses from the memsensitive system when UV illumination of the ZnO element was OFF/ON is show in black/purple. The red shaded area in the second pulse emphasizes current fluctuations that can be attributed to memristive reconfiguration in the gaps. A reference measurement of purely the memristive system and the 100 MΩ resistance with pulses of 8 V and 0.5 Hz showing that the memristive modifications can be retained between pulses (d).

For the simple drop-coating process, a dispersion of commercial ZnO powder in ethanol was produced in an ultrasonic bath. Droplets of the dispersion were placed via a micropipette onto the backelectrode substrate and the ethanol was allowed to evaporate at ambient conditions, leaving behind a solid ZnO powder film. An additional mechanical stabilization step was not applied. The memristive system was integrated on lithographically structured Pt-backelectrodes. On top of the Pt-electrodes, an insulating film of SiO_xN_y was deposited by reactive sputtering followed by a GAS deposition of a highly overpercolated AgPt-NP film. The whole overpercolated AgPt-NP film was finally encapsulated by another SiO_xN_y deposition (again via reactive sputtering). Accordingly, the memristive system is formed by two serial gaps between the Pt-backelectrodes and the overpercolated AgPt-NP film. Due to its overpercolated nature, the AgPt-NP film effectively acts short circuit, i.e. it will not limit the electron transport. Furthermore, a parasitic capacitance caused by the backelectrode structure must be taken into account and will be reflected in the current response of the memsensitive system. An effective equivalent circuit of the memristive system is given in the inset of Figure 7.2a. Additional information on the characteristics of the memristive system can be found in the Appendix A.1. A 100 MΩ resistor was incorporated with the intention to constrain the whole memsensitive system into a low-current regime, where the modifications in the memristive gaps are volatile over short timescales. The diffusive characteristics of the pure (the ZnO powder film was not included in this measurement) memristive system is depicted by a typical voltage sweep cycle in Figure 7.2b. The whole memsensitive system was characterized via application of voltage pulse trains under UV ON and OFF conditions, meaning that the ZnO element was illuminated with a UV LED (365 nm peak wavelength) and at dark conditions, respectively. The pulse trains had an amplitude of 0.8 V, zero volts between pulses and a frequency of 0.5 Hz. The response of the memsensitive system upon stimulation via pulse trains and at either UV ON or OFF conditions is shown in Figure 7.2c. Most dominantly, effects from the parasitic capacitance caused by the backelectrode structure become apparent. These are charging and decharging currents with an exponential-like decay in the moment where a pulse starts or ends. Besides of that, current fluctuations during a pulse can be recognized, which are attributed to memristive reconfiguration of the gaps. An example for such current fluctuations is emphasized for the second pulse at UV ON conditions in Figure 7.2c. There, current fluctuations originating from memristive reconfiguration, which is superimposed by the exponential-like charging current, is indicated by a red shaded area. More importantly, it was found that the magnitude of current fluctuations caused by memristive reconfiguration were higher at UV ON than at UV OFF conditions. It is noted here, that the reconfiguration of memristive gaps is highly volatile, i.e. they are not retained during the time between two pulses. Figure 7.2d shows a reference measurement, demonstrating that the memristive system could be programmed in such a way, that the modifications are retained between pulses. In this measurement, the memristive system (ZnO was not incorporated) was stressed by a 0.5 Hz pulse train with an amplitude of 8 V. It can be seen, that charging and decharging currents are absent (indicating good electron transport across the memristive gaps) and that the memristive

response from pulse to pulse growths to higher currents. In summary, also the secondly discussed memsensitive system indicates, that memristive responses can be modulated via UV light, when a memristive and a sensitive element are serially connected.

Discussion and Conclusion

The results from both systems demonstrate possible dynamics of memsensitive systems. In this section, they shall serve as a basis to discuss possible working principles and design concepts of memsensors. The working principle of both memsensor concepts discussed in this chapter can be explained by the schematic circuit in Figure 7.3. According to the voltage divider rule, the voltage across the memristive element U_{M} can be calculated as follows:

$$U_{\mathrm{M}} = U_{\mathrm{Total}} \frac{R_{\mathrm{M}}}{R_{\mathrm{M}} + R_{\mathrm{S}}} \tag{7.1}$$

where U_{Total} denotes the total voltage applied to the circuit and R_{S} and R_{M} are the momentary resistances of the sensor and memristive element, respectively. From the voltage divider rule, it can be seen that a decreasing resistance of the sensor element (e.g. through stimulation via UV light), increases the field across the memristive element. Consequently, because ECM-based mechanisms for filament formation are driven by electrical fields, a UV input to the memsensitive systems, promotes the formation of filamentary structures in the memristive part. Considering the von-Neumann bottleneck,

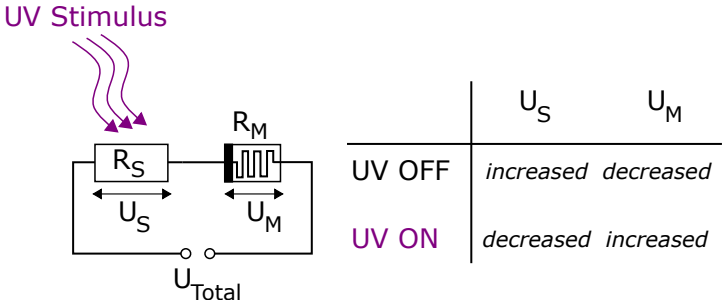

Figure 7.3: Working principle of the discussed memsensitive circuits. The resistances of the sensor and memristor elements are denoted by R_{S} and R_{M}, respectively. The partial voltages U_{S} and U_{M} resulting form the applied voltage U_{Total} can be calculated by the voltage divider rule.

a relevant question for the design of memsensitive systems is the capability of combining information storage, processing and sensory acquisition in one single device. Analogous to the unfavorable permanent information transfer between storage and processing units, information transfer between sensor and memristive elements may eventually form a comparable bottleneck if they are separated in larger arrays. With respect to the memsensor concepts discussed in this chapter, the first one (direct integration on TiO_2) represents a higher integration degree of combining storage, processing and sensing in one single device. The second concept (serial connection of ZnO powder film and memristive system)

includes wiring between the sensitive and memristive element, which makes them two separated units. Therefore, in order to eliminate any "von-Neumann-like" bottleneck, the first memsensor concept can be appreciated as superior to the second approach. Nevertheless, a high degree of memsensor integration obstructs opportunities to tailor the sensor and memristive properties independent from each other, which might be a drawback for the design memsensitive systems. To clarify this discussion, a pure TiO_2 thin film may be considered. The very same TiO_2 thin film can be endowed with both memristive and sensor functionalities. Experimental results that demonstrate the memsensitive behavior of pure TiO_2 films are added to the Appendix section A.2. Taking TiO_2 as a memsensor would imply the highest degree of integration (because storage, processing and sensing take place in the very same material), however, an independent tailoring of sensor and memristive properties becomes difficult. Moreover, when TiO_2 is applied in a MIM-structure, the choice of electrode materials is strongly limited to materials with a sufficient UV transparency. In conclusion, this chapter presented two concepts for the design of memsensitive systems based on serial combinations of NP-based diffusive memristive systems and wide-bandgap semiconductors as UV sensitive elements. The design of memsensitive systems was discussed regarding to the contrary demands on integration degree (i.e. eliminating "von-Neumann-like" bottlenecks) and possibilities to tailor the sensitive and memristive elements independent from each other.

8. Lateral NP-based Memristive Switching in CNT Networks

This chapter reports on the role of AgAu-NPs to mediate memristive switching within a higher level network defined by carbon nanotubes (CNTs). The device concept and this study were conceived by Maik-Ivo Terasa in the framework of his PhD thesis at the Chair for Functional Nanomaterials in Kiel. Own contributions to this work include the integration of AgAu-NP into the CNT network via GAS deposition, discussion of data and revision of the manuscript. In the context of the present thesis, this chapter demonstrates that Ag-based NPs synthesized by a GAS also facilitates memristive switching in lateral geometry and at exposed conditions. This reflects an extension of the applicability of Ag-based alloy-NPs in comparison to Chapters 5, 6 and 7, where the memristive dynamics were solely investigated in embedded systems.

This chapter is a reprint from the following publication:

M.-I. Terasa, P. Holtz, **N. Carstens**, S. Kaps, F. Faupel, A. Vahl and R. Adelung, *PLOS One*, 2022, 17(3):e0264846

PLOS ONE

RESEARCH ARTICLE

Sparse CNT networks with implanted AgAu nanoparticles: A novel memristor with short-term memory bordering between diffusive and bipolar switching

Maik-Ivo Terasa[1], Pia Holtz[1], Niko Carstens[2], Sören Kaps[1], Franz Faupel[2], Alexander Vahl[2], Rainer Adelung[1]*

1 Chair for Functional Nanomaterials, Institute for Materials Science, Faculty of Engineering, Kiel University, Kiel, Germany, **2** Chair for Multicomponent Materials, Institute for Materials Science, Faculty of Engineering, Kiel University, Kiel, Germany

* ra@tf.uni-kiel.de

Citation: Terasa M-I, Holtz P, Carstens N, Kaps S, Faupel F, Vahl A, et al. (2022) Sparse CNT networks with implanted AgAu nanoparticles: A novel memristor with short-term memory bordering between diffusive and bipolar switching. PLoS ONE 17(3): e0264846. https://doi.org/10.1371/journal.pone.0264846

Editor: Raghvendra Bohara, National University of Ireland, Galway, IRELAND

Received: September 14, 2021

Accepted: February 17, 2022

Published: March 31, 2022

Data Availability Statement: All relevant data are within the paper and its Supporting information files.

Funding: This work is funded by the Deutsche Forschungsgemeinschaft (DFG, German Research Foundation) – Project-ID 434434223 – SFB 1461. The funders had no role in study design, data collection and analysis, decision to publish, or preparation of the manuscript.

Abstract

With this work we introduce a novel memristor in a lateral geometry whose resistive switching behaviour unifies the capabilities of bipolar switching with decelerated diffusive switching showing a biologically plausible short-term memory. A new fabrication route is presented for achieving lateral nano-scaled distances by depositing a sparse network of carbon nanotubes (CNTs) via spin-coating of a custom-made CNT dispersion. Electrochemical metallization-type (ECM) resistive switching is obtained by implanting AgAu nanoparticles with a Haberland-type gas aggregation cluster source into the nanogaps between the CNTs and shows a hybrid behaviour of both diffusive and bipolar switching. The resistance state resets to a high resistive state (HRS) either if the voltage is removed with a retention time in the second- to sub-minute scale (diffusive) or by applying a reverse voltage (bipolar). Furthermore, the retention time is positively correlated to the duration of the *Set* voltage pulse. The potential for low-voltage operation makes this approach a promising candidate for short-term memory applications in neuromorphic circuits. In addition, the lateral fabrication approach opens the pathway towards integrating sensor-functionality and offers a general starting point for the scalable fabrication of nanoscaled devices.

Introduction

After the memristor's postulation by Chua *et al.* [1] and the reported link between memristor theory and resistive switching in TiO_2 thin films by Strukov *et al.* in 2008 [2], the potential of resistive switching phenomena has led to a broad variety of research directions. The application potential ranges from non-volatile memory [3] over bio-inspired neural networks as a promising approach to overcome the von-Neumann bottleneck [4] to the concept of a "memsensor" joining memristive with sensitive functionality, allowing for unique features such as habituation to a permanent background signal [5].

Competing interests: The authors have declared that no competing interests exist.

Different types of memristive devices based on their switching mechanisms have been reported such as valence change mechanism (VCM), phase change materials (PCM) or electrochemical metallization (ECM), with different characteristics e.g. bipolar, unipolar or diffusive switching [6–12]. ECM cells commonly consist of a dielectric layer of a few nm in thickness between two metal electrodes, where one is electrochemically active e.g. Cu or Ag [9, 13]. Field-driven oxidation and motion of metal ions as well as their subsequent reduction at the cathode lead to the formation of a metal filament switching the device resistance from matrix determined to metal determined. Due to their bipolar switching behaviour ECM cells have been commonly discussed as candidates for non-volatile memory applications [14]. However, recent advances in ECM systems included introducing metal nanoparticles into the dielectric matrix between inert electrodes to act as an ion reservoir under exploitation of the inherent local field enhancement of nanoparticles [15], with stable diffusive switching properties that have been reported for AgAu and AgPt nanoparticles (NP) embedded in a SiO_2 matrix in [16].

These and most other memristive devices are based on vertical stacks of thin films to achieve the nanometer scaled distances necessary for resistive switching phenomena to occur [6, 17–28]. Whereas designing memristive components in a lateral geometry makes the active interfaces on one hand accessible for investigation by surface sensitive or imaging methods such as electron microscopy and on the other hand allows them to be reached by external stimuli e.g. for surface plasmon resonance excitation [29–31] or for opening the path towards integrating sensor-features into memristive systems. However, while the layer thickness in a vertical sandwich structure can be precisely controlled by well-established deposition methods, obtaining nanoscaled distances laterally requires sophisticated and time-consuming techniques like electron beam lithography or focused ion beam deposition [10, 32].

In the scope of this work, we present a facile and scalable fabrication route for sparse CNT networks implanted with AgAu nanoparticles (in the following termed CNT/AgAu networks) in a lateral geometry, reaching the nanometer scale required for resistive switching by a combination of three length scales, as indicated in Fig 1a: Electrodes are fabricated with standard ultraviolet (UV) lithography to provide a spacing in the micrometer range (6–8 μm). The sparse CNT network provides gaps between the CNTs of up to a few hundreds of nanometers. The fabrication process uses a custom-made CNT dispersion circumventing the detrimental effects of the additives of commercially available CNT dispersions as well as allowing for a quick spin coating deposition method by using a volatile solvent. Finally, the AgAu nanoparticles, sputter deposited with a gas aggregation source (GAS) [33], yield spacings that reach the lower nanometer range. The nanoparticles implanted into gaps provided by the CNTs act as silver ion reservoirs for ECM-type switching, as illustrated in Fig 1b. The switching behaviour is a hybrid of diffusive switching with a retention time in the second- to sub-minute-scale and bipolar switching as it is possible to reset to the high resistive state (HRS) by applying reverse voltages. The retention time of a memristive system describes the time it is able to retain its resistive state, most commonly the low resistive state (LRS) [34]. For non-volatile memory applications the retention time is required to be as high as possible to prevent data loss. However, the CNT/AgAu networks with their short retention time are useful for implementing a "short-term-memory" in neuromorphic circuits. Short-term memories are efficient for storing information that becomes deprecated quickly, as the information does not have to be removed explicitly, and save power by automatically returning to a HRS. Additionally, the capability of the CNT/AgAu networks for explicit reset retains the flexibility of a traditional bipolar memory cell.

In the following sections of this work, first the fabrication route for the CNT/AgAu networks is presented. The challenges and applied methods at each fabrication step are discussed

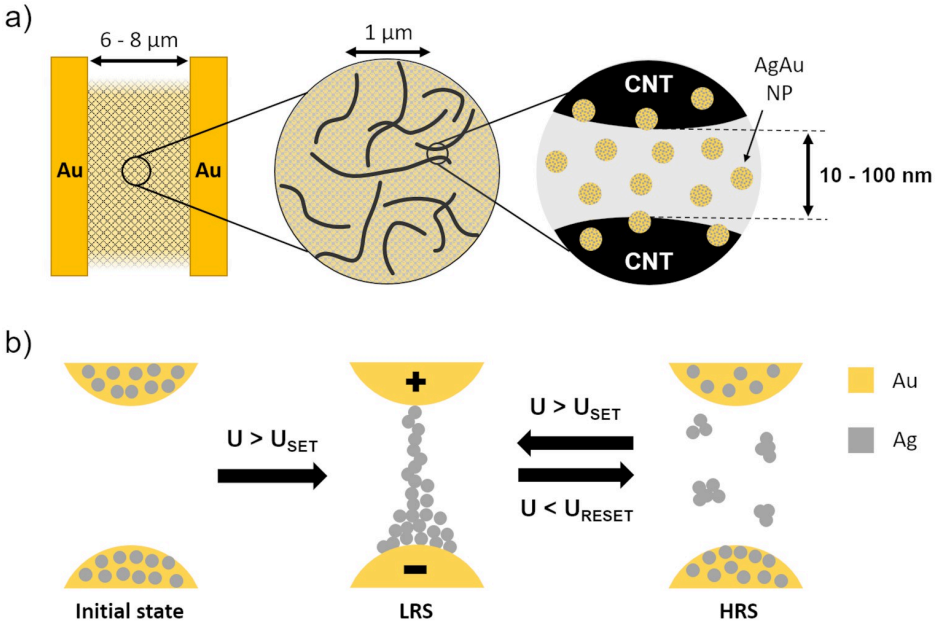

Fig 1. Schematic illustration of the key features and switching mechanism of the CNT/AgAu. a) Vital components of a CNT/AgAu network from left to right: The inert electrodes, the sparse CNT network and the AgAu nanoparticles inside a nanogap between two individual CNTs. b) The switching mechanism between two NPs when exposed to a potential U. LRS = Low resistive state, HRS = High resistive state.

https://doi.org/10.1371/journal.pone.0264846.g001

starting with the custom-made CNT dispersion. The discussion of the nanoparticle deposition includes the in-operando percolation measurement showing the sequential usage of three length scales to obtain the nanoscaled distances necessary for resistive switching. Afterwards, the results of the morphological characterization by means of scanning electron microscopy (SEM) are presented, revealing, that the fabrication route yielded an underpercolated network of CNTs and nanoparticles. In the following, the electrical characterizations are presented consisting of three different measurement modes:

- Current-voltage cycles showing the distinct high resistive and low resistive states.
- Current-voltage cycles into reverse voltage regimes showing the capability for voltage induced reset.
- Time-resolved current measurements showing the short-term memory effect of the decelerated diffusive switching behaviour and a positive correlation of the retention time to the duration of the *Set* voltage pulse.

Additionally, the data indicates that the CNT network acts as an integrated serial resistance limiting the current flow to the nA to µA regime without additional external circuitry [16] while also potentially being operable at low-voltages, resulting in a low power consumption. Finally, the proposed switching mechanism and retention are discussed with respect to filament formation and lifetime.

Results and discussion

Most resistive switching phenomena require nanometer scaled distances due to the resulting strong electrical fields acting as a driving force for the respective switching mechanism [17, 27,

28]. While there are reliable and scalable methods to achieve these distances in vertical orientation by the deposition of thin films, the available methods to obtain this in a lateral orientation are time-consuming and inscalable [10, 32]. We developed a new method for obtaining nanometer scaled gaps with a network of CNTs deposited on a substrate with patterned gold electrodes. This CNT network must meet certain requirements:

- The network must fill the space between the electrodes.
- The CNTs must be finely dispersed, so that there are no dense agglomerations of CNTs.
- The network must be just below the percolation point, so that the distance between individual tubes is in the nanometer range.
- The CNTs must not be heavily coated by surfactants or other additives, as that would inhibit to remove short-circuiting paths by Joule heating.

For the deposition of CNT networks a custom made CNT dispersion has been prepared by mixing the following ingredients:

- Pristine CNTs as dry powder, so that they are not coated with additives initially
- Ethanol as a fast evaporating solvent to facilitate a quick sequential application of dispersion droplets onto the substrate during spin coating
- Poly(3,4-ethylenedioxythiopene) polystyrene sulfonate (PEDOT:PSS) as an additive, keeping the CNTs finely dispersed [35]

The mixture has been sonicated with an ultrasonicator to break up the CNT particles and disperse them. The PEDOT:PSS prevents re-agglomeration without impeding the resistive heating step.

A thin film of dispersion has been deposited onto the substrates via spin coating. The dispersion was dropped onto the substrate sequentially dropwise during spinning, where each drop has been left to evaporate before applying the next one, allowing for precise control over the particle density.

After deposition of a CNT network a voltage ramp has been applied to it to remove any continuous CNT paths short-circuiting the electrodes by resistive heating, which has been indicated by a sudden drop in the current readout (see S1 Fig).

The AgAu nanoparticles have been deposited by direct current (DC) magnetron sputtering using a Haberland-type gas aggregation source (GAS) identical to the one reported in [36], with a AgAu target as in [33] attached to the DC planar magnetron source. This deposition method enables precise control over particle composition and density without affecting the CNT network on the substrate [33].

The deposition time for the nanoparticles has been set to stay below the percolation point [37]. The deposition time for the percolation point has been determined by performing electrical measurements in-operando during deposition. A schematic of the setup and the percolation measurement of a substrate with deposited CNT network is shown in Fig 2. After deposition of AgAu nanoparticles, a thin layer of SiN has been deposited on top as a protective layer without breaking vacuum. Experimental details about any step of the procedure can be found in the section "Materials & Methods".

Fig 3 shows a sequence of SEM images of a CNT/AgAu network revealing the homogeneous distribution and sparseness of the CNTs. A substantial fraction of CNTs have been broken into smaller pieces during the ultrasonication step, which we assume to provide two advantages for the fabrication process: Firstly, an alleviation of entanglement and

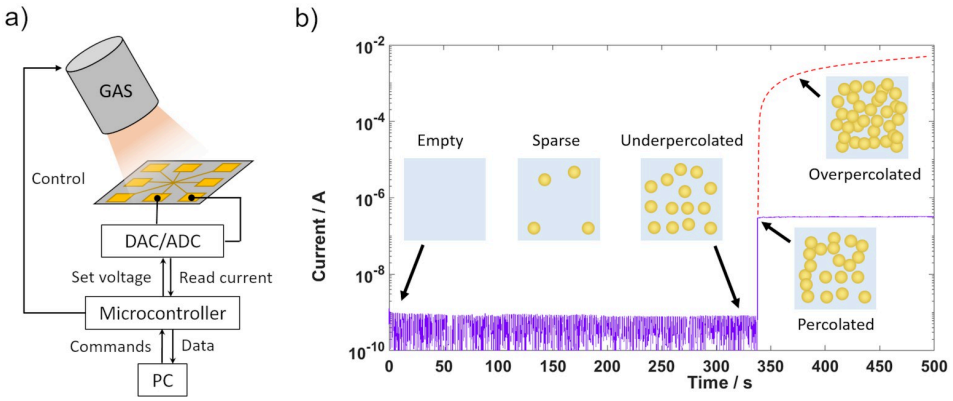

Fig 2. Percolation measurement for AgAu nanoparticle deposition. a) Schematic of the in-operando percolation measurement setup. b) Time-resolved current measurement across adjacent electrodes at a voltage of 3V. The time where the flowing current shows a significant increase is taken as the percolation time (337 s). The deposition has been stopped at the percolation point. The red dashed line indicates the progression of the current, if the deposition had continued, leading to an overpercolated layer of nanoparticles.

https://doi.org/10.1371/journal.pone.0264846.g002

agglomeration of CNTs and secondly an increased sparseness of the network providing more gaps between CNTs and preventing individual tubes from bridging the whole network.

Fig 3c shows a CNT network with deposited underpercolated AgAu nanoparticles. The particle distribution shows spacing in the lower nanometer range enabling ECM-type memristive switching between nanoparticles [16]. Samples solely prepared with AgAu nanoparticles with an equal filling factor showed no switching behaviour in the considered voltage regime (see S2 Fig) verifying that the sparse network of CNTs fulfils its expected functionality of providing suitable nanogaps to enable the resistive switching of the nanoparticles.

For CNT/AgAu networks, that did not show resistive switching below 10 V, an electric preforming step has been performed by cycling to a voltage of ± 20 V (0 V -> 20 V -> -20 V -> 0 V) over several cycles (see S3 Fig). A stable HRS corresponding to Fig 1b is reached during the second cycle, from where on the resistive switching occurs. This indicates that nanoparticle gaps in the conduction path become persistent conductive elements by forming stable filaments that are not collapsing, when the electrical field is removed. This yields lower switching voltages by decreasing the number of gaps over which the overall voltage drops. After the

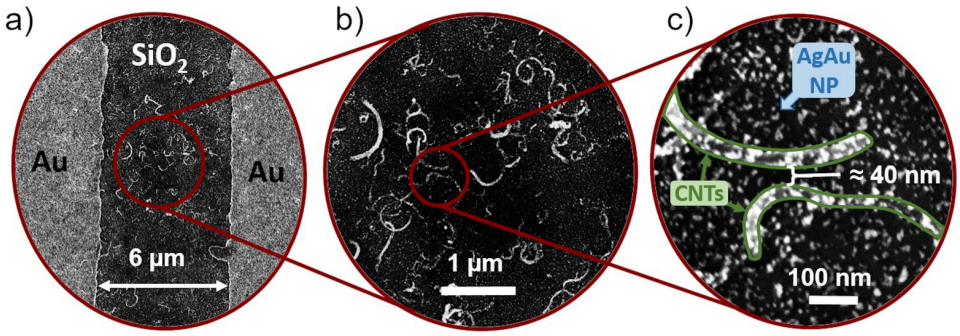

Fig 3. SEM micrographs of a finished [CNT/AgAu network] without SiN layer. a+b) Homogeneous sparse CNT network between the electrodes. c) A nanogap between two CNTs with deposited AgAu NP. The samples shown in the images have not been coated with SiN.

https://doi.org/10.1371/journal.pone.0264846.g003

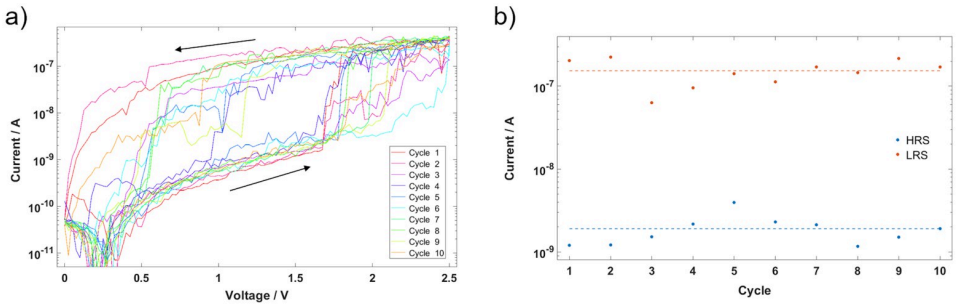

Fig 4. Resistive switching behaviour. a) Cyclic voltage pattern, showing resistive switching behaviour and an ON/OFF ratio of around 81 at a Read voltage of 1.5 V. b) HRS and LRS currents at Read voltage of 1.5 V for each cycle.

https://doi.org/10.1371/journal.pone.0264846.g004

preforming procedure, when cycled in low voltage regimes, operation becomes stable as shown in Fig 4.

Fig 4a shows a cyclic IV-measurement of a CNT/AgAu network with an 8 μm spacing between electrodes. The voltage has been cycled from 0 V to 2.5 V and back to 0 V at a rate of 250 mV/s over ten cycles, where after each cycle the voltage has been held at 0 V for 5 s. The current response shows a clear distinction of two resistive states (see Fig 4b) and stable operation across the ten cycles with the HRS current being 1.9 ± 0.8 nA and the LRS current being 155 ± 55 nA yielding a current ratio between HRS and LRS of ≈ 81 at a *Read* voltage of 1.5 V. The data indicates the potential for low-voltage operation and shows that the network itself acts as a series resistance limiting the current flow and thus ensuring low power consumption without additional circuitry (cf. [16]).

Fig 5 shows two subsequent cycles of a CNT/AgAu network, recorded at a ramp speed of 25 mV/s. The cycle shown in Fig 5a starts in an HRS, switching into the LRS and retaining it, until a negative voltage of -1.5 V is applied. The CNT/AgAu network then switches into its LRS again upon reaching its *Set* voltage of 2.5 V. The subsequent cycle seen in Fig 5b starts in the LRS and shows that this effect is symmetrical. Reducing the ramp speed of 10 mV/s did not change the reset voltage, indicating that the effect is not accountable to the diffusive reset behaviour. These measurements indicate that, while the CNT/AgAu network also returns to its HRS over time without the application of a voltage like a diffusive device, it shows the ability of bipolar switching i.e. to be reset from LRS to HRS by reverse voltages.

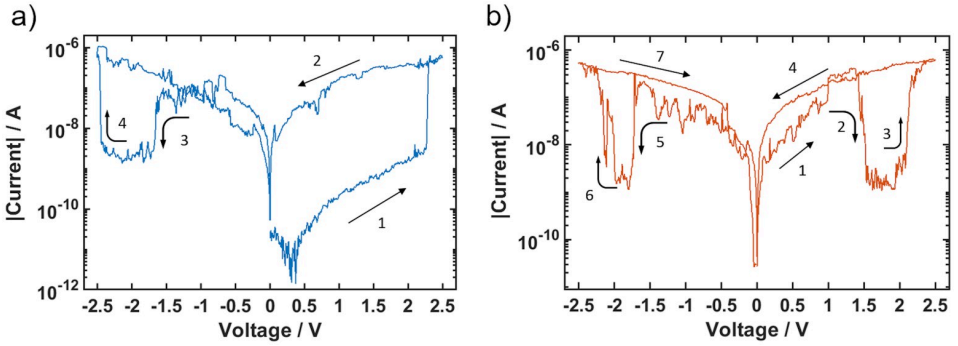

Fig 5. Reset behaviour with reverse voltage. a) Cycle starting in HRS. The LRS is retained until -1.5 V is applied. b) Subsequent cycle starting in LRS. The reset behaviour is symmetrical in the positive and negative voltage range. The numbers indicate in which order the resistive switching occurred.

https://doi.org/10.1371/journal.pone.0264846.g005

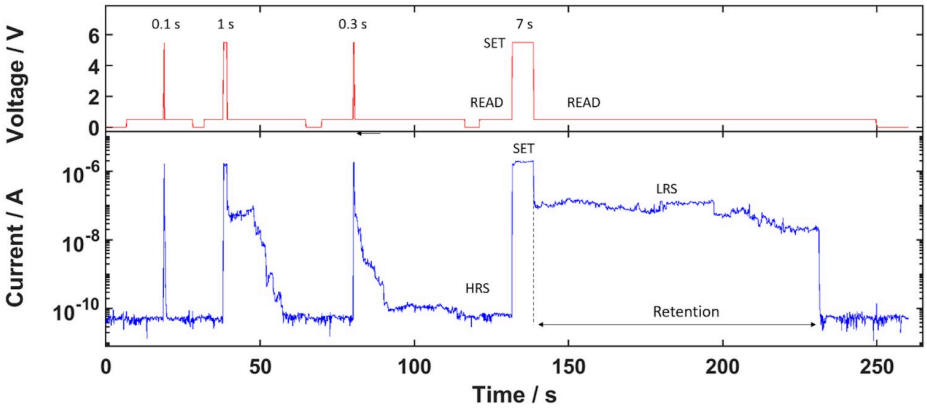

Fig 6. Time-resolved current measurements showcasing the retention. The upper graph shows the applied voltage pattern: Read voltage = 0.5 V, Set voltage = 5.5 V. The retention time is taken as the time from returning from Set to Read voltage to when the current reaches the HRS current. The numeric values indicate the duration of the Set voltage pulse. The Set time and retention time show a positive correlation, which can be found in the (see S4 Fig).

https://doi.org/10.1371/journal.pone.0264846.g006

The time-dependent retention has been investigated by time resolved current measurements with the voltage pattern shown in the upper graph of Fig 6. The measurement starts at 0 V for several seconds to serve as a reference. The current readout at the *Read* voltage of 0.5 V before the first *Set* pulse shows that the CNT/AgAu network is in its HRS initially. After each *Set* pulse, each with different pulse durations, the current readouts at the subsequent *Read* voltage indicate a switch of the CNT/AgAu network into the LRS. The *Read* voltage has been held until it returned into its HRS, where the time from returning to the *Read* voltage until the current returned to the HRS regime has been taken as the retention time (see Fig 6). The series of pulse durations for the *Set* pulses indicates a positive correlation between the time in the *Set* state and the resulting retention time of the CNT/AgAu network i.e. a longer *Set* pulse results in a longer retention time (see also S4 Fig).

In ECM devices the resistive states originate from metal filaments formed by movement and reduction of metal ions in the electrical field [12, 16, 38, 39]. With a formed filament the device is in its LRS. When the filament ruptures, it returns to its HRS, which is due to surface tension of the filament as a restoring force, making it energetically favourable to form spherical particles depending on the thickness of the filament and the surrounding matrix material [7, 40]. In bipolar memristive ECM devices the electrodes provide a metal reservoir large enough to form stable filaments with a retention of several years [40]. The CNT/AgAu networks use the AgAu nanoparticles as metal ion reservoirs limiting the amount of silver atoms available for filament formation. Singular or few nanoparticles have been reported to show no retention due to the formed filament being thin enough to immediately collapse as soon as the electrical field as a driving force is removed [16]. In this work, however, the density of deposited AgAu nanoparticles in the CNT networks' nanogaps yield a suitable silver reservoir to provide a substantial amount of silver ions for filament formation. The resulting filament in the gaps, where resistive switching occurs, is thick enough to be stable, so that the rupture does not happen right away without electrical field, but instead is delayed until diffusion thinned down the filament enough to collapse by surface tension.

At the same time though the amount of silver atoms is still limited such that the filament formed by an electrical field is not outright long-term stable, like in a typical bipolar device. Instead the filament formed initially is sufficiently thin to show diffusive switching. However, with prolonged application of the electrical field, the filament grows by material diffusion from

other nearby nanoparticles. The longer the *Set* voltage is applied, the thicker the filament becomes. Thus, the retention time increases i.e. the time it takes for the filament to collapse after removing the electrical field.

As long as the filament holds, a reverse voltage excitation is able to break the filament. In typical bipolar ECM type systems the electrode materials are asymmetrical, so that only one voltage polarity yields a filament while the reverse polarity leads to its dissolution [12, 14, 38]. As seen in Fig 5b however, it is evident, that the behaviour of the CNT/AgAu network is symmetrical. The reset mechanism is presumed to be based on drift of the filament's silver towards the cathode until the filament is sufficiently thinned down on the anode side to collapse, switching the CNT/AgAu network into its HRS.

Conclusion

In this work sparse CNT networks as a new approach for obtaining nanoscaled distances in a lateral geometry as well as those networks with implanted AgAu nanoparticles as a novel lateral memristor with short-term memory capabilities and a hybrid switching behaviour between diffusive and bipolar switching have been presented.

The sparse CNT networks have shown to offer a general starting point for introducing nanoscaled gaps into laterally oriented systems. The CNTs exhibit the function of bridging substantial distances between the electrodes while gaps between individual CNTs have shown to be in the nanometer range. AgAu nanoparticles implanted into this CNT network showed ECM-type resistive switching. The switching behaviour is based on providing a substantial but still limited reservoir of silver by deposited AgAu nanoparticles, yielding a diffusive switching behaviour with a second-scale retention as well as the ability of bipolar devices to reset to the HRS by reverse voltages. It has been shown that the "memory span", i.e. the retention, is positively correlated to the width of the *Set* voltage pulse since the retention is prescribed by the filament's lifetime and thus its thickness. Also, it has been shown that the CNT/AgAu networks are able to reach switching voltages in the range providable by chips fabricated with complementary metal-oxide semiconductor (CMOS) technology, while the network provides an integrated serial resistance limiting the current to the nA to μA range. This makes CNT/AgAu networks a promising approach for low-power short-term memory components in neuromorphic circuits, though for a deeper understanding further investigations with respect to the detailed correlation of *Set* pulse width and retention time as well as the impact of the network topology are necessary.

Materials & methods

The substrates were produced from commercially available Si wafers with a 500 nm thick oxide layer on top. The metal contacts have been deposited by a standard UV-lithography with a Süss Microtech MA6/BA6 mask aligner, followed by a sputtering and lift-off process. The sputter process was a DC magnetron sputter deposition of Cr with a thickness of 10 nm as an adhesive layer and on top Au with a thickness of 200 nm as a contact layer. The lift-off has been performed in an ultrasonicated acetone bath held at 40˚C. After the lift-off the wafer has been cleaned and dried after which it has been cut into 11 x 11 mm pieces with a DAD3350 automated dicing saw.

The CNT dispersions have been fabricated by mixing 10 g of ethanol (99.7% purity, provided by Carl Roth) with 40 μg pristine multi-walled carbon nanotubes (MWCNT, Baytubes C150P) and 1 μl of 1.3wt% aqueous solution of PEDOT:PSS (Ossila PH1000). The ultrasonication was performed with a Sonics Vibra-Cell VC 505 with 500 W at 70% amplitude. The dispersions have been sonicated for 15 minutes with cycles of 3 s pulsing and 3 s pause. The glass tube with the dispersion has been kept in a water bath cooled with a Peltier element during sonication.

The spin coater was a Laurell WS-650MZ-23NPPB and has been rotated at a constant rate of 1500 rpm. A total of 350 μl of dispersion has been deposited dropwise on each substrate.

For the resistive heating step the applied voltage ramp was 5 V/s up to a maximum of 30 V under a current compliance of 100 μA.

The sputter deposition of nanoparticles has been performed with a Haberland-type gas aggregation source with a AgAu multicomponent target [33]. Ar was used as a process gas at a flow of 50 sccm. The magnetron power has been set to 50 W. The shutter has been kept closed after turning on the magnetron power for 30 seconds to ensure a stable deposition rate before the sample has been exposed to the sputter source. The deposition time until the percolation point is reached has been determined to be 337 s. Samples have been sputtered for 330 s to stay below the percolation point.

A SiN layer has been deposited as a protective layer by reactive sputtering using a Si target with a nitrogen flow of 4.2 sccm and a magnetron power of 20 W. The deposition time was 7 minutes, resulting in a nominal film thickness of 21 nm.

For the IV-characterization a software-controlled Keithley 2400 Source Measure Unit has been used with gold plated spring contacts as probes placed on the electrode pads. The measurement delay between data points has been determined to be ≈100 ms.

SEM images have been recorded with a Zeiss Ultra Plus at 5 kV acceleration voltage using the in-lens detector.

Supporting information

S1 Fig. Typical current measurement for Joule heating of a CNT network. The voltage has been cycled two times. After the current dropped it stayed in the limit of detection (LOD) of the measurement device.
(TIF)

S2 Fig. Current measurement of a sample without CNT network.
(TIF)

S3 Fig. Electric preforming of a CNT/AgAu network over four cycles. Red = positive half-cycle, Blue = negative half-cycle. a) During the first cycle there is no distinct Set behaviour. The Ag-ions are located inside the AuNP and are gradually dragged out by the electric field. b) During the positive half-cycle the CNT/AgAu network reaches the LRS illustrated in Fig 1b, so that the following cycles show corresponding ECM-type resistive switching.
(TIF)

S4 Fig. Retention time vs. set pulse duration. The two points at each Set pulse duration indicate the time when the current degression starts after returning to the *Read* voltage and when the current reaches the HRS current regime.
(TIF)

S1 Data. Raw data for Figs 2 and 4–6, and S1–S3 Figs.
(ZIP)

S1 File. Original SEM micrograph for Fig 3.
(ZIP)

Acknowledgments

The authors would like to thank Dr. Fabian Schütt for proof-reading and fruitful discussion, as well as Jörg Bahr and Stefan Rehders for technical assistance.

Author Contributions

Conceptualization: Maik-Ivo Terasa, Pia Holtz, Niko Carstens, Sören Kaps, Franz Faupel, Alexander Vahl, Rainer Adelung.

Data curation: Maik-Ivo Terasa.

Investigation: Maik-Ivo Terasa, Pia Holtz.

Methodology: Maik-Ivo Terasa, Niko Carstens, Alexander Vahl.

Project administration: Rainer Adelung.

Resources: Niko Carstens, Alexander Vahl.

Software: Maik-Ivo Terasa, Sören Kaps.

Supervision: Rainer Adelung.

Visualization: Maik-Ivo Terasa.

Writing – original draft: Maik-Ivo Terasa.

Writing – review & editing: Niko Carstens, Sören Kaps, Franz Faupel, Alexander Vahl, Rainer Adelung.

References

1. Chua L. Memristor-The missing circuit element. IEEE Trans. Circuit Theory. 1971; 18: 507–519. https://doi.org/10.1109/TCT.1971.1083337
2. Strukov DB, Snider GS, Stewart DR, Williams RS. The missing memristor found. Nature. 2008; 453: 80–83. https://doi.org/10.1038/nature06932 PMID: 18451858
3. Yu S. Neuro-Inspired Computing With Emerging Nonvolatile Memorys. Proc. IEEE. 2018; 106: 260–285. https://doi.org/10.1109/JPROC.2018.2790840
4. Merolla PA, Arthur JV, Alvarez-Icaza R, Cassidy AS, Sawada J, Akopyan F, et al. Artificial brains. A million spiking-neuron integrated circuit with a scalable communication network and interface. Science. 2014; 345: 668–673. https://doi.org/10.1126/science.1254642 PMID: 25104385
5. Vahl A, Carstensen J, Kaps S, Lupan O, Strunskus T, Adelung R, et al. Concept and modelling of memsensors as two terminal devices with enhanced capabilities in neuromorphic engineering. Sci Rep. 2019; 9: 4361. https://doi.org/10.1038/s41598-019-39008-5 PMID: 30867493
6. Hansen M, Ziegler M, Kolberg L, Soni R, Dirkmann S, Mussenbrock T, et al. A double barrier memristive device. Sci Rep. 2015; 5: 1–12. https://doi.org/10.1038/srep13753 PMID: 26348823
7. Wang Z, Joshi S, Savel'ev SE, Jiang H, Midya R, Lin P, et al. Memristors with diffusive dynamics as synaptic emulators for neuromorphic computing. Nat Mater. 2017; 16: 101–108. https://doi.org/10.1038/nmat4756 PMID: 27669052
8. Chaudhary D, Munjal S, Khare N, Vankar VD. Bipolar resistive switching and nonvolatile memory effect in poly (3-hexylthiophene)–carbon nanotube composite films. Carbon. 2018; 130: 553–558. https://doi.org/10.1016/j.carbon.2018.01.058
9. Jeong DS, Thomas R, Katiyar RS, Scott JF, Kohlstedt H, Petraru A, et al. Emerging memories. Resistive switching mechanisms and current status. Rep Prog Phys. 2012; 75: 76502. https://doi.org/10.1088/0034-4885/75/7/076502 PMID: 22790779
10. Puzyrev YS, Shen X, Zhang CX, Hachtel J, Ni K, Choi BK, et al. Memristive devices from ZnO nanowire bundles and meshes. Appl. Phys. Lett. 2017; 111: 153504. https://doi.org/10.1063/1.5008265
11. Sokolov A, Ali M, Li H, Jeon Y-R, Ko MJ, Choi C. Partially Oxidized MXene Ti 3 C 2 T x Sheets for Memristor having Synapse and Threshold Resistive Switching Characteristics. Adv. Electron. Mater. 2021; 7: 2000866. https://doi.org/10.1002/aelm.202000866
12. Waser R, Dittmann R, Staikov G, Szot K. Redox-Based Resistive Switching Memories—Nanoionic Mechanisms, Prospects, and Challenges. Adv. Mater. 2009; 21: 2632–2663. https://doi.org/10.1002/adma.200900375
13. Lübben M, Valov I. Active Electrode Redox Reactions and Device Behavior in ECM Type Resistive Switching Memories. Adv. Electron. Mater. 2019; 5: 1800933. https://doi.org/10.1002/aelm.201800933

14. Valov I, Waser R, Jameson JR, Kozicki MN. Electrochemical metallization memories—fundamentals, applications, prospects. Nanotechnology. 2011; 22: 289502. https://doi.org/10.1088/0957-4484/22/25/254003 PMID: 21572191

15. Choi BJ, Torrezan AC, Norris KJ, Miao F, Strachan JP, Zhang M-X, et al. Electrical performance and scalability of Pt dispersed SiO2 nanometallic resistance switch. Nano Lett. 2013; 13: 3213–3217. https://doi.org/10.1021/nl401283q PMID: 23746124

16. Vahl A, Carstens N, Strunskus T, Faupel F, Hassanien A. Diffusive Memristive Switching on the Nanoscale, from Individual Nanoparticles towards Scalable Nanocomposite Devices. Sci Rep. 2019; 9: 17367. https://doi.org/10.1038/s41598-019-53720-2 PMID: 31758021

17. Zhu J, Zhang T, Yang Y, Huang R. A comprehensive review on emerging artificial neuromorphic devices. Appl. Phys. Rev. 2020; 7: 11312. https://doi.org/10.1063/1.5118217

18. Barnes BK, Das KS. Resistance Switching and Memristive Hysteresis in Visible-Light-Activated Adsorbed ZnO Thin Films. Sci Rep. 2018; 8: 2184. https://doi.org/10.1038/s41598-018-20598-5 PMID: 29391500

19. Yao J, Sun Z, Zhong L, Natelson D, Tour JM. Resistive switches and memories from silicon oxide. Nano Lett. 2010; 10: 4105–4110. https://doi.org/10.1021/nl102255r PMID: 20806916

20. Kwon D-H, Kim KM, Jang JH, Jeon JM, Lee MH, Kim GH, et al. Atomic structure of conducting nanofilaments in TiO2 resistive switching memory. Nature Nanotech. 2010; 5: 148–153. https://doi.org/10.1038/nnano.2009.456 PMID: 20081847

21. Han J-W, Meyyappan M. Copper oxide resistive switching memory for e-textile. AIP Advances. 2011; 1: 32162. https://doi.org/10.1063/1.3645967

22. Shih A, Zhou W, Qiu J, Yang H-J, Chen S, Mi Z, et al. Highly stable resistive switching on monocrystalline ZnO. Nanotechnology. 2010; 21: 125201. https://doi.org/10.1088/0957-4484/21/12/125201 PMID: 20182012

23. Rahaman SZ, Lin Y-D, Lee H-Y, Chen Y-S, Chen P-S, Chen W-S, et al. The Role of Ti Buffer Layer Thickness on the Resistive Switching Properties of Hafnium Oxide-Based Resistive Switching Memories. Langmuir. 2017; 33: 4654–4665. https://doi.org/10.1021/acs.langmuir.7b00479 PMID: 28420238

24. Terai M, Sakotsubo Y, Kotsuji S, Hada H. Resistance Controllability of Ta2O5/TiO2 Stack ReRAM for Low-Voltage and Multilevel Operation. IEEE Electron Device Lett. 2010; 31: 204–206. https://doi.org/10.1109/LED.2009.2039021

25. Chakrabarti B, Lastras-Montaño MA, Adam G, Prezioso M, Hoskins B, Payvand M, et al. A multiply-add engine with monolithically integrated 3D memristor crossbar/CMOS hybrid circuit. Sci Rep. 2017; 7: 42429. https://doi.org/10.1038/srep42429 PMID: 28195239

26. Yao P, Wu H, Gao B, Eryilmaz SB, Huang X, Zhang W, et al. Face classification using electronic synapses. Nat Commun. 2017; 8: 15199. https://doi.org/10.1038/ncomms15199 PMID: 28497781

27. Edwards AH, Barnaby HJ, Campbell KA, Kozicki MN, Liu W, Marinella MJ. Reconfigurable Memristive Device Technologies. Proc. IEEE. 2015; 103: 1004–1033. https://doi.org/10.1109/JPROC.2015.2441752

28. Ielmini D, Wong H-SP. In-memory computing with resistive switching devices. Nat Electron. 2018; 1: 333–343. https://doi.org/10.1038/s41928-018-0092-2

29. Emboras A, Goykhman I, Desiatov B, Mazurski N, Stern L, Shappir J, et al. Nanoscale plasmonic memristor with optical readout functionality. Nano Lett. 2013; 13: 6151–6155. https://doi.org/10.1021/nl403486x PMID: 24256313

30. Hoessbacher C, Fedoryshyn Y, Emboras A, Melikyan A, Kohl M, Hillerkuss D, et al. The plasmonic memristor. A latching optical switch. Optica. 2014; 1: 198. https://doi.org/10.1364/OPTICA.1.000198

31. Ratchford DC, Dunkelberger AD, Vurgaftman I, Owrutsky JC, Pehrsson PE. Quantification of Efficient Plasmonic Hot-Electron Injection in Gold Nanoparticle-TiO2 Films. Nano Lett. 2017; 17: 6047–6055. https://doi.org/10.1021/acs.nanolett.7b02366 PMID: 28850243

32. Le PY, Murdoch BJ, Barlow AJ, Holland AS, McCulloch DG, McConville CF, et al. Electroformed, Self-Connected Tin Oxide Nanoparticle Networks for Electronic Reservoir Computing. Adv. Electron. Mater. 2020: 2000081. https://doi.org/10.1002/aelm.202000081

33. Vahl A, Strobel J, Reichstein W, Polonskyi O, Strunskus T, Kienle L, et al. Single target sputter deposition of alloy nanoparticles with adjustable composition via a gas aggregation cluster source. Nanotechnology. 2017; 28: 175703. https://doi.org/10.1088/1361-6528/aa66ef PMID: 28294956

34. Yoshida C, Tsunoda K, Noshiro H, Sugiyama Y. High speed resistive switching in Pt/TiO2/TiN film for nonvolatile memory application. Appl. Phys. Lett. 2007; 91: 223510. https://doi.org/10.1063/1.2818691

35. Chang-Jian C-W, Cho E-C, Lee K-C, Huang J-H, Chen P-Y, Ho B-C, et al. Thermally conductive polymeric composites incorporating 3D MWCNT/PEDOT. PSS scaffolds. Composites Part B: Engineering. 2018; 136: 46–54. https://doi.org/10.1016/j.compositesb.2017.10.004

36. Polonskyi O, Solař P, Kylián O, Drábik M, Artemenko A, Kousal J, et al. Nanocomposite metal/plasma polymer films prepared by means of gas aggregation cluster source. Thin Solid Films. 2012; 520: 4155–4162. https://doi.org/10.1016/j.tsf.2011.04.100

37. Mirigliano M, Milani P. Electrical conduction in nanogranular cluster-assembled metallic films. Advances in Physics: X. 2021; 6: 1. https://doi.org/10.1080/23746149.2021.1908847

38. Peng S, Zhuge F, Chen X, Zhu X, Hu B, Pan L, et al. Mechanism for resistive switching in an oxide-based electrochemical metallization memory. Appl. Phys. Lett. 2012; 100: 72101. https://doi.org/10.1063/1.3683523

39. Menzel S, Tappertzhofen S, Waser R, Valov I. Switching kinetics of electrochemical metallization memory cells. Phys Chem Chem Phys. 2013; 15: 6945–6952. https://doi.org/10.1039/c3cp50738f PMID: 23549450

40. Wang W, Wang M, Ambrosi E, Bricalli A, Laudato M, Sun Z, et al. Surface diffusion-limited lifetime of silver and copper nanofilaments in resistive switching devices. Nat Commun. 2019; 10: 81. https://doi.org/10.1038/s41467-018-07979-0 PMID: 30622251

9. Critical Dynamics and Long-range Temporal Correlations in Memristive Ag-NP Networks

This chapter deals with large-scale memristive systems, namely Ag-NP networks poised at the electrical percolation threshold. These networks exhibit collective features, such as critical dynamics and long-range temporal correlations, that are similarly found in biological neuronal systems and are believed to endow systems with brain-like computational capabilities. The occurrence of criticality witness a dynamical complexity similar to biological systems, that could be used for neuromorphic approaches like reservoir computing. When critical dynamics arise, the knowledge about system parameters or dynamical characteristics that tunes the whole system into a critical state is of fundamental interest. Therefore, the dynamics of Ag-NP network with and without SiO_xN_y capping layers are compared. The presence of a ceramic capping layer is assumed to fundamentally alter the dynamics of the underlying memristive units across the network (and therefore potentially affecting the presence of a critical state). One important finding of this chapter is, that critical dynamics in Ag-NP networks are not disturbed upon presence or absence of a capping layer.

This chapter is a reprint of a manuscript accepted for publication:

N. Carstens, B. Adejube, T. Strunskus, F. Faupel, S. Brown and A. Vahl, *Nanoscale Advances*, *Accepted*, 2022

Nanoscale Advances

ROYAL SOCIETY OF CHEMISTRY

PAPER

View Article Online
View Journal

Cite this: DOI: 10.1039/d2na00121g

Brain-like critical dynamics and long-range temporal correlations in percolating networks of silver nanoparticles and functionality preservation after integration of insulating matrix†

Niko Carstens, [a] Blessing Adejube,[a] Thomas Strunskus,[a] Franz Faupel, [a] Simon Brown [b] and Alexander Vahl *[a]

Random networks of nanoparticle-based memristive switches enable pathways for emulating highly complex and self-organized synaptic connectivity together with their emergent functional behavior known from biological neuronal networks. They therefore embody a distinct class of neuromorphic hardware architectures and provide an alternative to highly regular arrays of memristors. Especially, networks of memristive nanoparticles (NPs) poised at the percolation threshold are promising due to their capabilities of showing brain-like activity such as critical dynamics or long-range temporal correlation (LRTC), which are closely connected to the computational capabilities in biological neuronal networks. Here, we adapt this concept to networks of Ag-NPs poised at the electrical percolation threshold, where the memristive properties are governed by electro-chemical metallization. We show that critical dynamics and LRTC are preserved although the nature of individual memristive gaps throughout the network is fundamentally changed by filling the gaps with an insulating matrix. The results in this work generate important contributions towards the practical applicability of critical dynamics and LRTC in percolating NP networks by elucidating the consequences of NP network encapsulation, which is considered as an important step towards device integration.

Received 21st February 2022
Accepted 7th May 2022

DOI: 10.1039/d2na00121g

rsc.li/nanoscale-advances

Introduction

Conventional computer technology is facing fundamental limitations, which are related to hardware architecture (von-Neumann bottleneck), the integration density of transistors (envisioned end of Moore's law) and a tremendous increase in estimated power consumption. These limitations have greatly stimulated the research into novel and unconventional computation concepts.[1] The field of neuromorphic engineering aims to solve these challenges by designing novel types of computational hardware, which draw inspiration from biological principles like signal thresholding, synaptic plasticity, parallelism and hierarchy or in-memory computing.[2] In the past decade, memristive devices played a key role as fundamental building units in the design of neuromorphic hardware and significant effort was focused on mass integration of memristive devices on wafer scales.[3–6] The key characteristic of a memristive device is its reconfigurable resistance state. Among different types of memristive devices, filamentary switching devices based on electrochemical metallization (ECM) principles[7] are of special interest. The major working principle of this type of memristive devices is the reconfiguration of metallic filaments in nanoscale switching gaps in response to the application of external voltage or current stimuli. Accordingly, the conductance of the nanogaps is determined by the state of the metallic filament. Diverse switching dynamics such as non-volatile filamentary switching,[7] diffusive switching[8] or highly dynamic spiking behavior[9,10] have been reported. However, the creation of networks of memristive devices approaching brain-like complexity *via* traditional top-down fabrication technologies poses several challenges as the performance of each memristive device and the enormous degree of connectivity within the network has to be under precise control.[1] In view of these challenges, fabrication of neuromorphic devices based on self-assembly approaches appears to be a promising and feasible alternative route.[11,12] Such devices are typically implemented *via* the formation of a complex network of memristive gaps with a stochastic distribution. In these networks, the emerging collective dynamical is exploited. Following such approaches neuromorphic

[a]*Institute for Materials Science, Chair for Multicomponent Materials, Faculty of Engineering, Kiel University, Kaiserstraße 2, D-24143 Kiel, Germany. E-mail: alva@tf.uni-kiel.de*

[b]*The MacDiarmid Institute for Advanced Materials and Nanotechnology, School of Physical and Chemical Sciences, Te Kura Matū, University of Canterbury, Private Bag 4800, Christchurch 8140, New Zealand*

† Electronic supplementary information (ESI) available. See https://doi.org/10.1039/d2na00121g

functionalities can be implemented, circumventing the necessity of a precise wiring, spatial assembly, and tailoring of switching characteristics of individual memristive units. Such approaches turned out to be feasible for reservoir computing, where complex dynamical systems showing short-term memory and spatio-temporal correlations are required.[13–16] Recently several reports have shown the existence of different potential building units from which complex emergent networks can be formed. Networks assembled from Au-NPs above the percolation threshold exhibit complex memristive switching patterns, which are caused by atomic rearrangements between adjacent Au-NPs induced by electrical currents.[17] Networks of polymer-coated Ag-nanowires formed by random self-assembly also show emergent dynamics applicable for the design of neuromorphic systems.[18,19]

Recently, the technical implementation of critical dynamics in neuromorphic systems *via* self-assembled networks of memristive switches gained considerable interest. This is motivated by findings from neuroscience indicating that biological neuronal networks operate in a regime of critical dynamics, which is seen as beneficial for solving computational tasks efficiently.[20] The presence of critical dynamics in biological neuronal systems was supported by the fact that spontaneous neural activity in cortical tissues takes place *via* brief bursts separated by periods of highly reduced activity, so-called "*neural avalanches*".[20,21] Experimental observations of this avalanche activity in cortical neuron tissues from rats suggest that avalanches exhibit scale-invariant dynamics where the occurrence of different avalanche sizes can be described by a probability distribution in the form of a power law.[21] The origin of such behavior is frequently related to self-organized criticality. Self-organized criticality can be seen as a generating mechanism for avalanches and associated scale-invariant dynamics.[22]

In general, critical dynamics universally occur in systems which are poised at the transition between two phases, which are composed of a multitude of dynamical units that influence each other.[20] There, a macroscopically observed avalanche may be triggered by a microscopic local change in the system that is collectively passed along the system due to the mutual interaction between single units. Several computational benefits have been described for this state, including the maximization of dynamic range, signal transmission and information capacity.[23] Based on this, it was hypothesized that the brain also operates at the edge of the transition between complete ordering and disordering.[24] With regard to memristive systems, hints on critical dynamics were found in networks of metal-insulator-metal switches (Ag–Ag_2S–Ag). This network showed spatially distributed switching throughout the network and power-law scaling of persistent metastable network states.[25] Recently, networks of Sn-NPs poised at the electrical percolation threshold (a second order phase transition) were shown to exhibit critical dynamics with corresponding avalanche patterns similar to those observed in neural tissues.[26] Critical dynamics in random networks of memristive switches are expressed by scale-invariance in dynamic features of the network. These dynamic features include the fluctuations in magnitude and temporal structure of network conductance that originate from the underlying memristive activity. Moreover, fluctuations of the network conductance are organized in avalanche patterns, which indicates that the memristive activity in the network is correlated. Characteristic for critical dynamics are scale-invariant distributions of avalanche sizes and durations.[26] Further, those networks implement long-range temporal correlations (LRTC), which is commonly a concomitant feature of critical dynamics. LRTC is a dynamical feature of a system, describing that the past activity of the system determines the future activity at any given time, which indicates capabilities to implement a dynamical memory. Such a dynamical memory is beneficial for mapping of temporal information into a system, a property that is important in the context of reservoir computing.[15,16] One common procedure for proving the presence of LRTC in a system is to demonstrate a power-law decay of the autocorrelation functions in the time domain.[27] Another indication for LRTC can be found by scale-invariant fluctuations in the network activity, also in the time domain. In this connection, detrended fluctuation analysis (DFA) is a frequently used method to characterize such scale-free fluctuation and to demonstrate LRTC.[28] Because of the dynamical memory properties, LRTC is seen as beneficial for neuromorphic computation approaches.[16] To implement critical dynamics and LRTC, both features that suggest brain-like degree of complexity, into neuromorphic systems tailoring the connectivity (by poising at the percolation threshold) within networks of NP-based memristive switches appear to be a feasible strategy. However, the practical applicability of this approach can be still debated and also the understanding of the origin of the emergent phenomena has to be improved. Particularly, an elaboration of this concept towards composite systems is still missing so far and would be beneficial to support practical applicability.

In this work, we extend the concept of implementing critical dynamics and LRTC for neuromorphic systems *via* Ag-NPs networks poised at the electrical percolation threshold (in the following named as "percolating NP networks") and address the question how filling the memristive gaps in the network with an insulating matrix influences the network dynamics and applicability. The use of Ag-NPs in this work is motivated by the fact, that the nanoscale behavior of Ag-NP-based memristive gaps is already well-understood,[8,29] which provides suitable complementary knowledge for future development, aiming to understand the emergence of collective phenomena in random memristive networks. A Haberland-type gas aggregation source (GAS)[30] was used for the vapor phase synthesis of Ag-NPs. Generally, a GAS offers a broad choice between elemental and alloy NPs and good control on the properties,[31] which allows to extend the engineering of memristive gaps towards Ag-based alloy NP systems with enhanced stability and degree of freedom.[29] For the practical application of percolating NP networks in neuromorphic systems maintaining their functionality within a composite system is highly relevant. This is because encapsulation of the network into an insulating medium is in most cases an inevitable step of electronic device integration. However, there is only insufficient knowledge

about the consequences on the overall network dynamics, when the character of the underlying memristive units are fundamentally altered by filling the gaps with an insulating material. This is because critical dynamics of percolating NP networks reported so far were in an exposed scenario, *i.e.* without encapsulation of the network. Although several reports on the electronic properties of composite systems comprising percolating NP networks exists,[32,33] a connection between the brain-like dynamics (*i.e.* critical dynamics and LRTC) and integration of percolating NP networks into insulating matrices has not yet been made. In particular, this poses questions regarding to the consequences for the network functionality (and therefore practical applicability), when the nature of the memristive gaps throughout the network is fundamentally altered by filling the gaps with an insulating matrix. Therefore, we fabricated exposed percolating NP networks and compared them with similar networks, which were covered with ceramic layers of SiO_xN_y. Comparing both network types, the nature of the memristive gaps is changed from air-type (for exposed NPs) to solid-state-type (for embedded NPs). Characterization of percolating NP networks is done by evaluating their temporal patterns of memristive switching activity in response to a constant stimulus (voltage input) towards hallmarks of brain-like behavior, such as critical dynamics[21] and LRTC.[27] For the quantification of LRTC, autocorrelation functions[34] and detrended fluctuation analysis[28] were applied. Critical dynamics in the network activity is demonstrated by the emergence of scale-invariance and the according power laws in dynamical network features. Particularly, this requires an avalanche analysis analogous to approaches used in neuroscience.[21] The main focus of this work is to demonstrate, that the network behavior applicable for neuromorphic systems (*i.e.* critical dynamics and LRTC) is preserved when an insulating matrix is added to the percolating NP network.

Results

Fig. 1 summarizes the fabrication route and illustrates morphological properties of percolating NP networks, as investigated in this work. Ag-NPs are synthesized following the GAS technique, as illustrated in Fig. 1a. Ag atoms are sputtered by a DC magnetron from a metallic target into a high-pressure sub-chamber leading to a vapor phase aggregation of NPs and transport along the pressure gradient from the GAS into a deposition chamber. High-resolution TEM images of individual Ag-NPs can be found in the ESI S1.† Networks of Ag-NPs were deposited onto lithographically structured Si wafer pieces with multiple electrode. The lateral filling fraction of the Ag-NPs corresponds to the electrical percolation threshold. To achieve this, the network conductance was monitored *in situ* during the deposition of Ag-NPs and the deposition was stopped after the onset of conduction, aiming for the critical dynamical regime.[26] This is elucidated in Fig. 1b, which shows the measured current flowing through the network during the deposition process with increasing Ag-NP filling fraction. The deposition of Ag-NPs was stopped at the steep slope of current increase (*i.e.* at the electrical percolation transition). For those samples in this work, where the dynamics were studied under the presence of an insulating matrix, networks were subsequently covered by a SiO_xN_y layer (from reactive magnetron sputter deposition) in the same vacuum system.

A schematic illustration of percolating NP networks is shown in Fig. 1c. In the critical regime around the percolation threshold, there is no conducting path of the size of the whole system scale, but a multitude of memristive gaps is randomly distributed through the whole network. It has been previously reported that NP networks poised at the percolation threshold have scale-free morphological properties, meaning that the number of potential memristive gaps per group of electrically connected NPs follows a power law distribution.[16] This means the conductance of percolating NP networks is not determined by a persistent conductive path, but by the states of all memristive gaps throughout the network. The state of memristive gaps are prone to be resistively switched by electrochemical metallization (ECM) upon application of external voltage stimuli. A SEM image showing the real morphology of a percolating NP network without matrix is given in Fig. 1d. An outline of the electrical behavior of percolating NP networks is given in Fig. 2a. There, a percolating NP network without matrix was tested under application of voltage pulses with varying amplitude. The current levels in response to external stimulation of 1 V can be interpreted by a persistent network state with stable conductance. This is reasoned by the fact, that fluctuations of the current level are too low to discriminate them against noise. In contrast to the response from 1 V pulses, the current levels exhibit distinct jumps between different levels at higher voltage amplitudes. These jumps originate from resistive switching activity of the memristive gaps, distributed through the whole network. Electrical fields across the memristive gaps are able to induce the formation or disintegration of filaments, switching the gaps to a conducting or insulating state, respectively.[35] Accordingly, resistive switching events, which are occurring in individual gaps, are changing the overall state of the network (in terms of conductance). We denote a distinct change of network conductance (which can be clearly discriminated against noise) as a network transition event. The exact definition of a network transition event used in this work is given in the methods part. While comparing the network responses at different voltages, it can be seen that the richness of network transition events appears to increase with the applied voltage, meaning that the frequency and magnitude of network transition events becomes larger with increasing the voltage amplitude. We quantified this observation by the coefficient of variations CV (ratio of standard deviation to the mean) calculated for the current responses from each individual pulse (see methods). By this, CV characterizes the fluctuation of network conductance observed within one applied voltage pulse. A scatter plot of the CV for nine pulses plotted against pulse voltage is given in Fig. 2b, which indicates that the fluctuation of the network conductance levels increase with voltage amplitude. This can be related to the typical threshold behavior of filament-type memristive gaps. It is commonly reported for Ag-based NP memristive switching[8,29] and individual Ag-filaments in a nanogap[10] that they exhibit a threshold behavior in their switching dynamics. The origin of

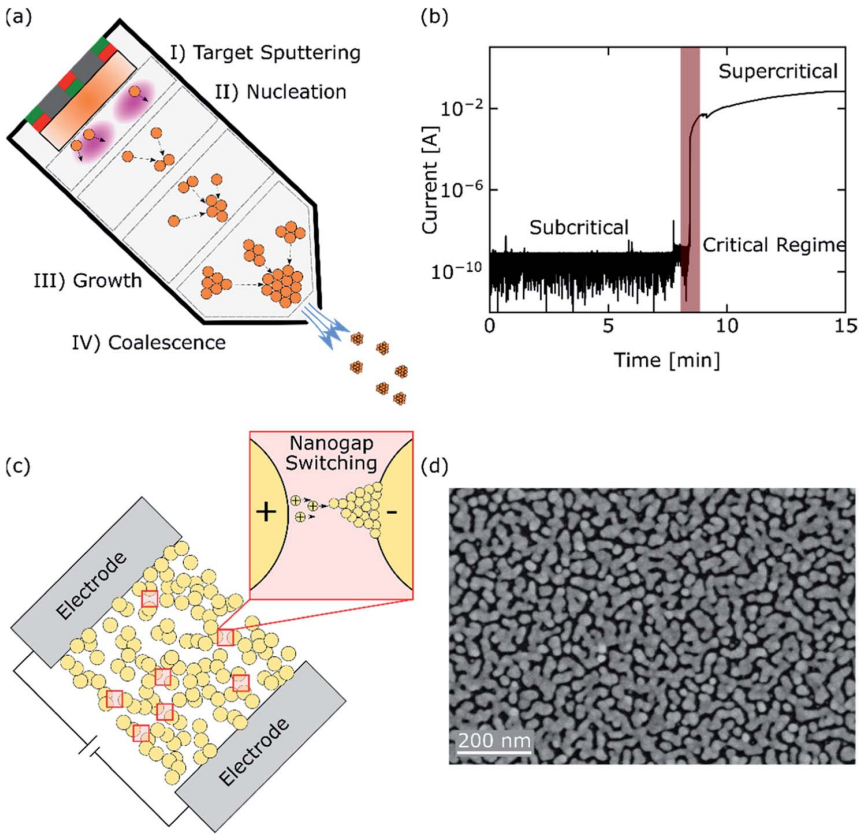

Fig. 1 (a) Principle of Ag-NPs deposition by GAS. Target sputtering *via* a DC magnetron and formation of NPs in the gas phase is done in a sub-chamber separated from the deposition chamber. The NPs are transported along the pressure gradient to the deposition chamber, forming a beam of NPs oriented towards the substrate. (b) Electrical percolation transition detected *via in situ* current measurements during the deposition of Ag-NPs. For the fabrication of percolating NP networks, the deposition of Ag-NPs was stopped at the onset of conduction, which marks the critical regime. (c) Schematic illustration of percolating a NP networks. The state of the network (in terms of overall conductance between the electrodes) is not defined by a dominating conducting path, but is subject to ongoing transitions between different metastable states due to the activity of memristive gaps throughout the network. The inset illustrates a growing filament by ECM, which is the dominating memristive mechanism in Ag-based systems. (d) SEM image of a percolating NP network without matrix.

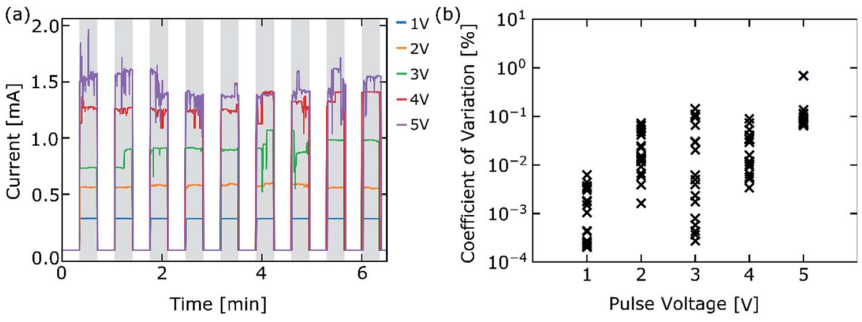

Fig. 2 (a) Dynamics of percolating NP networks under voltage pulse stimulation with different amplitudes. The voltage is pulsed between 0 (white regions) and the chosen voltage (1 V to 5 V, grey regions). An activity threshold can be observed, where no network transition events are observed for 1 V pulses and the dynamics becoming richer with increasing voltage amplitude. (b) Current fluctuations in individual pulses quantified in terms of coefficient of variation (standard deviation divided by mean) shown as scatter plot. It can be seen, that fluctuations of current levels, which indicates frequency and magnitudes of network transition events, are increasing with pulse voltage.

such a threshold behavior mainly comes from the underlying cation mobility and redox processes.[7] Presumably, the threshold behavior of the macroscopic percolating NP network is a reflection of the underlying threshold mechanisms of individual memristive gaps. The presence of a threshold behavior for switching activity was similarly observed in networks with insulating matrix, as illustrated in the ESI S2.†

Long-term sequence of network transition events

The percolating NP networks are investigated towards the emergence of brain-like dynamics (critical dynamics and LRTC) in their electrical response. A particular focus lies on the question whether the existence of an insulating matrix (filling the memristive gaps) changes the network functionality. For this purpose, in total six percolating NP networks were fabricated and an SiO_xN_y matrix was added to three of them. The other three samples remained exposed. To acquire the network dynamics (*i.e.* the temporal sequence of network transition events), long-term current measurements over similar measurement times of ≈11.5 h were conducted (see methods). All samples were stressed with the same external bias level of 5 V. A representative time window of 2 h of the current response for a network without matrix is plotted in Fig. 3 (top). It illustrates the complex memristive switching pattern with a multitude of transitions between different conductance states. For the sake of convenience, values related to the network conductance are given in units of conductance quantum $G_0 = 7.748 \times 10^{-5}$ S. Values in the order of G_0 are typical for percolating NP networks and emerges in the limit where the conductance is limited by nanoscale gaps and corresponding atomic scale filaments.[36] Microscopically the observed pattern results from the complex and recurrent interconnectivity of a large number of memristive gaps in the network. A memristive switching event locally at a certain gap leads to a redistribution of the electrical fields within the network, which in turn could trigger switching at other gaps. By this, disturbance of one memristive gap could lead to a prolonged cascade of transitions between multiple metastable conductance states of the whole network. This mechanism leads to the characteristic avalanche behavior of percolating NP networks. A thresholding routine (see methods) was applied to the temporal sequence of conductance changes to extract the network transition events and to discriminate them against noise. In particular, all transition events below 0.01 G_0 were omitted, which is above the noise level of the measurement setup. By this, all network transition events contributing to the evaluation are real effects from the samples and noise effects from the measurement setup are excluded. Illustrations of the thresholding procedure are further given in the ESI S3 and S4.† The temporal sequence of network transition events resulting from the 2 h window displayed in Fig. 3 is shown in the bottom panel. A first glance suggests that the network transition events appear to be more clustered than it would be expected by chance. This is a first indication on temporal correlations and avalanche-like dynamics in the temporal sequence of transition events.

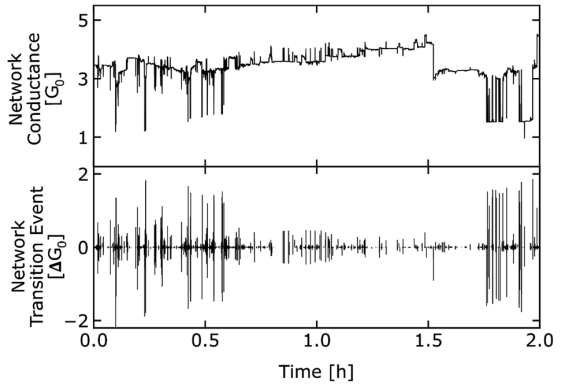

Fig. 3 Top: Measured conductance of a percolating NP network without matrix upon constant voltage application of 5 V. (2 h extract from the overall measurement). The representation is given in conductance units of G_0 for convenience ($G_0 = 2e^2/h = 7.748 \times 10^{-5}$ S). The dynamics corresponds to transitions between different metastable states in the network. Bottom: Temporal sequence of network transition events extracted from the upper panel.

Long-range temporal correlations

In biological neuronal networks, information is present in collective activity patterns showing self-affine properties and presence of LRTC.[27] Furthermore, LRTC is a phenomenon that frequently coexists with critical dynamics of biological neuronal networks.[27] To identify self-affine properties and LRTC in the temporal sequence of network transition events, temporal correlations were quantified by two different methods:

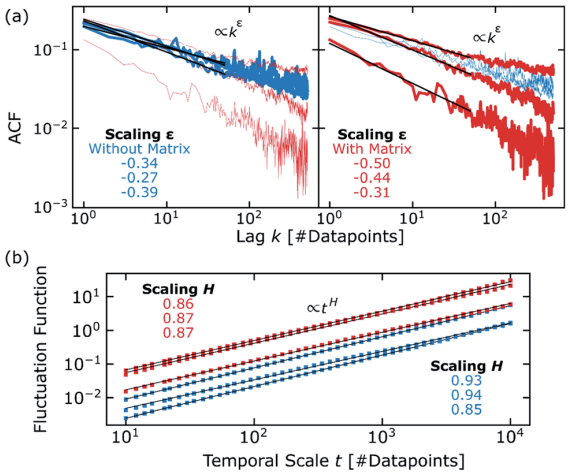

Fig. 4 Analysis for LRTCs in the temporal sequence of network transition events. Color code for samples without/with matrix is blue/red. Two different methods were applied: ACFs as shown in (a) and DFA as shown in (b). The ACFs (left/right panel emphasizes samples without/with matrix) are governed by slow decay in form of a power law, suggesting the existence of LRTCs. Decay slopes ε were estimated by linear regression unit a lag k of 50 data points. The determined slopes are annotated in the plots. The DFA confirms the positive LRTCs by means of Hurst exponents H over 0.85. The values for all Hurst exponents as determined by linear regression are given in the plot.

autocorrelation functions (ACFs) and detrended fluctuation analysis (DFA). The ACFs shown in Fig. 4a suggests a slow correlation decay in the form of a power law, which implies that network transition events in the past have a significant influence on current events. Such a behavior is considered as a long-term memory in temporal processes.[28] In addition, calculating the ACFs of shuffled temporal sequences of network transition events results in complete destruction of any correlation (see ESI S5†). Decay slopes ε of the ACFs were determined *via* linear regression in a shorter range until a lag k of 50 data points and showed that the slopes for percolating NP networks with insulating matrix tend to be only slightly higher than for networks without. More importantly, the presence of autocorrelation remains, even after addition of an insulating matrix. We note that the comparison in ACFs between networks with and without matrix is elaborated here based on a representation until a maximum lag of 500 data points, however, we emphasize that autocorrelation is still existent in all samples up to higher lags too (see ESI S6†).

The second method, DFA, is an already well-established tool in neurobiology to detect LRTC in neural oscillations and to find estimations for the Hurst exponent.[28] In this context, Hurst exponents are used to determine whether neuronal activity is positively or negatively correlated and to quantify the extent of temporal correlations.[28] The major advantage of DFA is that it can be applied to non-stationary temporal sequences. Since it is expected that critical dynamics imposes a considerable non-stationarity (due to the characteristically occurring avalanches, as described in the next sections), we applied DFA to the temporal sequence of network transition events to gain insights that are complementary to the ACFs. The results of the DFA, which are log-log plots of the fluctuation function (quantifies the temporal fluctuation of network transition events, see methods or ref. 28) *versus* temporal scale t (window size as number of data points showing the degree of fluctuation, see methods or ref. 28) where the linear scaling H is an estimation of the Hurst exponent. The DFA results are given in Fig. 4b. Here, the Hurst exponent describes correlations in the activity (*i.e.* temporal sequence of network transition events) of the percolating NP networks, analogously to approaches from neuroscience. Power law scaling is observed for the whole observed range indicating strong LRTC. Moreover, the magnitudes of Hurst exponents confirm positive correlations for all samples, as already observed from the ACFs.[28,34] Conducting the DFA with shuffled temporal sequences also leads to destruction of any temporal correlation, which is expressed by a strongly decreased Hurst exponent (see ESI S7†). The DFA supports the most important observation from the ACF analysis regarding the impact of adding an insulating matrix for the network functionality. Only minor variations on the qualitative level (networks with matrix exhibit slightly higher fluctuation functions and lower Hurst exponents) can be supposed, however, the presence of strong positive correlations does not considerably change after addition of an insulating matrix.

Scale-invariant dynamics

Further evaluation with respect to brain-like dynamics in percolating NP networks with and without matrix is dedicated to power-law behavior and occurrences of avalanches. For this purpose, the statistical features of thresholded network transition events (see Fig. 3 bottom for representative illustration) were investigated. This includes the magnitude of a network transition event ΔG, given as absolute change of network conductance. Further, the temporal structure of the network transition events was quantified by interevent intervals IEI, which is the time between two consecutive events. Probability density functions (PDFs) of the extracted magnitudes of network transition events are plotted together with the according power law fits (by maximum-likelihood method) in Fig. 5a and b. The power law fits show good agreement to the observed PDFs over the whole experimental range. To confirm the existence of heavy-tails in the distributions, likelihood-ratio tests[37] including the whole observed range were applied to test the power law fitting against a potentially better description by exponential PDFs. For all samples, power law fits were statistically more significant than exponential fits, which underlines the scale-invariance of the ΔG distribution over the observed range. A scale-invariant distribution of network transition events ΔG indicate, that numerous gaps distributed all over the network are involved in the observed dynamics. The calculated power law exponents β are describing the scaling of ΔG for the six samples and show close similarities. They were determined as 1.68, 1.65 and 1.72 for networks without and 1.69, 1.54 and 1.47 for networks with insulating matrix.

Furthermore, PDFs of the extracted IEIs together with the according power law fits involving the whole observed range are given in the panels of Fig. 5c and d. Again, likelihood-test confirmed that power laws are more significant representations of the data than exponential PDFs. The occurrence of scale-invariant IEI distributions is, besides the results from ACFs and DFA, another characteristic for a temporally correlated structure. We note that the observed range of IEIs for percolating NP networks without insulating matrix extends over 4 orders of magnitude, as given in Fig. 5c, whereas the observed range in case of existence of an insulating matrix is narrower, with a stronger truncation at higher IEI values. However, this is likely to be an effect of slightly higher event rates observed for networks with insulating matrix, as discussed in the ESI S8.† The power law exponent γ describes the scaling of IEIs. γ ranged from 1.48 to 1.58 for networks without insulating matrix and from 1.47 to 1.61 for networks with insulating matrix. Taking into account that the power law exponents β and γ, describing the magnitudes and temporal structures of network transition events, respectively, are closely similar, the results indicate that all samples behaved in a similar way.

Avalanche analysis

Fig. 6 depicts the evaluation of the temporal sequence of network transition events with respect to avalanches. The evaluation scheme for avalanche was adapted from approaches in neuroscience.[21] For avalanche analysis, the temporal sequence is cut into time bins, which have the size of the mean value of all IEIs. An avalanche is defined by a sequence of time bins where each bin shows at least one network transition

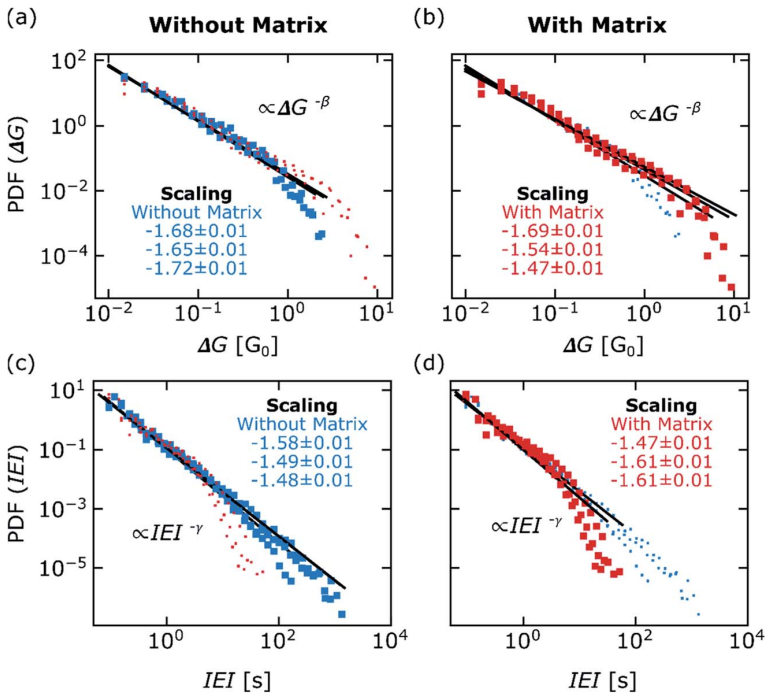

Fig. 5 Observed probability density functions (PDFs) of network transition event magnitudes ΔG quantified as changes in network conductance (a/b for samples without/with insulating matrix) and interevent intervals IEIs (c/d for samples without/with insulating matrix) together with power law fits calculated by maximum-likelihood estimation. Color code for samples without/with insulating matrix is blue/red. The estimated power law exponents β and γ, for the ΔG an IEI distributions, respectively, are annotated in the plots with standard errors as uncertainty.

event. Then, avalanche sizes S and durations T are defined as number of network transition events and number of time bins within one avalanche, respectively. The observed PDFs of avalanche sizes S together with the according power law fits over the whole observed range are shown in Fig. 6a and b. Plots of the observed PDFs for avalanche durations T are shown in Fig. 6c and d, again with power law fits over the whole observed range. In these plots, τ and α denote the power law exponents of avalanche sizes and durations, respectively. The representation scheme and color codes are the same as in Fig. 5. Likelihood-ratio tests including the whole observed range again showed that power laws are better descriptions for avalanche size and duration PDFs than the exponential form. To extract the power law exponents from avalanche size and duration PDFs, lower bounds $x_{\min}$ (see methods) were estimated to account for the apparent deviations from power law behavior at small scales. To estimate suitable bounds in the low value regime, we followed the guidelines developed in ref. 37 and 38. The power law exponents together with standard errors as uncertainties, which were calculated under application of a $x_{\min}$ value, are given as insets in the plots of Fig. 6. The corresponding fits of values above $x_{\min}$ are provided in the ESI S9.†

Differences in the avalanche statistics between percolating NP networks with and without insulating matrix are becoming apparent. Firstly, the probability for larger scale avalanche sizes and durations is higher for networks without insulating matrix. Secondly, different tendencies in the calculated power law exponents were observed. The power law scaling τ for networks without insulating matrix were 2.94, 1.98 and 2.15 whereas the scaling was steeper for networks with insulating matrix (3.55, 3.58 and 3.85). The same tendency was observed for avalanche durations where values for α were estimated as 4.09, 3.35 and 2.46 for networks without and 5.19, 4.78 and 5.26 for networks with insulating matrix.

In order to characterize another property of critical dynamics,[39,40] the dependence between the mean avalanche size $S(T)$ for given durations T is plotted, as shown in Fig. 6e and f. From this, the characteristic power law exponent $\frac{1}{\sigma\nu z}$ can be extracted *via* the slope of $S(T)$. For percolating networks without insulating matrix, the mean avalanche size for a given duration scales with 1.4, 1.5 and 1.3, whereas the scaling was 1.2, 1.2 and 1.2 for networks with insulating matrix. According to theory, the power law exponent for avalanche size τ and durations α are connected to $\frac{1}{\sigma\nu z}$ *via* the crackling noise relationship:[39,40]

$$\frac{\alpha - 1}{\tau - 1} = \frac{1}{\sigma\nu z} \quad (1)$$

An overview of the evaluation of this relationship for all samples is given in Table 1. Although the theoretical crackling noise relationship is not perfectly met by most of the samples, the experimentally determined values are in reasonable

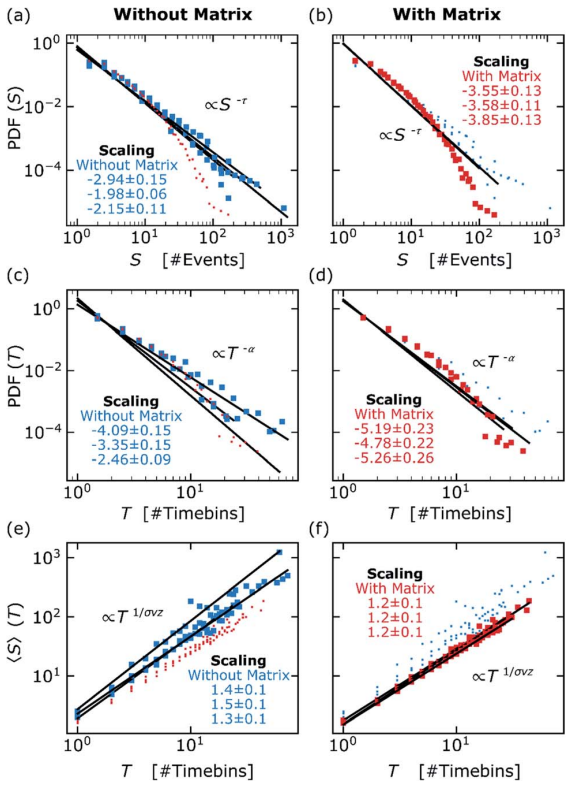

Fig. 6 Analysis of the temporal sequence of network transition events towards avalanches. Color code for samples without/with insulating matrix is blue/red. (a) and (b) show the PDFs of avalanche sizes S together with a maximum-likelihood power law fit over the whole observed range for samples without and with insulating matrix, respectively. The power law exponents τ noted within the plots were not calculated based on (the shown) fits over the whole range, but under application of a x_{min} value. Reduced plots showing the fits above x_{min}, which were decisive for extracting the exponents τ, are given in the ESI S9.† The uncertainties given for the power law exponents equals the standard error. (c) and (d) show the PDFs of avalanche durations T following the same evaluation scheme, as for avalanche sizes. (e) and (f) show the dependence between mean avalanche size $S(T)$ and avalanche duration T. From these slopes, the characteristic power law exponents $\frac{1}{\sigma\nu z}$ were extracted by linear regression for each sample.

Table 1 Evaluation of the crackling noise relationship for all percolating NP networks

System	Sample	$\frac{\alpha-1}{\tau-1}$	$\frac{1}{\sigma\nu z}$
Without insulating matrix	1	1.6 ± 0.2	1.4 ± 0.1
	2	2.4 ± 0.4	1.5 ± 0.1
	3	1.3 ± 0.3	1.3 ± 0.1
With insulating matrix	4	1.6 ± 0.2	1.2 ± 0.1
	5	1.5 ± 0.2	1.2 ± 0.1
	6	1.5 ± 0.5	1.2 ± 0.1

agreement, with only one sample without insulating matrix (sample 2) as exception. However, we note that this does not change the representative character of sample 2, because it exhibits all more significant hallmarks on critical dynamics (LRTC, scale-invariant network dynamics and avalanches) in line with all other samples. Generally, the evaluation of the crackling noise relationship crucially requires accurate estimations of the exponents α and τ, which could not have been the case for sample 2. Nonetheless, the crackling noise relationship provides additional support, that critical dynamics are observed in percolating NP networks without matrix, as well as for networks where an insulating matrix was added.

Discussion

The results in this work demonstrate that the implementation of brain-like behavior, such as critical dynamics or LRTC, *via* NP networks poised at the percolation threshold is feasible for a broader range of material systems. In contrast to similar NP-based memristive networks in the literature,[26,41] the memristive activity Ag-NP based networks presented here is expected to be significantly dominated by electrochemical metallization (ECM).[8,35,42] More importantly, the comparison between percolating Ag-NP networks with and without a SiO_xN_y matrix shows, that the switching dynamics is preserved after the addition of an insulating matrix. Similar network behavior, in terms of temporal correlations in the sequence of network transition events, scale-invariance of dynamical features like magnitudes of network transition events and interevent intervals and presence of scale-invariant avalanches, was observed in both systems. This indicates that the collective behavior of memristive gaps is preserved upon addition of SiO_xN_y. These observations lead to important implications regarding the practical application of percolating NP networks. The results imply that tailoring the network connectivity (which is done here by the electrical percolation threshold) and insulating matrix integration (through addition of a ceramic layer) can be treated as independent from each other in the fabrication procedure. This is highly beneficial, because the establishment of network functionality (*i.e.* critical dynamics and LRTC) still solely requires tailoring of the NP filling factor and a deliberate insulating matrix integration does not considerably affect these functionalities.

From a general point of view, the dynamics in a system of highly interconnected dynamical units crucially depends on the underlying network connectivity[23,43] and dynamical properties of the individual units,[44,45] which makes both features important for the engineering of critical dynamics and LRTC in memristive material systems. Regarding the properties of individual memristive gaps, it can be expected that their dynamics are governed by a volatile character. This can be argued from the fact that rather low currents are flowing through individual gaps during formation of filamentary structures, which commonly leads to formation of thin (and therefore volatile) filaments.[10,29] Comparable volatile dynamics were, for instance, also observed for Ag/PVP/Ag cross-points in Ag-nanowire networks.[46] Moreover, it is expected that the

memristive gaps do not behave uniformly, but that the degree of volatility underlies a certain variance. This is reasoned by the fact, that the time for spontaneous decay of a filament strongly depends on parameters like the filament thickness or curvature on the filamentary structures, which was comprehensively described for the dynamics in Ag-nanowire/silk/Ag-nanowire cross-point structures.[47] The observed similarity in the critical dynamics and LRTC of both systems is to a certain degree surprising, because the underlying ECM-based physical mechanisms, by which filaments within the memristive gaps are formed and disintegrated,[8,29,48] are presumably altered upon addition of an insulating layer like SiO_xN_y. Consequently, the dynamical properties of individual memristive gaps are also expected to be altered. Major consequences of adding a matrix would include for instance, that the migration of Ag^+-species is now enabled within a volume instead of migration on a surface (when a matrix is missing). Furthermore, the interfacial energies of filaments and diffusivity of Ag-species, which affects filament morphology, are altered.[8,47] Although the conditions, that are responsible for the memristive gap dynamics, are different for percolating NP networks with and without matrix, our results suggests that the underlying dynamics behave similarly. A possible explanation for this can be provided from a kinetic point of view, under the assumption that a common rate determining mechanism influences the dynamics of both systems similarly. According to literature,[35,42] the ECM-based memristive dynamics of filamentary Ag-structures can be kinetically limited by one of three different mechanisms, which contribute to the formation of filaments: Nucleation at cathodic sites (which initiates filamentary growth), migration of Ag^+-species across the gap or electron-transfer at the Ag-gap interface during electrochemical oxidation. If one of these three mechanisms is rate limiting for the percolating NP networks with and without matrix, from a kinetic viewpoint, this mechanism could determine the dynamics equally in both systems. We expect that rate limitation by nucleation does not play a role for percolating Ag-NP networks, because a growing filament and a cathodic site will be the same metal, which consequently excludes any significant nucleation barrier. Further, the migration of Ag^+-species across the gaps is not considered as a common rate-determining step, because surface migration (networks without matrix) and volume migration (with matrix) are expected to behave kinetically different. Only the electron-transfer rate at the Ag-gap interface, mainly depending on the kind of active metal, could contribute similar kinetics to both systems. Reasoning from a kinetic point of view, a common rate determining mechanism will most likely result in a similar behaviour of both systems. We thus propose that a similarity in the electron-transfer rate of both systems (with and without insulating matrix) could be an explanation for the similarity in the observed dynamics.

Conclusion and outlook

In conclusion, we expand the concept of implementing brain-like critical dynamics and LRTCs *via* percolating NP networks for neuromorphic applications[26] towards Ag-NP based systems, where the memristive gap dynamics is governed by electrochemical metallization. The network dynamics were characterized *via* ACFs and DFA (indicating the existence of LRTCs) and analysis of scale-invariant dynamical features and avalanches (indicating critical dynamics). More importantly, it was shown that these functionalities are preserved, when insulating SiO_xN_y matrices were added onto the percolating NP networks, which fundamentally changes the nature of memristive gaps from air-type to solid-state type. This was supported by the absence of qualitative differences in the critical dynamics and LRTCs of networks with and without matrix. Both systems exhibited long-range temporal correlations in the sequence of network transition events, scale-invariance of dynamical features like magnitudes of network transition events and interevent intervals and presence of scale-invariant avalanches. These findings strengthen the prospects regarding to practical applicability of percolating NP networks in neuromorphic systems, because embedding the system (which must be carefully poised at the percolation transition) without functionality loss is inevitable for a potential device integration procedure. For future progress in this field, we suggest to combine the understanding of nanoscale Ag-based electrochemical memristive switching dynamics (which has been extensively studies in a broad range of materials systems) with network science approaches, to model the collective network behavior. This may allow for understanding of the emergent features observed here for the percolating Ag-NP networks, and especially may elucidate further details on the impact of an insulating matrix.

Materials and methods

Preparation of percolating NP networks

Conventional UV lithography processes (application of image reversal photoresist and a lift-off process) were used to fabricate electrode structures on commercial Si-wafers with 1 μm thick thermal oxide (Siegert Wafer), as illustrated in the ESI S10.† Either Au or Pt in combination with an adhesion promoter were used as electrode materials (thickness varied between 50 nm and 80 nm) due to their electrochemical passivity. A custom-built Haberland-type GAS[30] attached to an in-house high vacuum deposition setup was used for the deposition of the Ag-NPs to build up the network in the spacing (~10 μm) between the electrodes. During the deposition of the Ag-NPs a potential of 3 V was applied across the electrodes and the current was monitored continuously using a Keithley 2450 source measure unit and an electrical feedthrough system. The deposition of Ag-NPs was stopped by a shutter system after detection of the electrical percolation transition (see Fig. 1b where the electrical percolation transition becomes apparent at around 8.5 min). When required, the insulating matrix was deposited from another DC magnetron in same deposition chamber without breaking the vacuum by reactive sputtering from a Si target and under a gas mixture of 50 sccm Ar and 0.44 sccm N_2. Qualitative XPS analysis (see ESI S11†) indicates that the resulting matrix material is silicon oxynitride, formed by oxidation subsequent to the deposition. The effective thickness of the covering matrix was 22 nm. The SEM micrograph that was taken from

a percolating NP network without matrix deposited on an electrode structure as described above, conducted on a Zeiss Ultra Plus microscope.

Measurement of network dynamics

For the present study, the dynamics of 6 percolating Ag-NP networks was probed with 3 samples having no matrix and 3 samples having a silicon oxynitride matrix. To probe the network dynamics, the samples were measured by continuous detection of the current response (with 84 ms temporal resolution) to the application of a constant DC bias using a Keithley 2400 source measure unit. For each of the 6 samples, a continuous long-term measurement of $\approx$11.5 h under a DC potential of 5 V was performed. The data in Fig. 2a was acquired under pulsed stimulation (with high levels at different amplitudes ranging from 1 V and 5 V and a low level of always zero) with a pulse width of approximately 20 s.

Coefficient of variation

The coefficient of variation (CV) was applied to characterize the fluctuations of current levels observed during the pulse stimulation measurement, as shown in Fig. 2a. The CV was calculated for the current data acquired at each pulse and is given as

$$\mathrm{CV} = \frac{\sigma}{\mu} \tag{2}$$

where σ is the standard deviation and μ is the mean. The scatter plot (Fig. 2b) shows the CV among all pulses of the measurement plotted *versus* pulse amplitude.

Autocorrelation function

The autocorrelation function (ACF) ρ_k of a discrete temporal for a given lag k can be estimated as[34]

$$\rho_k = \frac{\frac{1}{N-k-1}\sum_{i=k+1}^{N}(x_i-\mu)(x_{i-k}-\mu)}{\frac{1}{N-1}\sum_{i=1}^{N}(x_i-\mu)^2} \tag{3}$$

where N is the total length of the temporal sequence, x_i is an element of the temporal sequence and μ is the total mean of the temporal sequence. The ACF was applied for the temporal sequence of (non-thresholded) absolute changes in the network conductance. The power law scaling ε of the ACFs was determined by linear regression up to a lag of 50 datapoints.

Detrended fluctuation analysis

Detrended fluctuation analysis (DFA) was used as a second method to characterize temporal correlations and self-affinity in the temporal sequence of (non-thresholded) absolute conductance changes. The major advantage of DFA is that influences from non-stationaries (which are expected for the present data due to alternating periods with avalanche activity and absent activity) are reduced in the quantification. The following DFA algorithm according to ref. 28 was applied, which can be used to extract the Hurst coefficient H of a discrete time series:

Firstly, the mean subtracted cumulative sum series y_t of the time series x_i can be calculated

$$y_t = \sum_{i=1}^{t} x_i - \mu \tag{4}$$

where μ denotes the mean. For 50 different window sizes W (equally distributed on the logarithmic scale), the series y_t can be split into boxes with 50% overlap. For each box (with a specific window size W), the linear trend can be removed *via* linear regression and the standard deviation of the box σ_iW can be calculated. For all of the 50 different window sizes, the fluctuation function $F(W)$ can be calculated as the mean of all standard deviations with equal box size.

$$F(W) = \sigma_i \mathrm{W} \tag{5}$$

Finally, the fluctuation function $F(W)$ can be plotted *versus* window size W on a double logarithmic scale. The slope of $F(W)$ calculated *via* linear regression delivers an estimation of the Hurst exponent H.

Power law statistics and avalanche analysis

Prior to power law and avalanche analysis, a thresholding procedure (see ESI S3 and S4†) was applied to discriminate network transition events in the network state against noise. A network transition event in the context of this work means a measurable change in conductance of a percolated NP network, which in addition satisfies the following thresholding procedure. As a first thresholding condition, all changes in conductance smaller than 0.01 G_0 were discarded to account for the noise level of the electrical measurement instrumentation. As a second condition, only switching events were taken into the evaluation, which exceed fluctuations of 3 standard deviations (defined by the past 30 values in the temporal sequence). Only above-threshold transition events were subject to the power law and avalanche analysis. All probability density function (PDF) fittings in this work were done using the Python package "*Powerlaw*".[37] This Python package follows the principles developed in ref. 38. These fittings have the general power law form (where x is the distributed quantity and b is the power law scaling exponent)

$$f(x) \propto x^{-b} \tag{6}$$

PDF fittings of network transition event magnitudes ΔG and interevent intervals IEIs were done by maximum likelihood estimation of the power law exponents β and γ, respectively. Fitting of ΔG and IEIs PDFs was done over the whole observed range.

Avalanches were defined analogously to the common evaluation scheme as in neurobiology.[21] The temporal sequence of network transition events is separated into time bins having the width of the mean IEI value. An avalanche is defined as a sequence of bins, where each bin shows at least one transition event. Avalanches are separated by periods with absent activity (*i.e.* sequential bins having zero transition events). The avalanche size S is determined as number of transition events in one avalanche and the avalanche duration T is the number of time bins. The fitted PDFs for avalanche sizes and distributions

as shown in Fig. 6 are done *via* maximum likelihood estimation without a lower bound x_{min}, to show the good agreement of power laws with the whole observed range. The maximum likelihood estimations of the exponents τ and α, instead, were performed by constraining the PDF fitting to a lower bound x_{min}, to account for slight deviation at small scale occurrences. The value for x_{min} was determined by minimization of the Kolmogorov–Smirnov distance (as proposed by ref. 38) and under the additional constraint that $\sigma/b < 0.05$ (σ is the standard error of the estimated power law exponent) to exclude that x_{min} is chosen too high and valid data will be discarded. All fits above x_{min}, that were decisive for estimating the power law exponents τ and α as mentioned in Fig. 6 are given in the ESI S9.†

All fitted power law PDFs in this work were tested against exponential PDF (which could be indicative of non-correlated temporal sequences) with respect to the whole observed range *via* likelihood-ratios, as proposed in ref. 38. Each test suggested, that the power law form is the better description than the exponential form under confirmation of statistical significance (we observed p-values $\ll 0.1$). Furthermore, the whole power law and avalanche analysis was representatively done for a shuffled temporal sequence of network transition events from a sample without insulating matrix, as shown in the ESI S12.† There, it can be seen that power law statistics become destroyed upon shuffling the sequence of network transition events, which indicates loss of correlated activity.

Data availability

The data generated and analyzed in this study are available from the corresponding author on reasonable request.

Author contributions

Conceptualization: N. C., A. V., F. F.; Formal analysis: N. C., A. V.; Funding acquisition: A. V., F. F.; Investigation: N. C., B. A.; Methodology: N. C., S. B.; Supervision: A. V., S. B., F. F., T. S.; Visualization: N. C.; Writing – original draft: N. C.; Writing – review and editing: A. V., B. A., F. F., S. B., T. S.

Conflicts of interest

The authors declare no conflict of interest.

Acknowledgements

The authors would like to thank Ole Gronenberg and Lorenz Kienle for performing the TEM investigations and providing TEM images. Funded by the Deutsche Forschungsgemeinschaft (DFG, German Research Foundation) – Project-ID 434434223 – SFB1461.

References

1 M. A. Zidan, J. P. Strachan and W. D. Lu, *Nat. Electron.*, 2018, **1**, 22–29.
2 J. D. Kendall and S. Kumar, *Appl. Phys. Rev.*, 2020, 7(1), DOI: 10.1063/1.5129306.
3 T. Zhang, K. Yang, X. Xu, Y. Cai, Y. Yang and R. Huang, *Phys. Status Solidi Rapid Res. Lett.*, 2019, **13**, 1–21.
4 Y. Van De Burgt, A. Melianas, S. T. Keene, G. Malliaras and A. Salleo, *Nat. Electron.*, 2018, **1**, 386–397.
5 S. Saïghi, C. G. Mayr, T. Serrano-Gotarredona, H. Schmidt, G. Lecerf, J. Tomas, J. Grollier, S. Boyn, A. F. Vincent, D. Querlioz, S. La Barbera, F. Alibart, D. Vuillaume, O. Bichler, C. Gamrat and B. Linares-Barranco, *Front. Neurosci.*, 2015, **9**, 1–16.
6 J. Q. Yang, R. Wang, Y. Ren, J. Y. Mao, Z. P. Wang, Y. Zhou and S. T. Han, *Adv. Mater.*, 2020, **32**, 1–32.
7 J. H. Cha, S. Y. Yang, J. Oh, S. Choi, S. Park, B. C. Jang, W. Ahn and S. Y. Choi, *Nanoscale*, 2020, **12**, 14339–14368.
8 Z. Wang, S. Joshi, S. E. Savel'ev, H. Jiang, R. Midya, P. Lin, M. Hu, N. Ge, J. P. Strachan, Z. Li, Q. Wu, M. Barnell, G. L. Li, H. L. Xin, R. S. Williams, Q. Xia and J. J. Yang, *Nat. Mater.*, 2017, **16**, 101–108.
9 R. Midya, Z. Wang, S. Asapu, S. Joshi, Y. Li, Y. Zhuo, W. Song, H. Jiang, N. Upadhay, M. Rao, P. Lin, C. Li, Q. Xia and J. J. Yang, *Adv. Electron. Mater.*, 2019, **5**, 1–7.
10 N. Carstens, A. Vahl, O. Gronenberg, T. Strunskus, L. Kienle, F. Faupel and A. Hassanien, *Nanomaterials*, 2021, **11**, 1–16.
11 Z. Kuncic and T. Nakayama, *Adv. Phys. X*, 2021, **6**(1), DOI: 10.1080/23746149.2021.1894234.
12 S. K. Bose, J. B. Mallinson, R. M. Gazoni and S. A. Brown, *IEEE Trans. Electron Devices.*, 2017, **64**, 5194–5201.
13 H. O. Sillin, R. Aguilera, H. H. Shieh, A. V. Avizienis, M. Aono, A. Z. Stieg and J. K. Gimzewski, *Nanotechnology*, 2013, **24**(38), DOI: 10.1088/0957-4484/24/38/384004.
14 C. Du, F. Cai, M. A. Zidan, W. Ma, S. H. Lee and W. D. Lu, *Nat. Commun.*, 2017, **8**, 1–10.
15 G. Milano, G. Pedretti, K. Montano, S. Ricci, S. Hashemkhani, L. Boarino, D. Ielmini and C. Ricciardi, *Nat. Mater.*, 2022, **21**, 195–202.
16 S. Shirai, S. K. Acharya, S. K. Bose, J. B. Mallinson, E. Galli, M. D. Pike, M. D. Arnold and S. A. Brown, *Netw. Neurosci.*, 2019, **4**, 432–447.
17 C. Minnai, A. Bellacicca, S. A. Brown and P. Milani, *Sci. Rep.*, 2017, **7**, 1–8.
18 A. Diaz-Alvarez, R. Higuchi, P. Sanz-Leon, I. Marcus, Y. Shingaya, A. Z. Stieg, J. K. Gimzewski, Z. Kuncic and T. Nakayama, *Sci. Rep.*, 2019, **9**, 1–13.
19 J. Hochstetter, R. Zhu, A. Loeffler, A. Diaz-Alvarez, T. Nakayama and Z. Kuncic, *Nat. Commun.*, 2021, **12**, DOI: 10.1038/s41467-021-24260-z.
20 D. R. Chialvo, *Nat. Phys.*, 2010, **6**, 744–750.
21 J. M. Beggs and D. Plenz, *J. Neurosci.*, 2003, **23**, 11167–11177.
22 P. Bak, C. Tang and K. Wiesenfeld, *Phys. Rev. A*, 1988, **38**, 364–374.
23 W. L. Shew and D. Plenz, *Neuroscientist*, 2013, **19**, 88–100.
24 J. Hesse and T. Gross, *Front. Syst. Neurosci.*, 2014, **8**, 1–14.
25 A. Z. Stieg, A. V. Avizienis, H. O. Sillin, C. Martin-Olmos, M. Aono and J. K. Gimzewski, *Adv. Mater.*, 2012, **24**, 286–293.
26 J. B. Mallinson, S. Shirai, S. K. Acharya, S. K. Bose, E. Galli and S. A. Brown, *Sci. Adv.*, 2019, **5**, eaaw8438.
27 K. Linkenkaer-Hansen, V. V. Nikouline, J. M. Palva and R. J. Ilmoniemi, *J. Neurosci.*, 2001, **21**, 1370–1377.

28 R. Hardstone, S. S. Poil, G. Schiavone, R. Jansen, V. V. Nikulin, H. D. Mansvelder and K. Linkenkaer-Hansen, *Front. Physiol.*, 2012, 1–13.
29 A. Vahl, N. Carstens, T. Strunskus, F. Faupel and A. Hassanien, *Sci. Rep.*, 2019, **9**, 1–10.
30 H. Haberland, M. Karrais, M. Mall and Y. Thurner, *J. Vac. Sci. Technol., A*, 1992, **10**, 3266–3271.
31 A. Vahl, J. Strobel, W. Reichstein, O. Polonskyi, T. Strunskus, L. Kienle and F. Faupel, *Nanotechnology*, 2017, **28**(17), DOI: **10.1088/1361-6528/aa66ef**.
32 H. Takele, S. Jebril, T. Strunskus, V. Zaporojchenko, R. Adelung and F. Faupel, *Appl. Phys. A: Mater. Sci. Process.*, 2008, **92**, 345–350.
33 U. Schürmann, W. Hartung, H. Takele, V. Zaporojtchenko and F. Faupel, *Nanotechnology*, 2005, **16**, 1078–1082.
34 A. Eke, P. Herman, L. Kocsis and L. R. Kozak, *Physiol. Meas.*, 2002, **23**(1), DOI: **10.1088/0967-3334/23/1/201**.
35 S. A. Chekol, S. Menzel, R. W. Ahmad, R. Waser and S. Hoffmann-Eifert, *Adv. Funct. Mater.*, 2021, 2111242.
36 A. Sattar, S. Fostner and S. A. Brown, *Phys. Rev. Lett.*, 2013, **111**, 1–5.
37 J. Alstott, E. Bullmore and D. Plenz, *PLoS One*, 2014, **9**(1), DOI: **10.1371/journal.pone.0085777**.
38 A. Clauset, C. R. Shalizi and M. E. J. Newman, *SIAM Rev.*, 2009, **51**, 661–703.
39 J. P. Sethna, K. A. Dahmen and C. R. Myers, *Nature*, 2001, **410**, 242–250.
40 N. Friedman, S. Ito, B. A. W. Brinkman, M. Shimono, R. E. L. Deville, K. A. Dahmen, J. M. Beggs and T. C. Butler, *Phys. Rev. Lett.*, 2012, **108**, 1–5.
41 M. Mirigliano, D. Decastri, A. Pullia, D. Dellasega, A. Casu, A. Falqui and P. Milani, *Nanotechnology*, 2020, **31**(23), DOI: **10.1088/1361-6528/ab76ec**.
42 S. Menzel, S. Tappertzhofen, R. Waser and I. Valov, *Phys. Chem. Chem. Phys.*, 2013, **15**, 6945–6952.
43 D. B. Larremore, W. L. Shew and J. G. Restrepo, *Phys. Rev. Lett.*, 2011, **106**, 1–4.
44 R. Zeraati, V. Priesemann and A. Levina, *Front. Phys.*, 2021, **9**, 1–17.
45 M. D. Pike, S. K. Bose, J. B. Mallinson, S. K. Acharya, S. Shirai, E. Galli, S. J. Weddell, P. J. Bones, M. D. Arnold and S. A. Brown, *Nano Lett.*, 2020, **20**, 3935–3942.
46 G. Milano, G. Pedretti, M. Fretto, L. Boarino, F. Benfenati, D. Ielmini, I. Valov and C. Ricciardi, *Adv. Intell. Syst.*, 2020, **2**, 2000096.
47 W. Wang, M. Wang, E. Ambrosi, A. Bricalli, M. Laudato, Z. Sun, X. Chen and D. Ielmini, *Nat. Commun.*, 2019, **10**, 1–9.
48 S. H. Jo, T. Chang, I. Ebong, B. B. Bhadviya, P. Mazumder and W. Lu, *Nano Lett.*, 2010, **10**, 1297–1301.

Supplementary Information

Brain-like critical dynamics and long-range temporal correlations in percolating networks of silver nanoparticles and functionality preservation after integration of insulating matrix

Niko Carstens[a], Blessing Adejube[a], Thomas Strunskus[a], Franz Faupel[a], Simon Brown[b] and Alexander Vahl[a]*

[a] Institute for Materials Science, Chair for Multicomponent Materials, Faculty of Engineering, Kiel University, Kaiserstraße 2, D-24143 Kiel, Germany

[b] The MacDiarmid Institute for Advanced Materials and Nanotechnology, School of Physical and Chemical Sciences, Te Kura Mat̄u, University of Canterbury, Private Bag 4800, Christchurch 8140, New Zealand

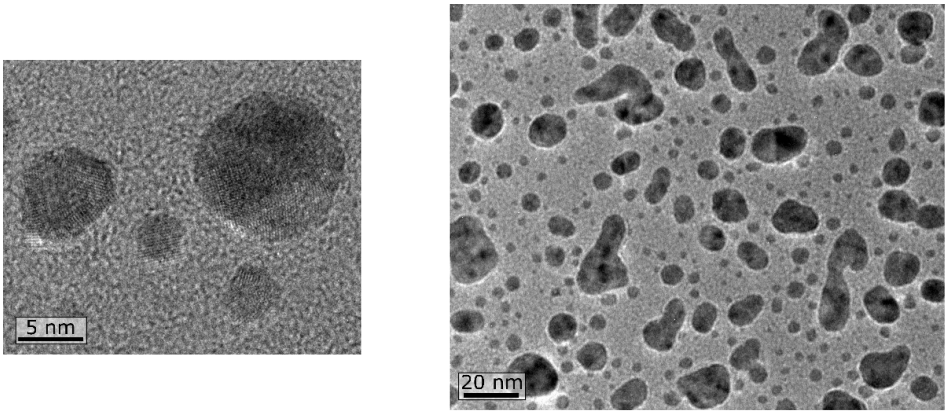

Figure S1. TEM images of Ag-NPs generated from GAS.

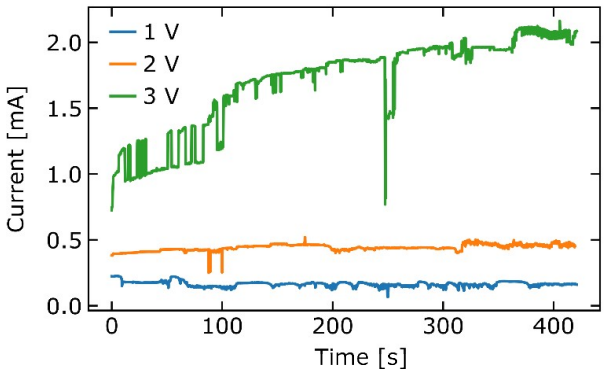

Figure S2. Current response of a percolating Ag-NP network with insulating matrix under different constant voltage inputs over time. A threshold behavior for switching activity can be observed, as typical for ECM-based systems.

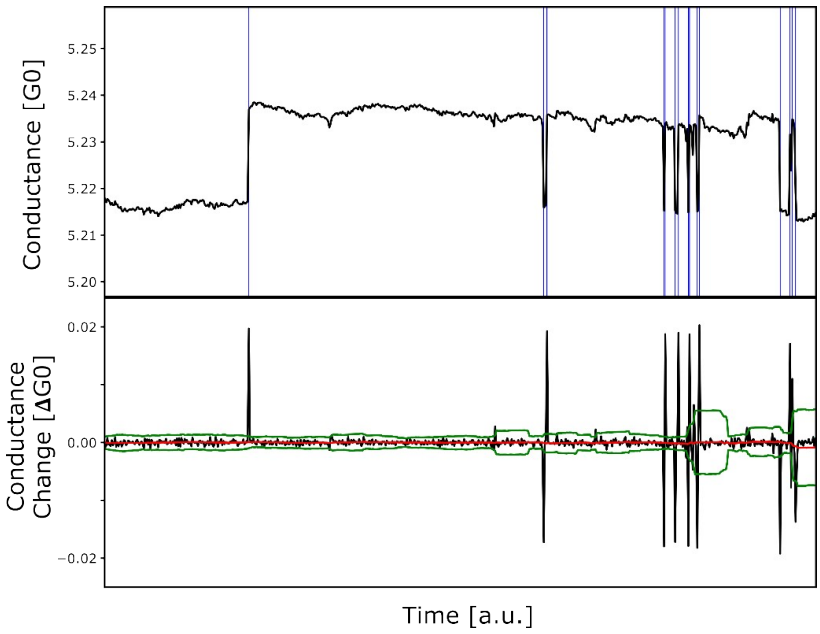

Figure S3. Illustration of transition event detection via a thresholding procedure for a sample without matrix. Top panel shows an exemplary time window of raw data in terms of network conductance versus time. Blue lines indicate transition events detected from the thresholding prodeduce. Thresholding was applied for the temporal sequence of conductance changes (lower panel). For each datapoint in the conductance change sequence, the mean level (red level) and threshold level (green level) were determined by calculating the mean and threefold standard deviation of the 30 past values in the sequence. When a conductance change exceeds the threshold level, it is designated as a network transition event. To account for a fundamental noise level, conductance change values lower than $0.01G_0$ were discarded. Conductance change values, which were detected as transition event, did not contribute to calculations of mean and threshold level.

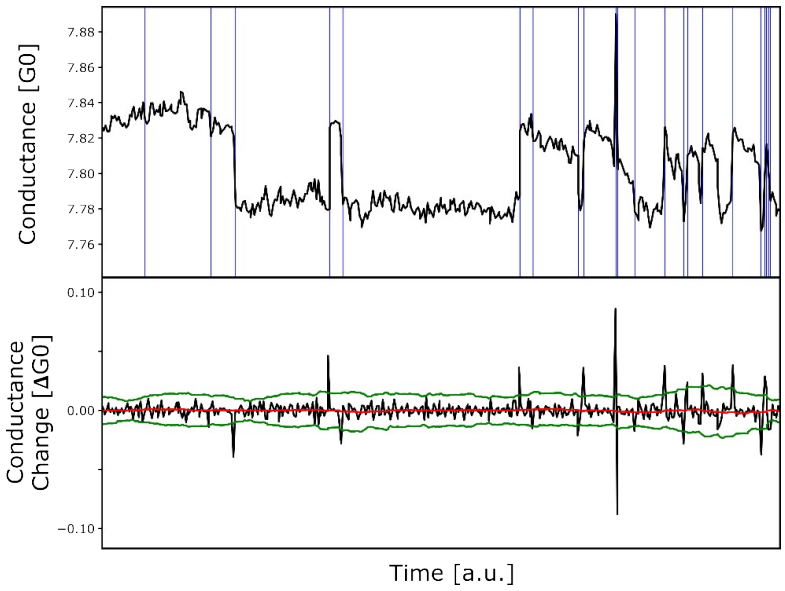

Figure S4. Same scheme as Figure S2, but with an exemplary time window of a sample with matrix.

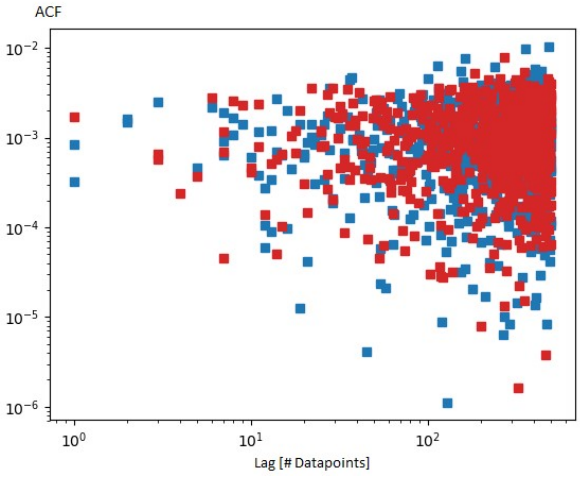

Figure S5. ACFs of all six samples (blue/red corresponds to samples without/with matrix) with shuffled time series of conductance changes. It can be seen that autocorrelation becomes destroyed upon randomizing.

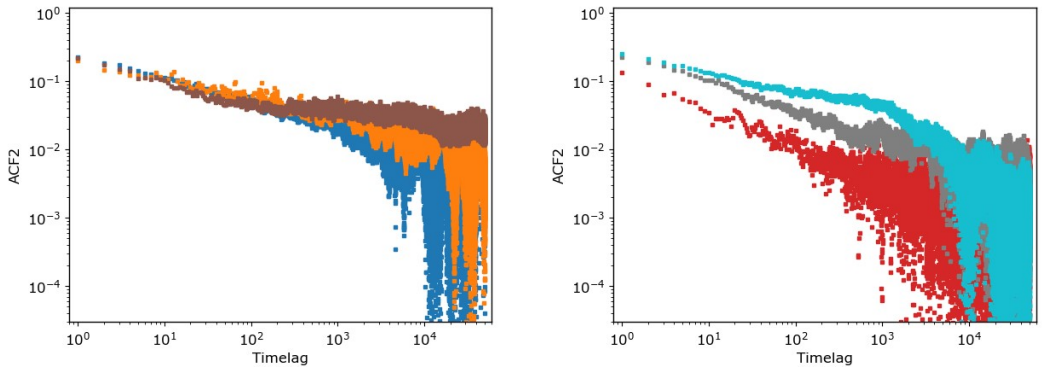

Figure S6. ACFs of samples without (left) and with (right) matrix shown to higher maximum lags. It can be seen, that long-range temporal correlations exists over several decades.

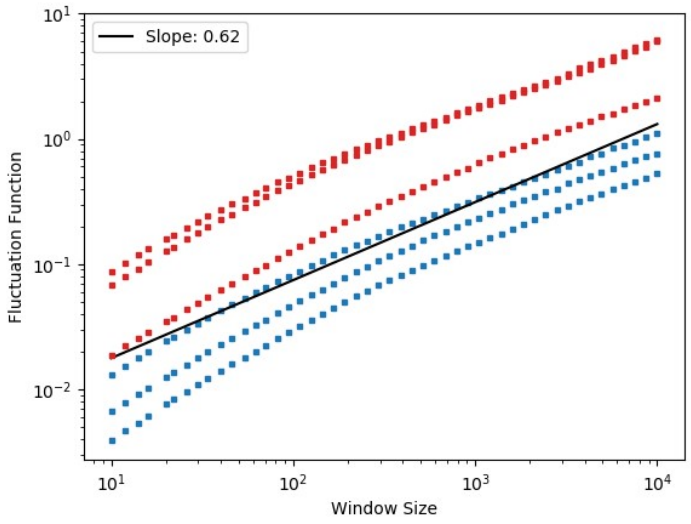

Figure S7. DFA of all six samples with shuffled time series. It can be seen that the slopes of the fluctuation functions are considerably decreased compared to the original data, indicating loss of temporal correlation. The Hurst exponents from the shuffled time series of conductance changes were determined as 0.62, 0.69 and 0.68 for samples without matrix and 0.68, 0.62 and 0.59 for samples with matrix. The black line shows the linear regression of fluctuation function versus window size for one sample without matrix for orientation.

Table S8. Observed event rates for all samples. Event rates were calculated for each sample as number of detected (i.e. thresholded) network transition events divided by total number current measurements over the whole long-term measurement. A higher event rate at equal measurement time decreases the probability of observing large interevent intervals, which was observed for samples with matrix (see Figure 4 bottom right). Although an unambiguous explanation for this observation is difficult, a possible hypothesis for the higher event rates of samples with matrix could be, that additional electron transport mechanisms are enabled by the presence of a matrix, which alters the activity of individual gaps. This is because in gaps without matrix, electron transport across a non-closed gap is only possible via direct tunneling, whereas in gaps with matrix nonlinear transport mechanisms like Fowler-Nordheim tunneling, Poole-Frenkel-emission or variable range or nearest neighbor hopping additionally contributes to the gap activity.

System	Sample	Datapoints of whole long-term measurement	Detected Network Transition Events	Event Rate [%]
Without Matrix	1	500000	28193	5.6
	2	500000	7558	1.5
	3	500000	12981	2.6
With Matrix	4	500000	33493	6.7
	5	500000	68043	13.6
	6	500000	82603	16.5

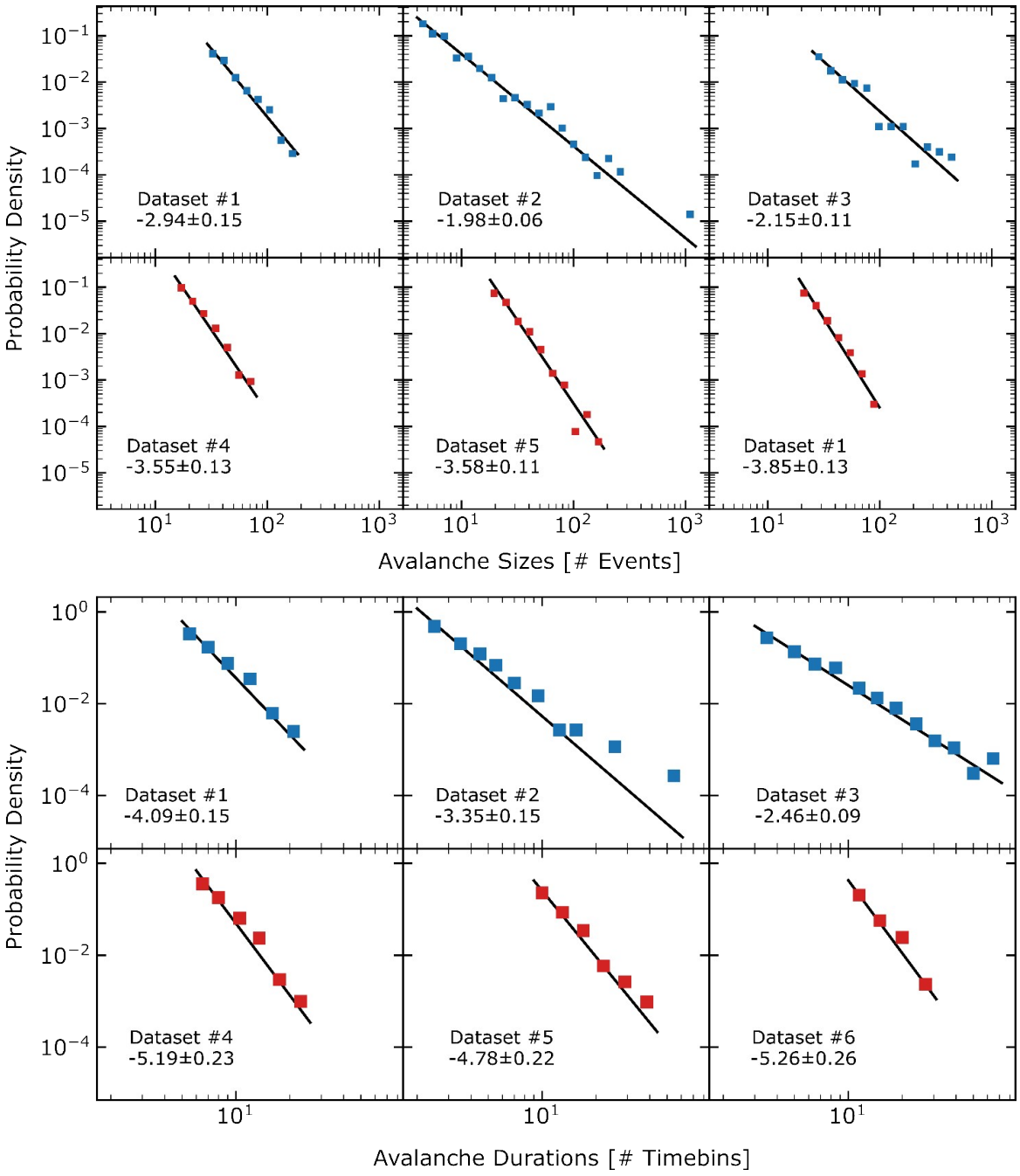

Figure S9. Fittings of avalanche size and duration distributions shown for each sample individually under application of a x_{min} value. From this, the power law exponents which were considered for the evaluation of the crackling noise relationship were extracted. Shown is the tail-part of the distribution above $x_{min.}$ The corresponding full empirical ranges are treated in Figure 6 in the main part.

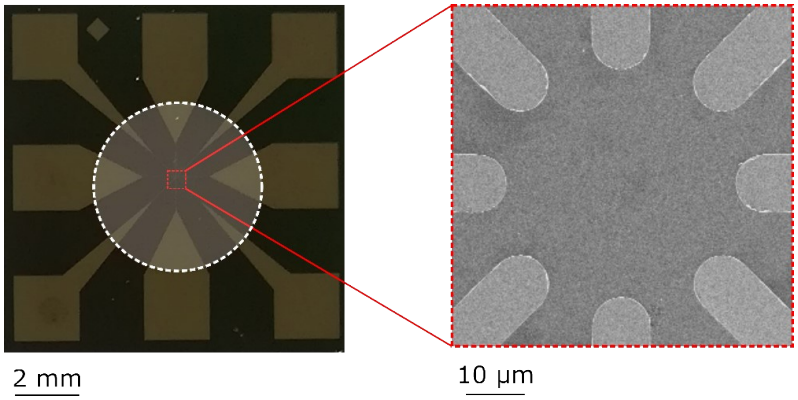

Figure S10. Optical image of a real sample (left) and an SEM image (right) showing the ends of electrodes. The white circle indicates the area of the NP film.

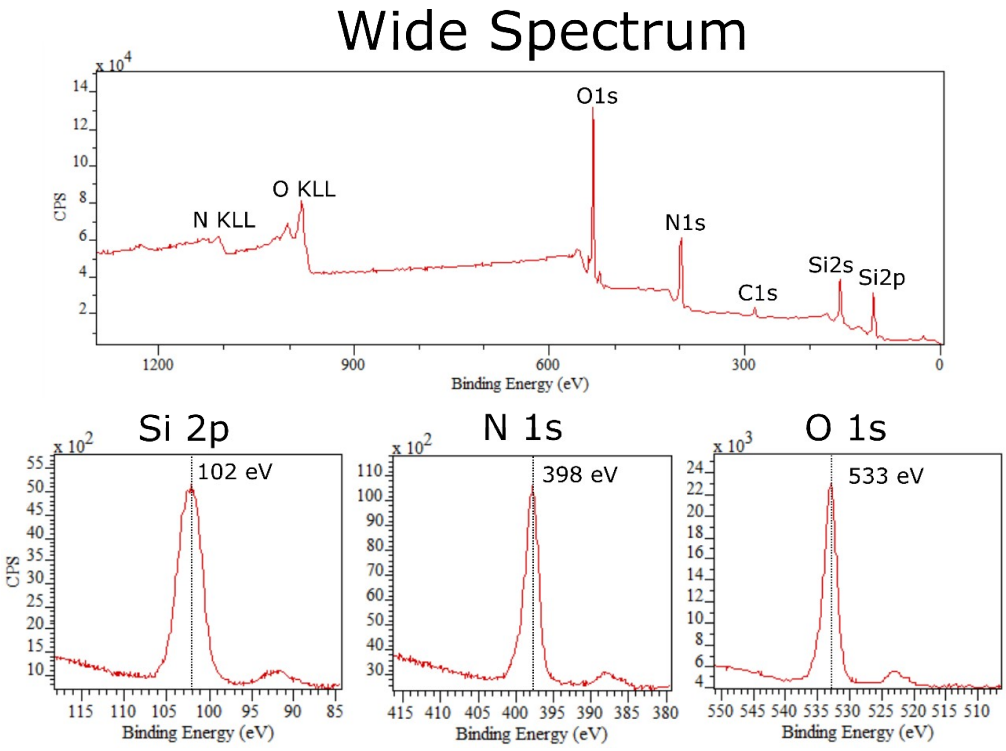

Figure S11. XPS analysis of matrix layer showing Si 2p, N 1s and O 1s peaks. The position of peaks suggests the existence of SiO_xN_y in the desposited matrix layer. The formation of an oxynitride can be attributed to an atmospheric oxidation of the matrix layer, which was deposited by a reactive gas mixture of Ar and N_2 from a Si target.

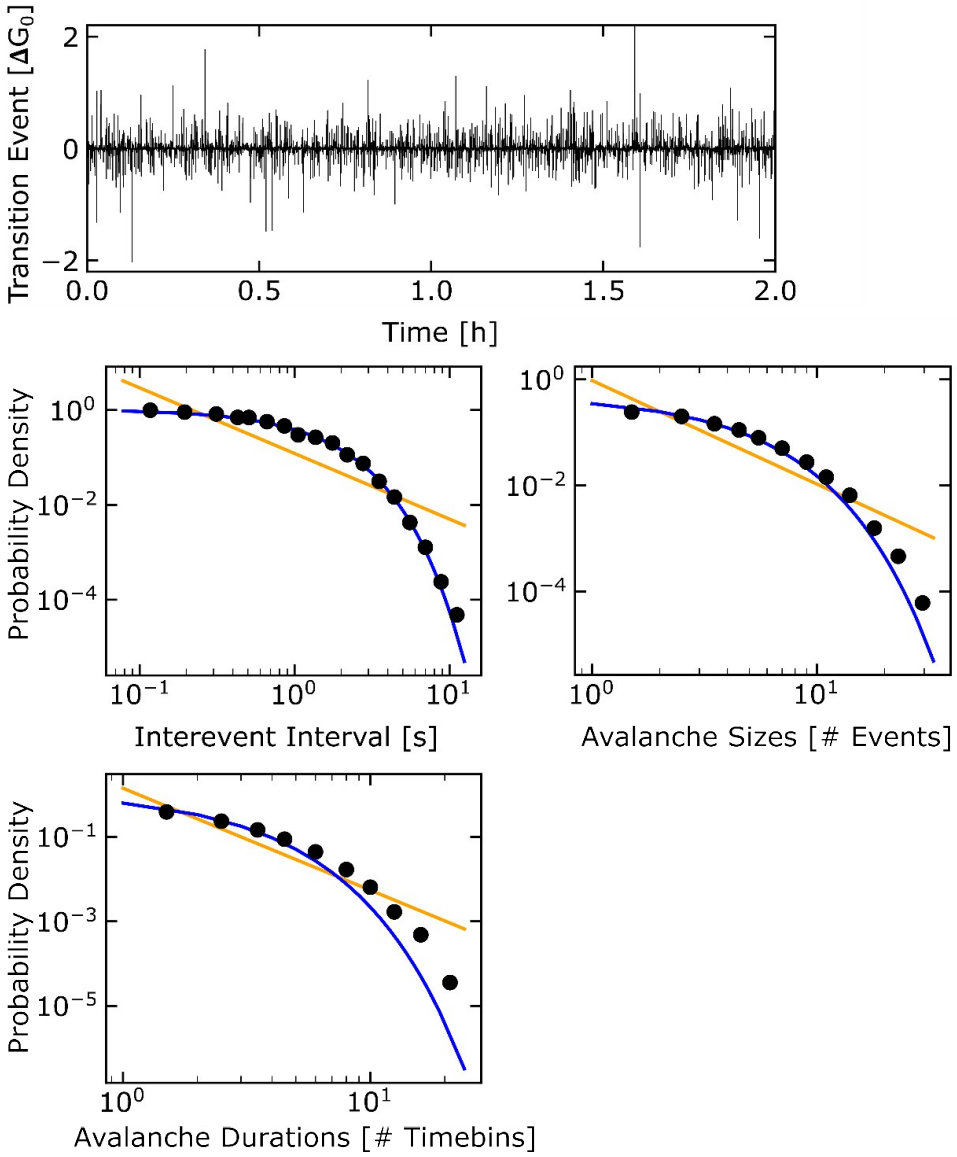

Figure S12. Power law analysis of IEIs and avalanches (following the same procedure as in the main text), but with randomized time series of network transition events. All in all, it can be seen that power law behavior becomes destroyed, as the distributions of dynamical characteristics now follow an exponential law (blue fit) instead of power law (orange fit).

10. Conclusion and Outlook

This thesis is dedicated to the development of Ag-based memristive systems, that allow for an imitation of certain features of biological neuronal dynamics in electrical circuits. Generally, memristive systems are playing a key role for the creation of novel computational systems in the framework of neuromorphic computing. Major inspiration for the development of memristive systems in this work was drawn from findings in neuroscience, stating that principles like short-term synaptic plasticity, excitatory and inhibitory synaptic contributions, criticality and long-range temporal correlations are essential to endow biological neuronal systems with computational capabilities. A central research question of this thesis is, to which extend Ag-based nanostructures are capable to emulate the aforementioned dynamical features of biological neuronal systems. At this point, it is noted again that Ag-nanostructures have been already extensively used for the design of memristive systems. However, only a small portion of approaches aimed to elaborate on design paradigms that are closely oriented towards the realistic behavior of biological neuronal systems. This is reasoned by the fact, that many established approaches to build neuromorphic systems are oriented towards artificial neurons and artificial neuronal networks, which are rather rigid mathematical (and man-made) constructs. Approaches motivated in such a way are frequently implemented in highly regular architectures of memristive devices, like crossbar arrays. In contrast to that, this dissertation was conceived, to emulate diverse principles of biologically plausible (i.e. made by evolution) information processing and representation known from biological neuronal systems. In this regard, the motivation of this work is discriminated against a large part of existing approaches in neuromorphic computing. Taking into account that computational capabilities of biological neuronal systems emerge from dynamical features on different system scales (i.e. ranging from local synaptic plasticity to the tuning of whole neuronal networks into a critical regime), comprehensive insights into Ag-based memristive systems were developed likewise across different system scales. Starting from the dynamics of individual Ag-filaments, the present work was continued over intermediate-scale assemblies of Ag-alloy NPs to macroscopic systems formed by Ag-NP networks. Each Ag-based memristive system developed in the course of this thesis, provides different capabilities of implementing dynamical features inspired by biological neuronal systems. A summary of the main findings is given in the following paragraphs.

Firstly, the memristive dynamics of an individual Ag-filament that evolved from a thin film electrode into an insulating matrix was investigated. Since filamentary switch-

ing phenomena typically occur on the nanoscale, accessing their memristive properties via analytical methods is commonly accompanied by problems related to the localization of probe and filamentary structure. To circumvent such issues, an unconventional cAFM approach was developed in this thesis. This approach intends a direct integration of the memristive system at the cantilever, instead of a conventional probing scenario. As a consequence, all memristive action during electrical characterization with usual cAFM instrumentation is constrained to the apex region of the cantilever. This facilitates long-term measurements on filamentary memristive features under mitigation of experimental uncertainties related to the localization of probe and filamentary feature, which is commonly evoked by thermal drift. This method proved well to acquire reliable insights into the diffusive switching dynamics of individual Ag-filaments. Generally, diffusive switching is highly relevant for pathways to emulate synaptic short-term plasticity in neuromorphic systems. In this context, it was found that the diffusive memristive dynamics of individual Ag-filaments are not completely random, but that threshold voltages are governed by a certain degree of temporal correlation. This is in contrast to frequent beliefs, that the threshold voltages of subsequent cycles can be treated as statistically independent from each other. For the future application as short-term plasticity emulation in neuromorphic systems, temporal correlations in the threshold voltages could add another dimension to diffusive memristive switching for the representation of information. In other words, the fact that threshold voltages are correlated from cycle to cycle can be understood as a dynamical memory.

A substantial advantage of the unconventional cAFM approach developed in this thesis is that it can be applied towards diverse memristive systems. In the further course of this dissertation, this cAFM approach was applied to investigate the dynamics of a memristive system built from an intermediate-scale assembly of AgPt-NPs. The focus during studying the intermediate-scale AgPt-NP assembly was set on complex memristive phenomena that emerge, when the operation of the system is constrained to a highly volatile switching regime. This investigation revealed, that operating an intermediate-scale NP-based memristive system in a highly volatile regime cause enduring fluctuations between insulating and conducting states, which resembles irregular spiking patterns of neurons. It was discussed, that such a memristive behavior emerges, when physical forces promoting the formation and decay of filamentary structures are approximately balanced. Interestingly, such a behavior shows certain similarities to inhibitory and excitatory synaptic contributions in biological systems. Inhibition and excitation determine likewise the state of a neuron by driving it towards a lower or higher probability for firing, respectively, and play an important role for information encoding schemes in biological neuronal systems. Findings from neuroscience indicate, that a balancing of inhibition and excitation in biological systems optimizes properties like the dynamical range of neuronal dynamics, a beneficial feature for solving computational tasks. The highly volatile switching regime of intermediate-scale assemblies of AgPt-NPs investigated in this thesis could provide pathways to emulate principles from synaptic inhibition and excitation for potential applications in neuromorphic systems.

Furthermore, capabilities to build memristive systems with diffusive switching dy-

namics via AgPt and AgAu-NPs were investigated. It was demonstrated (by conventional cAFM probing), that a single Ag-alloy NP embedded in SiO_2 acts as a fundamental building unit to implement stable diffusive switching. Moreover, investigation of larger scale systems (by probing with a macroscopic wire) fabricated by multiple stack of AgPt or AgAu-NPs embedded in SiO_2 showed likewise stable diffusive switching dynamics. Therefore, an important finding of this part was, that AgPt and AgAu-NPs are reliable building units to implement diffusive memristive dynamics in neuromorphic systems across different system scales, ranging from an individual NPs to macroscopic multistack systems.

Based on the applicability of Ag-alloy NPs for diffusive switching, concepts to expand memristive behavior towards memsensitive systems were discussed. Inspired by the fact that biological neuronal systems permanently adapt to stimulation from their environment, memsensors embody devices which combine capabilities for information storage, processing and stimuli detection. Two memsensor concepts were discussed that are based on serial connections of NP-based memristive system with wide-bandgap semiconductors, which incorporate UV sensitivity to the circuit. Preliminary indications were demonstrated experimentally, that the memristive response of the memsensor circuit is modulated by an external UV stimulus. The study regarding memsensors in this thesis builds on a work from Vahl *et al.* [152], that modeled the working principle of memsensor devices by serial connections of sensitive elements and memristive systems. The experimental findings in this dissertation are an additional indication, that this working principle could act as a guideline for future developments of memsensitive systems.

Furthermore, the applicability of AgAu-NPs as building units to mediate memristive switching in a higher level network consisting of CNTs was investigated. In this approach, AgAu-NP were added by GAS deposition to a preformed sparse network of CNTs. It was demonstrated that AgAu-NP located within gaps between adjacent CNTs incorporate volatile memristive dynamics to the behavior of the sparse CNT network. The main finding in the context of this thesis is the feasibility, to implement memristive switching via Ag-alloy NPs also in lateral geometries and at exposed conditions. Moreover, it was shown that the retention time of AgAu-NP mediated switching could be tailored within a second-to-minute range. In this regard, the application potential of Ag-alloy NP as memristive building units are expanded beyond the vertical composite systems, as investigated in Chapter 6. Because the NP deposition via GAS is compatible with the application of many kinds of substrates, random dispersion of Ag-alloy NP as memristive building units to any other predefined network architectures could act as a feasible fabrication step in the design of neuromorphic systems.

Finally, self-organized networks of memristive switches formed by Ag-NPs were investigated. Ag-NP networks poised at the electrical percolation threshold were fabricated and investigated towards large-scale neuronal-like behavior, such as critical dynamics and long-range temporal correlations. The results demonstrated the feasibility of implementing critical behavior and long-range temporal correlations in neuromorphic systems via Ag-NP networks. When criticality emerges in physical and neuronal systems, the following question is of fundamental interest: How is the network tuned into to a criti-

cal state based on the interplay of the underlying dynamical units? This question was approached by comparing Ag-NP networks with and without integration of a SiO_xN_y matrix, following the intention that memristive dynamics in individual gaps are fundamentally affected by the presence or absence of an insulating medium. It was found, that the emergence of criticality and long-range temporal correlations is unaffected by presence or absence of an integrated matrix. This is an important implication for the practical applicability of NP-based memristive networks. Established work on NP-based memristive networks in the literature characterizes the network behavior solely under exposed conditions, neglecting the fact that practical devices are embedded as a composite system. In this context, the finding that the behavior of Ag-NP networks poised at the percolation threshold is substantially unaffected after addition of an insulating matrix strengthens their practical applicability.

All in all, the complementary understanding of Ag-based memristive systems on different system scales elaborated in this thesis, ranging from an individual nanoscale Ag-filament to the collective behavior of macroscale Ag-NP networks, gives substantial contributions to the development of neuromorphic systems. An essential issue regarding the behavior in NP-based memristive networks is to unveil how a critical regime emerges from the underlying individual dynamical units, i.e. individual memristive nanogaps. In this regard, the nanoscale memristive systems that were investigated by the unconventional cAFM approach, i.e. single Ag-filaments and intermediate-scale AgPt-NP assemblies, could be seen as representative for individual units in larger-scale memristive networks. This means, the dynamical features that were revealed for single Ag-filaments and intermediate-scale AgPt-NP assemblies could be a reflection of the local behavior in larger-scale memristive networks. For future progress in the design of Ag-based neuromorphic systems, it could be elaborated on theories that explain the collective behavior in NP-based memristive networks on the basis of the observed dynamics for nanoscale memristive units. Similar questions are also of interest in current neuroscience approaches, which aim to understand the emergence of critical dynamics and long-range temporal correlations in biological neuronal systems. There, it is considered that a careful balancing of inhibitory and excitatory contributions at the local level tunes the whole system into a critical regime [64]. In other words, tailoring the activity on the local level is decisive to tune the whole system into a regime, that is most functional for solving computational tasks. Theoretical links between these scales could be established by network modeling approaches [62, 63]. Understanding the dependency of macroscale network behavior on the dynamical features of the underlying individual units could provide a substantial progress in the design of Ag-based neuromorphic systems.

Appendix

A.1 Volatile and Non-volatile Reconfiguration via Choice of Serial Resistor

In this section, the importance of a serial resistor for the dynamics of a memristive system is briefly illustrated. In particular, the magnitude of the serial resistor determines whether reconfiguration in the memristive system are volatile or non-volatile. Generally, operating a filamentary memristive system with a higher serial resistor constrains the memristive action into a more volatile regime (see theory section 2.3.2). This is demonstrated here by a system consisting of two serially arranged memristive gaps formed between Pt backelectrodes and an overpercolated AgPt-NP film, as shown in Figure A.1. Details of such a device structure were already discussed in the context of mem-

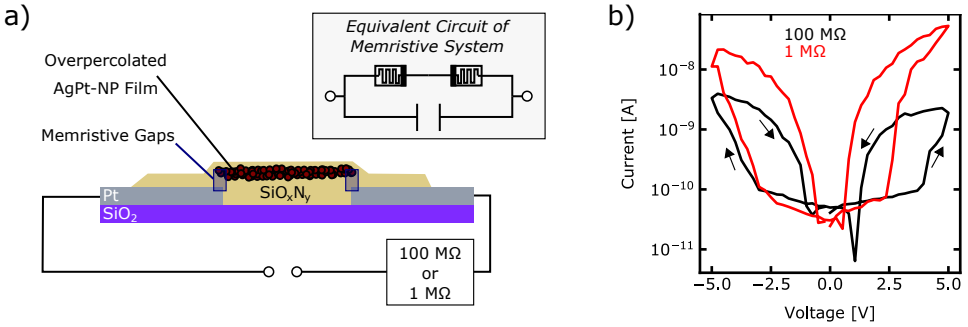

Figure A.1: (a) Memristive system formed by two serial gaps between Pt backelectrodes and an overpercolated AgPt-NP film. Details of this system are discussed in in Chapter 7. This system was operated under different serial resistances of either 1 MΩ or 100 MΩ. Respective IV characteristics are shown in (b).

sensor approaches in Chapter 7. Here, this system was stressed by 0.5 Hz voltage pulse trains with varying amplitudes, where the first pulse train had an amplitude of 1 V, the second pulse train 8 V and the third pulse train again 1 V. Moreover, either 1 MΩ or 100 MΩ was incorporated as a serial resistor. Results are shown in Figure A.2. In this figure, the red shaded areas indicate periods where the pulses were applied and the white shaded areas periods where the pulses were off (i.e. 0 V applied). It can be seen, that for the first pulse train of 1 V, only a high resistive state is observed in both cases (1 MΩ and 100 MΩ as serial resistor). The second pulse train of 8 V is above the threshold for memristive switching. For the third pulse train, it can be seen that the current response depends on the used serial resistor. In case of 1 MΩ, a considerable current is measured, indicating that the previous 8 V pulses reconfigured the memristive system in a non-volatile way. In contrast to that, when 100 MΩ were applied, the third pulse train again indicates a high resistive state, meaning that reconfiguration of the memristive system from the 8 V pulses did not persist.

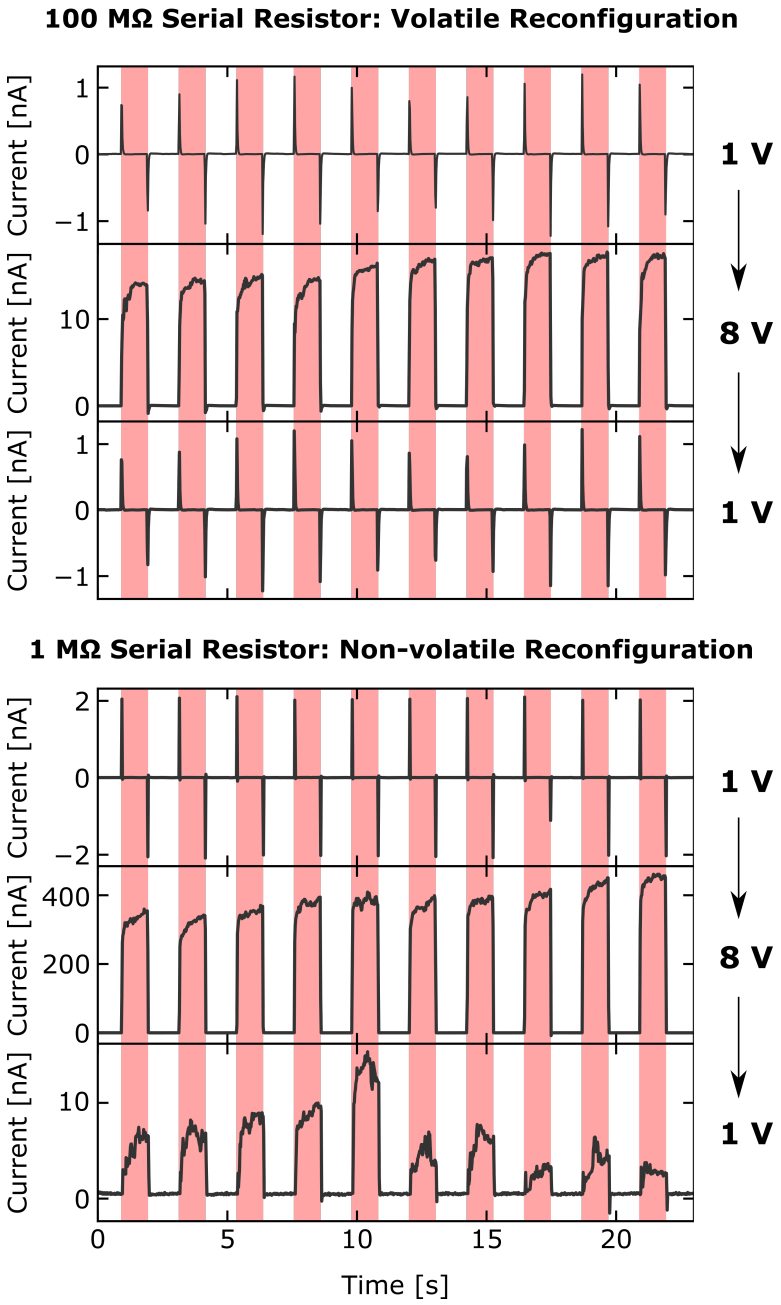

Figure A.2: Programming via 8 V pulses causes volatile or non-volatile reconfiguration of the memristive system, when a 100 MΩ or 1 MΩ is used, respectively.

A.2 Memsensitive Properties of TiO_2 Thin Films

Here, experimental results on the memsensitive properties of TiO_2 thin films are briefly reported, supplementary to the discussion of memsensor designs in Chapter 7. A thin film stack as sketched below was fabricated by a lithographic lift-off procedure and deposition of 120 nm thick TiO_2 (reactive sputtering under a pulsed DC input) and a Au topelectrode (DC sputtering) on commercially available ITO covered glass slides. An important design consideration for memsensors is, that external stimuli can reach the sensitive parts of the device. This might be challenging in case of UV light and thin film systems integrated between two electrodes, because most electrode materials only show weak transmission for UV light. In the design presented here, the backelectrode material (1 mm glass slide covered by ITO) exhibited sufficient UV transmission to probe the memsensitive features of TiO_2. The thin film stack and typical IV characteristics under UV ON and OFF conditions are shown in Figure A.3. There, a memristive response can be recognized that is modulated by the presence of an external UV input.

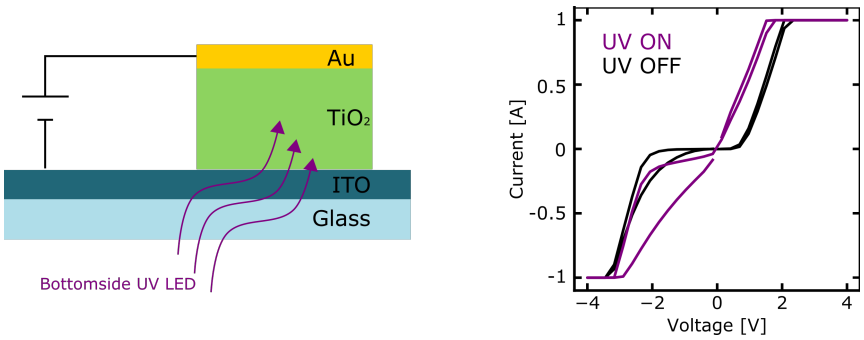

Figure A.3: Memsensitive properties of TiO_2.

List of Publications

Journal Papers

N. Carstens, T. Strunskus, F. Faupel, A. Hassanien and A. Vahl, Neuronal-like Irregular Spiking Dynamics in Highly Volatile Memristive Intermediate-scale AgPt-Nanoparticle Assemblies, *Submitted*, 2022

N. Carstens, B. Adejube, T. Strunskus, F. Faupel, S. Brown and A. Vahl, Brain-like critical dynamics and long-range temporal correlations in percolating networks of silver nanoparticles and functionality preservation after integration of insulating matrix, *Nanoscale Advances*, *Accepted*, 2022

M. Schwartzkopf, A. Rothkirch, **N. Carstens**, Q. Chen, T. Strunskus, F. C. Löhrer, S. Xia, C. Rosemann, L. Bießmann, V. Körstgens, S. Ahuja, P. Pandit, J. Rubeck, S. Frenzke, A. Hinz, O. Polonskyi, P. Müller-Buschbaum, F. Faupel, S. V. Roth, In Situ Monitoring of Scale Effects on Phase Selection and Plasmonic Shifts during Growth of AgCu Alloy Nanostructures for Anti-Counterfeiting Applications, *ACS Appl. Nano Mater.*, 2022, 5, 3, 3832–3842

M.-I. Terasa, P. Holtz, **N. Carstens**, S. Kaps, F. Faupel, A. Vahl and R. Adelung, Sparse CNT networks with implanted AgAu nanoparticles: A novel memristor with short-term memory bordering between diffusive and bipolar switching, *PLOS One*, 2022, 17(3): e0264846

N. Carstens, A. Vahl, O. Gronenberg, T. Strunskus, L. Kienle, F. Faupel and A. Hassanien, Enhancing Reliability of Studies on Single Filament Memristive Switching via an Unconventional cAFM Approach, *Nanomaterials*, 2021, 11, 265

S. Liang, W. Chen, S. Yin, S. J. Schaper, R. Guo, J. Drewes, **N. Carstens**, T. Strunskus, M. Gensch, M. Schwartzkopf, F. Faupel, S. V. Roth, Y.-J. Cheng, and P. Müller-Buschbaum, Tailoring the Optical Properties of Sputter-Deposited Gold Nanostructures on Nanostructured Titanium Dioxide Templates Based on In Situ Grazing-Incidence Small-Angle X-ray Scattering Determined Growth Laws, *ACS Appl. Mater. Interfaces*, 2021, 13, 12, 14728–14740

M. Schwartzkopf, S.-J. Wöhnert, V. Waclawek, **N. Carstens**, A. Rothkirch, J. Rubeck, M. Gensch, J. Drewes, O.r Polonskyi, T. Strunskus, A. M. Hinz, S. J. Schaper, V. Körstgens, P. Müller-Buschbaum, F. Faupel and S. V. Roth, Real-time insight into nanostructure evolution during the rapid formation of ultra-thin gold layers on polymers, *Nanoscale Horizons*, 2021, 6, 132-138

S. J. Schaper, F. C. Löhrer, S. Xia, C. Geiger, M. Schwartzkopf, P. Pandit, J. Rubeck, B. Fricke, S. Frenzke, A. M. Hinz, **N. Carstens**, O. Polonskyi, T. Strunskus, F. Faupel, S. V. Roth and P. Müller-Buschbaum, Revealing the growth of copper on polystyrene-block-poly(ethylene oxide) diblock copolymer thin films with in situ GISAXS, *Nanoscale*, 2021, 13, 10555-10565

J. Drewes, A. Vahl, **N. Carstens**, T. Strunskus, O. Polonskyi, F. Faupel, Enhancing composition control of alloy nanoparticles from gas aggregation source by in operando optical emission spectroscopy, *PlasmaProcess Polym.* 2021, 18:e2000208

A. Vahl, **N. Carstens**, T. Strunskus, F. Faupel and A. Hassanien, Diffusive Memristive Switching on the Nanoscale, from Individual Nanoparticles towards Scalable Nanocomposite Devices, *Scientific Reports*, 2019, 9, 17367

Conference Proceedings

O. Gronenberg, **N. Carstens**, A. Vahl, F. Faupel, L. Kienle, Fabrication and Application of TEM-Compatible Sample Grids for Ex Situ Electrical Probing, In: IFMBE Proceedings, 2020

N. Carstens, M. Mirigliano, T. Strunskus, F. Faupel, O. Lupan, P. Milani, A. Vahl, Nanoparticles as Building Units for Bio-Inspired Electronics –Switching and Sensing, In: Electronics, Communications and Computing IC—ECCO-2021, 2021

Bibliography

(1) Thompson, S. E.; Parthasarathy, S. *Materials Today* **2006**, *9*, 20–25.

(2) Waldrop, M. M. *Nature* **2016**, *530*, 144–147.

(3) Kendall, J. D.; Kumar, S. *Applied Physics Reviews* **2020**, *7*, 011305.

(4) Kish, L. B. *Physics Letters A* **2002**, *305*, 144–149.

(5) Zidan, M. A.; Strachan, J. P.; Lu, W. D. *Nature Electronics* **2018**, *1*, 22–29.

(6) LeCun, Y.; Bengio, Y.; Hinton, G. *Nature* **2015**, *521*, 436–444.

(7) Rawat, W.; Wang, Z. *Neural Computation* **2017**, *29*, 2352–2449.

(8) Shen, D.; Wu, G.; Suk, H.-I. *Annual Review of Biomedical Engineering* **2017**, *19*, 221–248.

(9) Jeong, D. S.; Kim, K. M.; Kim, S.; Choi, B. J.; Hwang, C. S. *Advanced Electronic Materials* **2016**, *2*, 1600090.

(10) Ielmini, D.; Ambrogio, S. *Nanotechnology* **2020**, *31*, 092001.

(11) Upadhyay, N. K.; Jiang, H.; Wang, Z.; Asapu, S.; Xia, Q.; Joshua Yang, J. *Advanced Materials Technologies* **2019**, *4*, 1800589.

(12) Van de Burgt, Y.; Melianas, A.; Keene, S. T.; Malliaras, G.; Salleo, A. *Nature Electronics* **2018**, *1*, 386–397.

(13) Wang, S.; Chen, X.; Huang, X.; Wei Zhang, D.; Zhou, P. *Advanced Intelligent Systems* **2020**, *2*, 2000124.

(14) Yang, J.-Q.; Wang, R.; Ren, Y.; Mao, J.-Y.; Wang, Z.-P.; Zhou, Y.; Han, S.-T. *Advanced Materials* **2020**, *32*, 2003610.

(15) Chua, L. *IEEE Transactions on Circuit Theory* **1971**, *18*, 507–519.

(16) Huang, H.-M.; Wang, Z.; Wang, T.; Xiao, Y.; Guo, X. *Advanced Intelligent Systems* **2020**, *2*, 2000149.

(17) Strukov, D. B.; Snider, G. S.; Stewart, D. R.; Williams, R. S. *Nature* **2008**, *453*, 80–83.

(18) Chua, L. In *Handbook of Memristor Networks*, Chua, L., Sirakoulis, G. C., Adamatzky, A., Eds.; Springer International Publishing: Cham, 2019, pp 197–230.

(19) Chang, T.; Jo, S.-H.; Lu, W. *ACS Nano* **2011**, *5*, 7669–7676.

(20) Edwards, A. H.; Barnaby, H. J.; Campbell, K. A.; Kozicki, M. N.; Liu, W.; Marinella, M. J. *Proceedings of the IEEE* **2015**, *103*, 1004–1033.

(21) Sangwan, V. K.; Hersam, M. C. *Nature Nanotechnology* **2020**, *15*, 517–528.

(22) Wang, Z.; Wang, L.; Nagai, M.; Xie, L.; Yi, M.; Huang, W. *Advanced Electronic Materials* **2017**, *3*, 1600510.

(23) Zhu, J.; Zhang, T.; Yang, Y.; Huang, R. *Applied Physics Reviews* **2020**, *7*, 011312.

(24) Ohno, T.; Hasegawa, T.; Tsuruoka, T.; Terabe, K.; Gimzewski, J. K.; Aono, M. *Nature Materials* **2011**, *10*, 591–595.

(25) Wang, Z. et al. *Nature Materials* **2017**, *16*, 101–108.

(26) Bian, H.; Goh, Y. Y.; Liu, Y.; Ling, H.; Xie, L.; Liu, X. *Advanced Materials* **2021**, *33*, 2006469.

(27) Yang, R.; Huang, H.-M.; Guo, X. *Advanced Electronic Materials* **2019**, *5*, 1900287.

(28) Ielmini, D.; Wong, H.-S. P. *Nature Electronics* **2018**, *1*, 333–343.

(29) Prezioso, M.; Merrikh-Bayat, F.; Hoskins, B. D.; Adam, G. C.; Likharev, K. K.; Strukov, D. B. *Nature* **2015**, *521*, 61–64.

(30) Serb, A.; Bill, J.; Khiat, A.; Berdan, R.; Legenstein, R.; Prodromakis, T. *Nature Communications* **2016**, *7*, 12611.

(31) Xia, Q.; Yang, J. J. *Nature Materials* **2019**, *18*, 309–323.

(32) Yao, P.; Wu, H.; Gao, B.; Eryilmaz, S. B.; Huang, X.; Zhang, W.; Zhang, Q.; Deng, N.; Shi, L.; Wong, H.-S. P.; Qian, H. *Nature Communications* **2017**, *8*, 15199.

(33) Clima, S.; Sankaran, K.; Chen, Y. Y.; Fantini, A.; Celano, U.; Belmonte, A.; Zhang, L.; Goux, L.; Govoreanu, B.; Degraeve, R.; Wouters, D. J.; Jurczak, M.; Vandervorst, W.; Gendt, S. D.; Pourtois, G. *physica status solidi (RRL) - Rapid Research Letters* **2014**, *8*, 501–511.

(34) Valov, I.; Waser, R.; Jameson, J. R.; Kozicki, M. N. *Nanotechnology* **2011**, *22*, 254003.

(35) Waser, R.; Dittmann, R.; Staikov, G.; Szot, K. *Advanced Materials* **2009**, *21*, 2632–2663.

(36) Chekol, S. A.; Menzel, S.; Ahmad, R. W.; Waser, R.; Hoffmann-Eifert, S. *Advanced Functional Materials* **2021**, 2111242.

(37) Menzel, S.; Tappertzhofen, S.; Waser, R.; Valov, I. *Physical Chemistry Chemical Physics* **2013**, *15*, 6945.

(38) Menzel, S.; Kaupmann, P.; Waser, R. *Nanoscale* **2015**, *7*, 12673–12681.

(39) Citri, A.; Malenka, R. C. *Neuropsychopharmacology* **2008**, *33*, 18–41.

(40) Deng, P.-Y.; Klyachko, V. A. *Communicative & Integrative Biology* **2011**, *4*, 543–548.

(41) Isaacson, J. S.; Scanziani, M. *Neuron* **2011**, *72*, 231–243.

(42) Shadlen, M. N.; Newsome, W. T. *The Journal of Neuroscience* **1998**, *18*, 3870–3896.

(43) Beggs, J. M.; Plenz, D. *The Journal of Neuroscience* **2003**, *23*, 11167–11177.

(44) Linkenkaer-Hansen, K.; Nikouline, V. V.; Palva, J. M.; Ilmoniemi, R. J. *The Journal of Neuroscience* **2001**, *21*, 1370–1377.

(45) Kim, M.-K.; Lee, J.-S. *ACS Nano* **2018**, *12*, 1680–1687.

(46) Wang, Z.; Rao, M.; Midya, R.; Joshi, S.; Jiang, H.; Lin, P.; Song, W.; Asapu, S.; Zhuo, Y.; Li, C.; Wu, H.; Xia, Q.; Yang, J. J. *Advanced Functional Materials* **2018**, *28*, 1704862.

(47) Avizienis, A. V.; Sillin, H. O.; Martin-Olmos, C.; Shieh, H. H.; Aono, M.; Stieg, A. Z.; Gimzewski, J. K. *PLoS ONE* **2012**, *7*, ed. by Hayasaka, S., e42772.

(48) Demis, E. C.; Aguilera, R.; Sillin, H. O.; Scharnhorst, K.; Sandouk, E. J.; Aono, M.; Stieg, A. Z.; Gimzewski, J. K. *Nanotechnology* **2015**, *26*, 204003.

(49) Stieg, A. Z.; Avizienis, A. V.; Sillin, H. O.; Martin-Olmos, C.; Aono, M.; Gimzewski, J. K. *Advanced Materials* **2012**, *24*, 286–293.

(50) Diaz-Alvarez, A.; Higuchi, R.; Sanz-Leon, P.; Marcus, I.; Shingaya, Y.; Stieg, A. Z.; Gimzewski, J. K.; Kuncic, Z.; Nakayama, T. *Scientific Reports* **2019**, *9*, 14920.

(51) Kuncic, Z.; Nakayama, T. *Advances in Physics: X* **2021**, *6*, 1894234.

(52) Minnai, C.; Bellacicca, A.; Brown, S. A.; Milani, P. *Scientific Reports* **2017**, *7*, 7955.

(53) Mirigliano, M.; Decastri, D.; Pullia, A.; Dellasega, D.; Casu, A.; Falqui, A.; Milani, P. *Nanotechnology* **2020**, *31*, 234001.

(54) Mirigliano, M.; Milani, P. *Advances in Physics: X* **2021**, *6*, 1908847.

(55) Mirigliano, M.; Borghi, F.; Podestà, A.; Antidormi, A.; Colombo, L.; Milani, P. *Nanoscale Advances* **2019**, *1*, 3119–3130.

(56) Fostner, S.; Brown, S. A. *Physical Review E* **2015**, *92*, 052134.

(57) Mallinson, J. B.; Shirai, S.; Acharya, S. K.; Bose, S. K.; Galli, E.; Brown, S. A. *Science Advances* **2019**, *5*, eaaw8438.

(58) Sattar, A.; Fostner, S.; Brown, S. A. *Physical Review Letters* **2013**, *111*, 136808.

(59) Hochstetter, J.; Zhu, R.; Loeffler, A.; Diaz-Alvarez, A.; Nakayama, T.; Kuncic, Z. *Nature Communications* **2021**, *12*, 4008.

(60) Pike, M. D.; Bose, S. K.; Mallinson, J. B.; Acharya, S. K.; Shirai, S.; Galli, E.; Weddell, S. J.; Bones, P. J.; Arnold, M. D.; Brown, S. A. *Nano Letters* **2020**, *20*, 3935–3942.

(61) Shirai, S.; Acharya, S. K.; Bose, S. K.; Mallinson, J. B.; Galli, E.; Pike, M. D.; Arnold, M. D.; Brown, S. A. *Network Neuroscience* **2020**, *4*, 432–447.

(62) Poil, S.-S.; Hardstone, R.; Mansvelder, H. D.; Linkenkaer-Hansen, K. *Journal of Neuroscience* **2012**, *32*, 9817–9823.

(63) Zeraati, R.; Priesemann, V.; Levina, A. *Frontiers in Physics* **2021**, *9*, 619661.

(64) Hesse, J.; Gross, T. *Frontiers in Systems Neuroscience* **2014**, *8*, DOI: 10.3389/fnsys.2014.00166.

(65) Indiveri, G. et al. *Frontiers in Neuroscience* **2011**, *5*, DOI: 10.3389/fnins.2011.00073.

(66) Kuzum, D.; Yu, S.; Philip Wong, H.-S. *Nanotechnology* **2013**, *24*, 382001.

(67) Bear, M. F.; Connors, B. W.; Paradiso, M. A., *Neurowissenschaften*; Engel, A. K., Ed.; Springer Berlin Heidelberg: Berlin, Heidelberg, 2018.

(68) Buonomano, D. V.; Merzenich, M. M. *Annual Review of Neuroscience* **1998**, *21*, 149–186.

(69) Basheer, I.; Hajmeer, M. *Journal of Microbiological Methods* **2000**, *43*, 3–31.

(70) Ielmini, D.; Pedretti, G. *Advanced Intelligent Systems* **2020**, *2*, 2000040.

(71) Yang, J. J.; Strukov, D. B.; Stewart, D. R. *Nature Nanotechnology* **2013**, *8*, 13–24.

(72) Sheng, M.; Hoogenraad, C. C. *Annual Review of Biochemistry* **2007**, *76*, 823–847.

(73) Capano, V.; Herrmann, H. J.; de Arcangelis, L. *Scientific Reports* **2015**, *5*, 9895.

(74) Zhou, S.; Yu, Y. *Frontiers in Neuroscience* **2018**, *12*, 46.

(75) Eichler, S. A. *Frontiers in Molecular Neuroscience* **2008**, *1*, DOI: 10.3389/neuro.02.002.2008.

(76) Denève, S.; Machens, C. K. *Nature Neuroscience* **2016**, *19*, 375–382.

(77) Stiefel, K. M.; Englitz, B.; Sejnowski, T. J. *Proceedings of the National Academy of Sciences* **2013**, *110*, 7886–7891.

(78) Froemke, R. C. *Annual Review of Neuroscience* **2015**, *38*, 195–219.

(79) Shew, W. L.; Yang, H.; Yu, S.; Roy, R.; Plenz, D. *Journal of Neuroscience* **2011**, *31*, 55–63.

(80) Yu, L.; Shen, Z.; Wang, C.; Yu, Y. *Frontiers in Cellular Neuroscience* **2018**, *12*, 123.

(81) Muñoz, M. A. *Reviews of Modern Physics* **2018**, *90*, 031001.

(82) Chialvo, D. R. *Nature Physics* **2010**, *6*, 744–750.

(83) Shew, W. L.; Plenz, D. *The Neuroscientist* **2013**, *19*, 88–100.

(84) *The Functional Role of Critical Dynamics in Neural Systems*; Tomen, N., Herrmann, J. M., Ernst, U., Eds.; Springer Series on Bio- and Neurosystems, Vol. 11; Springer International Publishing: Cham, 2019.

(85) Bak, P.; Tang, C.; Wiesenfeld, K. *Physical Review A* **1988**, *38*, 364–374.

(86) Bullmore, E.; Sporns, O. *Nature Reviews Neuroscience* **2009**, *10*, 186–198.

(87) Smit, D. J. A.; de Geus, E. J. C.; van de Nieuwenhuijzen, M. E.; van Beijsterveldt, C. E. M.; van Baal, G. C. M.; Mansvelder, H. D.; Boomsma, D. I.; Linkenkaer-Hansen, K. *Journal of Neuroscience* **2011**, *31*, 13128–13136.

(88) Meisel, C.; Bailey, K.; Achermann, P.; Plenz, D. *Scientific Reports* **2017**, *7*, 11825.

(89) Tappertzhofen, S.; Menzel, S.; Valov, I.; Waser, R. *Applied Physics Letters* **2011**, *99*, 203103.

(90) Liu, Q.; Long, S.; Wang, W.; Zuo, Q.; Zhang, S.; Chen, J.; Liu, M. *IEEE Electron Device Letters* **2009**, *30*, 1335–1337.

(91) Tappertzhofen, S.; Valov, I.; Waser, R. *Nanotechnology* **2012**, *23*, 145703.

(92) Qin, S.; Liu, Z.; Zhang, G.; Zhang, J.; Sun, Y.; Wu, H.; Qian, H.; Yu, Z. *Physical Chemistry Chemical Physics* **2015**, *17*, 8627–8632.

(93) Soni, R.; Meuffels, P.; Staikov, G.; Weng, R.; Kügeler, C.; Petraru, A.; Hambe, M.; Waser, R.; Kohlstedt, H. *Journal of Applied Physics* **2011**, *110*, 054509.

(94) Guan, W.; Liu, M.; Long, S.; Liu, Q.; Wang, W. *Applied Physics Letters* **2008**, *93*, 223506.

(95) Yang, Y.; Huang, R. *Nature Electronics* **2018**, *1*, 274–287.

(96) Schirm, C.; Matt, M.; Pauly, F.; Cuevas, J. C.; Nielaba, P.; Scheer, E. *Nature Nanotechnology* **2013**, *8*, 645–648.

(97) Hsiung, C.-P.; Liao, H.-W.; Gan, J.-Y.; Wu, T.-B.; Hwang, J.-C.; Chen, F.; Tsai, M.-J. *ACS Nano* **2010**, *4*, 5414–5420.

(98) Wang, W.; Wang, M.; Ambrosi, E.; Bricalli, A.; Laudato, M.; Sun, Z.; Chen, X.; Ielmini, D. *Nature Communications* **2019**, *10*, 81.

(99) Hua, Q.; Wu, H.; Gao, B.; Zhao, M.; Li, Y.; Li, X.; Hou, X.; (Marvin) Chang, M.-F.; Zhou, P.; Qian, H. *Advanced Science* **2019**, *6*, 1900024.

(100) Jeonghwan Song; Jiyong Woo; Prakash, A.; Daeseok Lee; Hyunsang Hwang *IEEE Electron Device Letters* **2015**, *36*, 681–683.

(101) Midya, R. et al. *Advanced Materials* **2017**, *29*, 1604457.

(102) Jeonghwan Song; Jiyong Woo; Prakash, A.; Daeseok Lee; Hyunsang Hwang *IEEE Electron Device Letters* **2015**, *36*, 681–683.

(103) Chae, B.-G.; Seol, J.-B.; Song, J.-H.; Baek, K.; Oh, S.-H.; Hwang, H.; Park, C.-G. *Advanced Materials* **2017**, *29*, 1701752.

(104) Jiang, L.; Xu, L.; Chen, J. W.; Yan, P.; Xue, K. H.; Sun, H. J.; Miao, X. S. *Applied Physics Letters* **2016**, *109*, 153506.

(105) Xue, W.; Gao, S.; Shang, J.; Yi, X.; Liu, G.; Li, R.-W. *Advanced Electronic Materials* **2019**, *5*, 1800854.

(106) Tsuruoka, T.; Hasegawa, T.; Terabe, K.; Aono, M. *Nanotechnology* **2012**, *23*, 435705.

(107) Terabe, K.; Hasegawa, T.; Nakayama, T.; Aono, M. *Nature* **2005**, *433*, 47–50.

(108) Yan, X.; Zhao, J.; Liu, S.; Zhou, Z.; Liu, Q.; Chen, J.; Liu, X. Y. *Advanced Functional Materials* **2018**, *28*, 1705320.

(109) Jo, S. H.; Chang, T.; Ebong, I.; Bhadviya, B. B.; Mazumder, P.; Lu, W. *Nano Letters* **2010**, *10*, 1297–1301.

(110) You, B. K.; Kim, J. M.; Joe, D. J.; Yang, K.; Shin, Y.; Jung, Y. S.; Lee, K. J. *ACS Nano* **2016**, *10*, 9478–9488.

(111) Joshua Yang, J.; Miao, F.; Pickett, M. D.; Ohlberg, D. A. A.; Stewart, D. R.; Lau, C. N.; Williams, R. S. *Nanotechnology* **2009**, *20*, 215201.

(112) Kim, K. M.; Jeong, D. S.; Hwang, C. S. *Nanotechnology* **2011**, *22*, 254002.

(113) Lanza, M. et al. *Advanced Electronic Materials* **2019**, *5*, 1800143.

(114) Sun, W.; Gao, B.; Chi, M.; Xia, Q.; Yang, J. J.; Qian, H.; Wu, H. *Nature Communications* **2019**, *10*, 3453.

(115) Lin, P.; Xia, Q. *Journal of Applied Physics* **2018**, *124*, 152001.

(116) *Memristor Networks*; Adamatzky, A., Chua, L., Eds.; Springer International Publishing: Cham, 2014.

(117) Midya, R.; Wang, Z.; Asapu, S.; Zhang, X.; Rao, M.; Song, W.; Zhuo, Y.; Upadhyay, N.; Xia, Q.; Yang, J. J. *Advanced Intelligent Systems* **2019**, *1*, 1900084.

(118) Lukoševičius, M.; Jaeger, H. *Computer Science Review* **2009**, *3*, 127–149.

(119) Tanaka, G.; Yamane, T.; Héroux, J. B.; Nakane, R.; Kanazawa, N.; Takeda, S.; Numata, H.; Nakano, D.; Hirose, A. *Neural Networks* **2019**, *115*, 100–123.

(120) Milano, G.; Pedretti, G.; Montano, K.; Ricci, S.; Hashemkhani, S.; Boarino, L.; Ielmini, D.; Ricciardi, C. *Nature Materials* **2022**, *21*, 195–202.

(121) Sillin, H. O.; Aguilera, R.; Shieh, H.-H.; Avizienis, A. V.; Aono, M.; Stieg, A. Z.; Gimzewski, J. K. *Nanotechnology* **2013**, *24*, 384004.

(122) Stieg, A. Z.; Avizienis, A. V.; Sillin, H. O.; Martin-Olmos, C.; Lam, M.-L.; Aono, M.; Gimzewski, J. K. *Japanese Journal of Applied Physics* **2014**, *53*, 01AA02.

(123) Lesne, A.; Lagües, M., *Scale Invariance*; Springer Berlin Heidelberg: Berlin, Heidelberg, 2012.

(124) Saberi, A. A. *Physics Reports* **2015**, *578*, 1–32.

(125) Schwabl, F., *Statistische Mechanik: mit 26 Tabellen und 186 Aufgaben*, 3., aktualisierte Aufl; Springer-Lehrbuch; Springer: Berlin Heidelberg, 2006; 591 pp.

(126) Schürmann, U.; Hartung, W.; Takele, H.; Zaporojtchenko, V.; Faupel, F. *Nanotechnology* **2005**, *16*, 1078–1082.

(127) Faupel, F.; Zaporojtchenko, V.; Strunskus, T.; Elbahri, M. *Advanced Engineering Materials* **2010**, *12*, 1177–1190.

(128) Bose, S. K.; Mallinson, J. B.; Gazoni, R. M.; Brown, S. A. *IEEE Transactions on Electron Devices* **2017**, *64*, 5194–5201.

(129) Simmons, J. G. *Journal of Applied Physics* **1963**, *34*, 1793–1803.

(130) Olsen, M.; Hummelgård, M.; Olin, H. *PLoS ONE* **2012**, *7*, ed. by Rini, M., e30106.

(131) Ring, M.; Weber, D.; Haiber, P.; Pauly, F.; Nielaba, P.; Scheer, E. *Nano Letters* **2020**, *20*, 5773–5778.

(132) Acharya, S. K.; Galli, E.; Mallinson, J. B.; Bose, S. K.; Wagner, F.; Heywood, Z. E.; Bones, P. J.; Arnold, M. D.; Brown, S. A. *ACS Applied Materials & Interfaces* **2021**, *13*, 52861–52870.

(133) Bose, S. K.; Mallinson, J. B.; Galli, E.; Acharya, S. K.; Minnai, C.; Bones, P. J.; Brown, S. A. *Nanoscale Horizons* **2022**, 10.1039.D1NH00620G.

(134) Ohring, M., *Materials Science of Thin Films: Deposition and Structure*, 2nd ed; Academic Press: San Diego, CA, 2002; 794 pp.

(135) Schwartzkopf, M.; Santoro, G.; Brett, C. J.; Rothkirch, A.; Polonskyi, O.; Hinz, A.; Metwalli, E.; Yao, Y.; Strunskus, T.; Faupel, F.; Müller-Buschbaum, P.; Roth, S. V. *ACS Applied Materials & Interfaces* **2015**, *7*, 13547–13556.

(136) Schwartzkopf, M.; Hinz, A.; Polonskyi, O.; Strunskus, T.; Löhrer, F. C.; Körstgens, V.; Müller-Buschbaum, P.; Faupel, F.; Roth, S. V. *ACS Applied Materials & Interfaces* **2017**, *9*, 5629–5637.

(137) *Gas-Phase Synthesis of Nanoparticles*; Huttel, Y., Ed.; Wiley-VCH Verlag GmbH & Co. KGaA: Weinheim, Germany, 2017.

(138) Sproul, W.; Christie, D.; Carter, D. *Thin Solid Films* **2005**, *491*, 1–17.

(139) Vahl, A.; Dittmann, J.; Jetter, J.; Veziroglu, S.; Shree, S.; Ababii, N.; Lupan, O.; Aktas, O. C.; Strunskus, T.; Quandt, E.; Adelung, R.; Sharma, S. K.; Faupel, F. *Nanotechnology* **2019**, *30*, 235603.

(140) Vahl, A.; Veziroglu, S.; Henkel, B.; Strunskus, T.; Polonskyi, O.; Aktas, O. C.; Faupel, F. *Materials* **2019**, *12*, 2840.

(141) Haberland, H.; Karrais, M.; Mall, M.; Thurner, Y. *Journal of Vacuum Science & Technology A: Vacuum, Surfaces, and Films* **1992**, *10*, 3266–3271.

(142) Polonskyi, O.; Ahadi, A. M.; Peter, T.; Fujioka, K.; Abraham, J. W.; Vasiliauskaite, E.; Hinz, A.; Strunskus, T.; Wolf, S.; Bonitz, M.; Kersten, H.; Faupel, F. *The European Physical Journal D* **2018**, *72*, 93.

(143) Huttel, Y.; Martínez, L.; Mayoral, A.; Fernández, I. *MRS Communications* **2018**, *8*, 947–954.

(144) Nikitin, D.; Hanuš, J.; Ali-Ogly, S.; Polonskyi, O.; Drewes, J.; Faupel, F.; Biederman, H.; Choukourov, A. *Plasma Processes and Polymers* **2019**, *16*, 1900079.

(145) Shelemin, A. et al. *Particle & Particle Systems Characterization* **2020**, *37*, 1900436.

(146) Vahl, A.; Strobel, J.; Reichstein, W.; Polonskyi, O.; Strunskus, T.; Kienle, L.; Faupel, F. *Nanotechnology* **2017**, *28*, 175703.

(147) Drewes, J.; Ali-Ogly, S.; Strunskus, T.; Polonskyi, O.; Biederman, H.; Faupel, F.; Vahl, A. *Plasma Processes and Polymers* **2022**, *19*, 2100125.

(148) Madou, M. J., *Manufacturing Techniques for Microfabrication and Nanotechnology.* Chapman and Hall/CRC: Boca Raton, 2011.

(149) Vahl, A. On the Development of Memsensors, 2019.

(150) Abraira, V. E.; Ginty, D. D. *Neuron* **2013**, *79*, 618–639.

(151) Lumpkin, E. A.; Caterina, M. J. *Nature* **2007**, *445*, 858–865.

(152) Vahl, A.; Carstensen, J.; Kaps, S.; Lupan, O.; Strunskus, T.; Adelung, R.; Faupel, F. *Scientific Reports* **2019**, *9*, 4361.

(153) Sun, F.; Lu, Q.; Feng, S.; Zhang, T. *ACS Nano* **2021**, *15*, 3875–3899.

(154) Wan, C.; Cai, P.; Wang, M.; Qian, Y.; Huang, W.; Chen, X. *Advanced Materials* **2020**, *32*, 1902434.

(155) Chen, S.; Lou, Z.; Chen, D.; Shen, G. *Advanced Materials* **2018**, *30*, 1705400.

(156) Zhang, C.; Ye, W. B.; Zhou, K.; Chen, H.-Y.; Yang, J.-Q.; Ding, G.; Chen, X.; Zhou, Y.; Zhou, L.; Li, F.; Han, S.-T. *Advanced Functional Materials* **2019**, *29*, 1808783.